University of Catania
Dipartimento di ingegneria civile ed architettura
Thesis for degree of Doctor of Philosophy in Valutazione e mitigazione dei rischi urbani e territoriali - Cycle XXXIII - 2017/2020

RIGID BODY SEISMIC VULNERABILITY AND PROTECTION BY MEANS OF LOW-COST ROLLING BALL SYSTEM ISOLATOR: NUMERICAL AND EXPERIMENTAL ANALYSES

Giuseppe **Cocuzza Avellino**

Coordinator:
Prof. *Massimo* **Cuomo**

Supervisors:
Prof. *Nicola* **Impollonia**
Prof. *Ivo* **Caliò**

Co-Supervisors:
Prof. *Francesco* **Cannizzaro**
Prof. *Enrico* **Tubaldi**

Rigid body seismic vulnerability and protection by means of low-cost rolling ball system isolator: numerical and experimental analyses

A thesis submitted for the degree of
Doctor of Philosophy

Giuseppe Cocuzza Avellino

Supervisors:
Prof. Nicola Impollonia – University of Catania
Prof. Ivo Caliò – University of Catania

Co-Supervisors:
Prof. Francesco Cannizzaro – University of Catania
Prof. Enrico Tubaldi – Strathclyde University

Coordinator:
Prof. Massimo Cuomo – University of Catania

Valutazione e mitigazione dei rischi urbani e territoriali
cycle XXXIII

Dipartimento di ingegneria civile ed architettura
University of Catania
2020

Dedications

to my love, Alessia

Abstract

The study, taking advantage of an extensive experimental campaign using a unidirectional shaking table, is focused on the mitigation of the response of small-scale rigid bodies.

After investigating their seismic vulnerability, a low-cost rolling ball system device is proposed to assure seismic protection. The experimental time history in terms of displacement was evaluated by tracking the motion with a contactless measuring method, making use of high frequency acquisition camera and tracking motion software.

Preliminarily, an experimental survey on the seismic response of small rigid blocks, with different aspect ratios and scale factors, is presented with the aim of identifying the features to be accounted for in order to gauge response variability. The results are reported in terms of *stability spectra* for one-cosine pulse input and *maximum rotation variability graphs* for a given earthquakes. The conclusive remarks help to assess the risk with respect to overturning under seismic excitation and enrich the interpretative model of the effects due to impairments in the contact surfaces. A marked uncertainty in the response of the blocks is identified and discussed. A novel numerical model based on rigid body motion able to account for the asymmetry of the object as well as for its flawed contact on the base is presented and duly validated against experimental tests.

The validation of the proposed model is achieved comparing the results of the numerical simulations with the experimental ones acquired on nine wooden prismatic blocks and on a scaled prototype of the masterpiece of Paolo Orsi museum in Syracuse (Italy): the statue of Venere Landolina. In the latter case, the experimental campaign is conducted on a physical prototype, built according to a highly detailed and complete digital model obtained by 3D survey. The numerical and experimental campaign is conducted with reference to compatible seismic

ground motions, conveniently scaled to cope with scale effects. The results are finally correlated and discussed, showing the potentiality of the proposed approach for modelling artworks in seismic conditions and the reliability of a combined experimental and numerical strategy to assess the seismic safety of real statues by experimentally investigating the nonlinear dynamic response of scaled objects on the basis of a detailed 3D digital model of the real object. The conclusive remarks could be of help to size the risk with respect to the overturning of rigid bodies under seismic excitation and to provide some considerations with respect to seismic protection strategies useful to design isolator devices. The proposed practiced solution to cope with overturning is the use of a wooden rolling ball system device, characterized by a series of balls rolling between two appropriately shaped plates carved by a milling machine. The efficiency of the proposed low-cost device is tested with a prototype designed to guarantee stability under minimum size constraint, while providing a long isolation period as well as recentring capabilities. Experimental tests have been carried out to characterise the behavior of the device also in case of rubber layers applied on the surface of spherical grooves to enhance the dissipation capacity.

The experimental campaign has allowed calibrating the device properties in terms of rolling friction and to investigate the response variability under different vertical loads. Furthermore, numerical analysed, where the restoring force is modelled using Bouc-Wen approach, were performed and validated by free vibrations and harmonic excitation tests. A second prototype, equipped with a supplemental mechanical fuse able to support vertical loads in static conditions, is realized and investigated. The efficiency of the device was experimentally evaluated by estimating the effectiveness for the protection of the statue of Venere Landolina.

Acknowledgements

I wish to express my sincere gratitude to Proff. Nicola Impollonia, Ivo Caliò and Francesco Cannizzaro for their invaluable supports, advice, and encouragement as supervisors of the project. This work would not have been possible without your great help.

My special appreciation and thanks to Prof. Nicola Impollonia, whose fundamental guide helped me for my growth at work and beyond.

My sincere thanks to Prof. Ivo Caliò for sharing the results of his research work.

A special note of gratitude to Prof. Francesco Cannizzaro for all his suggestions and mostly for helping me in the implementation of numerical code.

I wish to express my special appreciation to the staff of the Department of Civil and Environmental Engineering of the University of Strathclyde in Glasgow, in particular my special thanks are extended to Prof. Enrico Tubaldi for his support and hospitality.

I am grateful to the management, staff, and students of University of Catania who assisted me throughout my years of study.

I would like to acknowledge Prof. Gianfranco Gianfriddo and his collaborator Davide Cassarà and Michael Costantino for all the suggestions in the use of the equipment of wood facility at Sds Architecture in Syracuse.

I would like to extend my thanks to Prof. Rita Valenti and her collaborator Emanuela Paternò for the support provided during the survey phase of the statue of Venere Landolina.

I also thank the graduate student Alessia Di Martino for her contribution during the realization of Venere Landolina scaled prototype.

I express my gratitude to the management of the “Paolo Orsi” museum, in particular Dr. Maria Musumeci, for her thoughtfulness toward the seismic protection of the

museum content and for the authorization to carry out the survey of the Venere Landolina.

Moreover, I want to thank the management of the Regione Sicilia who believed in the research and financed my scholarship.

Finally, I am grateful for the unconditional love and support of my family.

List of figures

List of tables

Table of contents

Chapter 1 Introduction

This work presents an innovative rolling ball pendulum system device made with low-cost materials, designed for the protection of small-scale objects, e.g. machineries and free-standing art objects and more in general content of buildings, and developed for application on a large scale. The study aims at conceiving a new isolating device and the subsequent low-cost realization, experimentally identifying the dynamic behavior of the isolator, validating the theoretical models used for the numerical analysis and clarifying the aspects underlying the design of the device in relation to the performance of the assets to be protected. In fact, it is known that the buildings content presents high seismic vulnerability with respect to overturning, even in the occurrence of low intensity earthquakes. Within this framework, it is necessary a preliminary focus on the dynamic response of rigid blocks to define the level of seismic vulnerability. Consequently, the performance that the isolating device must guarantee and the study of the seismically protected systems should be investigated. This section elucidates the motivation and the aims of the research topic.

1.1 Motivation

In the last few years, researchers made important advances in the field of seismic engineering and structural damage mitigation. However, the damage is not limited to the structure but it often extends beyond the implants, countertops, and partitions. The loss of these assets represents an obstacle to the normal execution of human activities, prevents the efficient provision of services and stops the normal use of building. The operativity is not only connected to the protection of structural or non-structural parts but also by the functionality of the equipment (e.g. buildings with strategic functions). The protection of the content has recently gained the attention of the scientific community, mainly regarding three categories of assets.

The first asset typology is machinery located inside strategic buildings, such as *hospital equipment* which have to keep their operability in the aftermath of earthquakes. The second typology is constituted of *laboratory and electrical equipment,* whose malfunctions or outage in assembly lines may create significant inconveniences. The third typology is related to *artworks* (e.g. statues, vases, ceramics, and artifacts) whose damage may imply a significant cultural loss in terms of historical values, know-how and knowledge. Museum assets represent the category of objects capable of condensing many of the problems encountered in the seismic response of buildings content. In fact, these assets include a wide variety of geometric shapes, often characterized by extreme features, such as irregularities, caused by the passage of time, high aspect ratio values, and asymmetries. These characteristics make the artifacts more susceptible to the occurrence of phenomena that could compromise their stability and analysis, and the consequent seismic protection represents a challenging issue for the academic community.

In the case of museums content, their value is sometimes greater than the buildings itself. Some researchers devoted their efforts to the safeguard of single highly evocative pieces with ad hoc studies, on the other hand the huge quantity of less known yet important artifacts has been mostly neglected. In particular, aiming at the safeguard of large collections, more general large-scale approaches should be preferred to methodologies focused on individual case studies. A review of existing technologies readapted for extensive use[1], is therefore needed. Although the modern

[1] Nevra Ertürk, *Seismic protection of museum collections: lessons learned after the 1999 earthquakes in Turkey*, Metu Jfa, 2012, p.297.
The issue of the protection of museum collections through low-cost systems has already emerged from the reports drawn up after the 1999 earthquake in Turkey.

techniques of seismic protection, such as isolating systems, are widely used, their large-scale application is not been achieved yet. The reason of this incomplete success depends on the manufacturing cost, which requires the use of industrial materials and equipment. To overcome these limitations, the possible solution could be represented by the realization of a device made with low-cost materials, according to simple manufacturing. For this reason, the rolling ball pendulum system isolator has been chosen for this research also in view of the limited amount of parameters needed for its characterization. The simplicity of the manufacturing process and the limited production costs could make such an approach appealing and could open a way for large scale applications for an effective seismic protection of buildings content.

1.2 Aims and methods of the research

The thesis is focused on the structural behavior of museum collections and their seismic protection employing rolling ball system pendulum devices. The vulnerability assessment of museum assets cannot be treated as other simpler buildings content because of their extreme characteristics, related to complex geometric shapes or the use of perishable materials, which might increase the propensity of the objects to overturn. Different techniques have been conceived to increase the ability of an object to withstand earthquake events, but their application is often specific for certain object typologies. Unlike modern equipment, often characterized by simple geometry and good quality materials, the definition of the propensity to overturn of museum assets is more difficult due to their extreme attributes. For the latter reason, the simple rigid block model, commonly adopted to simulate the behavior of free-standing objects, must be updated and adapted to better define the performance of museum assets with geometric irregularities. It is known that the real behavior of the rigid block is chaotic and difficult to predict due to several factors. With regard to the specific features of irregular free-standing objects, three main aspects are faced in this study, namely the asymmetry of the objects, the

irregularities of the contact surface, and a straightforward identification of the impact conditions. The results obtained from shaking table tests on small bodies, affected by imperfections allow introducing convenient changes in the equation of motion and defining realistic impact condition to better interpret the rigorously unpredictable response. In fact, small blocks, due to the negative stiffness, avoid the undesired resonance phenomenon, and are not affected by permanent displacements thanks to the recentring effect guaranteed by gravity; but they are often keen to overturning because of the small rotational inertia involved, which is a consequence of their small size. The interpretation of the experimental results was crucial to develop a rigid block based numerical model effective in presence of contact impairments, necessary to predict the dynamic response of asymmetric bodies. The proposed numerical model implies the modification of the governing equation of rigid body motion and requires the introduction of two new parameters: the first one, that can be experimentally determined, takes into account the effects of imperfections and expresses a reduced uplift acceleration; the second one governs a transition between incipient uplift and full rocking motion. The numerical model set up is the outcome of a vast experiment campaign conducted on bodies with different size, aspect ratios, materials, shapes. Test protocols for the correct acquisition of the dynamic response have been defined according to the employment of a videogrammetric strategy.

This study is focused on the response of small objects essentially for two reasons. The first reason is related to the significant influence that imperfections have on the response small rigid bodies; in addition, low-cost isolating devices, may have a limited bearing capacity so they are suitable in the case of lightweight objects. As regards the device, the experimental analyses aim at defining the procedures for its characterization, at evaluating the effects of geometrical alteration of the grooves caused by concentrated vertical loads, at assuring an activating lateral force to avoid

undesired displacements in absence of horizonal accelerations, and at avoiding the formation of pits on the surface of spherical grooves due to the indentation phenomenon.

In summary, in this study the main aspects influencing the seismic performance of small rigid bodies related to geometric imperfections are accounted for; a novel numerical interpretation of the dynamic response of rigid bodies is proposed; in addition, a low cost isolating device based on a rolling ball system approach is designed, assembled and tested. The characterization of the proposed rolling ball system pendulum device was carried out and its main drawbacks are identified and tackled.

1.3 Outline

The thesis collects the contents in seven chapters as specified below.

Chapter 1 - Introduction

In this chapter the motivations, the objectives and the main topics of this research are described.

Chapter 2 – State of the art

In this chapter the literature was analysed to have useful information regarding the understanding of the structural behavior of objects considered as rigid blocks. The main criticisms on the rigid block classic theoretical formulations are highlighted. In this section the role of experimental analyses was also revealed in relation to the difficulties encountered in the study of rocking. This chapter highlights the problems related to the limits of existing numerical models, based on theoretical approaches, to characterize the behavior of the rigid block, and how experimental campaigns are crucial to identify phenomena otherwise difficult to observe. Then, the strategies for risk mitigation of museum content are described, presenting advantages and disadvantages of conventional and unconventional protection techniques.

Finally, the numerical formulations describing the ball pendulum system isolator response and the main problems emerged from previous experimental activities are presented.

Chapter 3 – Experimental equipment and measurement protocol

In this chapter the issues encountered in the study of the behavior of the rigid block are summarized. Considering that rocking systems are extremely sensitive to changes in the boundary conditions, an acquisition system was specifically conceived. The data acquisition was based upon monitoring target points suitably positioned on the specimen, using a camera with high-resolution and high frequency of acquisition. The lab equipment is described and a protocol for contactless measurement is presented. Finally, the advantages that derive from the use of the adopted methodology are described.

Chapter 4 – Dynamics of rigid body

The observation of the experimental tests guided towards the definition of a novel numerical model able to account for the asymmetry of the blocks, for a more accurate simulation of the contact conditions and for response variability caused by imperfections in the contact surface. The behavior of the rigid block is investigated from an experimental point of view with the aim of identifying the causes that influence the variability of the response. Nine wooden specimens, with different ratios of scale and slenderness, were subjected to free rocking motion and subsequently tested on a single degree shaking table under cosine pulse input and Friuli earthquake ground motion. The experimental results, reported in terms of *stability spectrum* and *maximum rotation variability graph*, show the limit of classical theoretical formulation. The numerical results are finally discussed showing the potentiality of the proposed procedure for modelling bodies with imperfections and pronounced asymmetries under seismic conditions.

Chapter 5 – Dynamics of rolling ball seismic isolator

This chapter is focused on the introduction of a low-cost rolling ball system pendulum isolating device. The proposed system is described, and a wooden prototype is made, according to a proper design methodology, and then experimentally tested. Experimental parametric analysis of the main variable that characterize the device are reported together with the procedure for identifying them through free vibration tests. The experimental results under forced vibration for sinusoidal input are compared with those obtained by numerical procedures.

To avoid undesired horizontal displacements in static condition associated to the low lateral stiffness of the device, it was endowed with an additional release mechanism that was further tested.

Chapter 6 – Case study: Venere Landolina statue

This chapter is focused on the seismic behavior of statues which generally present a quite complex geometry and are mostly characterized by a pronounced unsymmetrical response under seismic excitations. The proposed study involves both numerical analyses and experimental tests and is applied to the masterpiece of Paolo Orsi museum in Syracuse (Italy), that is the statue of Venere Landolina.

The study shows the results of the experimental campaign conducted on a scaled physical prototype with reference to compatible seismic ground motions, suitably scaled. The prototype was built according to a highly detailed and complete digital model obtained by 3D survey,.

The experimental results are finally correlated with those obtained using the numerical model in order to assess its potentiality and reliability.

Chapter 7 – Conclusion

This chapter summarizes the main results and achievements of the research.

Chapter 2 State of the art

The definition of seismic vulnerability of artworks which can be modelled as rigid bodies requires to understand their structural behavior, so to define the phenomena that influence their stability and the dynamic response. Pioneering studies, e.g. [1]-[2], are based on the calculation of response of the rigid body using a dynamic approach. From the structural point of view, the study can be carried out referring to the rigid block model. Over time, many authors contributed to refine the knowledge on the response prediction, in particular interpreting debated phenomena, such as the impact conditions or defining appropriate moment-rotation relationship. From the results of these studies it was possible to guide the choices for risk mitigation of artworks and to develop the methods aimed at increasing the protection of museum collections in case of earthquake. An overview of these techniques is shown in the following for traditional and innovative strategies. A proper solution for the seismic protection of artifacts is represented by seismic isolation. Indeed, this is capable of getting rid of many of the problems encountered in the case of risk mitigation of museum assets, such as the restoration of pre-intervention conditions or the possibility to avoid obscuring the visitors' view. An overview of several possible solutions is shown with preference to simple and low-cost devices. The behavior of ball pendulum device is analysed from a theoretical point of view, identifying those parameters that mainly affect the seismic response.

2.1 Seismic vulnerability of rigid bodies

The eastern Mediterranean Area is well known for its high seismic activity. Here the countries, such as Italy, Greece and Turkey, are often directly affected by earthquakes with high or moderate intensity causing, in the first scenario, even the loss of human life but in general, serious damage to buildings and their contents.

The latter aspect should not be neglected because these countries host much of the cultural heritage that characterizes the civilization of the West. Among the cultural assets to preserve, the focus is not only on the most famous masterpieces but also the multitude of artefacts exhibited in museums and inside their warehouses. Analysing the effects of the recent seismic events that involved Italy in 2009 (Aquila, magnitude 5,9) and Greece in 2007 (Kefalonia, magnitude 5,9), or even earlier, Greece in 1999 (Athens, magnitude 5,4), it is evident that the small free-standing art objects are characterized by a high seismic vulnerability even for earthquakes of moderate intensity, Figure 1.

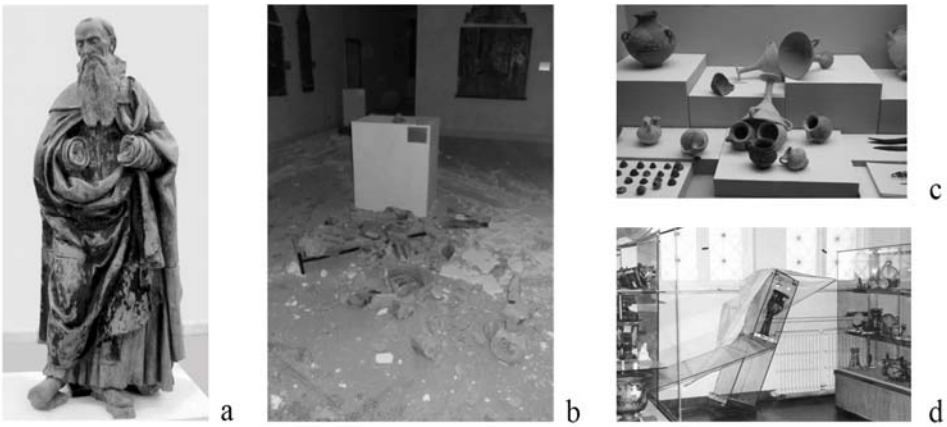

Figure 1 - Damage suffered by museum assets due the seismic event: (a) Saturnino Gatti statue before Aquila earthquake; (b) Saturnino Gatti statue after Aquila earthquake; (c) artifacts exposed at the Archeological Museum of Argostoli after Kefalonia earthquake; (d) artifacts exposed at the National Museum of Athens after Athens earthquake. [Images (a,b) from Borri and De Maria, 2011, (c,d) from Spyracos et al., 2008].

From the analysis of the damage caused by the main catastrophic events of the past, such as San Francisco earthquake in 1906, and Kobe earthquake 1995, which have affected the museum collections, it emerges that the exhibition methods can be considered inadequate. In Figure 2, it is evident that a large amount of lost assets was due to a lack of any seismic protection reasoning, both from the point of view of floor collocations, their supports and seismic protection measures.

Figure 2 - Damage suffered by museum assets due the seismic event: (a) artifacts exposed at the Stanford University of San Francisco after San Francisco earthquake, (b) artifacts exposed at the Archeological Museum of Kobe after Hanshin earthquake, (c) artifacts exposed at the National Prefecture Museum in Kobe after Hanshin earthquake. [Images from Podany, 2010 and 2016].

The fragility of historical artifacts such as those shown in Figure 1 and Figure 2 is high also because of the characteristics of their constitutive materials. Furthermore, the damage accumulated over time by artifacts, drastically modify their properties in terms of mechanical and geometrical characteristics. Consequently, it increases the propensity to collapse. Only after the San Francisco earthquake in 1989, as a consequence of the numerous lost collections, the specific vulnerability of small-sized museum assets was studied and primordial techniques for its risk mitigation were arranged. Only recently the effects of geometric imperfections have been considered in the vulnerability assessment of artifacts.

Nowadays, the sensitivity of researchers and governments has greatly increased. Alongside safeguarding museum assets with a high evocative content, protecting the infinite quantity of less known but yet important artifacts that compose the museum collections is a challenging concern.

In 2011 and in 2018 the Italian Code, introduced specific rules that still do not consider the uniqueness of the objects or the restrictions inherent their fragility, but consider innovative aspects and extend to artifacts the principles applicable to buildings. In particular, to preserve free-standing art objects, the Artistic Limit State (SLA)[2] was introduced. This sizes the seismic action for the risk assessment taking into account the location of artifacts within the building using specific floor response spectrum. The results of these analyses allow to define the expected losses and to evaluate the strategies for vulnerability mitigation, also applicable on a large scale as reported in section 2.3.

[2] Art objects contained in a building which during an earthquake of a certain level undergo limited damage and can be restored without significant loss of their cultural value.

2.2 Structural behavior of rigid bodies

The interest towards the seismic protection of artworks has been growing in the last decades. From the structural point of view, the dynamics of free-standing art objects can be carried out referring to the *Simple Rocking Model* (*SRM*). It is reasonable to assimilate the artifact to a rigid body because displacements are predominant over deformations. The *SRM* attracted the attention of many researchers who used the simple formulation to justify the overturning of structures with very different size factors and aspect ratios. A brief overview on the development of the research in the field of rigid block shows from one hand the great versatility of this model which can be successfully employed for very different cases and, on the other hand, the great difficulties encountered in providing a mathematical interpretation of the phenomena that influence the real behavior. This emerged from early research, as reported in the section 2.2.1.

2.2.1 Main evidence on dynamic response

The first studies involving the phenomena related to the stability condition of rigid bodies began with the work of John Milne in the late 19th century [3]. The author applied West's formula and the principles of Newtonian mechanics to determine the causes leading to the overturning of a body. The first complete studies on rigid block dynamics were conducted in [4] in which the equations of motion of the inverted pendulum were wrote and analytically solved in two-dimensional case. The model, Figure 3a, is based on the hypotheses of rigid block and foundation, assumes the instant change of the centre of rotation, the absence of sliding and bouncing, and energy dissipation at each impact.

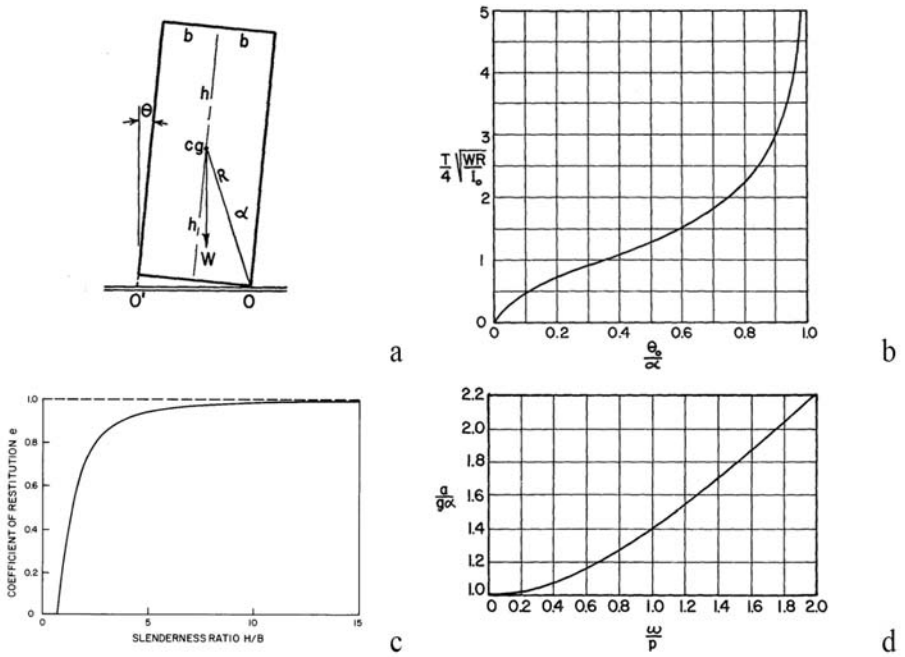

Figure 3 – (a) Housner rocking block; (b) Period T of block against rotation amplitude; (c) Stability spectrum for sine pulse; (d) Variation of the coefficient of restitution with slenderness ratio. [Images (a,b,d) from Housner 1963, and (d) from Yim et al., 1980].

The resolution of the equation of motion in the case of free vibrations showed that the block cannot be dynamically characterized by its fundamental vibration period, since the latter changes with the amplitude of the rotation. There is no natural period but a frequency parameter which changes the vibration period according to the amplitude of oscillation, as showed in Figure 3b. Moreover, the ability to dissipate energy depends on slenderness, Figure 3c. In [4], the author described a method for identifying the collapse of the block in case of seismic ground motion modelled as a succession of simple sine pulses. A remarkable result of this study is the definition of the stability spectrum where the capability of the block to rock without overturning is defined for each set of input parameters (half-cycle-sine-wave pulse), Figure 3d. Moreover, the minimum acceleration able to overturn the block was derived showing that the stability depends on the duration of the pulse.

Finally, by comparing cases with the same aspect ratio, in [4] was highlighted that blocks characterized by a smaller scale factor are more instable. So, there is a scale effect which makes larger blocks safer. The limits of the solution due to problem linearization, were overcome by the application of numerical integration procedures as proposed in [5]. The numerical results showed that the behavior is very sensitive to variations in slenderness, scale factor and characteristics of the seismic action. The results, shown in Figure 4a, underline that the response exponentially increases by assuming small variations of the initial conditions. An interpretation of this phenomenon was given by analysing the variations of potential energy in the condition of incipient overturning, Figure 4b. Therefore, the dispersion of the results shows that overturning is an unpredictable phenomenon that can occur also in case of low-intensity accelerograms. Consequently, the authors focused on the phenomena from a probabilistic point of view, modelling the seismic action as a random process, albeit preserving deterministic geometry. The analysis consisted in determining for different blocks the time-history rotation normalized by the critical angle for twenty scaled accelerograms.

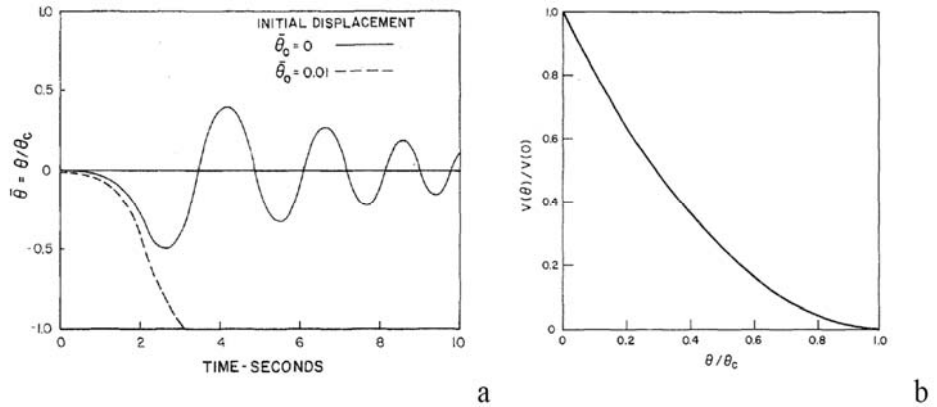

Figure 4 – Influence of variation of boundary condition: (a) experimental response of a block (r = 10 ft., h/b = 4) to a rectangular pulse of acceleration = 0.26 g and duration = 2.1 sec; (b) additional energy required to overturn a block with initial rotation. [Images from Yim et al., 1980].

The maximum rotation was re-arranged to plot a cumulative probability distribution function (CDF) that shows the behavior for different values of the coefficient of restitution and for different levels of intensity of the ground motion. The study demonstrates that the probability of the block to overturn increases with its aspect ratio and ground motion intensity, Figure 5a, whereas it decreases with the size, as already pointed out in [4]. Furthermore, the influence of the coefficient of restitution on the behavior of blocks is highlighted, Figure 5b.

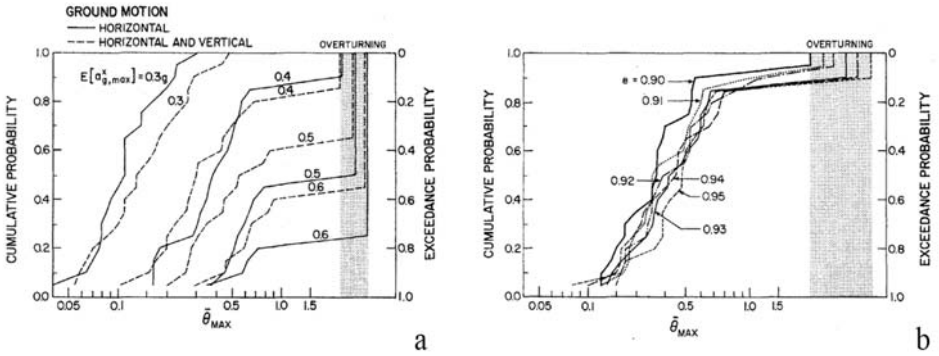

Figure 5 – Probabilistic analyses: (a) cumulative probability distribution functions for maximum rotation of a block and for various values of the coefficient of restitution; (b) cumulative probability distribution functions for maximum rotation of a block varying the peak acceleration. [Images from Yim et al., 1980].

This result is confirmed in [6] which emphasize that the difficulty of uniquely determining the restitution coefficient influences the correct interpretation of the structural behavior. The author reported: "*A small change in the value of coefficient of restitution completely changes the time-history response under the same ground motion*" (see Figure 6). Figure 6 shows that by tracing the time histories associated to two different coefficients of restitution, the response is not reproducible. Small changes in the coefficient of restitution, produce different responses as well as different instants of collapse.

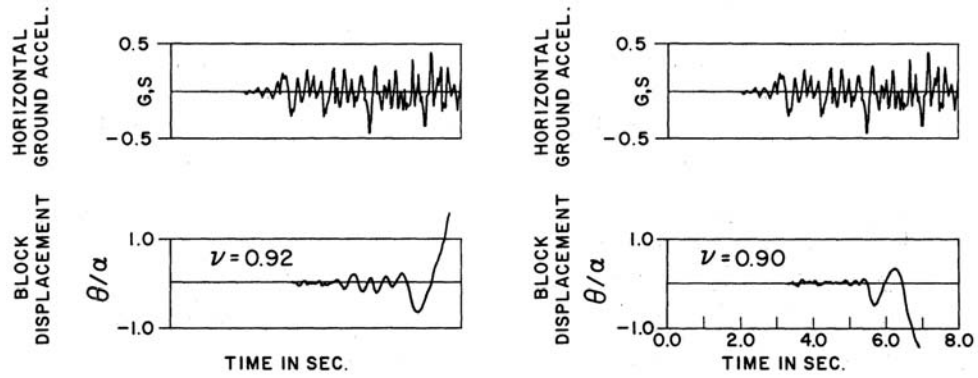

Figure 6 - Sensitivity to coefficient of restitution of rigid block 76,2x15,2 cm: (a) rocking response with restitution coefficient equal to 0,92; (b) rocking response with coefficient equal to 0,90. [Images from Aslam & Scalise, 1978].

The analyses summarized in [7], conducted on the two-dimensional rigid block model resting on a rigid foundation and subject to sinusoidal harmonic excitation, demonstrate the validity of the stability spectrum as a useful tool to characterize the behavior of the block. These maps, already introduced in an approximate way in [4], report the collapse mode related to the frequency and intensity of trigonometric input. The safe or unsafe zones are enucleated, and the modality of collapse is expressed by the number of impacts that the block exhibits before overturning.

The results were achieved through the development of analytical procedures (equivalent linearization method), that allows solving the dimensionless linearized equations of motion. The comparison with the direct non-linear integration is satisfactory for slender blocks with aspect ratios up to 2. Less accurate results are produced in the case of decreasing slenderness (squat blocks). Figure 7 confirms that the propensity to overturn decreases in case of greater dissipating capability of the system, i.e. for higher values of the coefficient of restitution. So, it has been analytically demonstrated that the safe zone of the stability spectrum significantly changes by varying the impact condition.

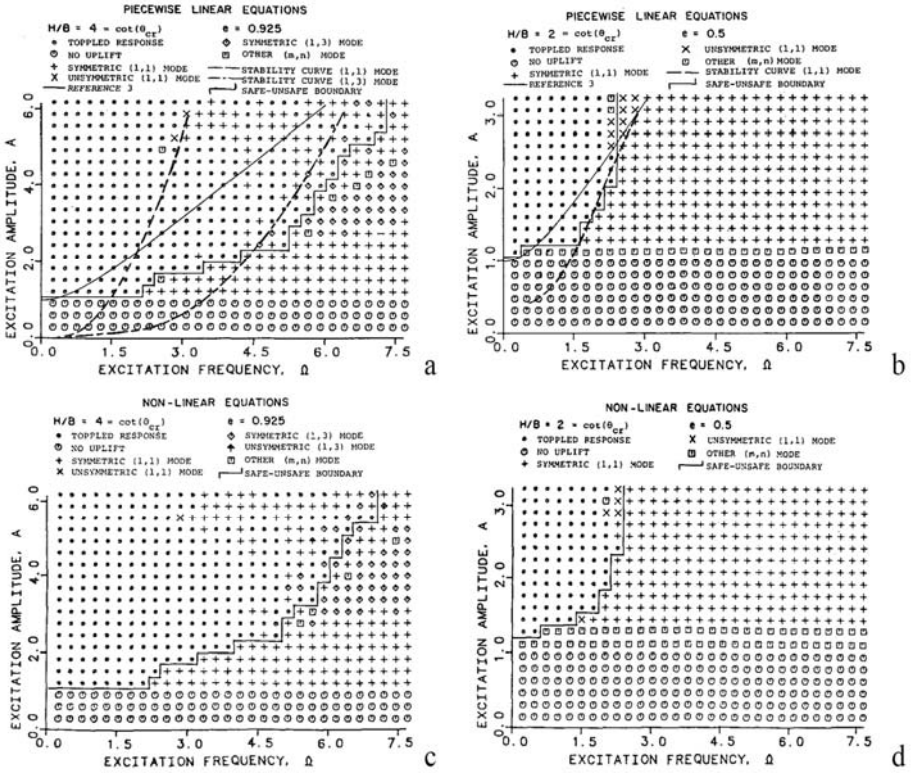

Figure 7 - Numerical stability spectrum obtained from linear and non-linear procedure. [Images from Spanos et al., 1984].

The revision of the hypotheses underlying the classical model was carried out in [8]. The unmatching between experimental and numerical outcomes was confirmed also in the case of free vibration. Numerical procedures have been developed to solve the equation of motion that is non-linear in two aspects. The first one is related to the presence of trigonometric functions, see Figure 8a, the second one is due to the discontinuity introduced by the instantaneous alteration of the velocity at each impact. When the block collides with the foundation, it goes from positive to negative rotations and *vice versa*, (this discontinuity is attested by the use of signum function as showed in section 2.2.2). The *SRM* is not able to describe all the phenomena that can occur during rocking and for this reason it often provides inaccurate results compared to the experimental data.

Although the standard model is able to interpret the behavior of slender blocks quite well, at least in the event of a limited number of impacts, the effects of geometric imperfections, such as an irregular base or absence of verticality, tend to accumulate discrepancies in subsequent oscillations, Figure 8b. More refined models, which remove some of these assumptions, focused on the response variability with the impact conditions. In particular, the coefficient of restitution should not be assumed constant for the entire duration of the test, Figure 8c.

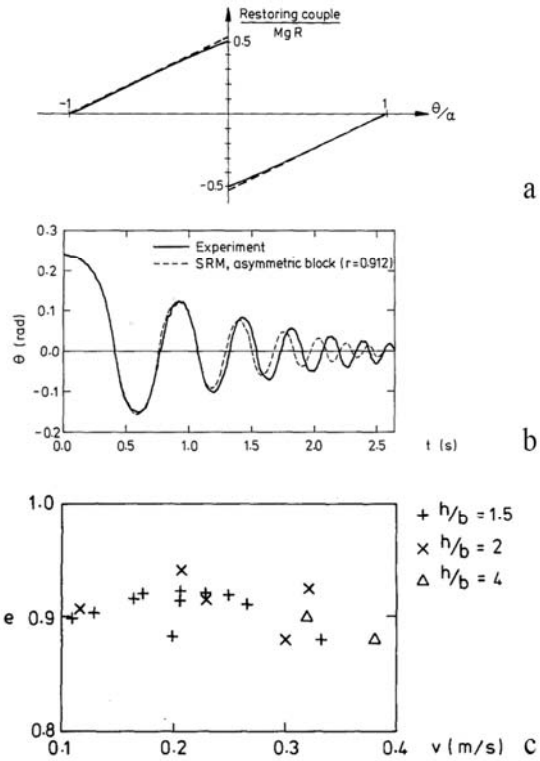

Figure 8 – Main characteristics of real behavior: (a) nonlinearity of the restoring force; (b) effect of imperfections in free vibration case; (c) validity range of the SRM model; (d) numerical variation of coefficient of restitution. [Images from Lipscombe & Pellegrino, 1993].

2.2.2 Classical formulation for symmetric rectangular block case

The first complete studies involving the rocking motion were conducted by G. W. Housner in 1963 who wrote and analytically solved for the first time the equations for the inverted pendulum in two-dimensional case. The formulation provides the study of the dynamic problem using two piecewise equations of motion which must be solved alternatively according to the sign of the rotation angle and the damping effects are accounted for by means of the coefficient of restitution. Although the *SRM* requires a significant computational effort, it was adopted in this study for its ability to relate physical phenomena to each parameter. As shown in section 4.1 this will be useful in the study of asymmetric systems[3]. The formulation referred herein as *classical theory* is shown below. A rectangular rigid block is here considered and characterized through its geometric properties, Figure 9. I_G is the moment of inertia respect to the centre of mass; b and h are the semi base and the semi height of block. The scale factor $d = \sqrt{b^2 + h^2}$ represents a measure of the size of the block, the aspect ratio, b/h, rules the incipient uplift, and finally the critical angle $\delta = \tan^{-1}(b/h)$ is associated to the overturning condition. When the block leaves the stick condition, it can exhibit different types of response, such as:

- sliding, when the block moves horizontally along its support and the friction force is lower than the seismic action;
- rocking, when the block exhibits rotations around its base pivot points;
- combination of the previous mechanism.

[3] In *Complex Coupled Rocking Rotations* (*CCRR*) method the rocking angle is assumed to be a complex quantity and the motion is governed by a single differential equation. In *Discrete Element Method* (*DEM*) the main parameters of model, as stiffness and damping, is obtained from fitting experimental results.

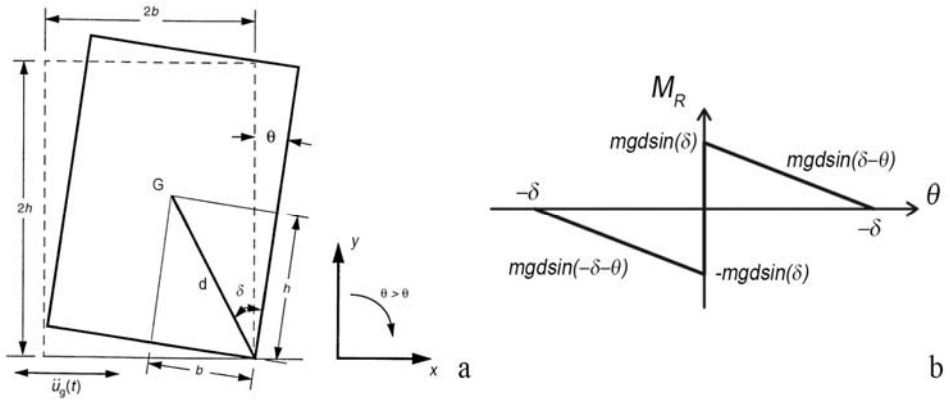

Figure 9 – Rigid block model: (a) scheme in rocking condition; (b) moment-rotation relationship. [Images from Zhang & Makris, 2001. Readapted by the author].

For each type of response, the behavior of the block can be described by suitable equations of motion. Here, only the rocking behavior is studied, so it is assumed that the friction coefficient is sufficient to prevent sliding at any instant. This condition is guaranteed when the friction coefficient is greater than $\mu = b/h$ as reported in [6]. The governing equation changes in relation to the phase of motion. Transition conditions are defined to govern the passage between the different phases. The first transition condition occurs when the uplift acceleration is reached causing the transition from full contact to the rocking phase [9]. The object begins to oscillate when the overturning moment M_D, due to external actions (Demand), is at least equal to the available stabilizing moment M_R (Resistance) associated to the gravity action. In this work the vertical component of the earthquake is neglected, and the stabilizing moment depends on the gravity acceleration only, eq. (3).

$$M_D = m\ddot{u}_g h \tag{1}$$

$$M_R = mgb \tag{2}$$

Re-arranging the eqs. (1) and (2) the uplift acceleration of the block, function of the geometric parameters only (West's formula), can be expressed as follows:

$$\ddot{u}^{(t)} = \frac{b}{h} g \tag{3}$$

where the superscript (*t*) indicates the theoretical uplift acceleration value. Eq. (3), determined from a static condition, shows that the block size d does not modify the uplift acceleration[4]. In the case of a "quasi-static" applied load, the contribution of inertia is not mobilized being the rotational accelerations negligible ($\ddot{\theta} \simeq 0$).
In the full contact phase, the object moves along with the ground, so that the block position is defined by the seismic displacement components. The equations that regulate the behavior when uplift has not occurred yet, are simply:

$$\theta = \dot{\theta} = \ddot{\theta} = 0 \tag{4}$$

When the block starts to oscillate, the equation takes the following form [10]:

$$\left(I_G + md^2\right)\ddot{\theta} + mgd\sin\left(-\delta - \theta\right) = -m\ddot{u}_g d\cos(-\delta - \theta),\ \theta < 0 \tag{5}$$

$$\left(I_G + md^2\right)\ddot{\theta} + mgd\sin\left(\delta - \theta\right) = -m\ddot{u}_g d\cos(\delta - \theta),\ \theta > 0 \tag{6}$$

Eqs. (5) and (6) show the dynamic equilibrium of the block: the seismic resistance (opposition to rocking) in on the left hand-side; the seismic demand (overturning seismic moment) is on the right hand-side. It is easy to notice that the seismic resistance contains a term proportional to d^2, being $I_G + md^2$ the rotational moment

[4] It can also be said that material properties, such as density, do not affect the uplift acceleration.

of inertia of the block around the pivot point. On the contrary, on the seismic demand side the terms are proportional to the first power of d . The introduction of the frequency parameter $p^2 = mgd/\left(I_G + md^2\right)$, expressed in rad/s, allows re-arranging the terms of the equation of dynamic equilibrium.

The frequency parameter, defined in [11] as: "*the frequency of the system due to the interaction between the block and its base, provides a measure of the dynamic characteristics of block.*". Clearly it should not be confused with any sort of natural frequency of the system, being the period related to the amplitude of oscillation. Introducing the frequency parameter and the signum function in eqs. (5) and (6), these can be expressed in the compact form:

$$\ddot{\theta} = -p^2 \left\{ \sin\left[\delta \operatorname{sgn}(\theta) - \theta\right] + \frac{\ddot{u}_g}{g} \cos\left[\delta \operatorname{sgn}(\theta) - \theta\right] \right\} \tag{7}$$

In case of rectangular block, the frequency parameter becomes $p = \sqrt{3g/4d}$ and the inertial properties are equal to $\left(I_G + md^2\right) = (4/3)md^2$.

The moment-rotation relationship shows that the block has infinite stiffness up to the magnitude $mgd \sin\delta$ of the unstabilizing moment, which represents the value of restoring moment immediately before the motion. Once this value is exceeded, the block begins to oscillate and the value of restoring moment decreases monotonically, reaching zero when $\theta = \delta$. The second transition phase is encountered at the end of each oscillation phase, when the rotation is equal to zero. In this case an impact occurs, and the centre of rotation passes from the right to the left edge in case of counterclockwise motion and *vice versa*. The phenomenon of the impact determines an energy loss which can be taken into account using the restitution coefficient, a parameter associated to the loss of kinetic energy at the impact. In case of rigid block

on a rigid foundation, this coefficient depends on geometric parameters only, however different formulations have been proposed by various authors (see section 2.2.3). Formally, it cannot be defined as damping because the path followed in the diagram (moment-rotation relationship) does not close any area [12].

The last transition phase is recognised when the vertical projection of the centre of gravity G falls outside the base footprint of the object. In this condition the block overturns[5]. The passage from one phase to another is marked by conditions that must be recognized and defined. Considering that the closed form solution of differential equation of rigid block is not available, numerical integration techniques are used. The numerical integration of eq. (7) is performed with standard ordinary differential equation solvers available in Matlab via a state-space formulation which can accommodate the non-linear nature of the problem [10]. The equation of motion can be effectively integrated using a 4^{th}-5^{th} order Runge-Kutta method and solved in terms of rotation. The rotational velocity reduction can be considered through the coefficient of restitution at every impact, that can be easily identified.

2.2.3 Contact models: the coefficient of restitution

One of the main problems affecting the rigid block is represented by the modelling of the dissipative effects through the determination of impact conditions. A wide literature on this topic was developed providing an interpretation of this phenomenon. The classical formulation, valid in the case of rigid block and rigid foundation, assumes that the collision is inelastic and models the impact with the adoption of a coefficient of restitution. It can be defined as a function of the geometry

[5] This condition is assumed as the ultimate capacity although the dynamic equilibrium equations also contemplates the possibility that the block returns from the critical configuration of incipient overturning to the rocking condition. Experimental evidence confirms that this phenomenon rarely occurs.

of the block, applying the principle of conservation of momentum in the conditions before and after the impact. The restitution coefficient is identified by equating the moments obtained from the rotational equilibrium around an edge, in the condition immediately before the impact, and the moments obtained from the rotational equilibrium immediately after the impact with respect to the same edge [8]. For instance, in the case of block rotating around the left corner, as in Figure 10, the left edge is the *contact point* and the right edge the *impact point*. In eq. (8), the terms on the left-hand and right-hand sides of the equation represent the linear and angular moments before and after the impact, respectively; the symbols $\dot{\theta}^-$ and $\dot{\theta}^+$ are the velocities before and after the impact, respectively. Consequently, the coefficient of restitution indicates the variation of kinetic energy due to the impact.

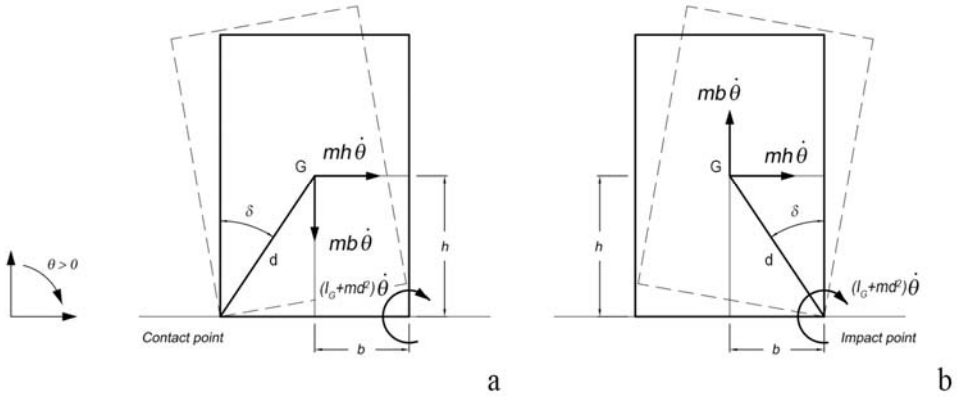

Figure 10 – Linear and angular momenta (a) before and (b) after the impact. [Author's image].

$$mh^2\dot{\theta}^- - mb^2\dot{\theta}^- + \left(I_G + md^2\right)\dot{\theta}^- = mh^2\dot{\theta}^+ - mb^2\dot{\theta}^+ + \left(I_G + md^2\right)\dot{\theta}^+ \tag{8}$$

$$e = \frac{\dot{\theta}^+}{\dot{\theta}^-} = \frac{\left[mh^2 - mb^2 + \left(I_G + md^2\right)\right]}{\left[mh^2 - mb^2 + \left(I_G + md^2\right)\right]} \tag{9}$$

There are various equivalent formulations to represent the coefficient of restitution. Without loss of generality, the theoretical coefficient of restitution e_T for a rectangular symmetric block is presented in the following eqs. (10)-(14). Rearranging eq. (8), the formulation proposed in [8] can be obtained, where the coefficient of restitution is a function of the geometric parameters b and h only:

$$e_T = \frac{2h^2 - b^2}{2h^2 + 2b^2} \tag{10}$$

Manipulating eq. (10), eq. (11) reported in [13] can be assumed as well :

$$e_T = \frac{2\dfrac{h^2}{b^2} - 1}{2\dfrac{h^2}{b^2} + 2} \tag{11}$$

The same expression in terms slenderness parameter $\lambda = h/b$ was adopted in [14]:

$$e_T = \frac{2\lambda^2 - 1}{2\lambda^2 + 2} \tag{12}$$

Starting from eq. (8), by carrying out simple algebra, the formulation proposed in [15] can be retrieved:

$$e_T = 1 - \frac{2b^2}{\dfrac{I_G}{m} + d^2} \tag{13}$$

Finally, considering the block base size in terms of scale factor, $b = d \sin\delta$, the classical formulation, valid for rectangular block, as proposed in [4], can be inferred as well:

$$e_T = 1 - \frac{3}{2}\sin^2\delta \tag{14}$$

The previous equations show that the behavior of slender blocks is characterised by inelastic impact and for values of $\delta > \sin^{-1}\sqrt{2/3}$, the impact becomes plastic [12]. The coefficient of restitution is a function of geometric parameters (in particular the slenderness λ), and assumes values between 0 and 1, where $e_T = 0$ means totally inelastic impact and $e_T = 1$ indicates a perfectly elastic impact. In the more general case of asymmetrical rigid block on rigid foundation, the restitution coefficient must be differentiated considering rotations around the left (subscript L) or the right edges (subscript R). In this case, the formulation reported in [16] can be adopted with reference to Figure 11.

$$e_{T,L} = \frac{\left(\frac{I_G}{m} + d_R^2\right) - \left(b_L + b_R\right) d_R \sin\delta_R}{\frac{I_G}{m} + d_L^2}$$
$$e_{T,R} = \frac{\left(\frac{I_G}{m} + d_L^2\right) - \left(b_L + b_R\right) d_L \sin\delta_L}{\frac{I_G}{m} + d_R^2} \tag{15}$$

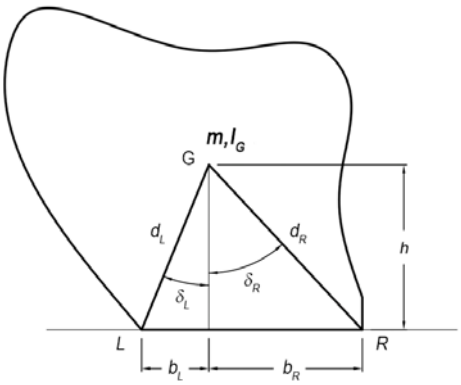

Figure 11 - Scheme for the determination of the coefficient of restitution in case of non-symmetric rigid body. [Images from Wittich, 2016. Readapted by the author].

In the literature there are alternative definitions of the coefficient of restitution, which take into consideration the simultaneous presence of rocking and sliding phenomena, as described in [17], or that the resultant of the impulsive forces does not pass through the edge of the block [13]. Although different theories have been formulated, in the following the classical theory is adopted, that is pure rocking is granted. For these reasons, the setup of the experimental campaigns described in Chapter 4 will reproduce the classical model assumptions.

2.2.4 Alternative moment-rotation relationships

There is a wide literature aiming at a correct modelling of rigid block systems in seismic conditions. The results of these models usually were compared with those of several experiments to validate the numerical response. The classical model is based on the perfectly rectangular geometry of the rigid block resting on a rigid foundation, with restoring force, depending on the weight of block, applied to the centre of gravity. The hypotheses assumed by the classical model are often irreproducible in practice. Consequently, the approach based on *SRM* must be abandoned. Over the years, several authors developed different approaches introducing alternative models trying to remove some of the hypotheses assumed by the standard model. In [18] and [19] an elastic contact element placed on the contact surface was introduced. The authors model a simple foundation using two sets of springs and dashpots, where each one consists of vertical and horizontal elements, Figure 12b. The separation of block from the ground is permitted modelling tensionless spring in vertical direction. Similar approaches, Figure 12c, consider a layer of springs and dampers at the base of the block as in [20].

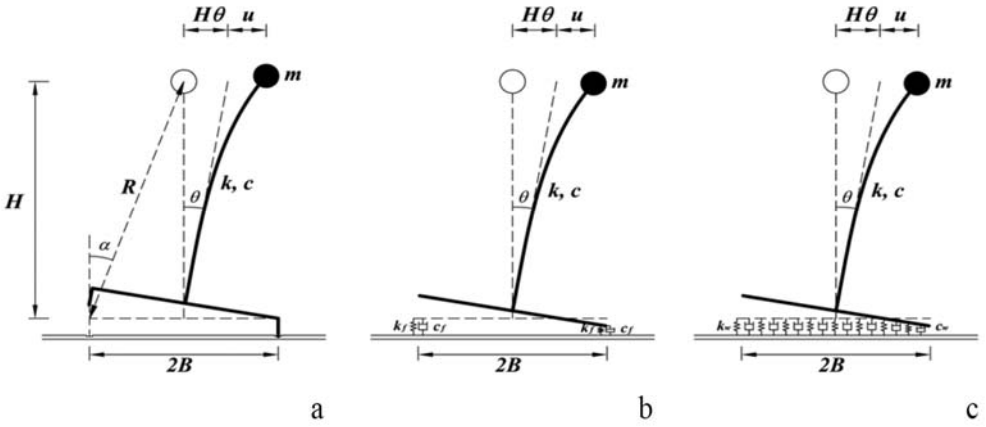

Figure 12 – The three categories of rocking interface: (a) rigid interface; (b) flexible rocking interface; (c) bed of compression-only spring (Winkler foundation). [Images from Chopra et al., 1985].

Starting from the analysis of the rocking behavior of masonry walls with base imperfections and subject to earthquake, three-branch models with finite initial rigidity have been developed in [21], Figure 13. This study, with regard to the capability to numerically reproduce the experimental results, highlights that: "*A marked improvement is achieved if the classical two-branch moment–rotation law is replaced by a three-branch law. The three branches are controlled by two nondimensional displacement parameters,* Δ_1 *and* Δ_2 *, which can be related to the geometrical imperfections of the base*". In fact, the experimental results reported in [21] show a reduced wall capacity due the reduction of the ultimate rotation caused by the deterioration of the edges and consequently of a not perfectly horizontal contact plane affecting verticality of the wall (in this case the specimen oscillates around an angle different than zero). The equations of motion were refined adding a function which modifies the shape of the classical moment-rotation relationship in relation to the oscillation amplitude, so to take into account all the mentioned imperfections. In case of semi rigid model, the hypothesis of rigid contact is removed.

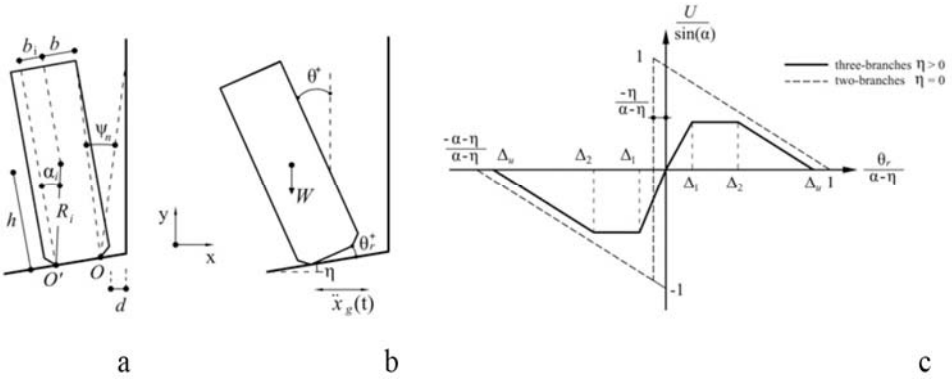

Figure 13 – Al Shawa model: a) scheme of the wall on tilt foundation; (b) causes of capacity reduction; (c) normalised restoring moment-rotation relationship in case of imperfections. [Images from Al Shawa et al. 2011. Readapted by the author]

A typical example is the *roll & rock model*, conceptually different from the previous one and more suitable for the aims of the present study, Figure 14. The effect of imperfections is treated by considering two phases associated to small and large oscillations [22], respectively. The behavior in the case of small vibration is modelled as linear elastic (not infinitely rigid) and only when a threshold angle value is exceeded, the block begins to exhibit negative stiffness, typical of rocking. This model is in agreement with the results of the experiments conducted in [13].

In fact, in the mentioned studies the following statement is reported: "*Experiments conducted on scaled model showed that is possible to measure a resonance frequency in systems composed by a single block that does not depend on the elastic deformability*". The author evidenced that the resonance frequency can be related to the convexity of the base of block and can be numerically interpreted by introducing an elastic branch in the classic model. The elasticity is a consequence of small rotations around a rounded base and is not referable to the rocking phenomenon.

In the case of small oscillations, the rolling phenomenon is recognized. Due to the presence of a rounded base, the centre of rotation moves continuously from one edge to the other; instead, in the case of rocking, the oscillation occurs alternately around the two pivot points, switching the centre of rotation at each impact. Although the

roll & rock law is applicable to cases of rigid contact models, it exhibits a behavior similar to the rigid blocks resting on an elastic support, which probably can be seen as an alternative interpretation of similar phenomena.

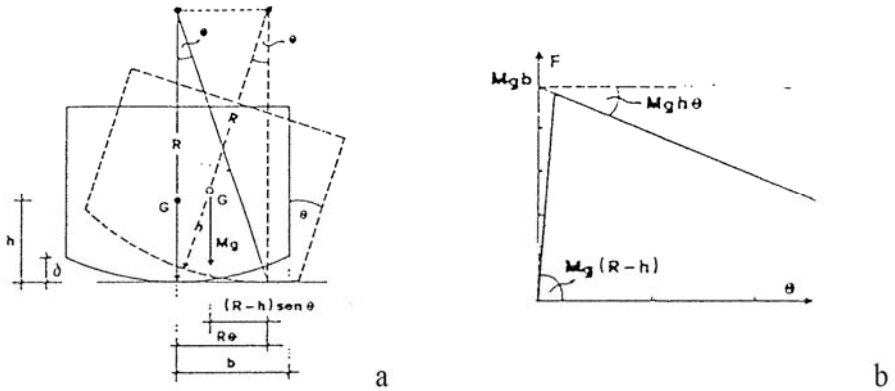

Figure 14 – Roll & Rock model: (a) scheme; (b) restoring moment-rotation law. [Images from Tocci, 1996].

More recently, a semi rigid block model has been presented where both phases of motion (rolling and rocking) have been modelled taking into account the fuse effect related to uplifting, Figure 15. In the model proposed in [23]-[24], the flat base of the rigid block presents massless curved wedges that extend the original base.

This trick allows adjusting the width of the base of the block, from $2B$ to $2B'$ and also changes the aspect ratio of the overall shape. The introduction of extension curved wedges introduces an additional form of motion, the rolling, which ends when the angle β is reached, Figure 15. The geometry of the curved wedge is regulated by the radius of curvature r, or by the dimensionless radius $\rho = r/2H$. When $\rho = \infty$, the characteristics of the block $2B'x2H$ are reproduced, vice versa when $\rho = 0$ block with size $2Bx2H$ is retrieved. Intermediate values of ρ influence the initial stiffness. Both the previous works employ linearized equations of motion.

However, considering the variety of shapes that can be found in the field of artistic heritage, it is preferable to adopt a large displacement approach.

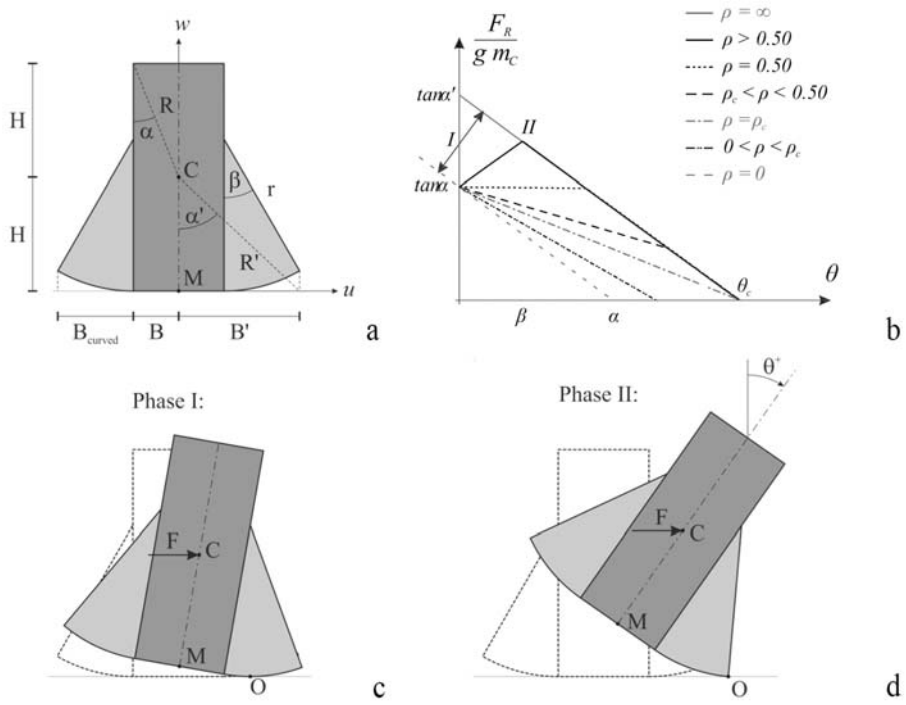

Figure 15 – Semi rigid block with curved wedges: (a) scheme; (b) rolling phase; (c) rocking phase. [Images from Bachmann et al., 2016 and 2019. Readapted by the author].

2.2.5 Chaotic character of rigid body motion

The correct interpretation of the rigid block response is a great challenge. One of the major problems is represented by the ability to correctly model the complexity of phenomena related to impact. Several studies have been carried out to compare the results of numerical integration with those obtained from experimental investigations. In particular, test results were shown in [6] in which free vibration tests and forced tests on concrete prismatic specimens with slightly concave base were performed. The results of this study suggest that an empirically restitution coefficient must be adopted in order to provide the best fit of the experimental

response with numerical data. Many authors, such as in [7] or [25], encountered the same issues, using different empirical values of coefficient of restitution, not derived from the conservation of the angular momentum, in their simulations. In general, such as in [6], a single representative coefficient of restitution (constant for all duration of test) is assumed for all impacts, Figure 16, achieving good match between experimental and numerical data[6]. From the analysis of the literature it emerges that the dynamics of the block is strongly influenced by the boundary conditions especially in case of forced tests[7]. Sensitivity to initial parameters is less pronounced in case of free vibrations test, if other conditions are fairly reproduced (for example specimens with a concave aluminium base or block equipped with steel rollers at the base edges). Without these artifices, the centre of rotation at each impact would not coincide with the two pivot points, being the impulse always placed at a generic distance from the edge.

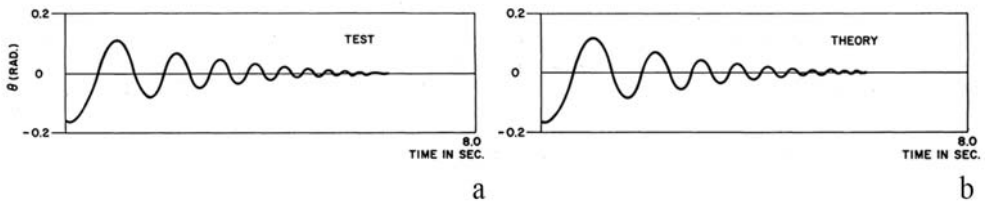

Figure 16 - Comparison of angular displacements of a freely rocking 76,2x15,2 cm block (coefficient of restitution equal to 0.925). [Images from Aslam & Scalise, 1978].

Consequently, the experimental results in case of free vibration can be repeatable as emerged also in [26], Figure 17a. Evidently, the coefficient of restitution fluctuates within a range of values that does not necessarily have a specific trend, especially in

[6] In this case the best match derives from the convexity given to the contact surface of the block.
[7] Very small perturbation drastically changes the character of the rocking response.

the case of materials that are incline to accentuate imperfections, (e.g. rubbers), as demonstrated in [26], Figure 17b. When the specimen exhibits high velocity, the sensitivity to inaccuracy of measurements, peaks detection, specimen imperfections, and small vibrations in the laboratory, is small. The author in fact reports: "…*for rotation amplitudes greater than 1º, the results were more uniform… predicting the free rocking amplitude response using SRM is possible if a reliable value for the coefficient of restitution is used…*". This may suggest the range in which measurements can be considered reliable and repeatable.

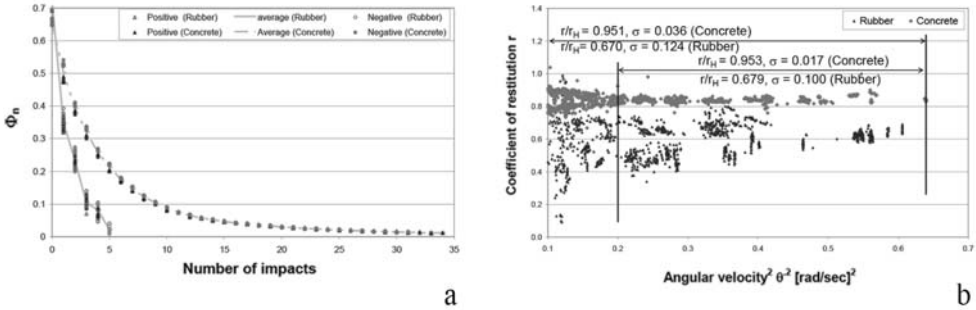

Figure 17 - Free vibration tests: (a) repeatability of results; (b) fluctuation of the coefficient of restitution. [Images from ElGawady et al., 2006].

In [16] the author considers that the differences between the theoretical and empirical values of coefficient of restitution depends upon geometric anomalies.

For this reason, the author suggests the use of a modified coefficient of restitution to match the experimental response. In the case of forced tests, the response of the block is more influenced by the anomalies (not-flat base, asymmetries, rounded edges) which cause the effects capable of drastically modifying the response also in case of accurate determination of the coefficient of restitution. This aspect was experimentally detected by Aslam [6] testing a specimen with a concave aluminium base. In fact, the author evidences:"…*the rocking response is extremely sensitive to the boundary condition at the base of the block… any slight convexity in the surface of the block or of the ground invalidates the results*". Furthermore, in [5] the author

highlights that: "*Experiments on the Berkeley shaking table indicated that the rocking response of a rigid block can be extremely sensitive to ground motion details. Repeated measurements of the response of a block subjected to prescribed table accelerations were not identical to one another. These differences were apparently due to the fact that the table undergoes slightly different pitching motions, even with the same prescribed horizontal accelerations*". Many authors tried to provide an explanation capable to identify the causes that influence the chaotic behavior of the rigid body motion. From the analysis of the literature, it emerges that the causes must be searched in the small perturbations of the properties of the oscillator, in the initial conditions, in the seismic excitation and in the impact modelling. Although models have been prepared capable of interpreting these aspects even today it is still difficult to accurately predict the response of the rigid body subject to ground input.

It must also be taken into account that some of these anomalies are difficult to model, as evidenced for example in [19] that reported: "*it is very difficult to predict exactly the location of the centre of rotation and the exiting angular speed after a rocking impact. This is due to a large number of uncertainties involved in the impact problem*". Indeed, the continuous degradation at the block corners, reduces the probability that the pivot point is located always at the same position representing another source of uncertainty. A methodology that abandons the idea of numerically retracing experimental time histories has been recently re-proposed in [23]-[24]. According to the authors, the response can be predicted in a statistical sense by adopting the strategy already proposed in [5]. The numerical analyses were validated considering the results of experimental activity using a specimen designed to minimize imperfections and to reproduce the conditions underlying the standard model (rigid body and impact on two infinitesimal contact areas). Moreover, the estimation of the restitution coefficient from experimental data allows to minimize

the uncertainties that characterize the problem. In this perspective, the experimental activity provides an important support for understanding the phenomena underlying the real behavior and exteriorizing the limits of theoretical formulations, Figure 18.

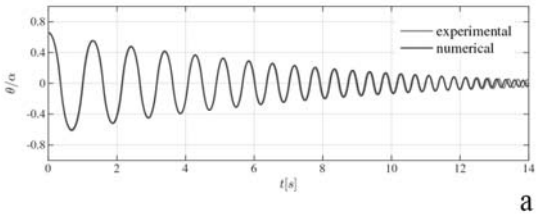

p_{exp}	r_{exp}	$r_{Housner}$	$\frac{r_{exp}-r_{Housner}}{r_{exp}}$
$4.8883s^{-1}$	0.9532	0.9465	0.70%

b

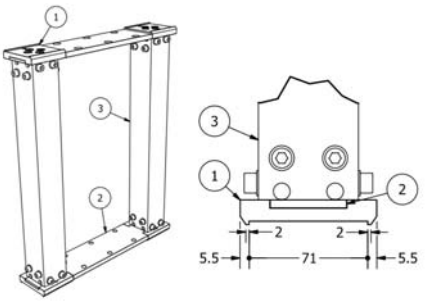

c

Figure 18 – Validation of numerical results using appropriate equipment: (a) comparison of numerical and experimental results in case of free vibration; (b) error respect theoretical formulation related to the identification of coefficient of restitution; (c) appropriate specimen. [Images from Bachmann et al., 2018].

In most of the published research based on experimental campaigns, a single restitution coefficient was used to numerically to interpret the experimental results. The differences between calculated and measured response emerge just after few cycles when the imperfections have a major role. Evidently the theoretical formulation is not always suitable for correctly interpreting the phenomena also when the coefficient is empirically identified. As seen, there are several phenomena that influence the real response of the block and they do not always play the same role in every experimental test; however, the interpretation of phenomena is facilitated when the anomalies are reduced. It is often hard to quantify the effect of a single irregularity because it is difficult to identify and measure. For this reason, it is suggested to opt for a strategy that evaluates the effects of anomalies on the response through the introduction of experimentally determined representative parameters.

2.3 Risk mitigation of small rigid bodies

The propensity to slide, rock or overturn of a rigid body can be mitigated using techniques that can be traced back to two major categories. Generally, the methods increasing the restoring forces or introducing some restraints are considered conventional strategies; on the other hand, all the techniques that alter the dynamic response using supplemental devices are considered non-conventional strategies. Many traditional methods are available for the mitigation of the seismic risk, but their effectiveness can be debated when compared to the use of innovative technologies. In the case of the protection of museum contents, the use of non-conventional strategies through passive methods as seismic isolation, is often preferable [27]. The cost is lower than that required by active systems, not requiring the use of electronic devices, sensors, actuators, and therefore its application on a large scale is possible [28]. Their effects on structural system can be clarified by analysing the terms of the classical equation of motion of a single degree of freedom system:

$$m\ddot{u} + c\dot{u} + ku = -m\ddot{u}_g \tag{16}$$

The introduction of a *Base Isolation System* (*BIS*), Figure 19, allows shifting the fundamental period of the system out of the range of dominant earthquake energy frequencies [29].

Figure 19 – Application of passive control: scheme to mitigate structural response using *BIS*. [Author's image].

Although the theoretical concepts which govern the structural behavior of isolated assets are the same as for buildings, the application of isolation technologies in the

case of content is quite different. The causes requiring a revision of the isolating strategy depends on the characteristics of the structural response of these objects, namely predominant displacements with respect to deformation, high vulnerability also for low seismic actions and the limited mass. A summary of the main advantages and disadvantages related to both protection strategies is reported below, Figure 20.

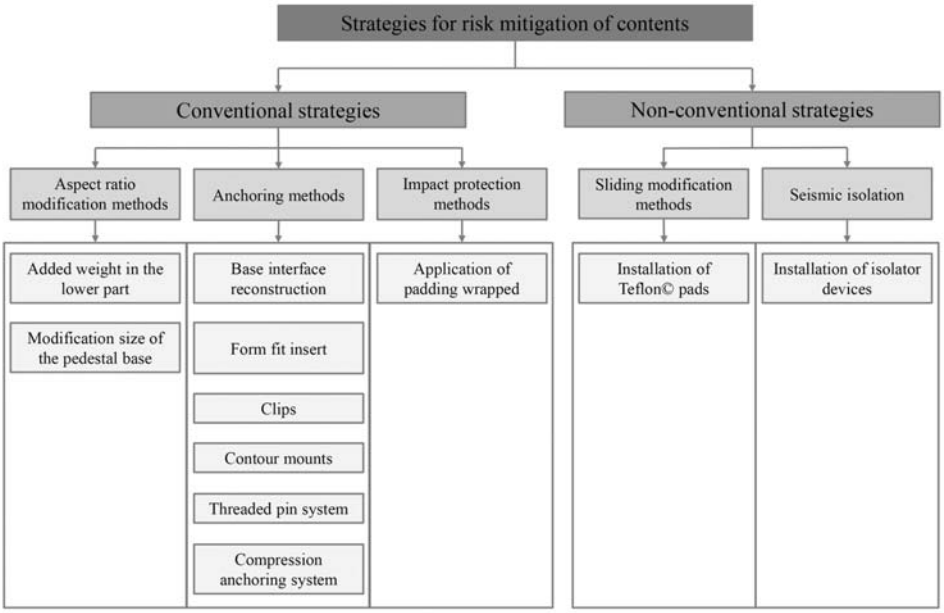

Figure 20 – Summary of risk mitigation strategies suitable for buildings content. [Author's image].

2.3.1 Conventional methods

Several inexpensive and simple tricks able to reduce the seismic risk of collections usually aim at altering the mass distribution of the object, for example adding weight, or securing the object to an additional mass. The West's formula, postulated in 1882, reveals that the geometric base-height ratio represents the critical acceleration which defines the uplift condition of the body. By observing the equation, it can be noticed how it suggests a first criterion to reduce the propensity to uplift by re-positioning the centre of mass. In particular, the stability grows up lowering the barycentre, and

this can be achieved by adding weight in the lower part or by increasing the size of the base. So, the definition of the position of the centre of gravity is a very important aspect. In all cases when specific instruments are not available, the position of the centre of gravity can be determined following simplified procedures based on measuring of the dimensions of the volume surrounding the object and assuming a uniform distribution of the weight [30].

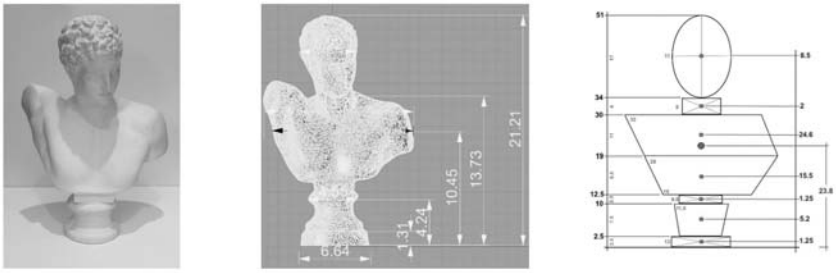

Figure 21 - Identification of the centre of gravity: (a) bust exposed at Getty Museum; (b) digital scanner of a bust at Getty; (c) example of multiblock approximation in case of complex volume. [Images from Podany, 2015].

A similar procedure, leading to a more precise evaluation, can be followed in the case of complex objects with an eccentric distribution of mass[8], Figure 21a-b.

The procedure considers the properties of simplified sub-blocks, which approximately reconstruct the shape of object by assemblage [31],[34], Figure 21c.

The strategy based on the repositioning of the centre of gravity is certainly a good solution, but it is not decisive or might not be pursued.

Another solution to reduce the overturning propensity, especially in the case of objects with high aspect ratio, consists in inhibiting the uplift through the use of

[8] Podany: "If the parts cannot be weighed, calculations can be made based on standard material property references"

supports, which must be made of resistant, non-corrosive and non-abrasive materials. Their shape is chosen to be easily replaceable and to distribute forces in large areas avoiding concentrations of stress in concentrated contact points.

This approach has some limitations. Fixing the object to its support produces a stress increase near the support areas which could lead to unexpected local damage. A portion of the forces transferred from the pedestal to the object, through the support, could damage the asset, so it is necessary to carry out an accurate definition of the state of stress in static and dynamic conditions. In addition, such strategy is difficult to apply in the case of assets made with low-strength materials, which are unable to tolerate even low-level stress [32]. More specifically, simple *anchoring methods* include interface reconstruction, *clips*, *contour mounts* and *anchor*. Objects not resting on flat support bases, require the regularization of the contact through the realization of a new surface, usually employing materials with high compressive strength as thixotropic epoxy resin, Figure 22a. The procedure is delicate because it must be ensured that the resin does not contaminate the object. Intact objects can be fixed to the support with *clips*, Figure 22e-f, generally applied to the base. In the case of objects with circular base, the elements are placed every 120 degrees whereas for square bases four elements are required, one on each side. An alternative is represented by *contour mounts*. This support system is made using a profile in cardboard, brass, aluminium or acrylic, which perfectly follows the shape of the object, Figure 22b-c-d-h-i. The frame must have felted internal surfaces, must be anchored to the pedestal and has to accommodate a monofilament to secure the object safely, Figure 22g.

Ultimately, when it is possible to drill the object, the threaded pin system represents a valid alternative.

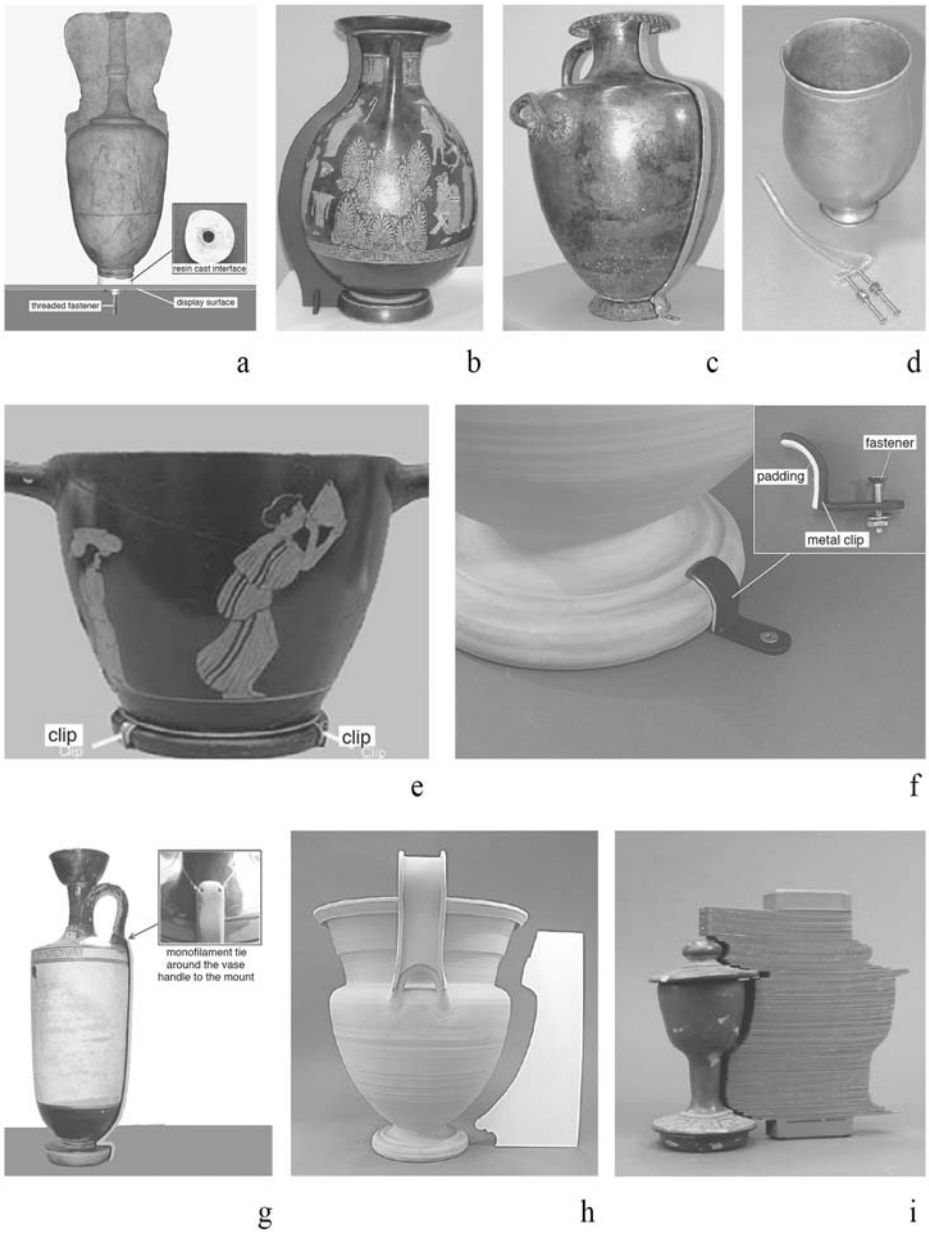

Figure 22 - Fixing systems for artifacts of Getty Museum. [Images from Podany, 2007 and 2009].

A further system, called *compression anchoring system*, was developed at Getty Museum, Figure 23a-d. The system is valid for objects with an irregular base surface [31]. Any movement is inhibited thanks to the application of a compression in correspondence of plates which perfectly adapt to the base of the object. The *compression anchoring system*, just like the previous ones, requires the control of the stress state at the contact surface of objects[9].

Finally, the preservation of objects in storage areas can be guaranteed with the use of *padding wrapped* around each object [33], Figure 24b-c, or applying woven plastic mesh on the free front of the shelves, Figure 24a.

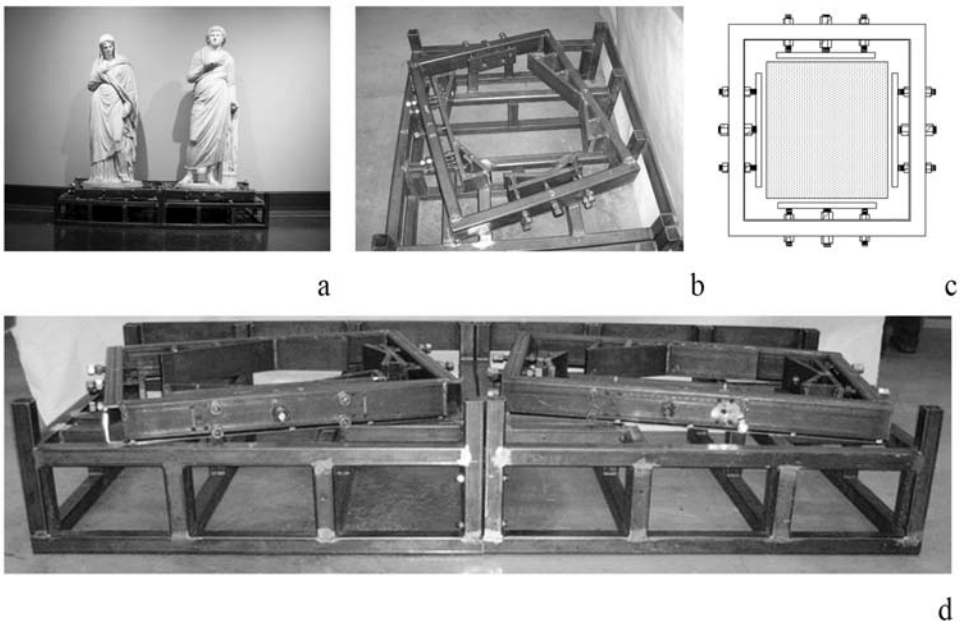

Figure 23 - Compression anchoring system: (a) example at Getty Museum; (b) single pedestal; (c) structural scheme of frames; (d) example of combining several pedestals. [Images from Podany, 2015].

[9] Stress analysis in historical heritage is complicated because the limits of the material are not always clear due to the passing of the centuries and the absence of specimens to be tested.

Figure 24 – Example of protection in storage areas: (a) application of mesh on the free front of the shelves; (b) wrapping objects in sheets of Ethafoam; (c) example of correct storage). [Images from Ertürk, 2012 and Podany, 2009].

2.3.2 Non-conventional methods

Seismic isolation is not a recent invention, as it was well known by builders and architects of antiquity such as Theodoros di Samo (VI sec. B.C.) who introduced some precautions in the construction of the foundations of temples. The first modern proposal of isolation for buildings was made by the engineer David Stevenson in 1868 who suggested to use steel balls between curved steel plates under the foundations of constructions. A rudimentary form of this technology is reported in the patent registered by Stevenson in 1889 (Figure 25a), Touallion in 1870 (Figure 25b), and later by Viscardini in 1909 [36], (Figure 25c). Subsequently, in 1987 the first application with the development of single concave friction pendulum isolator was presented by Victor Zayas [37], (Figure 25h). Although in first decade of the 1900s a rudimentary form of seismic isolation was proposed, as showed in Figure 25a-f, the simple principles underlying this technology were formalized only in recent years. The simple idea of decoupling the construction from the ground, in fact, is directly related with the ability to understand the dynamic behavior of structures. In the case of contents, the decoupling can be achieved by inserting an isolator device at objects base or pedestal. So, three parts of the system can be recognized: the

content (called superstructure), the isolating interface represented by the device, and the substructure (ground or pedestal).

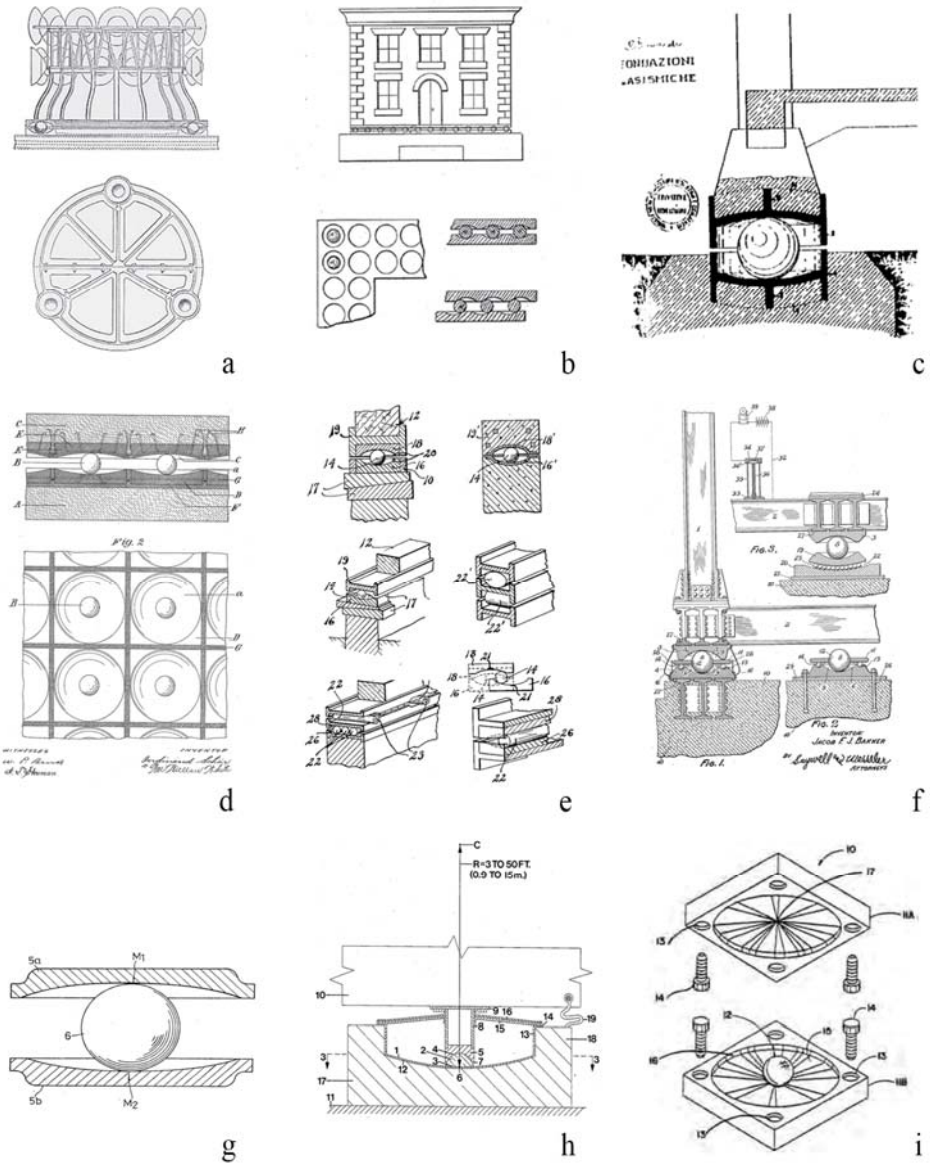

Figure 25 – Primordial seismic isolation: (a) Stevenson 1868; (b) Tuallion 1870; (c) Viscardini 1909; (d) Schär 1910; (e) Cumming 1930; (f) Bakker 1935; (g) Wu 1989; (h) Zayas 1987; (i) Kemeny 1997. [Images from Tsai 2012 and Podany, 2015].

The advantages deriving from the use of the seismic isolation include the reduction of inertia forces which are unstabilizing, and the stress reduction in the object and particularly at the base; the main disadvantage is the necessity to leave the surrounding area clear of obstructions to accommodate the estimated horizontal displacements.

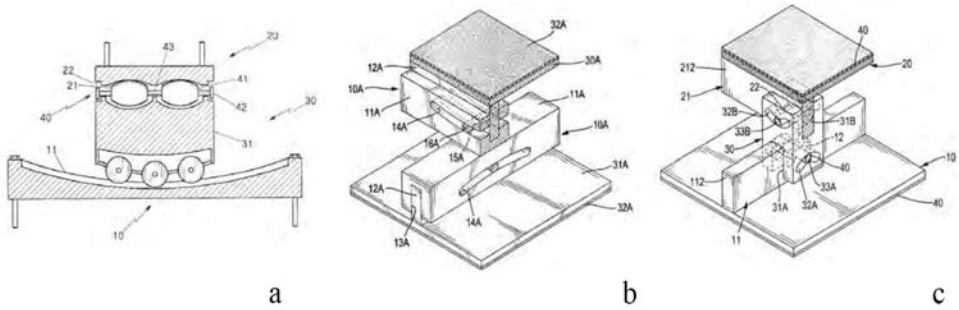

Figure 26 –Base isolation system for contents: (a) Kim 2004; (b) Tsai 2008; (c) Tsai 2008. [Images from Tsai, 2012].

The first cases of modern seismic isolation for museum collections were applied at Getty Museum based on a project drawn up in 1985 by Quantec Systems of California [31], (Figure 27). The device was made with a lower steel plate with concave shape where a vertical spring element is placed. The top frame completes the device and rests on the bottom frame through ball bearings. When the device comes out of the rest position, the spherical curvature causes the compression of the central pin, which has a high displacement capacity and increases the restoring force. This solution was later discarded, due to the lifting of the top plate and for problems deriving from the occurrence of large displacements at low accelerations.

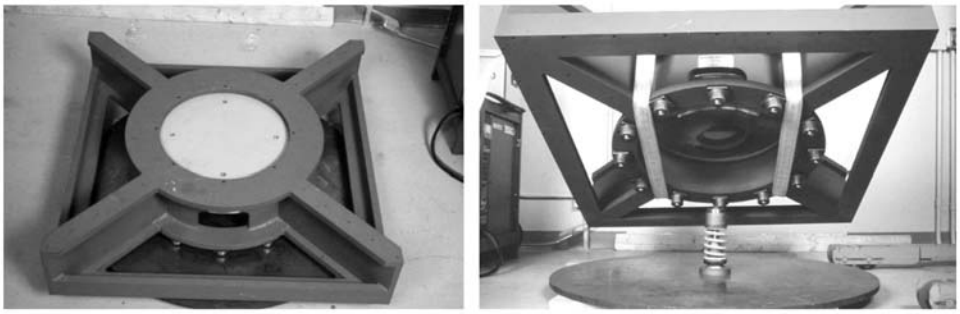

a b

Figure 27 – Device prototype made by Quantec Systems in 1985 for the Getty Museum: (a) top view of the top frame of device; (b) bottom view of the top frame of device. [Images from Podany, 2015].

Rubber system	**RRS -** Rubber Recentering Springs
Pendulum Sliding system	**SCFPS -** Single Concave Friction Pendulum System **DCFPS -** Double Concave Friction Pendulum System **VCFPS -** Variable Curvature Friction Pendulum System **MFPS -** Multiple Concave sliding surfaces Friction Pendulum System **XY-FPS -** Uplift Restrain Friction Pendulum System **TFPS -** Trench Friction Pendulum System
Pendulum rolling system	**BPS -** Ball Pendulum System **SDI-BPS -** Static Dynamic Interghangeable Ball Pendulum System **RPT-TMD -** Rolling Pendulum Tuned Mass Damper
Flat rolling system	**LRD -** Linear Rail Device **ERIS -** Eccentric Rolling Isolation System
Cone rolling system	**BNC -** Ball and Cone **SDI-BNC -** Supplementally Damped Isolation Ball and Cone **CFPBS -** Cone-type Friction Pendulum Bearing System **ISO-BSIP -** ISO-Base Seismic Isolation Platform
Simple Rolling system	**SSRB -** Sloping Surface Roller Bearing **OPRCB -** Orthogonal Pairs of Rollers on Concave Beds **PSBIS -** Pillow Shape Base Isolation System **ERIS -** Eccentric Rollering Isolation System
Hybrid system	**RBRL -** Rolling Ball Rubber Layer (Flat+Rubber Layer+Rubber Spring) **RLRB -** Rubber Layer Roller Beaing (Flat+Rubber Layer system) **DOFP -** Direction Optimized Friction Pendulum (SCFPS+TFPS) **RPTMD** – Rolling pendulum Tuned Mass Damper (BPS+TMD)
Foundation system	**PB -** Pendulum Base **RNC -** Roll in Cage **TROCKSISD** – Tribological Rocking Seismic Isolation Device

Figure 28 - Seismic isolation for seismic vulnerability mitigation of contents. [Author's image].

The disconnection of the content from the ground or pedestal can be realized with different techniques, see Figure 28. The first simple way to disconnect the object from ground or pedestal can be achieved by inserting flat plates resting on rubber cylinders (RRS). In this type of isolator, the fundamental frequency is related to the objects weight and to the stiffness provided by the rubber cylinders; therefore the design of the isolation system has to be adapted case by case. In addition, the characterization of the rubber can be done through experiments that require the use of expensive equipment and highly qualified workers. For these reasons, this solution can be expensive.

Friction Pendulum technology, widely used for buildings, can be adapted more easily than rubber spring systems in case of contents. In [38] it was demonstrated the applicability of this technology to the Francesco I D'Este's bust sculpted by Gian Lorenzo Bernini and exhibited in the Estense Gallery collection in Palazzo dei Musei in Modena. The simplest type of this device is the Single Concave Friction Pendulum Systems (SCFPS, Figure 29a) which requires the use of a skate that slides on a single spherical groove. The performance of the SCFPS has been improved with the development of the Double Concave Fiction Pendulum System (DCFPS) where the skate slides along two concave surfaces. As for all pendulum systems, the period of isolation does not depend on the weight of the isolated object but simply on the radius of curvature of the spherical groove [35]. Furthermore, the characterization of these devices is relatively simple being necessary the determination of the friction coefficient only. To avoid resonance issues, related to the period of isolated system, different devices were developed such as the Variable Curvature Fiction Pendulum System (VCFPS) and the Multiple Concave sliding surface Fiction Pendulum System (MFPS, Figure 29b), the DCFPS with an articulated slider, and the Direction Optimized Fiction Pendulum (DOFP, Figure 29c) with different shape of grooves which can be applied also in contexts where earthquake is characterized by long

dominant periods. The introduction of the Trench Fiction Pendulum System (TFPS, Figure 29d) made possible changing the dynamic property of the device (e.g. curvature radius) independently respect to two orthogonal directions. However, these systems are prone to collapse due to the uplifting of the upper plate and to occurrence of torsional movements. These problems were overcome by constraining the top plate of the device along the vertical direction as done with the Uplift Restrain Friction Pendulum System (XY-FPS, Figure 29e). The latter device consists of two orthogonal opposing concave beams interconnected through a sliding mechanism that prevents the uplift; in addition, it is able also to provide different stiffnesses and energy dissipations along two different directions. Isolators with rolling balls consist of two plates with a grooved face, not necessarily with a spherical shape (Figure 29h). As for sliding isolators, rolling Ball Pendulum System Isolator (BPS, Figure 29g) supports a simple design procedure, is capable of recentring and does not show any residual displacements after removing the applied excitation. Thanks to these qualities, this type of seismic isolation was proposed for the safeguarding of numerous assets such as for the “Annunciation” and the “St. Michele Arcangelo” at the Opera in Duomo Museum of Orvieto and for “Michelangelo's David” preserved in the Galleria dell'Accademia in Florence. Undesired displacements caused by human activities and the damage produced by the application of the static load in the operating condition can be avoided with the introduction of supplementary spheres, as proposed with the Static Dynamic Interchangeable Ball Pendulum System (SDI-BPS, Figure 29f). This type included additional spheres to support the top plate in static condition. The BPS may also be improved by mixing the effects of multiple technologies such as in the case of Rolling Pendulum Tuned Mass Damper (RPTMD, Figure 29q), a vibration absorber obtained with the addition of a pendulum able to oscillate in the horizontal plane along two orthogonal directions, thus allowing a significant vibration reduction [41]. A further strategy aimed at eliminating resonance issues, consists in designing the rolling surfaces with a cone shape [42].

Also, in this case the horizontal force is directly proportional to the vertical weight. Consequently, the centre of stiffness of the device coincides with the centre of mass and the torsional effects are minimized. Moreover, to avoid jumps when the balls passes from the rest position, the head of the cone is suitably shaped. The damping properties are essentially given by the contribution of the rolling friction; therefore, to increase the dissipative capacity, the concave surface can be carved such as in Cone-type Friction Pendulum Bearing System (CFPBS, Figure 29i). Another way to increase the rolling resistance can be obtained by gluing layers of rubber to the concave surfaces, as for the Supplementally Damped Isolation Ball and Cone (SDI-BNC, Figure 29l, also called Lightly Damped Rolling Isolation System - RISs). The rolling mechanism can be achieved with cylindrical rods with circular or pillow sections as in the Pillow Shape Base Isolation System (PSBIS, Figure 29o). In this case, the recentring of the system is ensured by the shaped section of the roller and with U-shape retainers. The latter interact with the pillow and avoid the uplift of the top plate [43]. In the case of rollers with circular section, the rods can be placed between two plates with a flat shape, V-shape, or concave surface, respectively for the RTID, the Sloping Surface Roller Bearing (SSRB, Figure 29p) and the Orthogonal Pairs of Rollers on Concave Beds (OPRCB, Figure 29n) devices. These allow increasing the contact surface along the faces of the grooves with the double advantage of avoiding damage due to excessive vertical load and increasing dissipation due to friction. The resonance issues can be also eliminated by making use of circular isolator, e.g. Eccentric Rollering Isolation System (ERIS, Figure 29r), [44]. In this device, the main mass is eccentric with respect to a rotating system, so the restoring force becomes non-linear. Another type of isolation system was conceived according to the principle of smooth rocking, such as the case of the Tribological Rocking Seismic Isolation Device (TROCKSISD, Figure 29t), where a spherical joint is compressed between two spherical grooves [45].

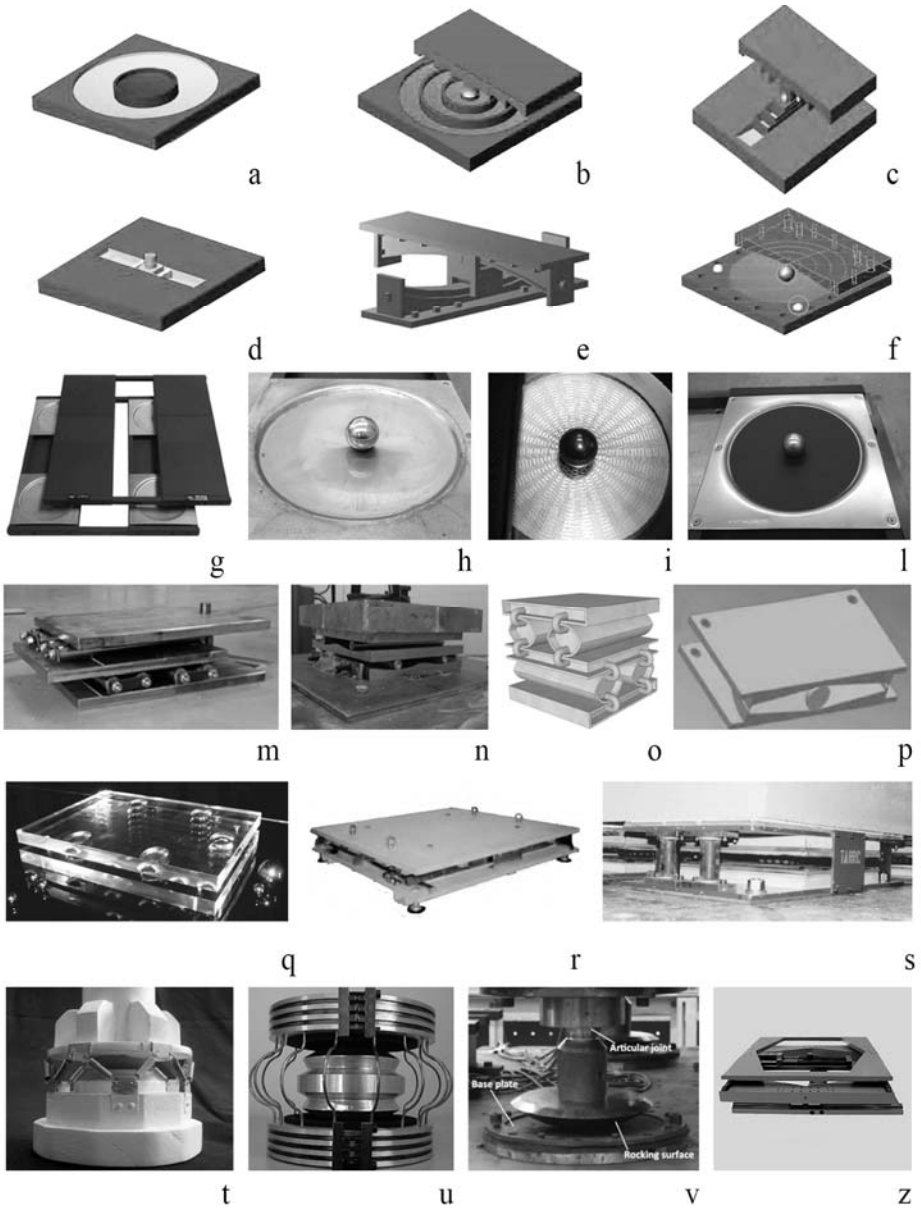

Figure 29 - Main isolation systems for contents: (a) SCFPS; (b) MFPS; (c) DOFP; (d) TFPS; (e) XY-FPS; (f) SDI-BPS; (g) BPS; (h) BNC; (i) CFPBS; (l) SDI-BNC; (m) RLRB; (n) OPRCB; (o) PSBIS; (p) SSRB; (q) RPTMD; (r) ERIS; (s) RBRL; (t) TROCKSISD; (u) RNC; (v) PB. [Images from Roussis & Constantinou, 2006, Podany 2007, Tsai 2008 and 2012, Matta et al. 2009, Ismail et al. 2009 and 2016, Jeon et al 2011, Hosseini and Soroor 2011, Harvey 2013 and 2014, Donà et al. 2015, Tayaran and Hosseini 2015, Froli et al. 2019, innovagora.it. Readapted by the author].

A recent proposal in the framework of seismic isolation is achieved using bearings placed between two rigid circular plates, as in the Roll in Cage device (RNC, Figure 29u) [46]. It has additional yield dampers, arranged to have the same shear stiffness in all directions, which also connect the two plates to limit horizontal displacements. An alternative solution is achieved by simply connecting a spherical surface to a bracket, as in the Pendulum Base (PB, Figure 29v) isolator [47]. In this case, the moment generated by the vertical reaction and the restoring force given by the weight, is able to move the system to its initial position. An example of a device widely used in the museum context is the Linear Rail Device (LRD, Figure 30). The LRD is made by overlapping three metal frames which slide horizontally along two perpendicular directions thanks to rollers. The small trolleys at each level are constrained to move in one direction only; however, by combining the movements of each level, the effects of earthquake are mitigated respect to all directions, with the advantage of avoiding torsional effects. The restoring force is provided by springs installed at each level. The movement of the frames compresses the springs which provide larger restoring force when the displacement increases. The shift of the isolation period is still related to the spring stiffness and to the masses of objects, thus requiring a customized design for each application. Although the LRD system has some advantages (absence of torsional motions and uplift inhibition), its application on a large scale is prohibitive because every different application requires a design customization with specific adaptation of stiffness characteristics[10]. Hybrid systems, such as Rubber Layer Roller-Bearing (RLRB, Figure 29m) or the Rolling Ball Rubber Layer (RBRL, Figure 29s) isolation proposed by A.G.Thomas [48], try

[10] The reduction of seismic forces is linked to the displacement capacity of the device. Consequently, the isolator can reach considerable dimensions and aesthetic issues rise up.

to overcome some drawbacks common to other isolating devices. RBRL was developed at the Tun Abdul Razak Research Centre (TARRC), and employs rubber layers, capable of dissipating energy, glued to rigid flat plates. In this system, vertical loads are beared by balls or steel rods which roll horizontally in case of earthquake and the recentring function is guaranteed by rubber springs.

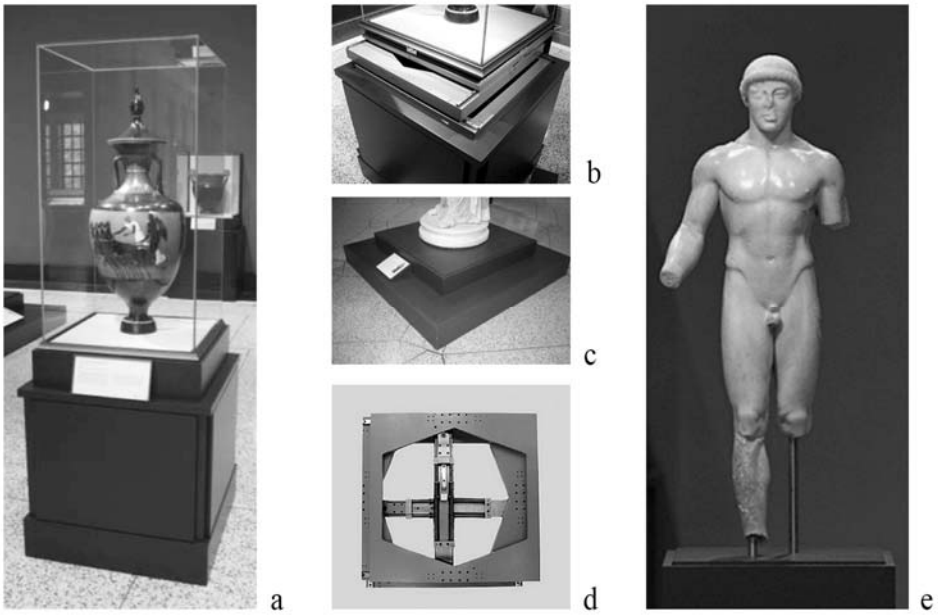

Figure 30 - Linear Rail Devices (LRD) installed at Getty Museum. [Images from Podany, 2009].

2.4 Dynamic behavior of rolling ball isolator system

Isolators with rolling balls consist of two plates with a grooved face, not necessarily with a spherical shape. The rolling system can be made using cylinders or balls that roll on flat, conical, curved surfaces or a mix of these [42]. In the case of flat surfaces, horizontal forces would push the device indefinitely, so it is necessary introduce the restoring forces thanks the use of other mechanisms, such as high-tension springs and elastomeric bearings, to guarantee that the structure can return to its equilibrium position. In the case of conical or curved surfaces, the recentering force is given

simply by gravity and consequently, the system does not show any residual displacements after removing the applied excitation[11]. The restoring force-displacement relationship depends on the shape of the rolling surface, as reported in Figure 31 under the hypothesis of absence of friction. It should be remembered that the rolling friction is very small, so additional damping sources can be introduced to reduce the seismic displacement and consequently the device dimensions. Anyway, in case of spherical plate surface a linear restoring force is achieved, while Heaviside restoring is proper for conical surfaces. In this case the device has not a natural period, the resonance phenomenon cannot occur. The cone apex is often rounded for smooth response avoiding impact when the plate returns to zero position, consequently bilinear restoring law is generated[12].

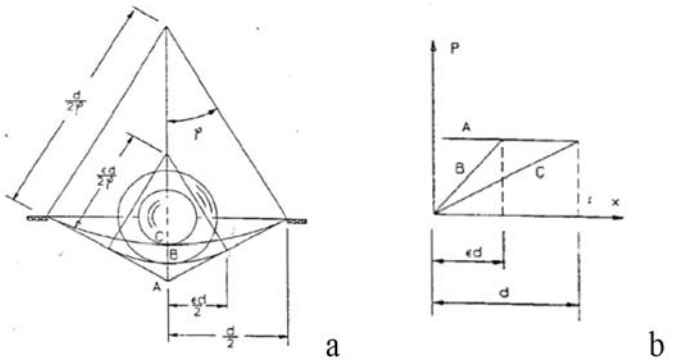

Figure 31 - Geometry of grooves and corresponding restoring force-displacement relationship. [Images from Kesti and Karakale, 2010].

[11] This condition occurs if the coefficient of rolling friction is not excessively high.

[12] In the case of cone apex radius larger than the ball radius, vice versa the behavior is similar to that of simple cone apex.

The first advantage of curved shape devices is that the lateral force is directly proportional to the supported weight; therefore, in absence of any imperfection on the grooves or bad positioning of the upper plate, adverse torsional motions of the supported structure are minimized. Moreover, such a device typology leads to quite small size in plan and are suitable for free-standing art objects and museum displays because it does not also interfere with the object's view. The rolling ball isolation system supports a simple design procedure, low cost of production and easy implementation. The BPS system has also some drawbacks: tendency to move under very small loads, stress concentration in the contact surface, high propensity to damage due the application of concentrated loads and small damping. Solutions have been proposed to overcome these deficiencies. In the case of small objects, the simplest solution is to cover the spheres and the grooves with plastic material; on the other hand, for the protection of heavier objects, a possible solution is to equip the isolator with suitable dissipating cables (adopted in the case of the Bronzes of Riace exhibited at the Archaeological Museum of Reggio Calabria). Undesired displacements caused by human activities and the damage produced by the application of the static load in the operating condition can be avoided with the introduction of supplementary spheres, as proposed with the Static Dynamic Interchangeable Ball Pendulum System [40]. In this case the device presents two orders of balls. The first order, called "primary sphere", supports the top plate under horizontal load; the second order, called "secondary sphere", supports the top plate in static condition. The top plate starts to roll on the primary spheres when the horizontal force exceeds the small friction force. The geometry of the secondary spheres must be carefully chosen to guarantee the contact of the top plate with the primary spheres when the rolling starts. Moreover, the first version of this system proposed in [40] does not offer the possibility of avoiding the impact between the top plate and the secondary spheres during the oscillation phase. In the original proposal, the damping effect is given only by the frictional forces deriving by

primary balls rolling on the spherical surface. In order to evaluate the efficiency of the damping introduced by coating the primary balls, some authors carried out experimental tests in the configuration without secondary spheres. Although the efficiency of the damping system was evaluated, the effects related to secondary spheres are still not known [40]. The presence of the secondary spheres could indeed modify the kinematics of the problem, since the top plate might jump passing through the rest position.

2.4.1 Theoretical approaches

The behavior of the rigid block, as mentioned in section 2.2.1 and better stressed in Chapter 4, is characterized by a chaotic behavior. For this reason, it is convenient to set up the isolation design by adopting a cautious design strategy that avoids the rocking phenomenon. Although the introduction of an isolation system requires an additional degree of freedom (the displacement of the isolator), in addition to the block rotation, in the following the block is always considered stuck to the isolator surface. This assumption implies that the block uplift is prevented, and a single degree of freedom is again sufficient. This section analyses the behavior of a rigid body, with inhibited uplift, seismically isolated using a rolling ball pendulum system. The nonlinear equation of motion in large displacements describes the behavior of a ball pendulum isolator assuming that the body is in full contact phase.

The formulation assumes that the system is subjected to horizontal earthquake only. The two plates are characterised by a concave surface with interposed rolling spheres with radius r .

The rolling surface has radius of curvature R and rolling friction μ .

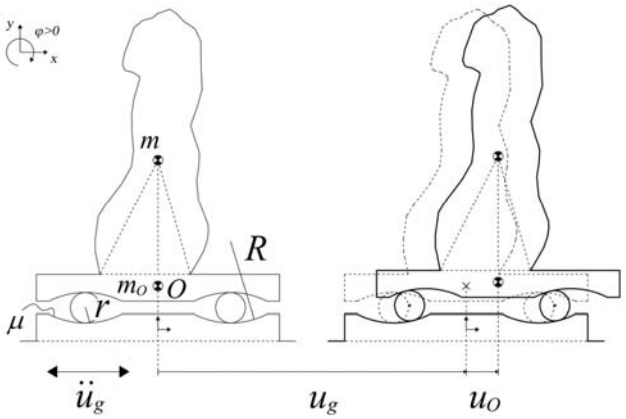

Figure 32 – Rolling Ball System pendulum scheme. [Author's image].

The device exhibits a predominantly horizontal displacement, being the radius of the sphere much smaller in relation to the radii of curvature of the grooves. Considering the diagram reported in Figure 33, the equations of motion can be written considering the horizontal equilibrium of the forces acting on the top plate. The unknown reaction P, which varies continuously according to the horizontal displacement of the top plate and influences the magnitude of the non-conservative frictional forces, can be obtained from the vertical equilibrium according to Figure 33b.

$$-W + \mu P \sin\varphi + P\cos\varphi = 0 \tag{17}$$

Considering $W = Mg$ and manipulating eq. (17), the vertical reaction can be expressed as

$$P = \frac{Mg}{\pm\mu P \sin\varphi + \cos\varphi} \simeq \frac{Mg}{\cos\varphi} \tag{18}$$

where the double sign refers to the positive and negative velocities of the top plate, respectively, and the term $\mu P \sin\varphi$ can be neglected, being the rolling friction coefficient very low. The equation of motion can be obtained assuming inhibited uplift of the top plate, simply writing the equilibrium in the horizontal direction:

$$F_i + P_H + F_{fH} = 0 \tag{19}$$

with $F_i = M\left(\ddot{u}_g + \ddot{u}_O\right)$ (inertial forces), $M = m_O + m$ (masses of top plate and statue), $P_H = P\sin\varphi$ (horizontal component of the reaction P) and $F_{fH} = \mu P\cos\varphi$ (horizontal component of the non-conservative forces due to friction phenomena). Considering the schematic diagram in Figure 33c, the displacement u_o of the top plate can be related to the rotation φ using the relation $\tan\varphi = u_o/\hat{R}$, valid in the case of large radius of curvature, where $\hat{R} = 2(R - r)$ is the equivalent radius of curvature of the grooves. Substituting eq. (18) into eq. (19) and introducing the signum function, the equation of motion can be written as

$$M\ddot{u}_O + \frac{W}{\hat{R}}u_O + sign\left(\dot{u}_O\right)\mu W = -M\ddot{u}_g \tag{20}$$

The equilibrium of horizontal and vertical forces leads the horizontal force-displacement relation for the BPS device to assume the form $F = \left(W/\hat{R}\right)u_O + \mu W sign\left(\dot{u}_O\right)$, Figure 33d. The term $\hat{k} = W/\hat{R}$ represents the horizontal stiffness and implies that the vibration period can be expressed as $T = 2\pi\sqrt{\hat{R}/g}$.

$$F = \hat{k}u_O + \mu W sign\left(\dot{u}_O\right) \tag{21}$$

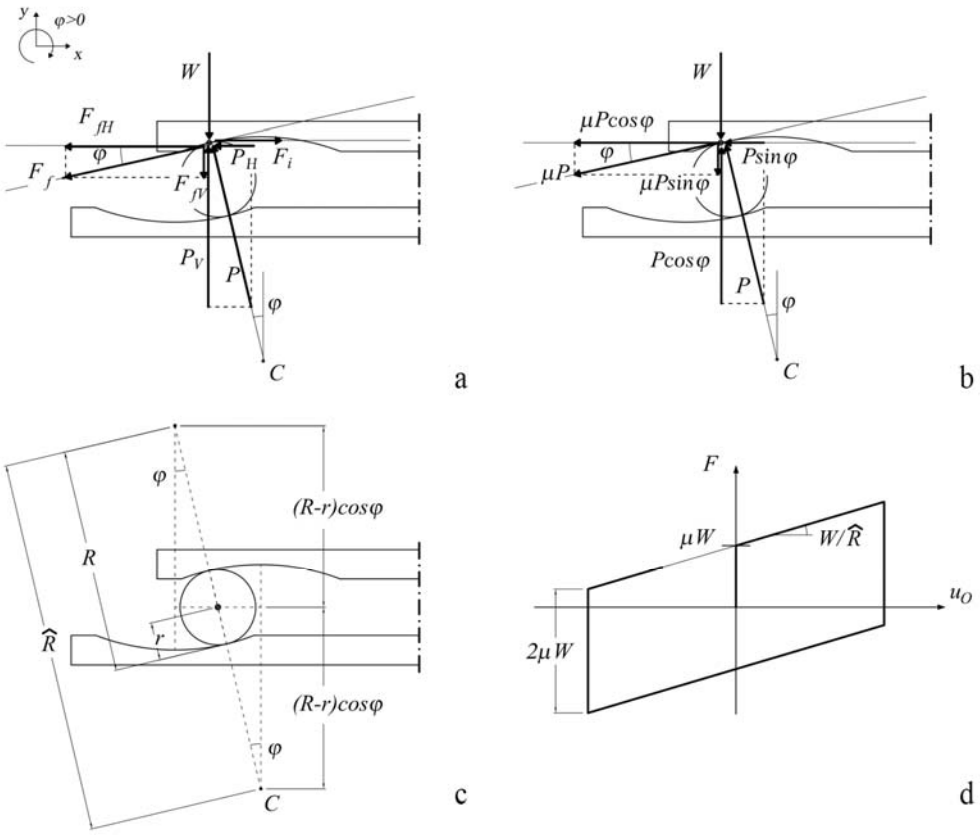

Figure 33 - Schematic diagram for the equation of motion: (a) forces acting in horizontal direction; (b) forces acting in the vertical direction; (c) horizontal displacement components; (d) force-displacement relation for the BPS. [Author's image].

It may be noted that the restoring force relationship in Figure 33d can be effectively replaced by the Bouc-Wen model [49] that is more versatile and can model wide ranges of hysteresis behaviour, which is useful for modelling the isolator with added rubber layers, for instance (see also Chapter 5).

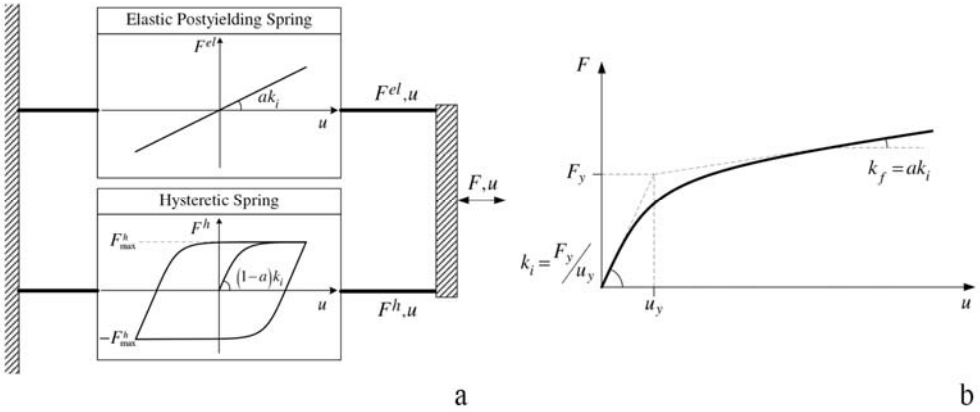

Figure 34 - Bouc-Wen model: (a) scheme; (b) force-displacement relationship.
[Images from Charalampakis, 2010].

The Bouc-Wen model, whose rheological scheme is depicted in Figure 34a, is governed by the equation,

$$F = a\frac{F_y}{u_y}u_O + (1-a)F_y z \tag{22}$$

where u_O is the displacement of the top plate, F_y the yield force, u_y the yield displacement, $a = k_f / k_i$ the ratio of post-yield to pre-yield (elastic) stiffness (see Figure 34b), z a dimensionless hysteretic parameter that is the solution of the following non-linear differential equation with zero initial condition.

$$\dot{z} = \frac{A - |z|^n \left[\beta + sign(\dot{u}z)\gamma\right]\dot{u}}{u_y} \tag{23}$$

The dimensionless parameters A, β, γ, n, control the behavior of the model, and $sign(\cdot)$ is the signum function. The parameter A is set to unity [49], indeed $A = 1$

returns the initial stiffness $k_i = F_y / u_y$. The parameters β and γ control the size and shape of the hysteretic loop. In the special case of $\beta = \gamma = 0{,}5$, the unloading branches are straight lines with stiffness equal to $k_i = F_y / u_y$ [49]. The value of n influences the transition from elastic to post-elastic branch; in particular, for small values of the positive exponential parameter, the transition is smooth, whereas for large values the transition becomes abrupt, approaching a bilinear model.

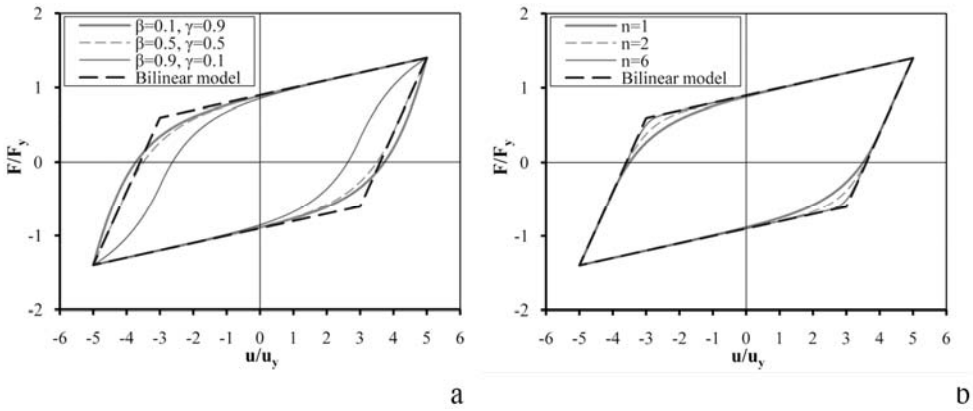

Figure 35 – Meaning of the dimensionless parameters: (a) hysteretic loops (a=0.10, n=1, u_{max}/u_y=5); (b) hysteretic loops for various values of n (β=γ=0.5, a=0.10, u_{max}/u_y=5). [Images from Charalampakis, 2010].

The equation of motion used to describe the behavior of BPS devices can be replaced with the following one,

$$M\ddot{u}_O + ak_i u_O + (1-a)k_i u_y = -M\ddot{u}_g \tag{24}$$

where the stiffness of the post-elastic branch is the same as that given by the radius of the grooves. Re-adapting the equations to the case of BPS, the initial stiffness can be considered as a multiple of the stiffness given by the grooves $k_i = qk_f$ where q could be experimentally estimated. The value of the yielding force can be assumed equal to $F_y = \mu W$ and consequently the yielding displacement becomes $u_y = F_y / k_i$.

This assumption is more realistic for high initial stiffness values. The numerical integration of eq.(24) is performed with standard ordinary differential equations solvers available in Matlab via a state-space formulation. The equation of motion was integrated using a 4^{th}-5^{th} order Runge-Kutta method and can be solved in terms of displacement.

2.4.2 Rolling ball isolation systems

There are many studies in which various isolation devices were experimentally analysed, but only a few of them focus on evaluating the effects caused by damage to the grooves. An important contribution is represented by the results achieved at the TARRC. Extensive experimental investigations were performed, in the period from 1995 to 2002 and then in 2014, to evaluate the effects of prolonged application of the vertical load in the case of deformable materials in a Rolling Ball Rubber Layer (RBRL) isolator. The RBRL device, ideated by Prof. A.G. Thomas, is made of spheres, which have the function of bearing the vertical load, interposed between two plates horizontally arranged. The top plate can move with respect to the bottom one (fixed to the ground) thanks to the rolling mechanism provided by the balls which can roll on rubber layers glued on the internal faces of the plates. Furthermore, the recentring capacity of the system was guaranteed through the insertion of rubber springs. The results, reported in [50], demonstrate that the behavior is rate independent because the force in hysteresis loop does not vary with the frequency of the sine cycles set during the test. A peculiarity is the peak force observed during the roll-out phase or when the balls come out from the pit. Muhr et al. [50] evidenced that the roll-out force is an indefinite quantity, but this does not seem to be a serious obstacle for the practical implementation of the system.

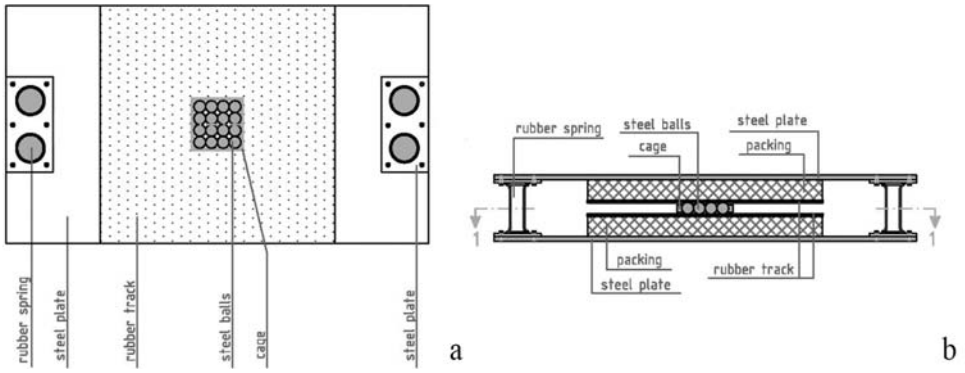

Figure 36 - Rolling Ball Rubber Layer isolator: (a) horizontal and (b) longitudinal sections. [Images from Donà, 2015].

The study demonstrates that the properties of rubber layer do not significantly influence the response of the isolator when subjected to large excitations. In the latter case the restoring forces is given only by the rubber springs and consequently, the ball rolling on the rubber layers provides a damping force similar to frictional sliders. Instead, in the case of small displacements, the properties of the rubber layers should be carefully determined in order to predict the response. Therefore, the system can be defined as displacement amplitude dependent, Figure 37. The study highlights that the peak given by the roll out force represents the acceleration capable of inducing rolling motion. For lower forces, the system seems to be connected by a rigid constraint with a kind of mechanical fuse. Figure 37 shows how, once the roll out force is exceeded, the rolling resistance is characterized by a constant force with an almost instantaneous change of its verse when the velocity sign changes. Moreover, the graph shows that, after a long resting time, the balls tend to cause indentation on the rubber surface. The model prepared in [51] considers indentation effects. The authors modelled the effects of the pit by means of an additional elastic force that disappears when the ball completely rolls outside the indented area, Figure 38a-b.

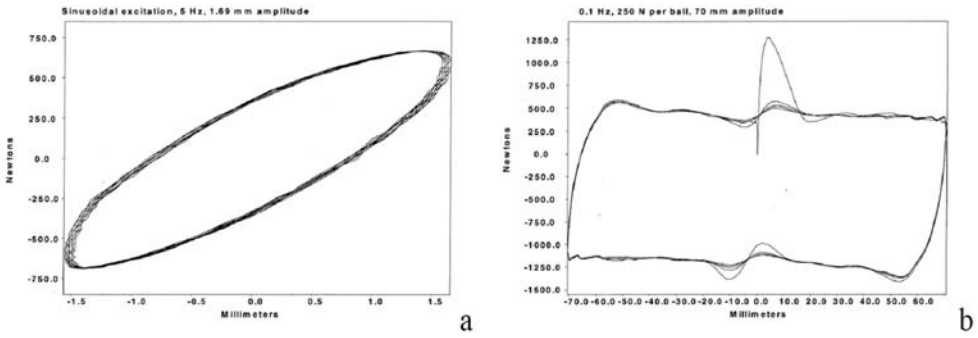

Figure 37 - Hysteresis loop of Rolling Ball Rubber Layer: (a) small and (b) large displacements. [Images from Muhr 2010].

The same phenomenon was highlighted in [52] by the experiments conducted by M. Donà in 2015. In this work the dependency of the rolling force upon the position of the balls (in presence of the pit) was confirmed.

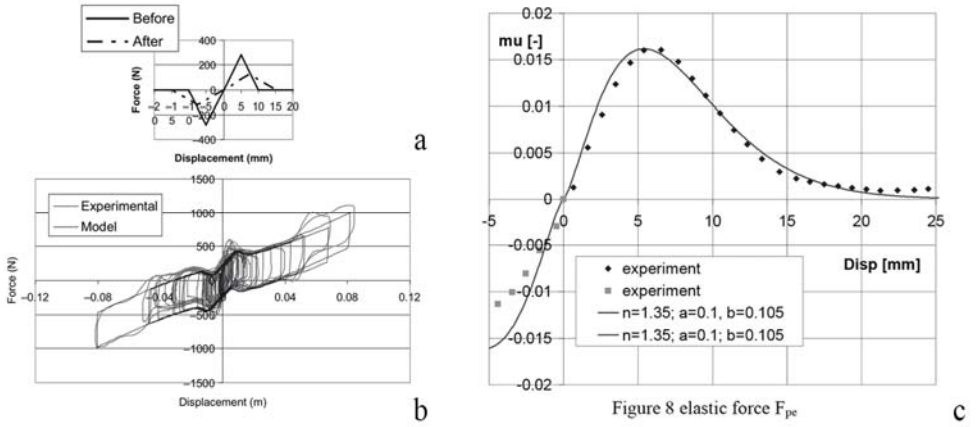

Figure 38 – Force-displacement relationship of a RBRL device: (a) linear analytical model of indentation; (b) comparison experimental vs numerical response; (c) exponential analytical model of indentation. [Images from Guerreiro 2007, Donà, 2014 and 2015].

Accordingly, Figure 38c, the author proposed a formulation where the elastic pit force was fitted using a double exponential function.

The behavior can therefore be schematized in three phases according to the balls position. The first phase is associated to small displacements inside the pit, and to a non-linear response characterized by high damping and stiffness, Figure 39a. As reported by Donà: "*In this regime the behavior is dominated by the continued location of the balls within a viscoelastic depression*". The second phase occurs when a certain threshold value is exceeded (roll out force) and the sphere gets out of the pit. The system behaves like a mechanical fuse, in which the ball tends to fall into the pit, regaining its original position, Figure 39b. Once the roll out force is exceeded, the system assumes the characteristics of a typical rolling system, Figure 39c. The recentring springs provide additional stiffness and the isolator behaves like a classic linear isolation system, Figure 39d. Each of these phases is associated with a specific form of the hysteresis loop, which is reported in terms of dimensionless horizontal forces or rolling friction μ (horizontal force / weight) versus displacement in case of sinusoidal tests, Figure 39. For small oscillation amplitudes, less than 5 mm, the shape of the cycle is elliptical. For large amplitudes (greater than 15 mm) of the oscillations, the shape of the cycle is rectangular (in absence of elastic spring) with amplitude depending on the rolling friction. Two zones can be recognized, one characterized by maximum roll out force, and the other associated to the rolling friction. For intermediate displacements, the force is influenced by the presence of the pit, whose depth depends on the resting time of the load. The shape of the dimensionless horizontal forces (rolling friction) observed in Figure 39c, in the case of displacements lower than 15 mm, changes at each loop according to the velocity of application of the horizontal load. In the intermediate phase, a dependency of the pit force from the velocity is clearly visible as showed in Figure 40a.

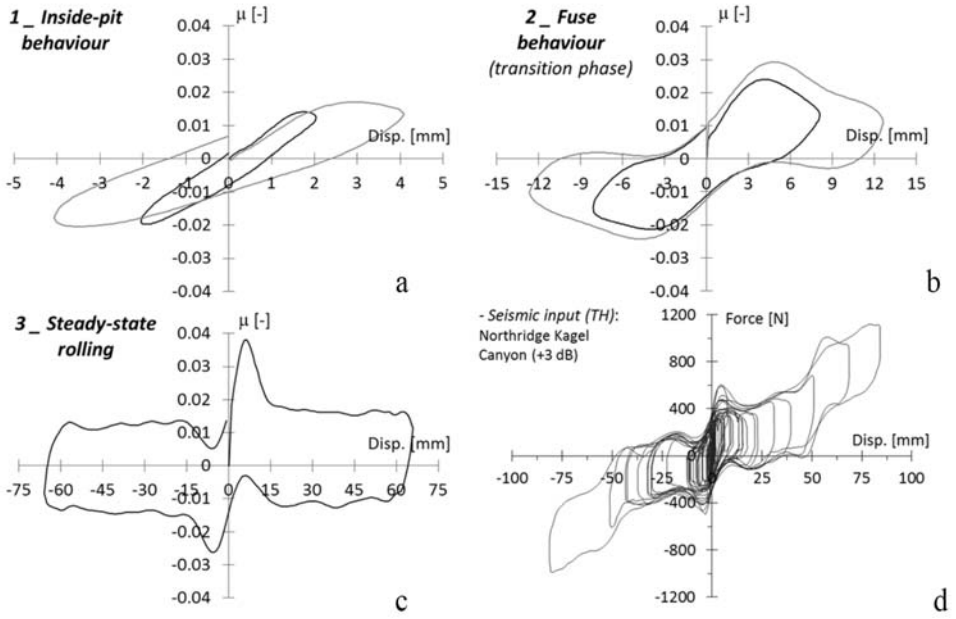

Figure 39 - Rolling friction-displacement loops representative of the RBRL response. [Images from Donà, 2015].

This typical shape can be evaluated as the mean value of rolling friction of the corresponding positive and negative μ values of the loop [52], Figure 40b.

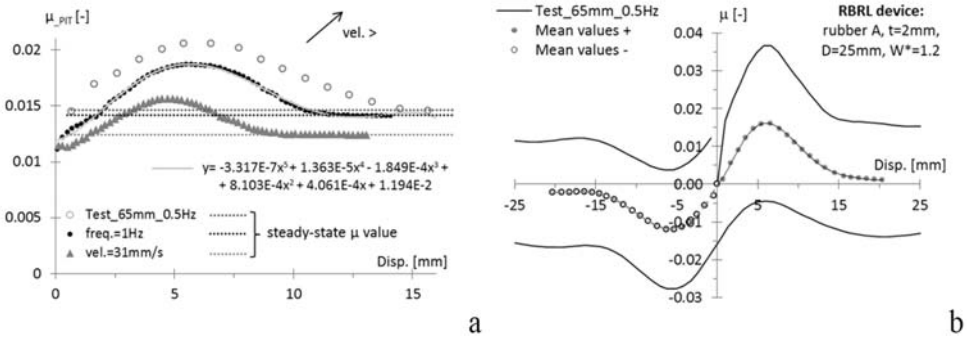

Figure 40 - Influence of the pits on the rolling friction resistance for small displacements: (a) weakly rate dependent behavior; (b) identification of the nonlinear elastic behavior associated to the presence of the initial depression. [Images from Donà Phd thesis, 2015 and Donà & Muhr, 2015].

The issues related to the development of pits was overcome in [39] and [40]. The authors employed additional spheres to support vertical loads in static conditions. The system, which is called *Static Dynamic Interchangeable - Ball Pendulum System* (SDI-BPS), involves the use of rubber-coated balls during the oscillating phase to manipulate the friction along the rolling surfaces. The behavior of the device can be summarized in two stages. The first step is governed by the behavior of the small spheres in case of low-intensity earthquakes, whereas the large spheres contribute to the motion when the system begins rolling. At this stage, the large spheres withstand the vertical load as well. This strategy avoids the formation of permanent deformations along the rolling surfaces because the large spheres are vertically loaded only during the earthquakes. Rolling devices essentially present two main issues, namely low damping values provided by the rolling friction and stress concentration caused by the small contact area between the spheres and the concave surfaces. The experimental investigations concerning the SDI-BPS were carried out separately with and without the presence of the additional spheres to individually evaluate the contribution of the rubber-coated spheres. The results presented in the form of displacement force show the typical behavior of friction oscillators, Figure 41b, but they do not clarify the effect of the support spheres, which seem to impact at each passage of the upper plate from the rest position. The scheme shown in Figure 41a requires very high execution tolerances to guarantee the contact of all the balls in static conditions and that the support balls do not provide any contribution when the oscillation starts. The results of the shaking table tests conducted at the Center for Research on Earthquake Engineering (NCREE) in Taiwan do not clarify this aspect [40], Figure 42.

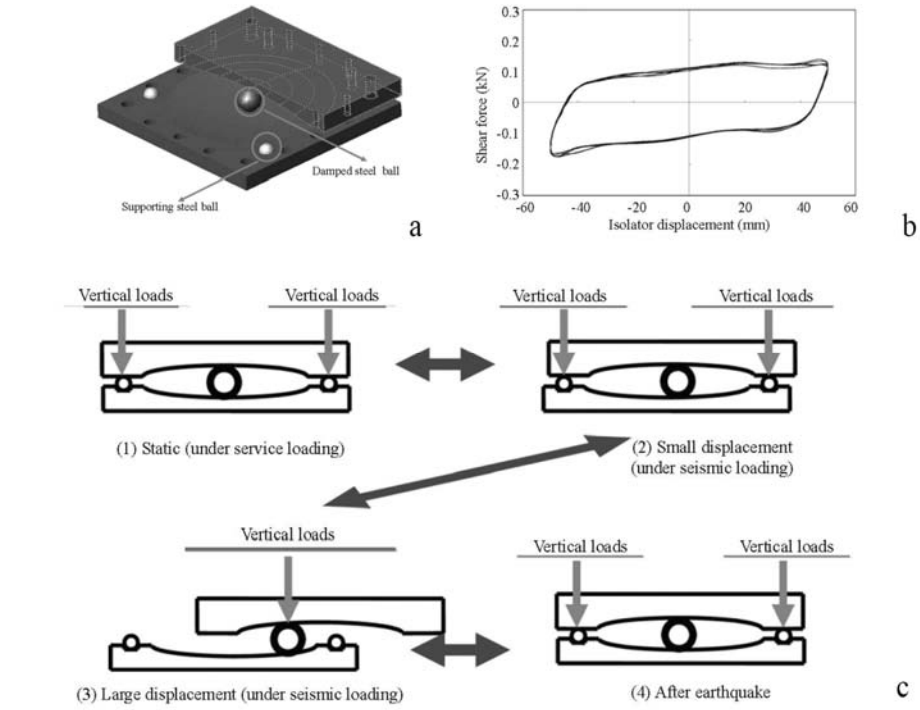

Figure 41 – Static Dynamic Interchangeable - Ball Pendulum System: (a) axonometry; (b) force-displacement relationship in absence of small balls; (c) operating phases. [Images from Tsai, 2012].

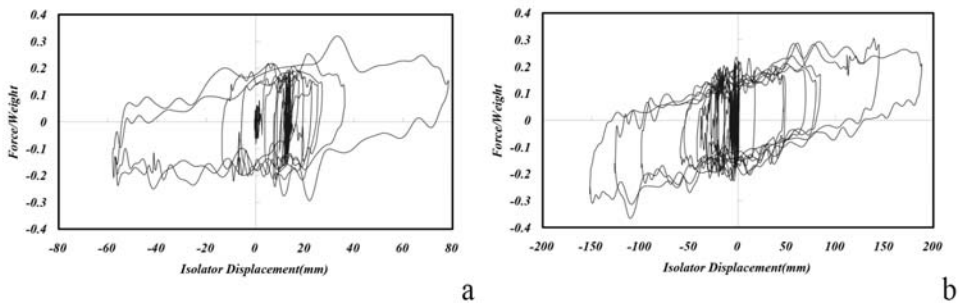

Figure 42 - Hysteresis loops of SDI-BPS isolator: (a) x direction under tri-directional Kobe earthquake; (b) x direction under tri-directional Chi-Chi earthquake. [Images from Tsai, 2008].

2.5 Experimental investigations on rigid bodies

The rocking phenomenon has been extensively studied although most of previous researches have been analytical in nature [53]. Herein, the effects are investigated from an experimental point of view so as to highlight the deviations from the theoretical models. Indeed the laboratory results represent a good guide for understanding the phenomena, to explain the behavior of rigid body and for the insight on new numerical models. The study of the results of the experimental campaigns previously carried out provides important suggestions.

2.5.1 Free-standing objects

Several researchers tried to estimate the intensity of earthquakes from the observed effects on experimental results on free-rigid objects. However, experimental data are generally obtained in relation to the characterization of the dissipative properties so mainly free oscillation tests results are available.

One of the main problems tackled in the literature focuses on the possible effect of interface material (e.g. concrete and rubber) because it exerted significant influence on the rocking response. In [54] experimental measures of the loss of energy at each impact during free vibrations on a concrete specimen are performed for different values of hardness of the interface material. It was observed how such a parameter affects the dynamic behavior of the system in terms of energy dissipation (expressed in the article as the square of the ratio of the kinetic energy before and after impact, called r factor). It was experimentally demonstrated that the vibration energy decreases more rapidly when the body impacts with a rubber surface and slowly for a concrete one, Figure 43a. In the article, the best fit between the experimental data and those obtained by applying the equations of the *SRM* is obtained by considering up to about 80% of the value predicted by the classical formulas. This deviation is actually consistent with the test set up. It should be recalled that classic formulation measures energy loss at each impact, which is reliable only for the case of a rigid

block on a rigid foundation. Although useful measures have been used to build specimens closer to the ideal ones (to have point impacts, lower steel plate was welded to two horizontal steel rods at base minimizing the impact area), the application of the rubber layer moves the behavior away from this hypothesis. Finally, the authors also conclude that "*the experimental results were very sensitive to small imperfections existing in the specimens as well as the surface where the experiments were carried out…In addition, development of SRM or an alternative model is required to accurately predict free rocking characteristics*".

Many experiments on rocking blocks have considered the behavior of rigid blocks on rigid foundations and the problem of rigid blocks on flexible foundation is less investigated; however, in [53] the free oscillation behavior of marble blocks on dissipative foundation is studied, Figure 43b-c-d.

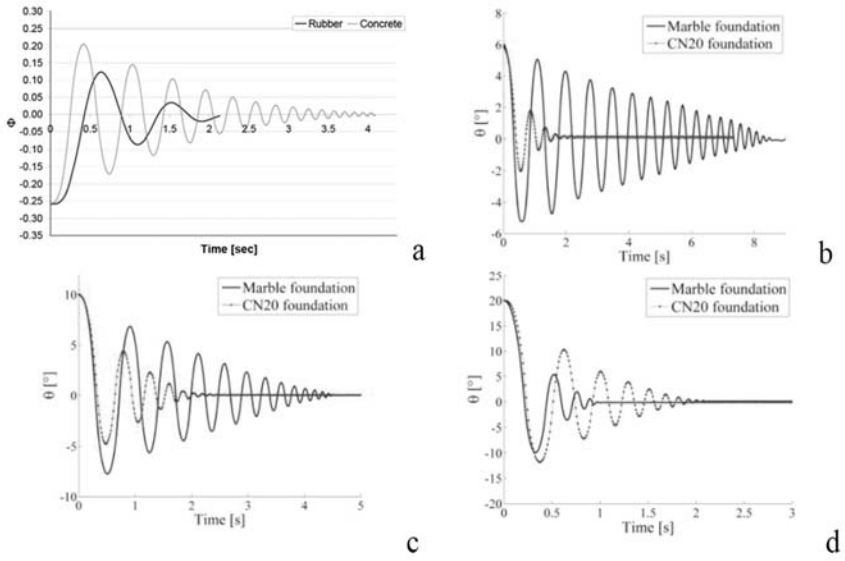

Figure 43 - Oscillation amplitude ratio for different interface material: (a) rubber VS concrete; (b,c,d) rubber VS marble. [Images (a) from ElGawady et al., 2006; (b,c,d) from and Spanos et al., 2017].

Following the same results reported in [54], in [53] is confirmed that "*rocking behavior cannot be presumptuously treated if viscoelastic materials are used, for instance for vibration isolation of art objects*". For these reasons, the effectiveness of the Hunt-Crossley nonlinear impact force model[13] is tested and calibrated on the results of an experimental campaign conducted on 3 marble blocks (with different slenderness) resting on two different foundation materials[14]. Measurements were made using Laser sensors.

Experimental experiences have analysed imperfections in the member-foundation interface (for example, a slightly skewed or damaged interface following multiple impacts) with energy dissipation [55]. An asymmetric response is experimentally evaluated, Figure 44a-b, that is largely attributed to the imperfect contact surface.

This problem has been overcame by representing the surface imperfection as an inclined surface in the plane of motion. Consequently, an energy gain was detected following any impact that could also be due to the release of the elastic energy stored in the vicinity of the impact zones[15], Figure 44c. The equations of motion were written evaluating a modified critical angle β in relation to the adopted slope. The displacement response, when β is not zero, is characterized by an asymmetric sequence of displacement peaks due to the assumed inclined rocking interfaces. It was shown that even when the input excitation is zero or relatively simple (simple harmonic movement), the rocking problem is highly nonlinear in nature.

[13] The foundation has been treated as a bed of continuously distributed vertical springs in parallel with nonlinear dampers.

[14] Marble slab to simulate rigid foundation, a mat of Aerstop CN20 to simulate viscoelastic materials.

[15] Kalliontzis: "*Such behavior can occur due to the flexural response of the rocking body, at the member-to-foundation interface, or a combination thereof*".

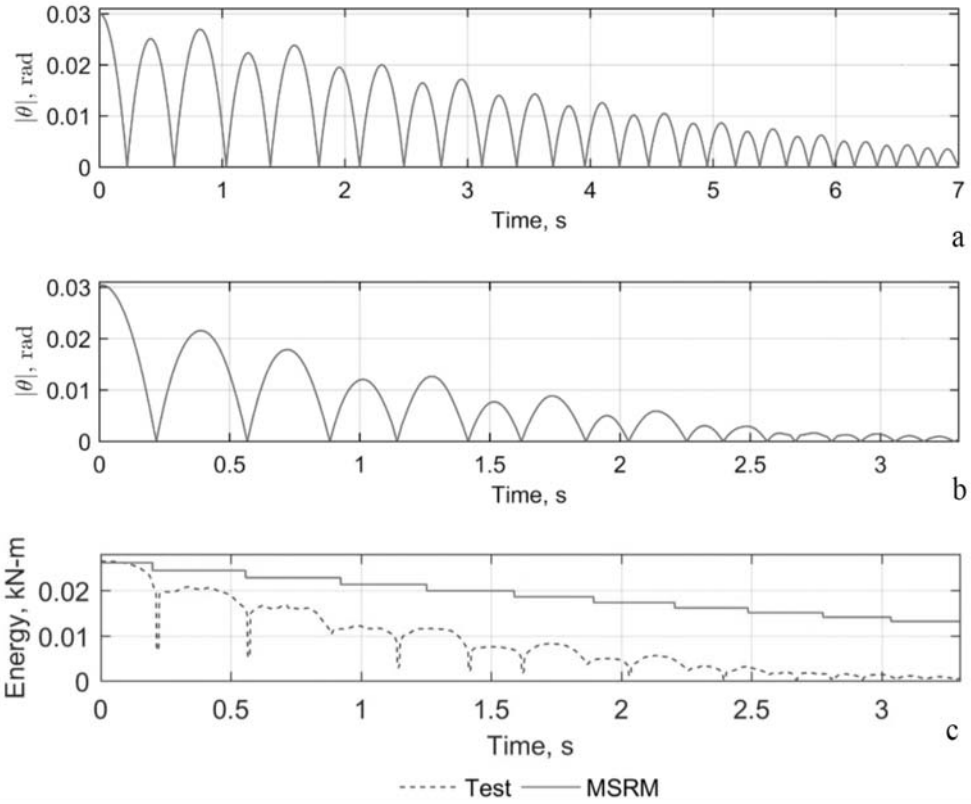

Figure 44 – Absolute experimental angular displacement responses: (a) block 35,56 cm x 35,56 cm with added mass on top; (b) simply prismatic block 35.56 cm x 35.56 cm without added mass. [Images from Kalliontzis and Sritharan, 2018].

In case of forced vibration the rocking response is chaotic [6]; however, it was possible to observe systematic trends when the rocking response of rigid blocks was studied from a probabilistic point of view [5]. In [56] , authors suggest: "*Even if the coefficient of restitution is estimated accurately, or determined experimentally, the rocking oscillator is so sensitive that predicting the entire seismic response time history is practically impossible*". In [56] this statement is supported by the results obtained numerically and compared with those obtained in the laboratory. Figure 45,

compares the tilt angle time histories of rocking oscillators with heights equal to 5, 10, and 20 m.

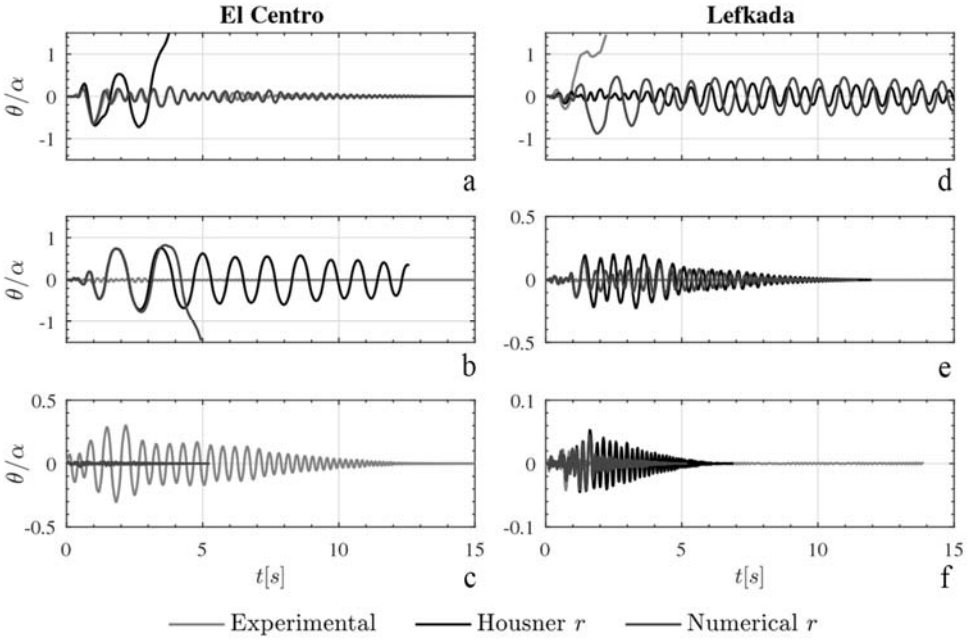

Figure 45 - Comparison of the tilt angle response time histories: (a) block *h*=5m and El Centro earthquake; (b) block *h*=10m and El Centro earthquake; (c) block *h*=20m and El Centro earthquake; (d) block h=5m and Lefkada earthquake; (e) block *h*=10m and Lefkada earthquake; (f) block *h*=20m and Lefkada earthquake. [Images from Bachmann et al., 2017].

In no case the numerical model correctly predicts the occurrence of overturning. Therefore, the *SRM* does not provide an accurate estimate of the maximum rotation reached by the rocking oscillator.

Recent studies showed that by appropriately modifying the moment-rotation relationship of the rigid block behavior (three branch law) and calibrating its parameters, it is possible to retrace the results of a time history [21]. The paper investigates the behavior of masonry façades that behaves approximately as a rigid body undergoing a rocking motion.

The three-branch model, delimited by two dimensionless displacement parameters, was able to predict the experimental response once a reduced restitution coefficient was assumed, Figure 46.

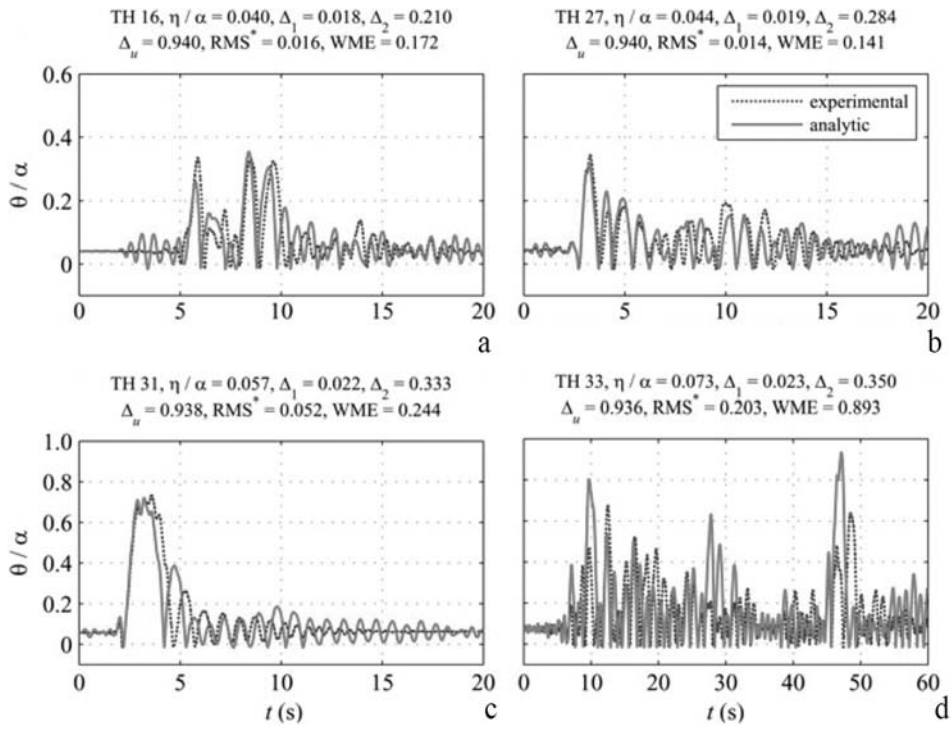

Figure 46 - Comparison between experimental and analytic time histories using model with three branches: (a) BagnirWE earthquake; (b) SturWE earthquake; (c) R1168EW earthquake; CalitWE earthquake. [Images from Al Shawa et al., 2012].

In conclusion, although the classical model is strongly nonlinear, the numerical response computed for the same initial conditions and the same ground motion excitation is deterministic and repeatable. Thus, the classical model does not introduce variability in the response. For these reasons, this Thesis aims to introduce model in which the uncertainties are treated considering small perturbations of its governing parameters will be introduced in Chapter 4.

2.5.2 Seismically isolated objects

Among the interventions to prevent the falling of objects during an earthquake, seismic isolation certainly represents an effective strategy. There is a vast literature on the effects of this protection strategy. The effectiveness of seismic isolation applied to rigid bodies was numerically [57]-[58] and experimentally [59] studied. This section discusses, from an experimental point of view the dynamic behavior of rigid bodies placed on isolation devices and verifies the effects of these measures during an earthquake. Examples have been extracted from the literature that resemble the experience carried out in the present study, in terms of chosen specimen geometry, acquisition technique, features of the shaking table adopted during the experiment.

Although a slider was adopted, Figure 47a, in [59] there are a similarities with the cases discussed in section 4 (dimension of specimens 9x13x62 cm and 2,03 kg of mass, use of contactless measurement techniques for the response measure, shaking table dimension 100x100 cm, isolator with recentering property thanks to gravity). In [59] the effectiveness of the isolation system is evaluated by comparing the behavior of the free-standing rigid block with the isolated one.

In the first case the specimens showed oscillations a few times before the overturning; in the second case the specimen showed many small rocking vibrations without overturning. The experiments evaluate the effectiveness of the isolation device by comparing the acceleration on the vibrating table with that on the device, recording a decrease from 0,61 g to 0,24 g in the *x* direction and from 0,97 g to 0,24 g in the y direction. By applying the formula of the theoretical uplift acceleration of the block, which is equal to 0,15 g, the small oscillations recorded on the block are justified even if seismically isolated.

Past experiences, such as on the occasion of the 2004 Niigata-ken Chuetsu earthquake, revealed that there was the overturning the subsequent breakage of many terracotta objects also placed on seismic isolators probably due to the achievement

of the limit displacement of the device. For this reason, in [59] the effects of the displacement limit on the isolator motion was studied, reducing the original displacement of 19 cm (evaluated in the absence of displacement limitation devices) to 15 cm. In Figure 47b it is evident that as soon as the device impacts on the displacement limitation devices, the block overturns. This suggests that it is important on the one hand to correctly assess the displacement demand and on the other hand to set strategies for a proper design of the device.

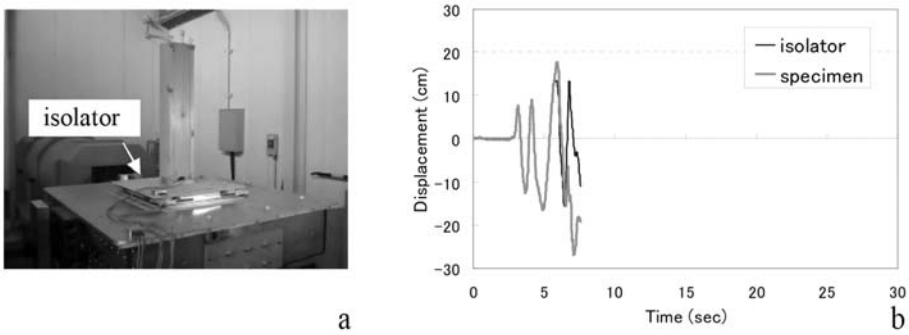

Figure 47 – Protection of rigid body with seismic device: (a) experimental setup; (b) response in the case of achieved limit displacement. [Images from Kishi et al., 2008].

Chapter 3 Experimental equipment and measurement protocol

The dynamics of a rigid body and of the isolator device can be investigated from a numerical point of view, via integration of the differential equations, or performing experimental campaigns. Despite the simplicity of the problem formulation, the results of experimental campaigns can be very heterogeneous due to the chaotic behavior of the system. Even in the case of simplified geometry, the rigid body motion is difficult to predicted due the impairments in the contact surface that produce the chaotic character of the response. Considering that the rocking systems are extremely sensitive to changes in the boundary conditions, an acquisition system is here specially conceived. In this context, the data acquisition is based upon monitoring target points suitably positioned on the specimen, using a camera with high-resolution and high frequency of acquisition. Measurements carried out starting from a sequence of frames are particularly useful in the case of systems characterized by low frequencies, such as in the case of rolling of a ball pendulum device. The effectiveness of contactless measurement techniques is finally confirmed by the analysis of the rocking motion for the rigid block. This chapter highlights the issues encountered in the study of the behavior of the rigid block, to evaluate the advantages that derive from the use of the adopted methodology.

3.1 Main issues related to the measurement of rocking motion

As reported on most of previous research comparing rigid block dynamic response derived by numerical and experimental investigation, it is necessary to correctly model the complexity of phenomena, for example related to impact, to reproduce during the test the assumptions of classical theories. For this reason, as evidenced in section 2.2.5, many authors performed experiments with prismatic specimens properly prepared, for example with slightly concave aluminium base or equipped with steel rollers at the base edges. As expected, the experimental results and their

interpretation play a crucial role, nevertheless in this context the test preparation and the used protocol represent issues that should not be underestimated. It is known that the dynamics of the block is chaotic and strongly influenced by the geometric anomalies such as not-flat base, asymmetries, rounded edges as a result of continuous degradation at the block corners, small perturbations of the seismic excitation, properties of the oscillator (real position of centre of mass), boundary conditions and impact modelling. Therefore, the experimental activity must be carefully conducted to spot the limits of theoretical formulations. For these reasons, it was decided to use a *contactless measuring method* to measure the rocking response of rigid blocks thanks to which the specimen is tested without changing its real and original geometric and inertial properties, thus reducing the uncertainties and anomalies during the tests.

3.1.1 Videogrammetry measurements protocol and validation procedure

In the last decades, thanks to the advances in digital photographic tools and the ability to buy affordable high-resolution cameras, videogrammetry has been widely used in engineering and applied to the study of the dynamic response of structures. The contactless measurement techniques can be classified in two categories, namely using laser beam and white light (*image-based system)*, respectively.

In this context, the two-dimensional (2D) photogrammetry technique was used [60] just measuring the displacement of a limited number of tracking points placed on a planar surface, using a single fixed camera. The adopted method is known as *point tracking technique*. This approach is based on the identification of the coordinates of discrete points mounted to the structure thanks to the use of optical target (high contrast circular points), Figure 48. The markers layout must be carefully chosen considering that 2D photogrammetry returns reliable results in the case of tracking points positioned in a plane. In the case of curved shape, 2D photogrammetry is no

longer able to provide accurate results. Consequently, in the case of specimens with irregular shape, it is advisable to equip them with special extensions.

The correct acquisition depends on the adopted configuration, consequently the position of the camera is chosen to frame the centre of the vertical plane containing the markers with a 90° angle of incidence. In addition, the camera must be positioned on stable supports placed outside the shaking table because its vibrations would affect the acquisition phase. Finally, it should be emphasized that the lighting conditions must also be kept stable, for example by using LED lamps. The adopted tracking motion free software must allow determining the centres of the optical marker using a search algorithm that identifies the optical targets at each instant and must compare them with a reference stage. The reflecting markers have very little weight and size and are also placed on the shaking table to reconstruct its trajectory with respect to a fixed reference system. The tracking of the shaking table position is useful for the calibration phase and to determine measurement accuracy.

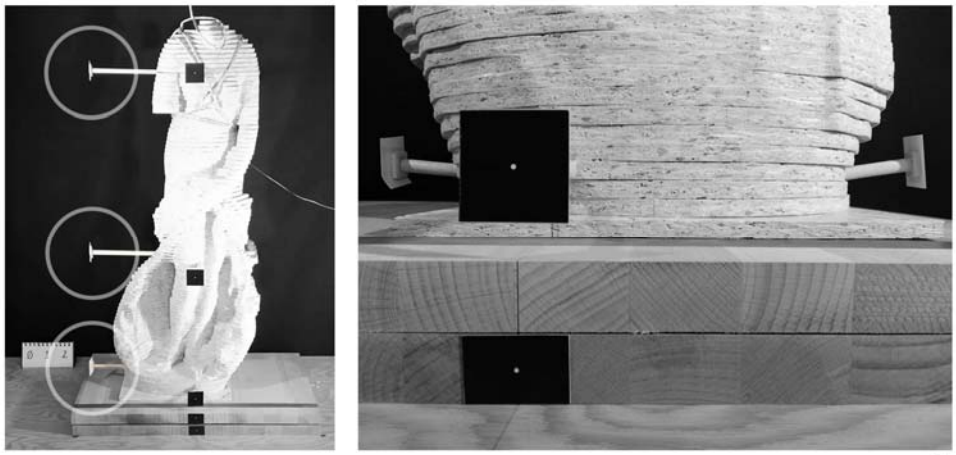

a b

Figure 48 - Specimen preparation: (a) extensions vertically aligned; (b) high contrast circular points. [Author's image].

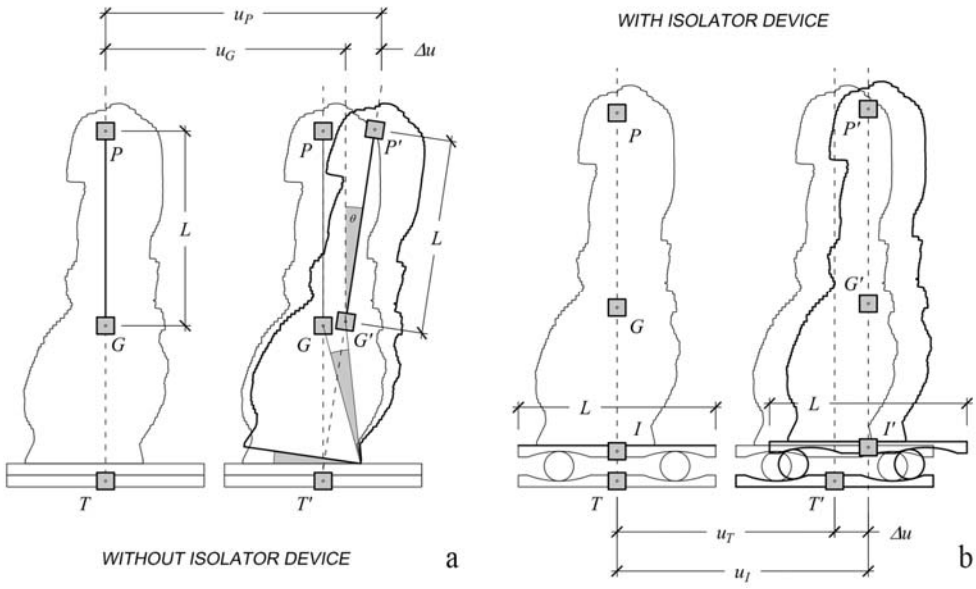

Figure 49 - Relative displacement calculation: (a) angle sizing for the free-standing statue; (b) relative displacement of the isolator top plate. [Author's image].

The error is evaluated in the post processing phase when a known real length (L dimension in Figure 49) is related to the corresponding dimension in pixels.

The length of a single pixel has been fixed in the measurement unit to be adopted (meters) and is related to the distance between the camera and the target, to the size of the specimen and to the camera resolution.

The accuracy of the measurements was determined by measuring the position of a marker at rest over a long period of time [61]. For the adopted configurations, the accuracy of the measurements is about $\pm 0,05$ mm, Figure 50. As with all measurement tools, a calibration process must be performed to identify the lens alterations.

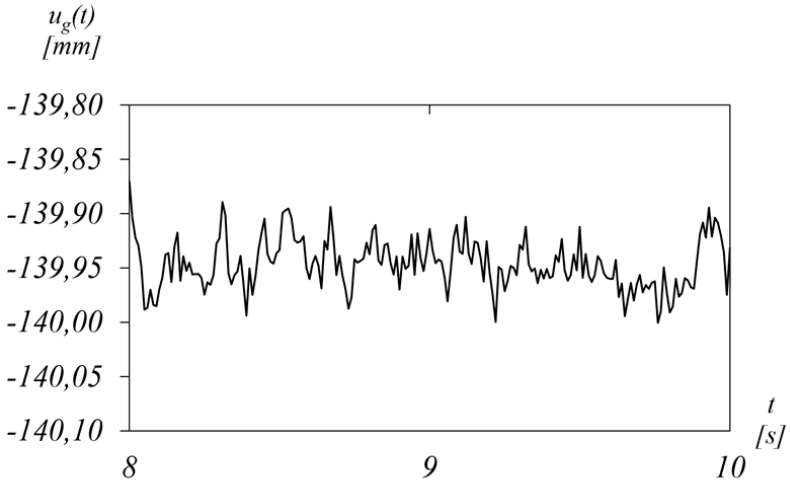

Figure 50 - Measurement error in correspondence of a static marker.
[Author's image].

The elimination of barrel distortion can be obtained realigning the curved lines in post processing phase through a procedure that corrects the measurements at the periphery of the frame. The calibration was carried out by choosing a model whose geometry is known and recording the position of some target points constrained to the table and to the object. In particular, the data recorded by the optical reader when the table is pushed to the maximum displacement is used as a reference to correct the measure, Figure 51.

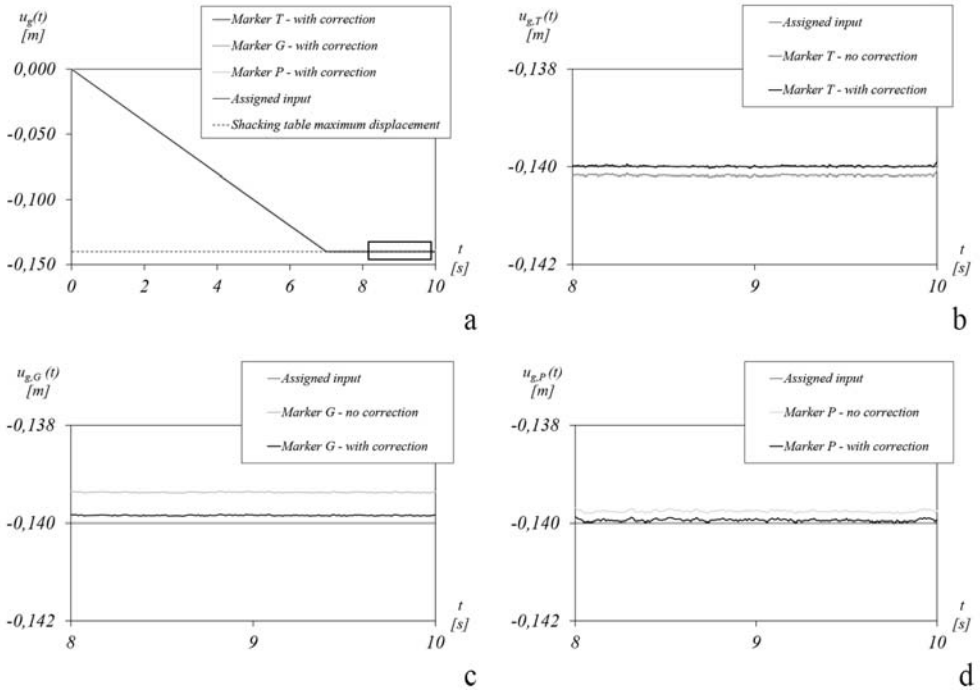

Figure 51 – Application of calibration curves: (a) comparison camera measurements with shaking table input; (b) correction at maximum displacements of points T, (c) G (d) and P. [Author's image].

The output of the shaking table can then be compared with that acquired through the acquisition process. It turned out that the correction to be applied is proportional to the distance from the central point of the shaking table, Figure 52; thus, a corrective coefficient can be calibrated to get unbiased data[16].

[16] The quality of the measurements was favoured by the choice of using a video camera that is not equipped with a wide-angle lens and by its good positioning.

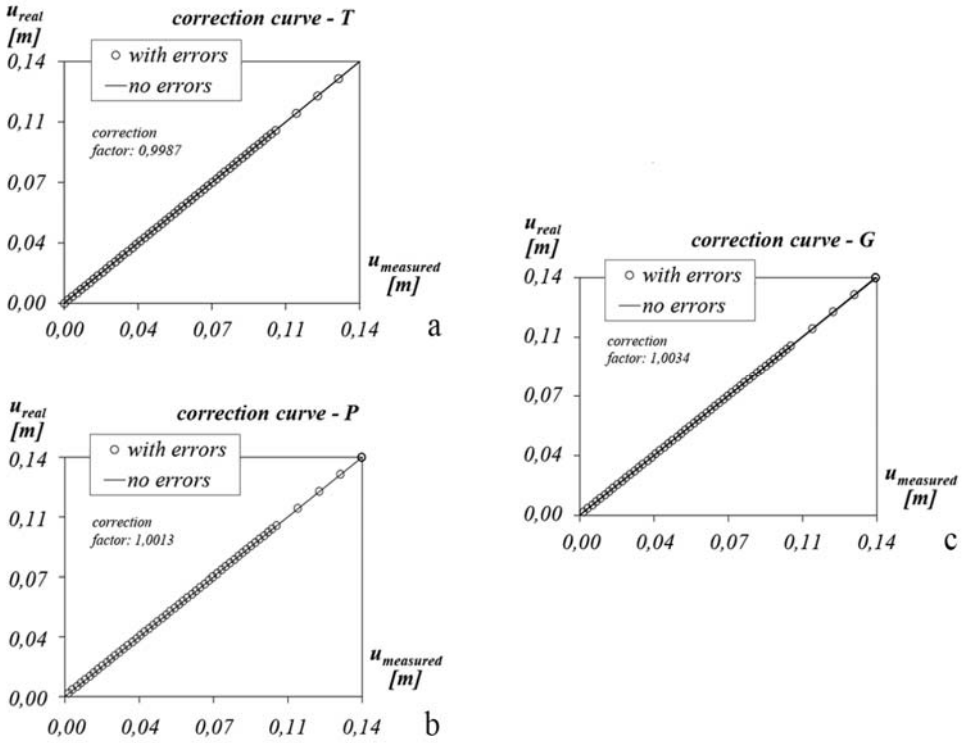

Figure 52 - Calibration curves: points (a) T, (b) G and (c) P. [Author's image].

Once the procedure is calibrated, the rotation of the block at each step is computed considering the horizontal displacements of vertically aligned markers. Horizontal displacements were detected and used in the post-processing phase to infer the rotations and the relative displacements of rigid blocks and isolator devices, respectively.

According to Figure 49a, the determination of the rotations for the rigid body was carried out as described below. Two suitable vertically aligned points *G* and *P* have been chosen in correspondence of the centre of gravity and the centre top of the rigid body, respectively. Then, the rotation can be simply retrieved as:

$$\theta_i = sin^{-1}\left(\frac{\Delta u_i}{L}\right) \tag{25}$$

being $\Delta u_i = u_{i,P} - u_{i,G}$ the horizontal relative displacement between the top of the block and the centre of gravity for the *i*-th generic instant. The angular velocity is calculated as follows:

$$\dot{\theta}_i = \frac{\theta_{i+1} - \theta_{i-1}}{t_{i+1} - t_{i-1}} \tag{26}$$

The characterization of the isolator device is carried out using two additional points along the same vertical alignment chosen for the block, and are employed to identify the absolute horizontal displacement of the shaking table (point *T*) and the horizontal displacement of the top plate of the isolator (point *I*), see Figure 49b.

The relative displacement, velocity and acceleration can be straightforwardly obtained according to the following equations:

$$\Delta u_i = u_{I,i} - u_{T,i} \tag{27}$$

$$\Delta \dot{u}_i = \frac{\Delta u_{i+1} - \Delta u_{i-1}}{t_{i+1} - t_{i-1}} \tag{28}$$

$$\Delta \ddot{u}_i = \frac{\Delta \dot{u}_{i+1} - \Delta \dot{u}_{i+1}}{t_{i+1} - t_{i-1}} \tag{29}$$

The absolute velocity and acceleration are calculated through numerical differentiation of the displacement measurements as follows:

$$\dot{u}_{I,i} = \frac{u_{I,i+1} - u_{I,i-1}}{t_{i+1} - t_{i-1}} \tag{30}$$

$$\ddot{u}_{I,i} = \frac{\dot{u}_{I,i+1} - \dot{u}_{I,i-1}}{t_{i+1} - t_{i-1}} \tag{31}$$

To avoid the white noise characterizing the recording, the quality of the data can be improved after the differentiation. To this purpose, the numerical derivation tends to magnify the measurement error. The noise associated to the resolutions of cameras is evaluated starting from specific tests and the filtering operation was based on commonly adopted algorithms [61]. The filtering of the displacement data is carried out by applying the *moving average technique* considering that the frequency of the systems, close to 1 Hz, is much smaller than the sampling rate equal to 100 Hz[17]. The average method consists in calculating the output value y as the average of $k = 2N + 1$ values y_k (where k is necessarily odd) and attributing the calculated value to the central point.

$$y_{N+1} = \frac{\sum_{k=1}^{2N+1} y_k}{2N+1} \tag{32}$$

In practice, a very small amplitude window is slid over the signal and replaces a generic value with that derived from the average of the window. The smoothing action of the moving average increases with the width of the considered window. In the following it is assumed $N = 3$. Details on the experimental setup and on the contactless data acquisition are reported in the following section.

3.2 Lab equipment

The contactless displacement data acquisition system was adopted for its advantages. In fact, it does not require the use of additional mass constrained to the specimen, which could interfere during the test, changing the dynamic properties of the system.

[17] The *sampling rate* is assumed equal to the number of frames per second that the camera can record. The number of *frames rate* is expressed as FPS (Frame Per Second).

Furthermore, the measurements are not affected by environmental noise, the tests are easily repeatable, and no cabling is required.

The low frequency content of the problem at hand assures that displacement acquisition is appropriate and accurate. It is useful to remember that in case of high frequency the set up used for this work could lead to gross errors. A further disadvantage is that data processing for digital image correlation can take a long time. In the case of test repetitions, to guarantee a faithful guided repositioning of the block a traced footprint on the shaking table can be employed. In addition, to inhibit the sliding of the block a wrinkled sheet is inserted at the base of the block.

Finally, the block response is determined employing markers whose position can be traced during the tests by means of a high-frequency acquisition camera located on a tripod in front of the shaking table, as shown in Figure 53. Once the video acquisition is completed, the frames are processed using the *Tracker Video Analysis and Modelling Tool software ver. 5.0.7*, Figure 54.

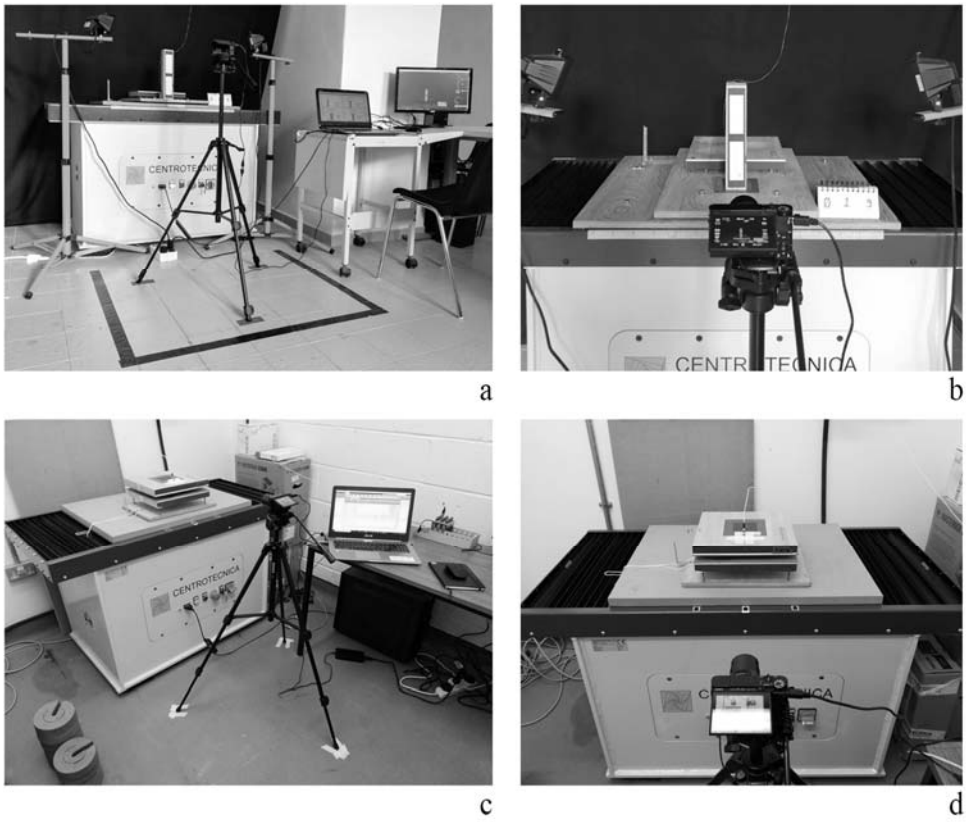

Figure 53 – Experimental setup: (a-b) University of Catania; (c-d) Strathclyde University. [Author's image].

Before starting the post-processing tracing phase, a reference calibration with a known length is introduced to relate the physical space and the frame coordinates. The starting frame of the test is then aligned with the ground motion time axis. At this point, the software returns the horizontal displacements of the markers with respect to the fixed reference system, Figure 54. The ground motion is applied through a unidirectional shaking table designed to perform seismic simulations or vibration tests. The shaking table, from the *LO.F.HI.S. series ND13014* (Low Frequency High Stroke and Velocity Shaker) distributed by *CENTROTECNICA S.R.L.*, consists of an aluminium plate forced to move in one direction using the linear motor technology that defines the position of the plate over time. It has a total

weight of 6500 N and a working area of 650x660 mm (expandable by introducing a top plate bolted to the table supports) to accommodate a maximum payload of 100 kg. The vibrating table, with displacement control, allows a maximum displacement capacity of 28,6 mm (± 14,3 mm), maximum speed of 2.5 m/s and works in a frequency range 0 ÷100 Hz [62].

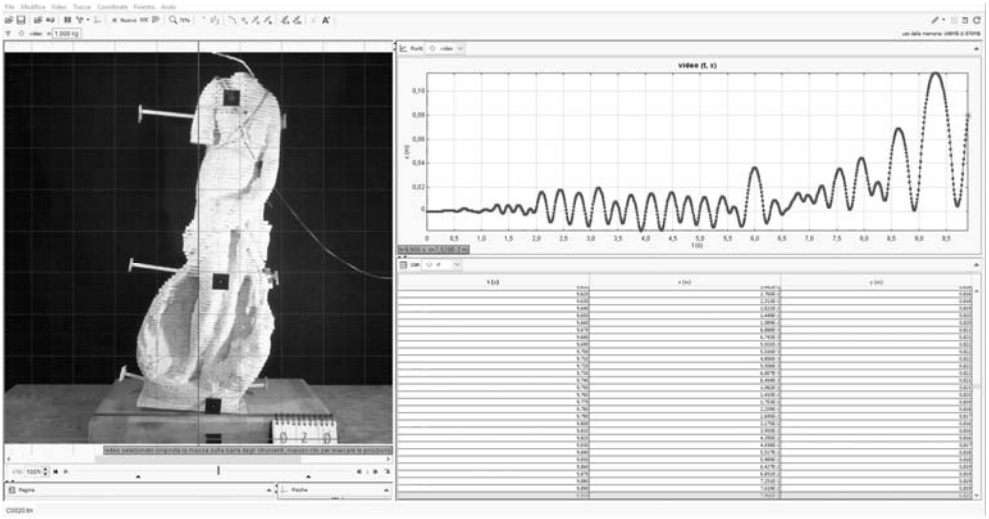

Figure 54 – User interface Tracker software. [Author's image].

The displacements of aluminium plate are managed by means of an input *.txt* file that collects the displacement time histories expressed in micrometres with the desired time step. Therefore, the applied ground acceleration must be integrated twice using *SeismoSignal* software and assigned after checking that the generated input is compatible with the specifications of the shaking table.

A further check requires to verify that the input signal and that recorded by the optical reader installed are close enough. For example, the comparison of signals in terms of displacements of the Friuli earthquake, Figure 56, is satisfactory.

The *Sony DS-RX100 M5* camera used for video records is equipped with a 20.1-megapixel *Exmor RS® CMOS* sensor with the ability to record in 4K up to 120 fps, and 1,920 x 1,080 to 240, 480 and 960 fps in HFR (High Frame Rate) mode.
In particular, the recording is made at 100 FPS (one frame every 0.01 seconds) and setting the focal length to decrease the image distortion at 25,7 mm. The camera is located on a *VCT-R640* stand and activated by means of a remote control, Figure 55, which avoids any interference in the initial frames.

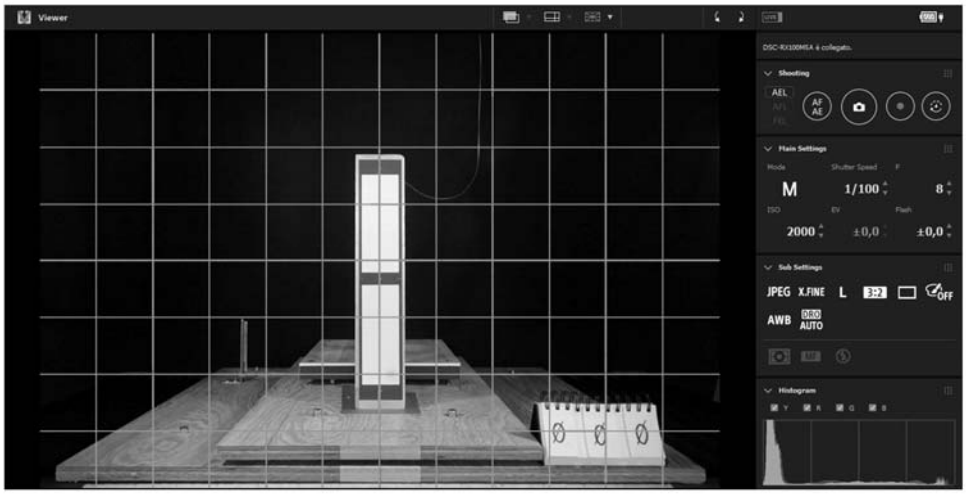

Figure 55 - Remote camera control.
[Author's image].

The large amount of data is managed with *SF-UX2 series SD* memory card (Speed Class 10) with high acquisition speed. To improve the lighting conditions, the block was lit with three 120W halogen lamps.

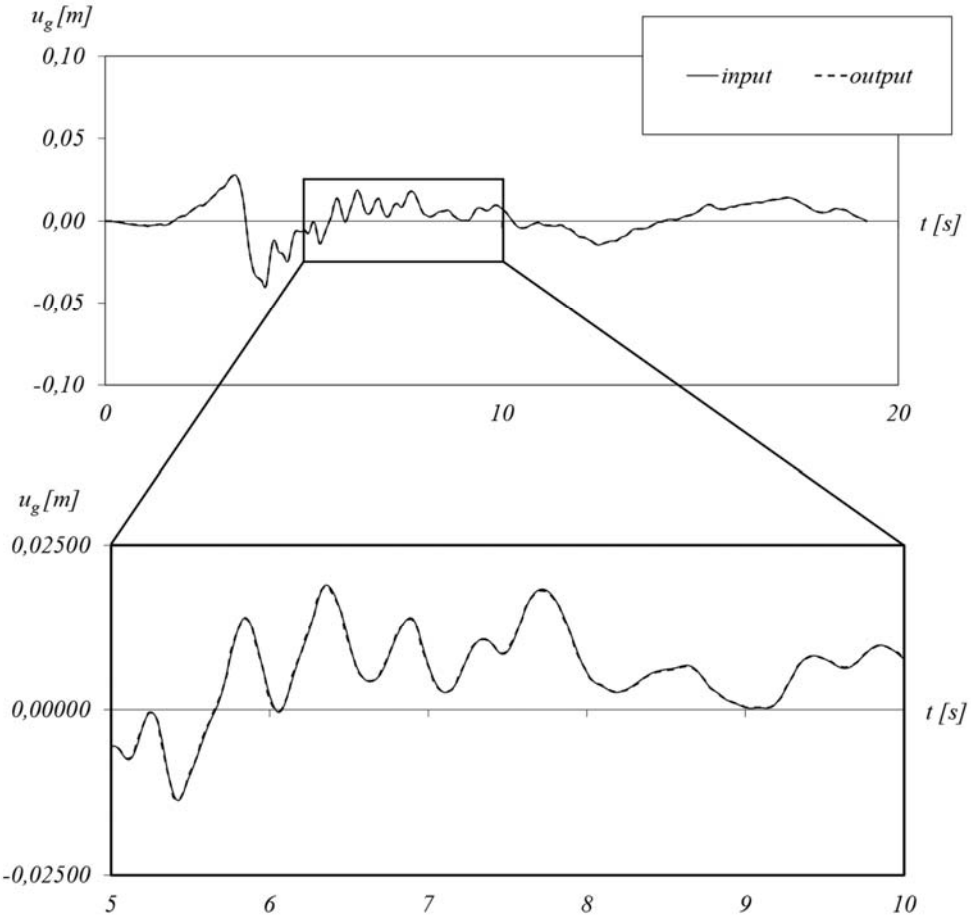

Figure 56 – Displacement check of the shaking table during a practice test.
[Author's image].

Chapter 4 Dynamics of the rigid body

This chapter presents the experimental investigations focused on the seismic response of small rigid blocks characterized by different aspect ratios and scale factors. Nine wooden specimens were subjected to free rocking motion (9 tests) aiming at the identification of the coefficient of restitution and subsequently have been tested on the shaking table under cosine pulse inputs (9.326 tests) and Friuli earthquake (5.940 tests, 660 for each block) for a total of 15.266 tests.

The experimental campaign was designed to identify the factors that must be considered in order to capture the main results and features.

A marked uncertainty in the response of the blocks is recognized under specific conditions which are identified and discussed. The experimental results, reported in terms of stability spectra and fragility curves, show the limits of numerical models based on classical theory that can fail in the prediction of the dynamic response. To this purpose, a novel numerical model able to account for the contact imperfections and for a variable coefficient of restitution calibrated on free rocking experimental tests is proposed and then validated against the extensive experimental campaign. The conclusive remarks help to assess the overturning risk of rigid blocks under seismic excitation and to provide some considerations to better interpret the behavior of rigid blocks.

4.1 An asymmetric rigid block model accounting the imperfections

In Chapter 2 it was highlighted that even in the case of simple geometry, the rigid body motion is strongly affected by impairments in the contacts with the base which introduce chaotic behavior under dynamic loadings. Several studies reported the importance of a correct determination of the coefficient of restitution, e.g. in [6], but few of them analysed the effect of geometric imperfection and the defects on contact surface.

In this section a novel numerical model based on the rigid block motion able to account for the asymmetry of the object as well as for its flawed contact on the base is presented and duly validated against experimental tests. A physical-mathematical interpretation to the issues, which will be highlighted in section 4.2, is provided. The validation of the proposed model is presented in the next section and an application is presented in Chapter 6 by comparing the results of the numerical simulations with the experimental ones of a scaled prototype of the statue representing the Venere of Landolina. The nomenclature presented in section 2.2.2 has been further specified for the case of asymmetrical body changing the previous notation and avoiding misunderstandings due the introduction of more parameters.

The 2D structural model (Simple Rocking Model), depicted in Figure 57 is a rigid body which herein represents a free-standing art object, characterized by its mass m and polar moment of inertia I_G with respect to its centre of gravity G. The height h is introduced as well as the horizontal distances b_L and b_R between the projection of the centre of gravity on the base and the left and right base edges, respectively. The block is assumed to oscillate on the rigid support/foundation without sliding[18]. The asymmetry of the block implies that the polar moments of inertia I_L and I_R

[18] Regarding the rigid block analysis, the rocking response of bodies is modelled assuming the following hypotheses:

- the body is rigid;
- the foundation is rigid;
- the impact is inelastic and modelled through the coefficient of restitution
- the density is homogeneous.

with respect to the two pivot points depend on the distances d_L and d_R. The dynamics of the model can be described considering as single Lagrangian parameter the rotation θ of the body, assumed positive if clockwise i.e. when the right edge is in contact with the base. The present model aims at accounting for unavoidable impairments in the contact of the block with the base and represents an extension of a previously model reported in section 2.2.2 for symmetric blocks to the case of asymmetric ones. A survey of the alternative conditions during motions is given in the following.

The initial stick state holds during the time lapse when the ground acceleration is bounded by right and left uplift accelerations

$$\ddot{u}_R \le \ddot{u}_g(t) \le \ddot{u}_L \tag{33}$$

which are derived as follows by reducing the theoretical ones according to the coefficients α_L and α_R:

$$\ddot{u}_R = -\alpha_R g\, b_R/h\,; \quad \ddot{u}_L = -\alpha_L g\, b_L/h\,; \tag{34}$$

where g is the gravity acceleration.

The coefficients α_L and α_R account for presence of various flaws occurring in real cases such as base irregularities, absence of verticality, flexible foundation, presence of smoothed edges which contribute to reduce the theoretical stabilizing moment. The coefficients can be experimentally evaluated as shown in section 4.1.2.

The conventional differential equation of the rigid block motion is updated herein to account for possible irregularities of the object/base contact interface by introducing a transition phase (rolling motion) between the full contact and the complete uplift of the block (rocking motion) ruled by the function $\alpha(\theta)$ described in section 4.1.1.

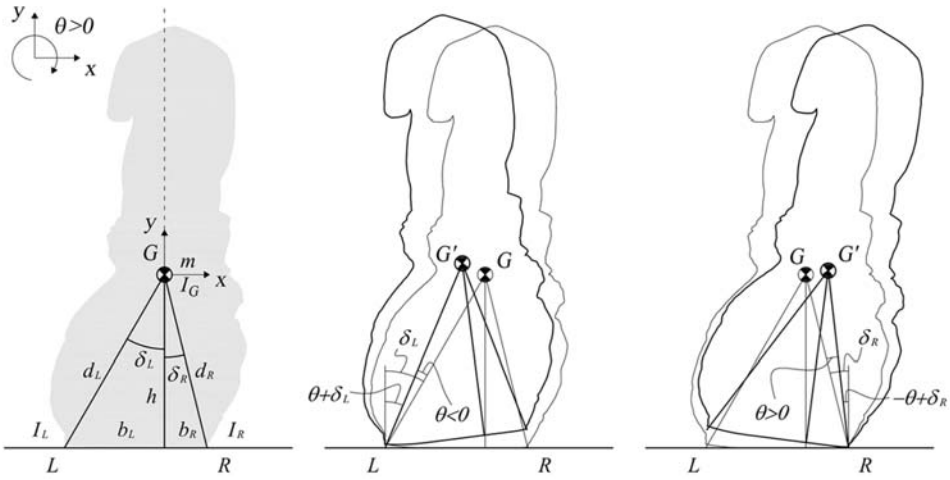

Figure 57 – Asymmetric simple rocking model: 2D schematic model, rocking motion considering negative and positive uplift. [Author's image].

$$\ddot{\theta} = -p_L^2 \left\{ \frac{\ddot{u}_g}{g} \cos\left[\delta_L \operatorname{sgn}(\theta) - \theta\right] + \alpha(\theta) \sin\left[\delta_L \operatorname{sgn}(\theta) - \theta\right] \right\} \quad \theta(t) < 0$$
$$\ddot{\theta} = -p_R^2 \left\{ \frac{\ddot{u}_g}{g} \cos\left[\delta_R \operatorname{sgn}(\theta) - \theta\right] + \alpha(\theta) \sin\left[\delta_R \operatorname{sgn}(\theta) - \theta\right] \right\} \quad \theta(t) > 0 \tag{35}$$

where $\delta_L = \tan^{-1}(b_L/h)$ and $\delta_R = \tan^{-1}(b_R/h)$ are the critical angles leading to the overturning of the block when it rocks around left and right edges, respectively (see Figure 57), being $-\delta_L \le \theta \le \delta_R$. The frequency parameters are defined as

$$p_L^2 = \frac{mgd_L}{I_G + md_L^2} = \frac{mgd_L}{I_L}; \quad p_R^2 = \frac{mgd_R}{I_G + md_R^2} = \frac{mgd_R}{I_R} \tag{36}$$

where $d_L = \sqrt{b_L^2 + h^2}$, $d_R = \sqrt{b_R^2 + h^2}$.

4.1.1 Quasi-Roll & rock model with imperfections

The function $\alpha(\theta)$ guides the transition phase (rolling motion) between the full contact and the complete uplift of the block (rocking motion). As the block leaves the full contact condition entering the rolling phase, the stabilizing moment increases up to the limit value where the fully theoretical contribution of the ideal block is restored and the rotation θ reaches the uplift threshold (the *transition rotation* θ_L on the left side and θ_R on the right one), as described by Figure 58.

The transition function is assumed to be linear so that, for the asymmetric block one gets

$$\alpha(\theta)=\begin{cases}\alpha_L+\dfrac{1-\alpha_L}{\theta_L}\theta; & \theta_L\le\theta<0 \quad or \quad \{\theta\equiv 0 \quad and \quad \dot\theta>0\}\\ \alpha_R+\dfrac{1-\alpha_R}{\theta_R}\theta; & 0<\theta\le\theta_R \quad or \quad \{\theta\equiv 0 \quad and \quad \dot\theta<0\}\\ 1; & \theta<\theta_L \ or \ \theta>\theta_R\end{cases} \tag{37}$$

The proposed stabilizing moment-rotation law, Figure 58b, modifies the linear model proposed for perfect slender blocks in three main aspects:

- the softening branch of the moment-rotation law is refined introducing a smoothed transition from the full contact to the rocking condition, indicative of a so called rolling phase;
- the uplift acceleration decreases as a consequence of contact imperfections;
- the rocking phase is characterized by a nonlinear softening branch.

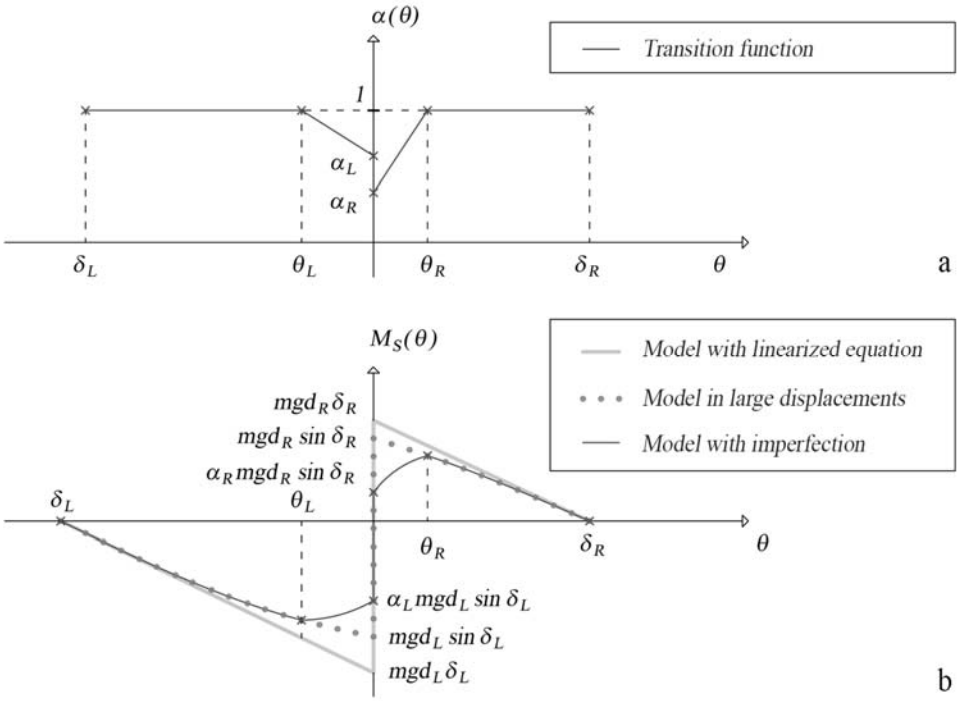

Figure 58 - Model for asymmetric blocks with imperfections: (a) coefficients of reduction of the stabilizing moment; (b) stabilizing moment vs rotation. [Author's image].

To fillet the first uplift point with the softening branch, the transition phase associated to the coefficient introduced in eq. (37) is of crucial help. Some authors employed analogous models interpreting the transition phase as a rolling motion which precedes the rocking of the block [56]. It is worth mentioning that eq. (35) can simulate both the rolling and rocking phases.

4.1.2 Characterization of the main governing parameters

The uplift accelerations and the coefficients of restitution were obtained by means of simple tests. Primarily the transition between the full contact and rocking phase must be identified. This is pursued by analysing the response when the body is

subjected to a base cosine pulse with increasing amplitude. The identification of the real uplift acceleration can be achieved by reading the initial frames of the recordings made with a close-up at the base of the block.

When the body passes from clockwise (positive) to anticlockwise (negative) rotation, or *vice versa*, an impact occurs ($\theta = 0$). This phase implies a loss of energy associated to an empirical coefficient of restitution, and a subsequent jump of the angular velocity, usually defined as follows

$$\dot{\theta}^{+} = e\dot{\theta}^{-} \tag{38}$$

where $\dot{\theta}^{-}$ and $\dot{\theta}^{+}$ represent the angular velocities immediately before and after the impact, respectively. In an ideal case of rigid body and foundation, the coefficient of restitution, depends on geometrical parameters [63] only, but in the reality a more complex scenario is encountered. To minimize discrepancies between experimental and numerical results due to interface material or imperfections [26], the calibration of the coefficient of restitution will be directly obtained processing the experimental response from tests in free vibrations with an initial rotation.

The impact conditions can be assumed according to several theoretical formulations. To numerically reproduce the stability spectra, since the response is characterized by one or two impacts, it is sufficient to refer to the strategy proposed in [64] valid for symmetrical blocks (with critical angle δ) by considering the peak rotations θ_i and θ_j at two generic rocking phases i and j, being $i > j$, eq. (39).

$$e_E = \sqrt[2(i-j)]{\frac{\cos(\delta-\theta_i)-\cos\delta}{\cos(\delta-\theta_j)-\cos\delta}} \tag{39}$$

To reduce the measurement errors peak rotations delayed of several phases are usually considered (here it is assumed $i = 6$ and $j = 0$.

A variable coefficient of restitution differentiated according to the side of the impact and to the impact velocity seems to be more appropriate to get reliable numerical simulations in case of response characterised by a significant amount of impacts. The impact velocity of the single block is a measure that can be indirectly estimated considering the peaks of rotation before and after each impact during free rocking motion. Under the assumption of conservation of energy during the rocking phase, the potential energy of the block at the peak of rotation θ_i before the impact converts to kinetic energy at the impact, associated to the velocity $\dot{\theta}_i^-$.

Similarly, the kinetic energy of the block after the impact (associated to the velocity $\dot{\theta}_i^+$) completely converts to potential energy at the subsequent rotation peak θ_{i+1}.

The measured experimental potential (E_u), kinetic (E_k) and total (E_t) energies of the block during a free rocking motion at the i - th motion phase, can be obtained as follows:

$$E_u = \begin{cases} mgd_L\left[\cos\left(\delta_L+\theta_i\right)-\cos\left(\delta_L\right)\right] & \text{for } \theta_i<0 \\ mgd_R\left[\cos\left(\delta_R-\theta_i\right)-\cos\left(\delta_R\right)\right] & \text{for } \theta_i>0 \end{cases} \tag{40}$$

$$E_k = \begin{cases} \frac{1}{2} I_L \dot{\theta}_i^2 & \text{for } \theta_i<0 \\ \frac{1}{2} I_R \dot{\theta}_i^2 & \text{for } \theta_i>0 \end{cases} \quad \text{with:} \quad \dot{\theta}_i = \frac{\theta_{i+1}-\theta_{i-1}}{t_{i+1}-t_{i-1}} \tag{41}$$

$$E_t = E_k + E_u \tag{42}$$

Application of eqs. (40)-(42) leads to an experimental evaluation of the coefficients of restitution according to the observed energy decay at each impact. Due to the asymmetry of the block, the results must be differentiated depending on the edge around which the block is rotating at the impact. As the total energy of the block

decreases, the impact angular velocity reduces, and a trend of the coefficient of restitution versus the impact velocity can be reconstructed.

After simple algebra, the experimental coefficient of restitution associated to a certain impact velocity can be written as follows

$$e_{E,L}\left(\dot{\theta}_i^-\right)=\frac{\dot{\theta}_i^+}{\dot{\theta}_i^-}=\sqrt{\frac{d_L}{I_L}\frac{I_R}{d_R}\frac{\left[\cos\left(\delta_L-\theta_{i+1}\right)-\cos\delta_L\right]}{\left[\cos\left(\delta_R-\theta_i\right)-\cos\delta_R\right]}} \quad i=1,3,5,... \tag{43}$$

$$e_{E,R}\left(\dot{\theta}_i^-\right)=\frac{\dot{\theta}_i^+}{\dot{\theta}_i^-}=\sqrt{\frac{d_R}{I_R}\frac{I_L}{d_L}\frac{\left[\cos\left(\delta_R-\theta_{i+1}\right)-\cos\delta_R\right]}{\left[\cos\left(\delta_L-\theta_i\right)-\cos\delta_L\right]}} \quad i=0,2,4,...$$

In Figure 59, a scheme of a free rocking motion is reported, where even and odd impacts correspond to right and left pivot points, respectively.

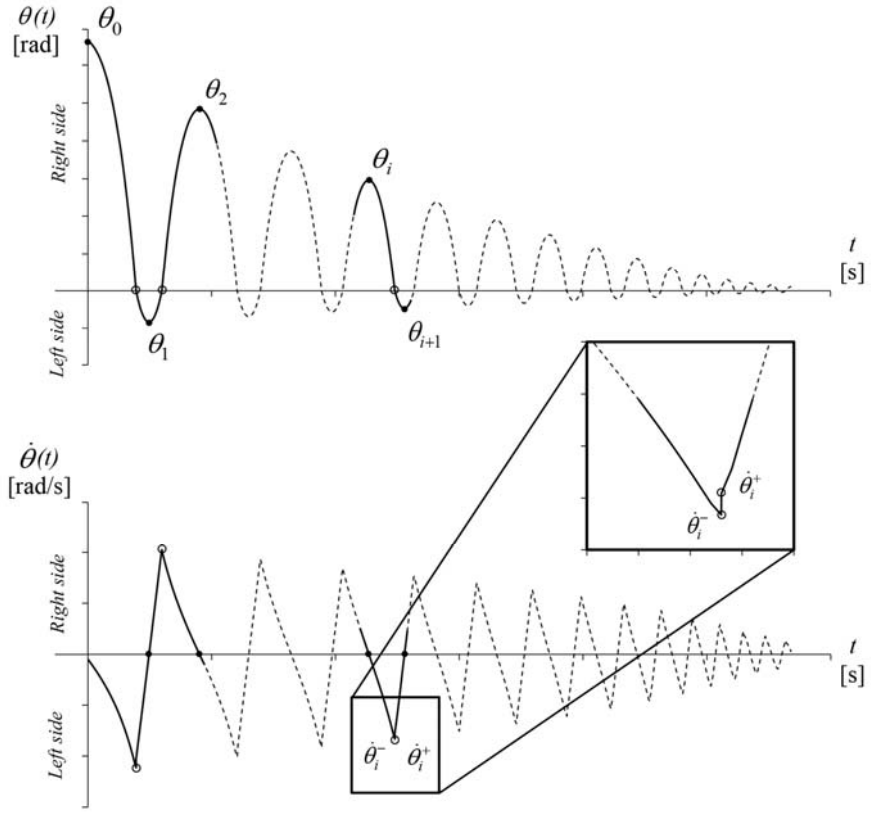

Figure 59 - Measuring scheme of the coefficient of restitution. [Author's image].

4.2 Experimental and numerical investigation for symmetrical small bodies

By employing the unidirectional shaking table and making use of a contactless acquisition data strategy, some aspects of the dynamic behavior of several specimens with different aspect ratios and size factors are preliminary investigated. The experimental setup was briefly described in section 3.2. Nine wooden specimens were tested, Figure 60, considering three different aspect ratios and three size factors, as better specified in Table 1. The Scale factor (Sc.f.) represents the semi-diagonal of the generic *i*-th block normalized by the corresponding value d_1 of the reference

largest block; the slenderness (λ) is the ratio between the height and the base of the *i*-th block. The specimens were placed on a sheet of sandpaper (whose effectiveness was experimentally verified).

The characteristics of the specimens are identified by an alphanumeric code in which the letters from A to C define the slenderness that gradually decreases (type A means slender, type C means squat), whereas the numbers from 1 to 3 characterize the scale factors of the blocks with gradually smaller dimensions (type 1 is the biggest, type 3 is the smallest).

Aspect ratio		***A***			***B***			***C***	
$\lambda=(h/b)$	5,21	4,99	5,00	3,89	3,78	3,78	2,57	2,51	2,64
Scale factor	*Sc.f.* ***1***	*Sc.f.* ***2***	*Sc.f.* ***3***	*Sc.f.* ***1***	*Sc.f.* ***2***	*Sc.f.* ***3***	*Sc.f.* ***1***	*Sc.f.* ***2***	*Sc.f.* ***3***
d_i / d_1	1,00	0,74	0,48	1,00	0,73	0,48	1,00	0,73	0,47
m [kg] $(^1)$	1,286	0,435	0,113	0,995	0,300	0,084	0,641	0,201	0,059
b [m] $(^1)$	0,0384	0,0285	0,0184	0,0385	0,0282	0,0184	0,0389	0,0283	0,0184
h [m] $(^1)$	0,2000	0,1423	0,0920	0,1500	0,1065	0,0695	0,0998	0,0710	0,0485
d [m] $(^2)$	0,2037	0,1451	0,0938	0,1549	0,1102	0,0719	0,1070	0,0764	0,0519
δ [rad] $(^2)$	0,1897	0,1978	0,1974	0,2515	0,2586	0,2588	0,3714	0,3787	0,3623
μ [-] $(^2)$	0,1920	0,2005	0,2000	0,2569	0,2645	0,2647	0,3895	0,3979	0,3790
p [rad/s] $(^2)$	6,011	7,121	8,856	6,893	8,172	10,116	8,290	9,813	11,910

Table 1 – Tested specimens: measured and theoretical parameters. Values (1) measured on the specimens and values (2) indirectly obtained from theoretical formulation.

Figure 60 - Tested specimens. [Author's image].

The analysis of the characteristics of natural accelerograms shows a similarity with specific functions, especially in the case of near-faults seismic events. In the latter case, the time history can be seen as a sum of wavelets from which it is possible to extract a predominant one. Consequently, the strong phase of the accelerogram can be approximated with a simple trigonometric pulse defined by the amplitude $\ddot{u}_{g,0}$ and the duration T_p [10].

One-sine or one-cosine pulses can be used in relation to the characteristics of the accelerogram and can provide useful information about the response of the rocking systems. By using these simple pulses and solving numerically the nonlinear equation of motion for ideal rigid blocks, in [10] the *stability spectra* are presented

reporting the minimum overturning amplitude of block as the frequency parameter changes.

The variability of the response in case of earthquakes distant from the source was studied by exciting the specimens with the Friuli ground motion registered in Tolmezzo (Italy) in 1976 (EW component).

This approach is useful to identify rocking or overturning conditions, as well as uncertainties associated with imperfections and causes of instability. Afterwards, the numerical analyses involving the nine blocks were carried out in accordance with the formulation reported in section 2.2.2 and with that proposed in section 4.1.1.

The parameters experimentally obtained, that describe the transition between the full contact and rocking phase and, employed in the numerical analysis are shown in the following Table 2.

A1			*A2*			*A3*		
$\ddot{u}^{(t)}$ [g]	$\ddot{u}^{(e)}$ [g]	α (^{3}) [-]	$\ddot{u}^{(t)}$ [g]	$\ddot{u}^{(e)}$ [g]	α (^{3}) [-]	$\ddot{u}^{(t)}$ [g]	$\ddot{u}^{(e)}$ [g]	α (^{3}) [-]
0,192	0,120	0,65	0,200	0,140	0,70	0,200	0,130	0,65

a

B1			*B2*			*B3*		
$\ddot{u}^{(t)}$ [g]	$\ddot{u}^{(e)}$ [g]	α (^{3}) [-]	$\ddot{u}^{(t)}$ [g]	$\ddot{u}^{(e)}$ [g]	α (^{3}) [-]	$\ddot{u}^{(t)}$ [g]	$\ddot{u}^{(e)}$ [g]	α (^{3}) [-]
0,257	0,190	0,75	0,264	0,240	0,92	0,265	0,150	0,56

b

C1			*C2*			*C3*		
$\ddot{u}^{(t)}$ [g]	$\ddot{u}^{(e)}$ [g]	α (^{3}) [-]	$\ddot{u}^{(t)}$ [g]	$\ddot{u}^{(e)}$ [g]	α (^{3}) [-]	$\ddot{u}^{(t)}$ [g]	$\ddot{u}^{(e)}$ [g]	α (^{3}) [-]
0,389	0,290	0,76	0,398	0,350	0,88	0,379	0,280	0,73

c

Table 2 - Comparison between theoretical (*t*) end experimental (*e*) uplift accelerations for each block and corresponding reduced uplift coefficient (3): (a) type A; (b) type B; (c) type C.

Once the free vibration test is processed, Figure 61, the results of the evaluation of the coefficient of restitution to be considered in order to reproduce numerically the stability spectra, are reported in Table 3.

Aspect ratio		***A***			***B***			***C***	
$\lambda=(h/b)$	5,21	4,99	5,00	3,89	3,78	3,78	2,57	2,51	2,64
Scale factor	*Sc.f.* ***1***	*Sc.f.* ***2***	*Sc.f.* ***3***	*Sc.f.* ***1***	*Sc.f.* ***2***	*Sc.f.* ***3***	*Sc.f.* ***1***	*Sc.f.* ***2***	*Sc.f.* ***3***
d_i / d_1	1,00	0,74	0,48	1,00	0,73	0,48	1,00	0,73	0,47
e_T [-] (2)	0,947	0,942	0,942	0,907	0,902	0,902	0.802	0,795	0,812
e_E [-] (3)	0,953	0,950	0,934	0,860	0,852	0,893	0,827	0,780	0,840

Table 3 – Measured coefficient of restitution according to the formulation for symmetric blocks. Values (2) indirectly obtained from theoretical formulation and values (3) obtained from specimens through experimental measures.

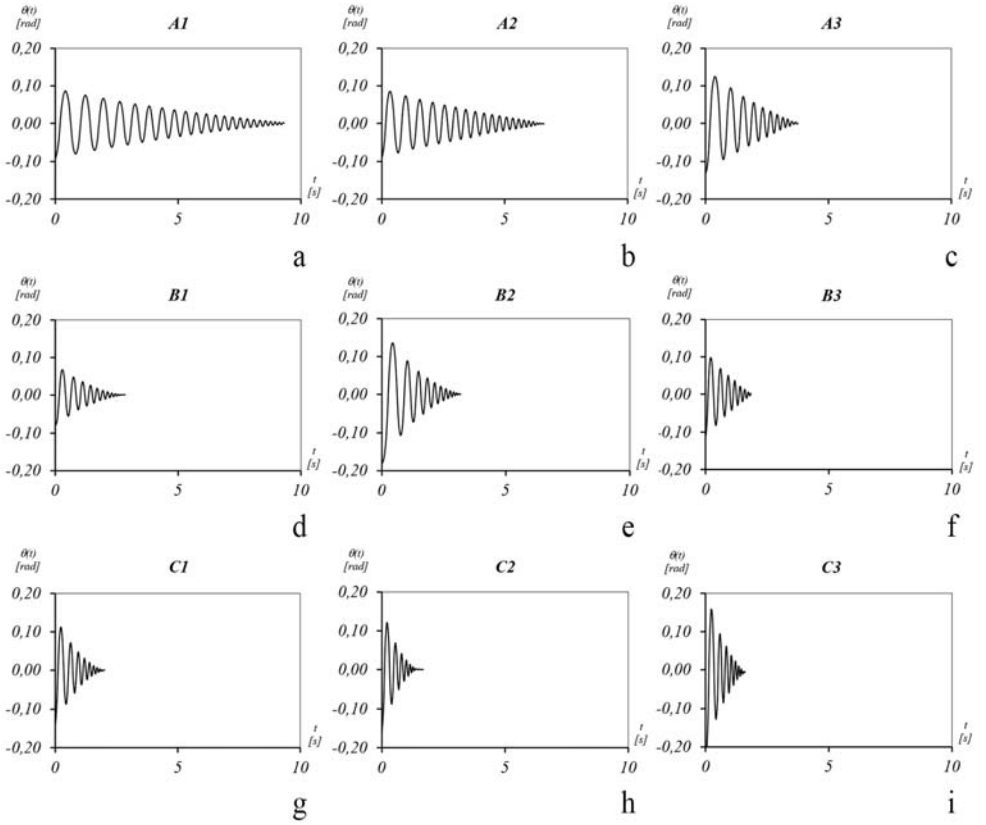

Figure 61 - Free vibration tests for determining the coefficient of restitution. [Author's image].

With reference to the free rocking motion test of Figure 61, the trend of the coefficients of restitution and the relevant correspondence with the angular velocity of the impact are depicted in Figure 62. The results, summarized in Table 4-Table 12, are differentiated according to the edge around which the block is rotating at the impact. As the total energy of the block decreases, the angular velocity of impact reduces and a trend of the coefficient of restitution versus the impact velocity is reconstructed. Once experimental values of the coefficient of restitution are evaluated for several impacts, the experimental points collected through eq. (43) can be interpolated considering regression curves, Figure 62.

i	t	$\lvert\dot{\theta}\rvert$	$e_{E,R}$	i	t	$\lvert\dot{\theta}\rvert$	$e_{E,L}$
[·]	[s]	[rad/s]	[·]	[·]	[s]	[rad/s]	[·]
0	0,21	0,8593	0,9844	1	0,63	0,8073	0,9736
2	1,03	0,7969	0,9791	3	1,43	0,7977	0,9724
4	1,79	0,7540	0,9773	5	2,14	0,7034	0,9708
6	2,48	0,7434	0,9770	7	2,79	0,6472	0,9790
8	3,10	0,6395	0,9796	9	3,40	0,6135	0,9871
10	3,69	0,6480	0,9790	11	3,97	0,6147	0,9867

Table 4 - Measured restitution coefficients for right, $e_{E,R}$ and left, $e_{E,L}$ impacts for block type *A1*.

i	t	$\lvert\dot{\theta}\rvert$	$e_{E,R}$	i	t	$\lvert\dot{\theta}\rvert$	$e_{E,L}$
[·]	[s]	[rad/s]	[·]	[·]	[s]	[rad/s]	[·]
0	0,16	1,0013	0,9906	1	0,52	0,9407	0,9618
2	0,82	0,9035	0,9816	3	1,13	0,9272	0,9642
4	1,41	0,8737	0,9801	5	1,69	0,8787	0,9697
6	1,94	0,8550	0,9794	7	2,20	0,8219	0,9699
8	2,44	0,7587	0,9794	9	2,68	0,7263	0,9555
10	2,89	0,7332	0,9803	11	3,12	0,7188	0,9536

Table 5 - Measured restitution coefficients for right, $e_{E,R}$ and left, $e_{E,L}$ impacts for block type *A2*.

i	t	$\lvert\dot{\theta}\rvert$	$e_{E,R}$	i	t	$\lvert\dot{\theta}\rvert$	$e_{E,L}$
[·]	[s]	[rad/s]	[·]	[·]	[s]	[rad/s]	[·]
0	0,19	1,4367	0,9860	1	0,58	1,3530	0,9184
2	0,88	1,2427	0,9919	3	1,18	1,2003	0,9185
4	1,42	1,1268	0,9898	5	1,66	1,0353	0,9199
6	1,87	0,9569	0,9789	7	2,07	0,9276	0,9216
8	2,24	0,8976	0,9729	9	2,42	0,8002	0,9243
10	2,57	0,7635	0,9553	11	2,73	0,6714	0,9279

Table 6 - Measured restitution coefficients for right, $e_{E,R}$ and left, $e_{E,L}$ impacts for block type *A3*.

i	t	$\lvert\dot{\theta}\rvert$	$e_{E,R}$	i	t	$\lvert\dot{\theta}\rvert$	$e_{E,L}$
[·]	[s]	[rad/s]	[·]	[·]	[s]	[rad/s]	[·]
0	0,15	0,9835	0,9397	1	0,41	0,9124	0,9106
2	0,63	0,7944	0,9469	3	0,83	0,7117	0,9130
4	1,02	0,6841	0,9488	5	1,19	0,5982	0,9149
6	1,35	0,5775	0,9490	7	1,50	0,5203	0,9165
8	1,63	0,4678	0,9476	9	1,76	0,4059	0,9192
10	1,87	0,3112	0,9426	11	1,98	0,2843	0,9225

Table 7 - Measured restitution coefficients for right, $e_{E,R}$ and left, $e_{E,L}$ impacts for block type *B1*.

i	t	$\lvert\dot{\theta}\rvert$	$e_{E,R}$	i	t	$\lvert\dot{\theta}\rvert$	$e_{E,L}$
[·]	[s]	[rad/s]	[·]	[·]	[s]	[rad/s]	[·]
0	0,26	1,6884	0,9238	1	0,62	1,5231	0,9182
2	0,91	1,3955	0,9305	3	1,17	1,2900	0,9194
4	1,38	1,0935	0,9332	5	1,58	1,0196	0,9161
6	1,76	0,9833	0,9332	7	1,93	0,8717	0,9123
8	2,07	0,8054	0,9319	9	2,20	0,7270	0,9070
10	2,33	0,6323	0,9292	11	2,33	0,6323	0,9028

Table 8 - Measured restitution coefficients for right, $e_{E,R}$ and left, $e_{E,L}$ impacts for block type *B2*.

i	t	$\lvert\dot{\theta}\rvert$	$e_{E,R}$	i	t	$\lvert\dot{\theta}\rvert$	$e_{E,L}$
[·]	[s]	[rad/s]	[·]	[·]	[s]	[rad/s]	[·]
0	0,11	1,7023	0,9401	1	0,33	1,5776	0,9293
2	0,52	1,4691	0,9355	3	0,69	1,3539	0,9331
4	0,85	1,1843	0,9304	5	1,00	1,0812	0,9285
6	1,13	1,0629	0,9283	7	1,25	0,8996	0,9198
8	1,36	0,7679	0,9237	9	1,46	0,6776	0,9030
10	1,56	0,5753	0,9210	11	1,56	0,5753	0,8930

Table 9 - Measured restitution coefficients for right, $e_{E,R}$ and left, $e_{E,L}$ impacts for block type *B3*.

i	t	$\lvert\dot{\theta}\rvert$	$e_{E,R}$	i	t	$\lvert\dot{\theta}\rvert$	$e_{E,L}$
[·]	[s]	[rad/s]	[·]	[·]	[s]	[rad/s]	[·]
0	0,12	1,8976	0,9212	1	0,35	1,7481	0,8970
2	0,54	1,5214	0,9163	3	0,73	1,3545	0,9072
4	0,88	1,1829	0,9122	5	1,02	1,0753	0,9048
6	1,14	0,9543	0,9095	7	1,25	0,8049	0,8949
8	1,36	0,7168	0,9068	9	1,45	0,6131	0,8832
10	1,53	0,5138	0,9046	11	1,61	0,4376	0,8693

Table 10 - Measured restitution coefficients for right, $e_{E,R}$ and left, $e_{E,L}$ impacts for block type *C1*.

i	t	$\lvert\dot{\theta}\rvert$	$e_{E,R}$	i	t	$\lvert\dot{\theta}\rvert$	$e_{E,L}$
[·]	[s]	[rad/s]	[·]	[·]	[s]	[rad/s]	[·]
0	0,12	2,3119	0,8932	1	0,32	1,9921	0,8706
2	0,48	1,7293	0,9000	3	0,63	1,4585	0,8694
4	0,75	1,2917	0,9050	5	0,86	1,1194	0,8576
6	0,96	0,9424	0,9089	7	1,04	0,7669	0,8362
8	1,12	0,6512	0,9121	9	1,18	0,4985	0,8137
10	1,24	0,4080	0,9148	11	1,29	0,3222	0,7959

Table 11 - Measured restitution coefficients for right, $e_{E,R}$ and left, $e_{E,L}$ impacts for block type *C2*.

i	t	$\lvert\dot{\theta}\rvert$	$e_{E,R}$	i	t	$\lvert\dot{\theta}\rvert$	$e_{E,L}$
[·]	[s]	[rad/s]	[·]	[·]	[s]	[rad/s]	[·]
0	0,14	3,2204	0,8789	1	0,35	2,8293	0,9195
2	0,52	2,4848	0,8868	3	0,66	2,2565	0,9588
4	0,79	2,0405	0,8639	5	0,90	1,8067	0,9743
6	1,01	1,5097	0,8092	7	1,09	1,4107	0,9767
8	1,18	1,1972	0,7631	9	1,25	1,0137	0,9686
10	1,33	0,7943	0,6884	11	1,37	0,5898	0,9482

Table 12 - Measured restitution coefficients for right, $e_{E,R}$ and left, $e_{E,L}$ impacts for block type *C3*.

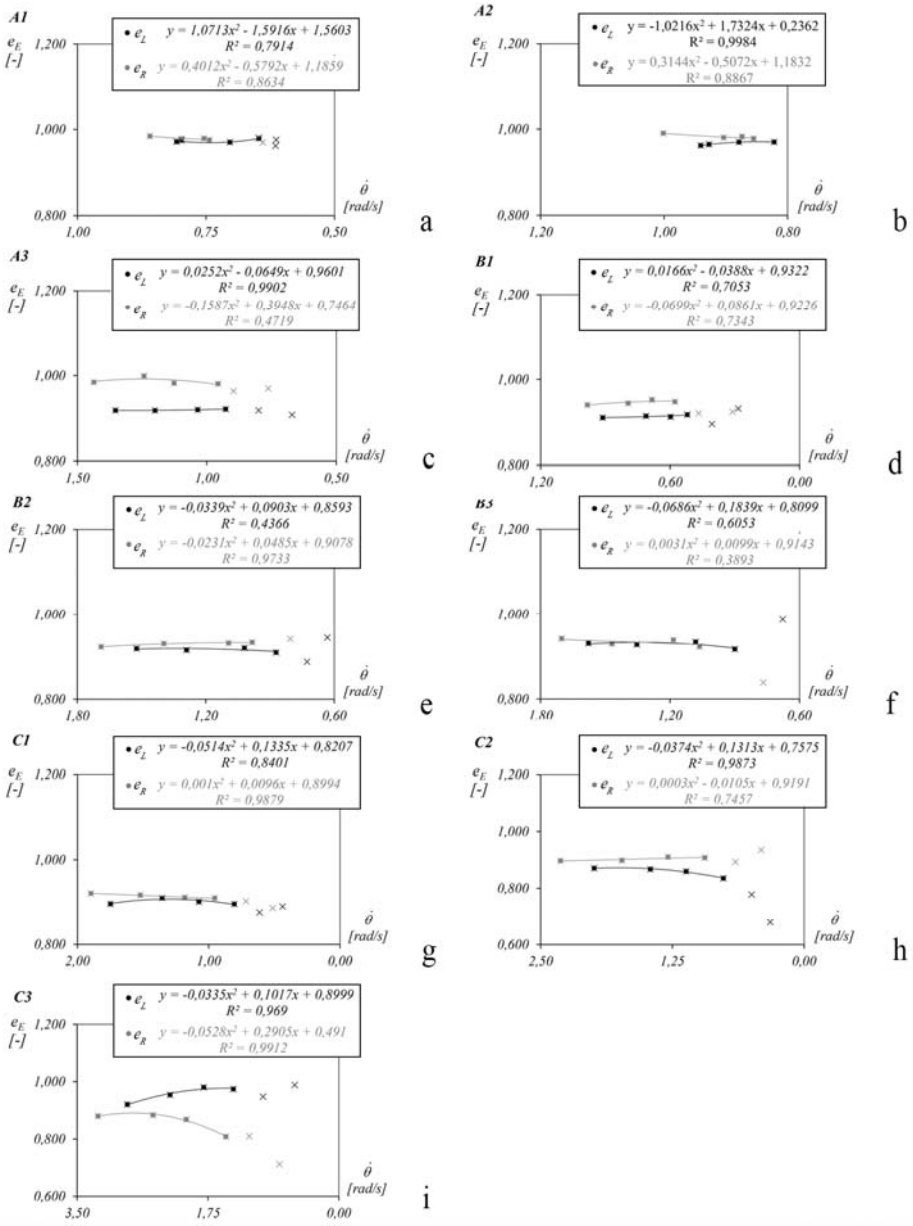

Figure 62 – Interpolation of all measured restitution coefficients for right, $e_{E,R}$ and left, $e_{E,L}$ impacts.

[Author's image].

The reference properties adopted for the analyses are summarized in Table 13-Table 16. Most of the properties of the block are considered deterministic and obtained as follows:

- some of the geometric (h , b) and inertial (m) parameters are directly inferred from the specimens and in Table 1 are identified with the subscript (^{1});
- other geometric (d , δ) and inertial (I_G , $I_G + md^2$) parameters of the blocks are indirectly evaluated considering the formulation in section 2.2.2 and are identified with the subscript (^{2});
- the coefficients of restitution are considered differentiating the case characterized by few impacts (stability spectra), considering the values shown in Table 3, from those characterized by many impacts (*maximum rotation variability graphs*) considering $e_{E,L}$ and $e_{E,R}$ as described in section 4.1.2, Table 4-Table 12.

In case of blocks with imperfections the numerical analyses require additional parameters according to the formulation reported in section 4.1.1

- the coefficients for the reduction of the uplift accelerations ($\alpha = \alpha_L = \alpha_R$), identified with the subscript (^{3}) in Table 2, since they were experimentally evaluated;
- the remaining independent parameter of model, i.e. the transition rotations θ_L and θ_R, are considered as uncertain variable.

In case of response spectra, a rough estimation of the angles θ_L and θ_R is provided considering that the full uplift of the blocks, for both sides, is approximately

associated to the normalized values of $\theta_L/\delta = \theta_R/\delta = 7{,}00\times10^{-2}$ for both sides. The considered normalized value correspond for each block to the rotation angles reported in Table 13.

	A			**B**			**C**		
	A1	A2	A3	B1	B2	B3	C1	C2	C3
θ_L [rad] $\times10^{-2}$	1,33	1,38	138	1,76	1,81	1,81	2,60	2,65	2,54
θ_R [rad] $\times10^{-2}$	1,33	1,38	138	1,76	1,81	1,81	2,60	2,65	2,54

Table 13 – Transition rotation angle for each block.

The response of the block did not show appreciable sensitivity differentiating the transition angle θ_L and θ_R.

Specifically, the interval of the normalized transition angle $\theta_L/\delta = \theta_R/\delta = [1{,}00;13{,}00]\times10^{-2}$ is adopted (with reference value $7{,}00\times10^{-2}$ and radius $6{,}00\times10^{-2}$), assuming equally spaced steps of $2{,}50^{-3}$ for a total amount of 49 outcomes. The determination of the stability spectra was obtained using the maximum transition angle extrapolated from the defined range, that is $\theta_L/\delta = \theta_R/\delta = 13{,}00\times10^{-2}$.

Geometric parameters

	A1	***A2***	***A3***	***B1***	***B2***	***B3***	***C1***	***C2***	***C3***
h [m] (1)	0,2000	0,1423	0,0920	0,1500	0,1065	0,0695	0,0998	0,0710	0,0485
b [m] (1)	0,0384	0,0285	0,0184	0,0385	0,0282	0,0184	0,0389	0,0283	0,0184
d [m] (2)	0,2037	0,1451	0,0938	0,1549	0,1102	0,0719	0,1070	0,0764	0,0519
δ [rad] (2)	0,1897	0,1978	0,1974	0,2515	0,2586	0,2588	0,3714	0,3787	0,3623

Table 14 – Reference properties adopted for the numerical model: geometric parameters. Values (1) measured from specimens, values (2) indirectly obtained from theoretical formulation and values (3) obtained from specimens through experimental measures.

Inertial parameters

$\times 10^{-3}$	***A1***	***A2***	***A3***	***B1***	***B2***	***B3***	***C1***	***C2***	***C3***
m [kg] (1)	1.286	435	113	995	300	84	641	201	59
I_G [kg m^2] (2)	17,80	3,00	0,33	7,87	1,20	0,14	2,42	0,39	0,05
I_G+md^2 [kg m^2] (2)	71,14	12,16	1,32	31,73	4,84	0,57	9,78	1,56	0,21

Table 15 - Reference properties adopted for the numerical model: inertial parameters. Values (1) measured from specimens, values (2) indirectly obtained from theoretical formulation and values (3) obtained from specimens through experimental measures.

Uplift coefficient

	A1	***A2***	***A3***	***B1***	***B2***	***B3***	***C1***	***C2***	***C3***
α [-] (3)	0,65	0,70	0,65	0,75	0,92	0,56	0,76	0,88	0,73

Table 16 - Reference properties adopted for the numerical model: uplift coefficient. Values (1) measured from specimens, values (2) indirectly obtained from theoretical formulation and values (3) obtained from specimens through experimental measures.

4.2.1 Stability spectra

The real overturning potential is experimentally determined when the blocks undergo one-cosine pulse with variable intensity and duration. The maximum acceleration corresponds to the initial instant, whereas the one-sine pulse is characterized by null ground acceleration at the same instant[19]. The displacement input for the shaking table is obtained by double integration of the one-cosine pulse

[19] The experimental stability spectrum was built considering the cosine pulse because in the case of one-sine pulse the acceleration gradually increases and it does not allow clearly identifying the incipient motion.

acceleration with amplitude $\ddot{u}_{g,0}$ and enforcing zero initial conditions on the displacement and velocity (Figure 63),

$$\ddot{u}_g = \ddot{u}_{g,0}\cos\left(\omega_p t\right),\ 0 \le t \le T_p \tag{44}$$

$$\dot{u}_g = \frac{\ddot{u}_{g,0}}{\omega_p}\cos\left(\omega_p t\right),\ 0 \le t \le T_p \tag{45}$$

$$u_g = \frac{\ddot{u}_{g,0}}{\omega_p^2}\cos\left(\omega_p t\right) + \frac{\ddot{u}_{g,0}}{\omega_p^2},\ 0 \le t \le T_p \tag{46}$$

where ω_p is the radial frequency of the pulse related to the period $T_p = 2\pi/\omega_p$.

In the case of one-cosine pulse, by increasing its amplitude and achieving the critical uplift acceleration, the action capable of initiating rocking is given at the beginning of the test, Figure 63c.

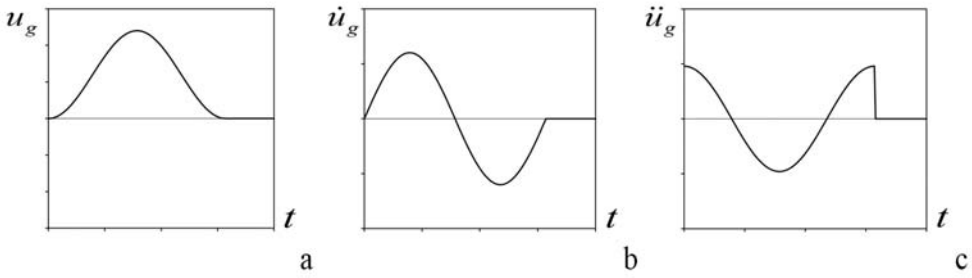

Figure 63 – One-cosine pulse: (a) displacements (b) velocity and (c) acceleration time histories. [Author's image].

The experiments were conducted placing the specimen on the shaking table with the same face in front of the camera and taking note of the collapse mode without recording the time history response. The pulse was reproduced by moving the shaking table from the left to the right, thus identifying modes 1 and 3 when the specimen overturns on the left, and mode 2 in the case it overturns on the right.

The results of the 9.326 experimental[20] tests are showed in Figure 65 in which the outcomes are reported to highlight the transition areas of the spectrum.

The experimental stability spectrum in Figure 65, obtained for each of the nine blocks, identifies the unsafe region where the block overturns but also the modes of collapse in relation to the characteristics of the input.

The shape changes with the input (sinusoidal, co-sinusoidal or according to any other chosen acceleration law), but the regions are in any case identified according to the number of impacts before collapse. The experimental results show that in the case of one-cosine pulse, three modes of collapse are recognized, namely with no impact (mode 1), one (mode 2) or two impacts (mode 3). The experimental safe zone is characterized by three possible behaviors, that is the block does not uplift, rolls or rocks, Figure 65.

The graphs show that the uplift acceleration limits the safe zone independently of the input frequency. It should be noted that the safe zone reduces as the scale factor reduces. By comparing the surface of the safe zone of block A1 and A3, it can be seen that in the second case the safe zone is smaller than in the first one. Moreover, comparing the results for blocks characterized by the same scale factor (graphs arranged along the columns), it is evident that the blocks characterized by the highest slenderness (type A) overturn more easily than the squat blocks (type C). Finally, the separation between safe and unsafe zones at low to medium frequencies for moderate acceleration values is not sharp as occurs through a jagged transition zone. This effect tends to disappear when higher acceleration and frequencies are considered.

[20] The number of tests that involved the single specimen is summarized as follows: 940 tests for block A1, 906 tests for block A2, 917 tests for block A3, 1289 tests for block B1, 1236 tests for block B2, 1536 tests for block B3, 876 tests for block C1, 782 tests for block C2, 844 tests for block C3.

During the tests, a further phase of motion was recognized in addition to the canonical ones in which the specimen exhibited small and imperceptible movements similar to a tremor. This micro-rocking could be mistaken as pure rocking, but the movements were so small that the centre of rotation at the base of the block could not pass from one edge to another. Consequently, these movements can be somehow interpreted as rolling caused by imperfections at the base of the block.

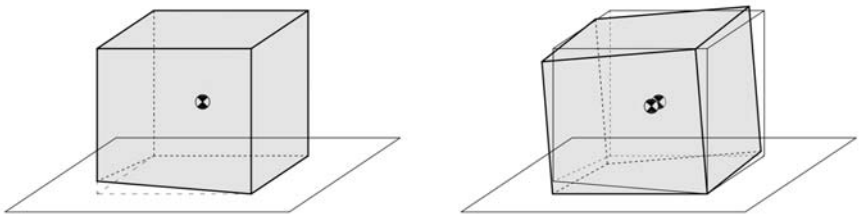

Figure 64 . Interpretation of real behavior. [Author's image].

For the latter reason, the experimental stability spectrum is characterized by six regions in which the rolling phase is added to the possible theoretical results.

The micro imperfections that characterize the base of the block modify the response also in relation to the positioning of the block on the shaking table. The block is apparently positioned in the same way at each test, but this operation introduces uncertainty, Figure 64. For this reason, the separation between no motion and rolling zones is not marked by a perfectly horizontal line. The experiments also confirmed that the stability spectra of slender blocks have a smaller safe zone than those of squat blocks and that maps of larger blocks are characterized by larger unsafe zones, but the passage from one region to another does not occur abruptly. The behavior of the block is well established when the input falls inside each region, but it is rather chaotic in proximity of transition zones. In these ranges, the repeatability of the experiments is not guaranteed. The experimental results will be compared with the numerical simulations, showing the limit of numerical models in simulating the dynamic behavior of rigid bodies, especially when the response is characterized by rocking with many impacts.

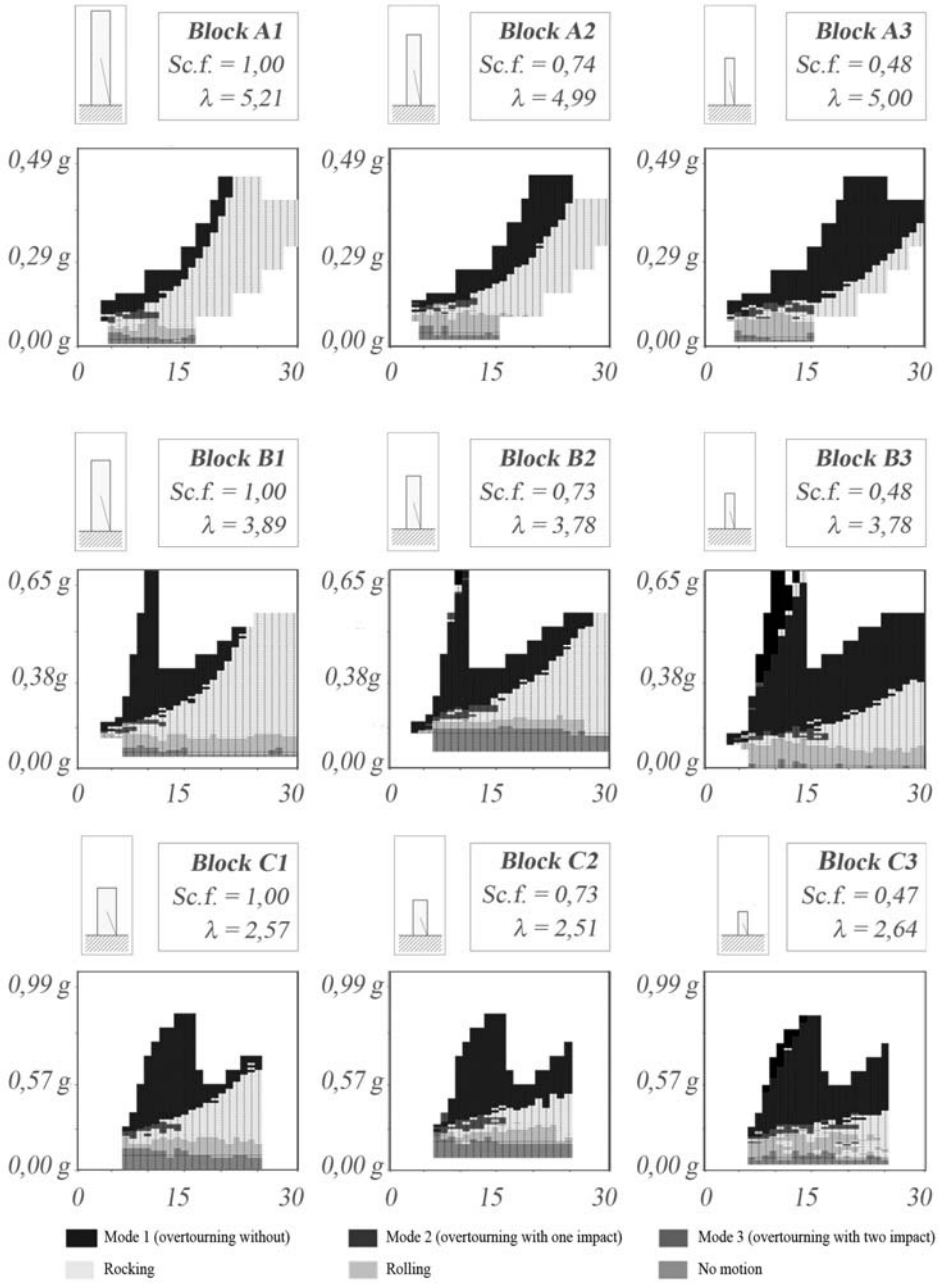

Figure 65 – Experimental stability spectrum. [Author's image].

In this context, the numerical analyses involving the nine blocks were carried out in accordance with the classical and new proposed formulation. The theoretical stability spectra in Figure 66-Figure 68, obtained for each of the nine blocks, identifies the unsafe region where the block overturn but also the modes of collapse in relation to the characteristics of the input.

The numerical analysis show that the same collapse modes detected during the experiments are encountered but for lower PGA, instead the possible behaviors characterizing the safe zones change in relation to the adopted model.

At first, the stability spectra are numerically produced by applying the coefficient of restitution of Housner, Figure 66, and that experimentally determined, Figure 67. Its calibration is carried out from experimental tests in free vibrations with an initial rotation. In both cases (Figure 66, Figure 67), five areas can be recognized, three of which characteristics of the unsafe domain. The first safe region (no motion zone) does not depend on the characteristics of the pulse; the second safe region (rocking zone) decreases its amplitude for smaller block (decreasing scale factors) or considering lower values of slenderness. Almost all regions are characterized by a clear separation, with the exception of the range where the peak acceleration is slightly larger than the uplift acceleration in the frequency band 0.8-0.16 Hz. The experimental results were compared with the numerical simulations showing the limit of numerical classical models to simulate the dynamic behavior of rigid bodies, also when it refers to an experimentally determined coefficient of restitution.

From the comparison of the results obtained with the new proposed model it emerges that the limits of each transition phase are consistent with the real behavior, thanks to the reduced uplift acceleration and the introduction of the rolling phase.

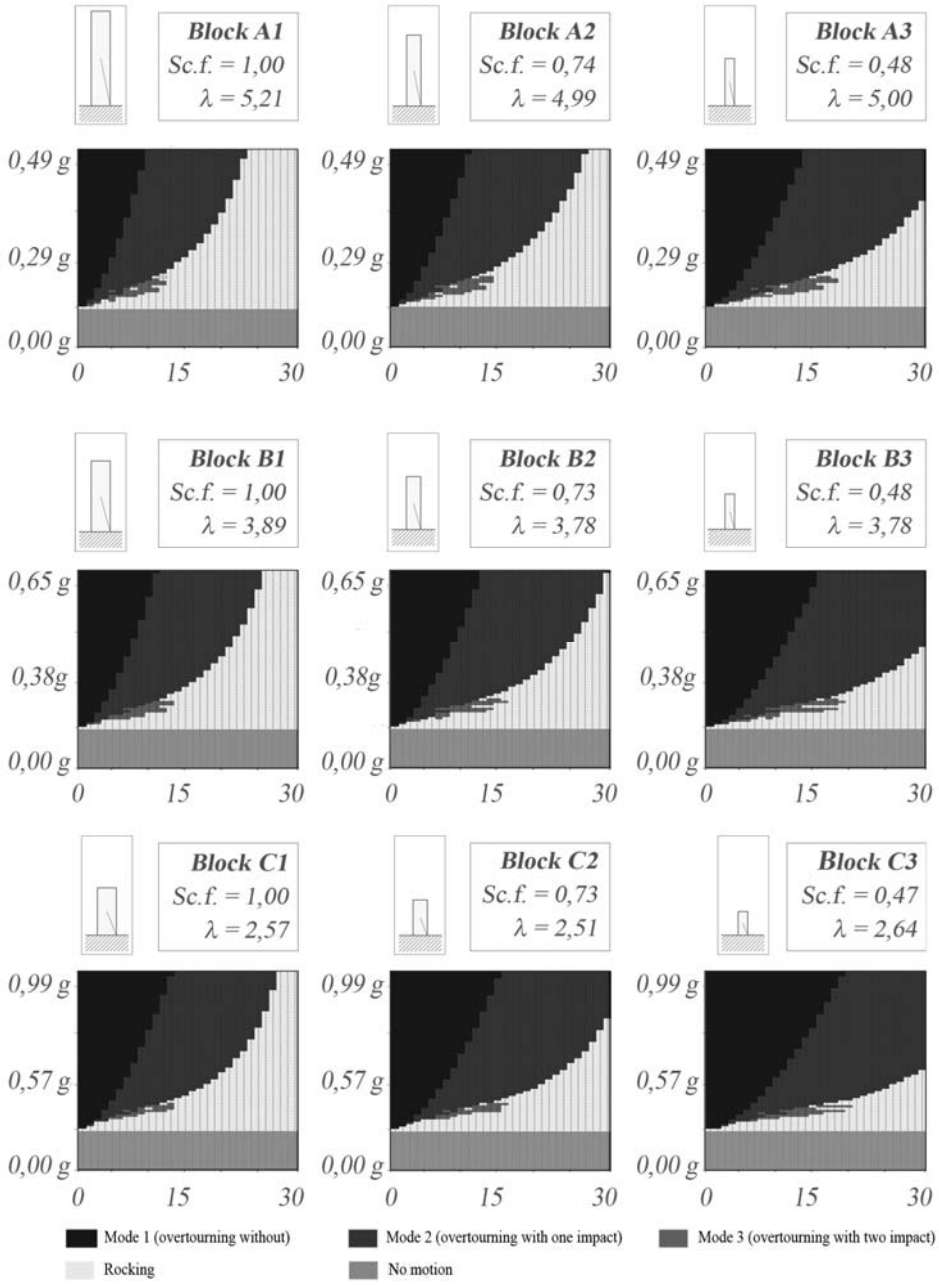

Figure 66 - Numerical stability spectrum adopting Housner's coefficient of restitution. [Author's image].

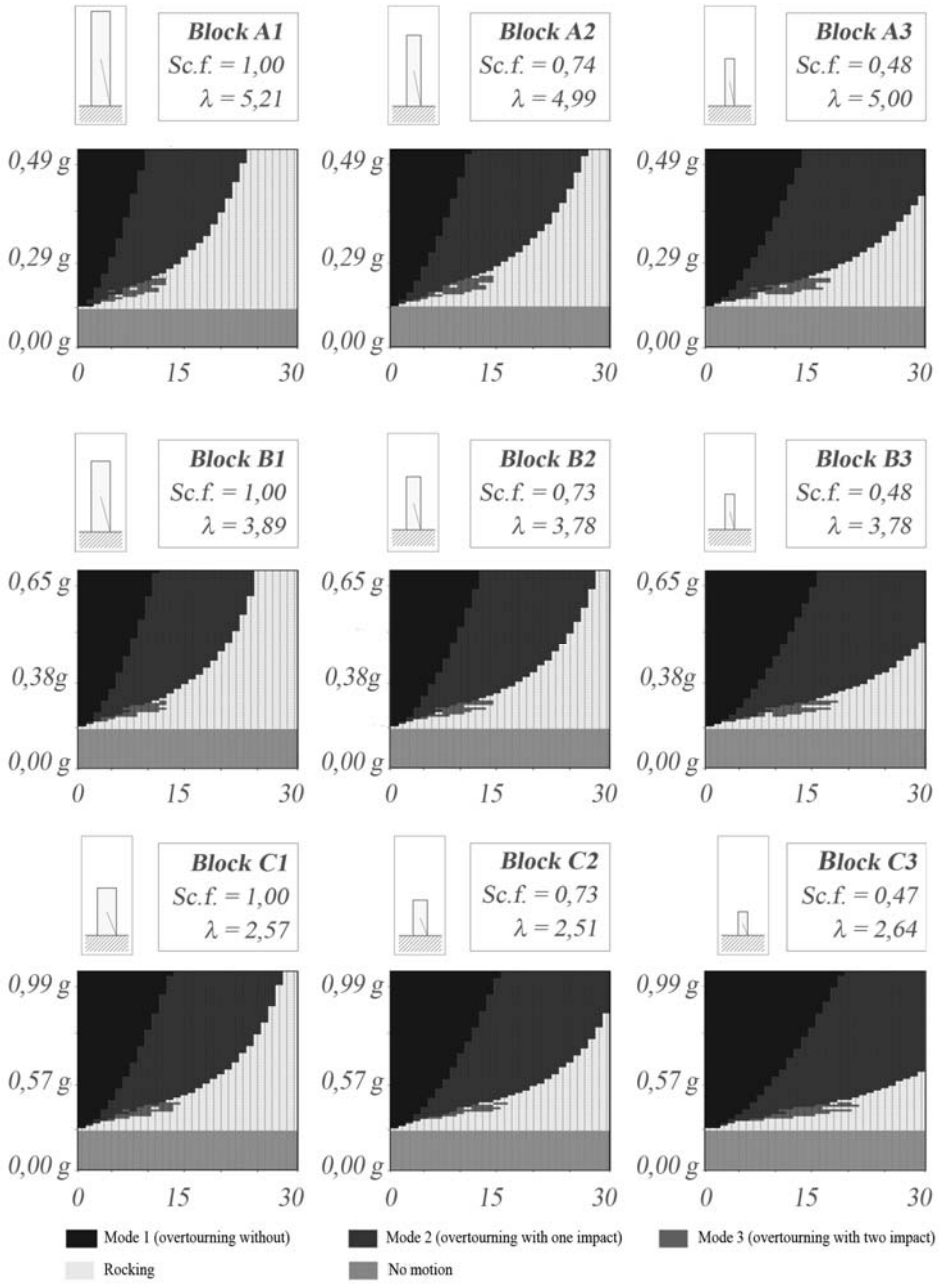

Figure 67 – Numerical stability spectrum with experimental coefficient of restitution. [Author's image].

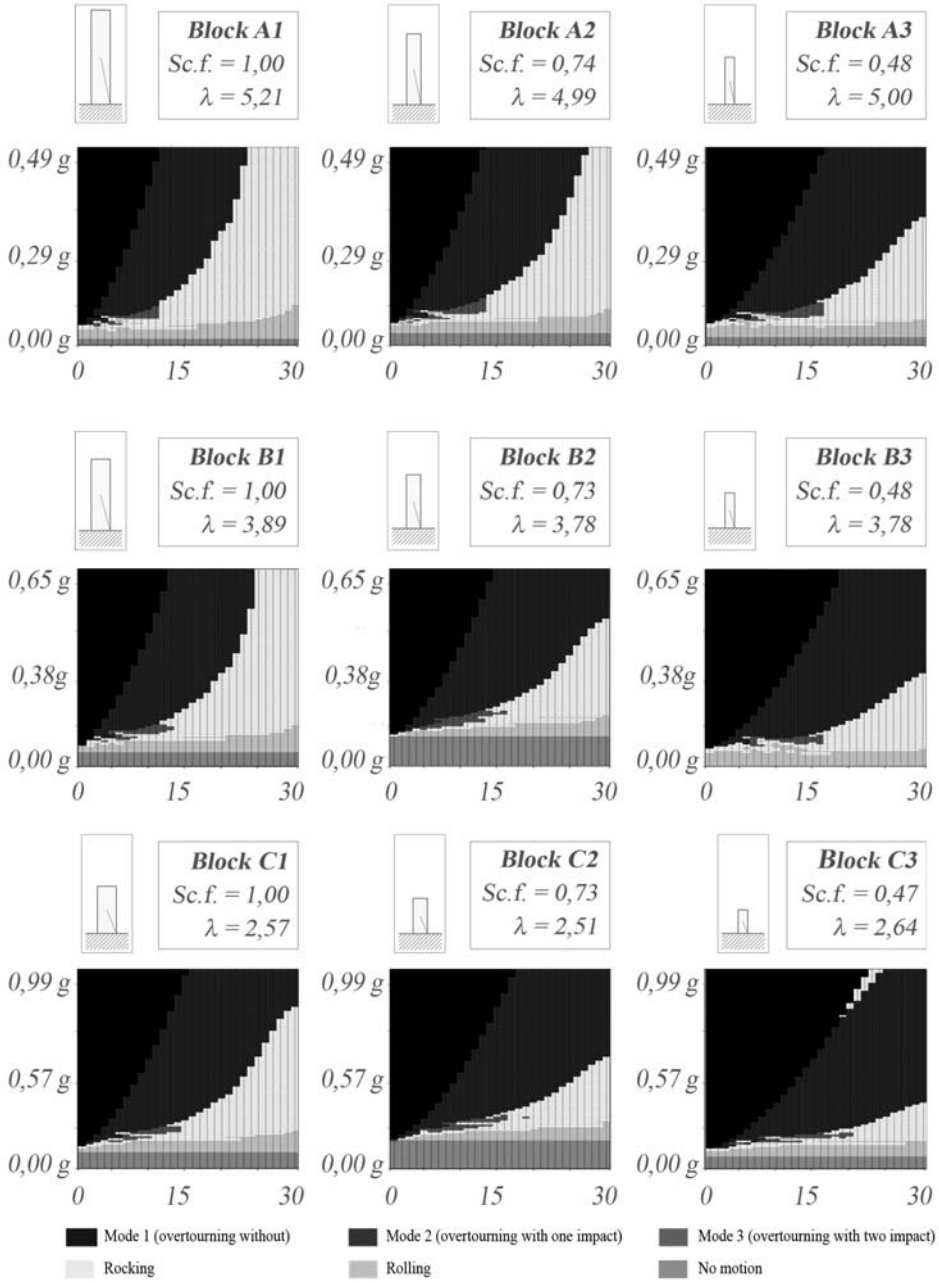

Figure 68 – Numerical stability spectrum: proposed model with imperfection and experimental coefficient of restitution. [Author's image].

4.2.2 Maximum rotation variability graphs

In this paragraph the results of a further experimental campaign on the dynamic behavior of small rigid blocks, excited by a single ground motion, is presented. The experimental responses of nine wooden specimens with different aspect ratios and size factors are evaluated using the contactless measurement strategy presented in section 3.1.1. The normalized rotations vs Peak Ground Acceleration (PGA) are presented in graphs here called *maximum rotation variability graphs*.

The experimental *maximum rotation variability graph* is obtained with reference to the Friuli earthquake registration in 1976 (EW component, Tolmezzo), with a PGA 0.3513 g, (see Figure 69). The signal was scaled in amplitude, and 60 tests were performed for each specimen considering a variable PGA ranging between 0.01 and 0.60 g, with a step size 0.01 g. The tests are then processed according to the procedure described in section 3.1.1 to obtain the maximum rotation normalized by the critical angle.

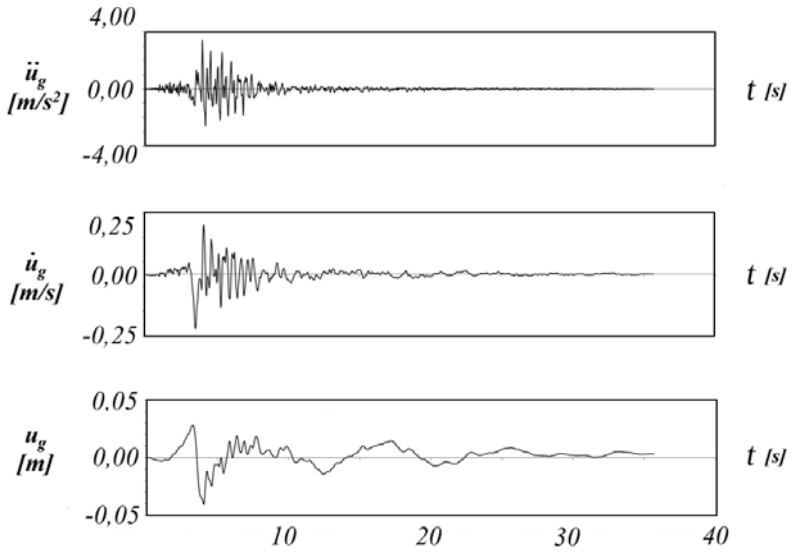

Figure 69 - Ground motion assigned to the shaking table.
[Author's image].

The role of the aspect ratio, size factor and small imperfections on the response variability is investigated. In particular, for each PGA value, eleven tests are repeated and processed for a total amount of 660 tests. Figure 70-Figure 72 identify the upper and lower bound of the maximum normalized angle. The plots, albeit affected by the characteristics of the seismic input, lead to some general consideration.
Four behaviors bands were identified, namely *full contact* (Band 1), *small rocking* (Band 2), *large rocking* (Band 3), *overturning* (Band 4). Such behaviors can be better described as follows:

- *full contact* (Band 1): for all the duration of the ground motion the incipient rocking condition is not achieved;
- *small rocking* (Band 2): encountered for low values of the PGA, the block oscillates but does not rock and the response variability is limited;
- *large rocking* (Band 3): for higher values of the PGA, the block rocks and occasionally can overturn;
- *overturning* (Band 4): is associated to a band that starts when the block always overturns.

In the case of block *A1*, a less pronounced dispersion of the outcomes than for the other specimens is observed, establishing that the imperfections have less effect on the response. The dispersion of data increases by reducing the scale factor even showing the two extreme situations of rocking and overturning. The data are quite irregular even in the case of squatter blocks with a high scale factor, as in the case of blocks *B1* and *C1*. In all the considered cases, it can be recognized a band (Band 3) where the response is markedly chaotic. The width of this band seems to be related to the size of the specimen (generally it is larger for scale factors type 1 and thinner for scale factors type 3).

This indicates that small blocks have low capacity of resistance once the rocking starts[21], for this reason it is suggested to consider safe the setting on the left of the acceleration value that identifies the real uplift of the blocks. Although the bandwidth of the chaotic zone decreases as the scale factor reduces for each slenderness value, the lower propensity of overturning of the thicker blocks is confirmed because bands 2 and 3 move towards higher values of PGA. This shift towards the right side of the graph is partly affected by the uplift acceleration.

In all the figures the symbol $\ddot{u}^{(t)}$, that represent theoretical uplift acceleration in case of symmetrical block and numerically computed according to eq. (3), is associated to a vertical dash-dot line; the symbol $\ddot{u}^{(e)}$ that represent the real uplift acceleration in case of symmetrical block and experimental computed according the procedure reported in section 4.2, is associated to a vertical continuous line.

As shown by the graphs, the experimental PGA at rocking outset is in all the considered cases slightly lower than the theoretical one, mainly due to the imperfections in the contact surface of the blocks. In addition, it should be mentioned that asymmetries or zones with different density material may affect the response[22].

In terms of first overturning, slender blocks collapse for lower values of the PGA than thicker blocks and smaller blocks are keener to overturning than larger blocks. The experimental results compared with the numerical simulations, showed the limit of numerical models to simulate the dynamic behavior of rigid bodies, especially when the response is characterized by rocking with many impacts

[21] On the basis of this evidence, it is advisable to design the isolation system in order to prevent the block from starting to oscillate considering that the response seems unpredictable.

[22] The incorrect determination of the uplift acceleration may lead an inadequate device design

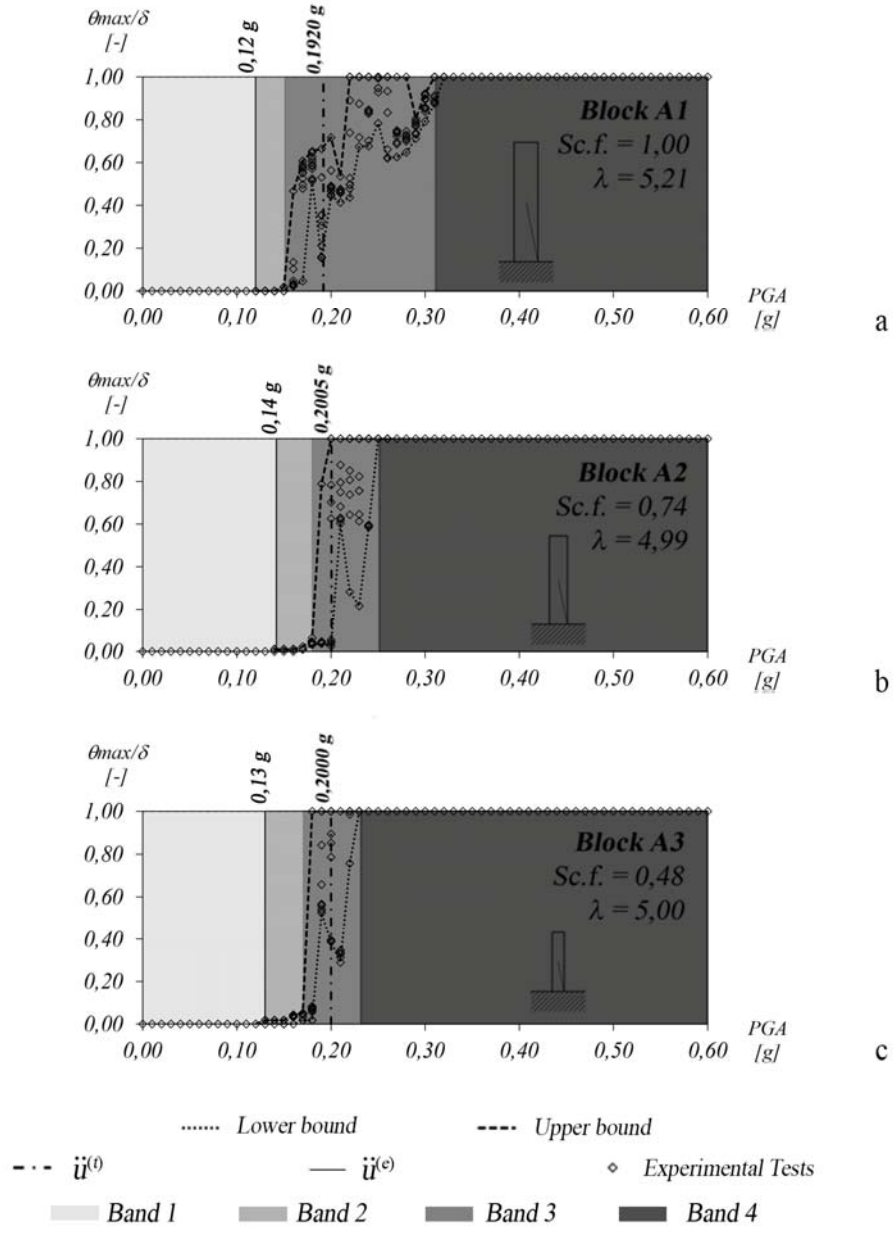

Figure 70 - Response variability for Blocks A: (a) A1; (b) A2; (c) A3. [Author's image].

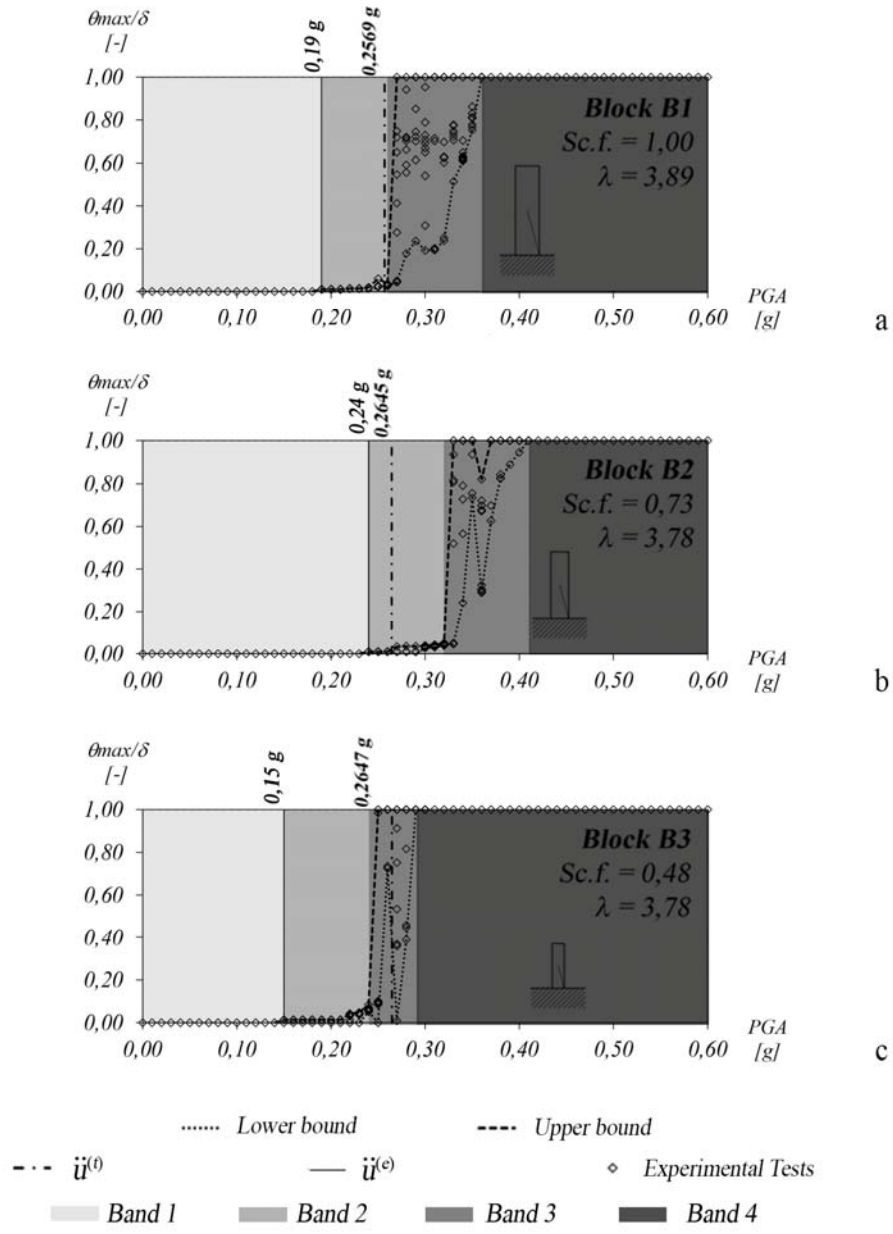

Figure 71 - Response variability for Blocks B: (a) B1; (b) B2; (c) B3. [Author's image].

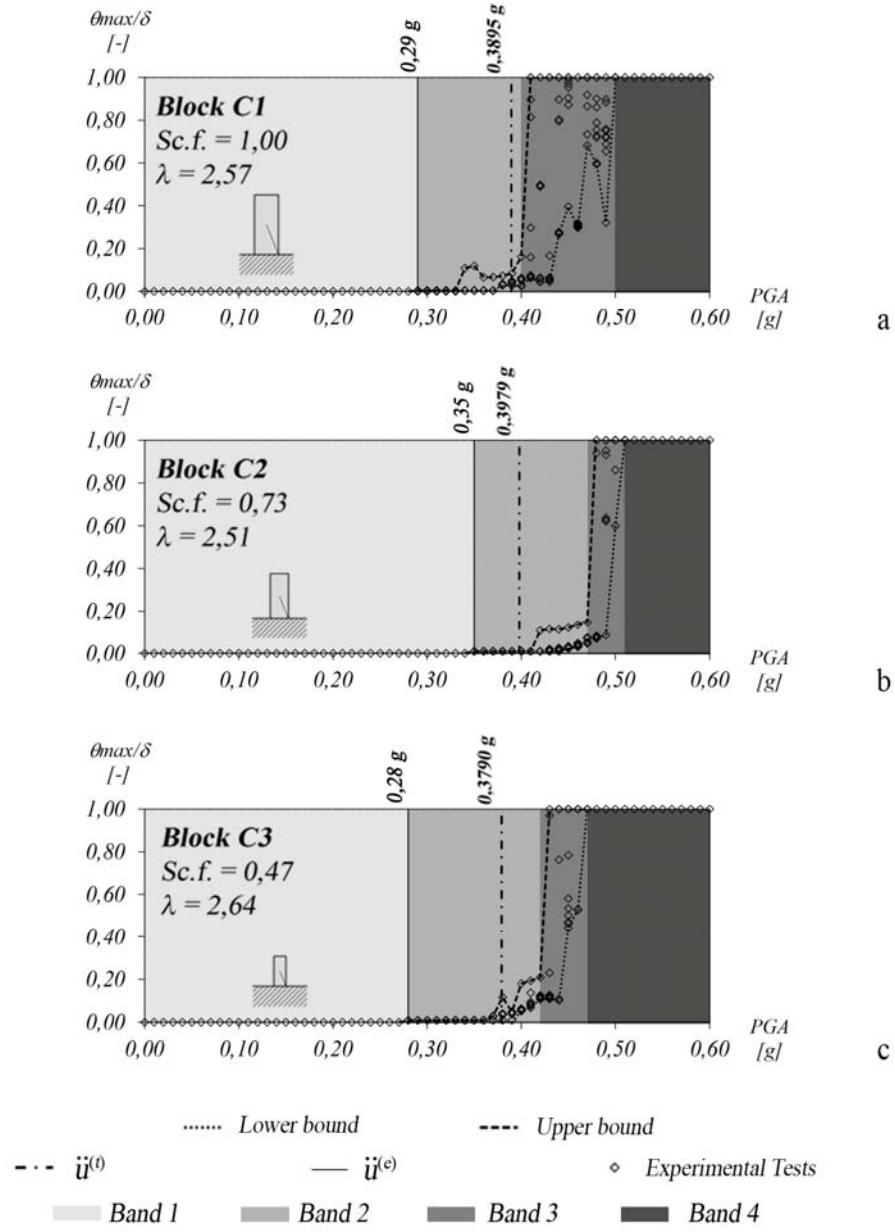

Figure 72 – Response variability for Blocks C: (a) C1; (b) C2; (c) C3. [Author's image].

The numerical analyses involving the nine blocks were carried out in accordance with the formulations proposed in [65] considering the ideal dimensions of the blocks and applying the coefficient of restitution as proposed by Housner.

In Figure 73, Figure 74 and in Figure 75 the experimental outcome are identified by the grey region delimited by the lower and upper bounds provided by the experimental results. Figure 73 shows that the numerical outcome (dot line) tends to shift towards the right side of each graph, overestimating the real capacity. This effect is caused by the wrong evaluation of the uplift acceleration which obviously does not correspond to that associated with the West's formula. Then, the formulation that defines the condition of incipient motion cannot be considered reliable because it does not take into account imperfections. This inevitably leads to the incorrect evaluation of the time history. When the actual block geometry is very close to the ideal one, the theoretical and real uplift accelerations tend to coincide. This is the case for the shape of the theoretical curve on the stability for block *B2*.

Occasionally, even within Band 4, the block overturns for a certain intensities but returns to rock for a higher values of the PGA. This circumstance is more likely encountered when slenderness decreases. The block response is affected by the characteristics of the coefficient of restitution that influence the response above all when many impacts occur. In order to minimize the errors, the numerically responses were determined using the experimentally measured coefficients. The same procedure was repeated considering the application of the experimental coefficient of restitution, reported in Figure 62, aiming at evaluating the changes in the numerical curves. The latter improvement is not decisive to avoid the overestimation of the block capacity, since the main drawback is the incorrect identification of uplift conditions. Therefore, the employment of the experimental coefficient of restitution does not produce significant improvements of the maximum rotation variability graph.

As already highlighted, the classical numerical model incorrectly estimates the instant in which the block leaves the full contact phase and likewise fails to identify the overturning PGA. Furthermore, Figure 73 and Figure 74 demonstrate that the model can lead to incorrect safety predictions.

The overestimation of the uplift acceleration can lead to a delayed start of rocking when the energy content of the strong phase of the earthquake begins to decrease, drastically modifying the instant in which the maximum rotation peaks occur. For this reason, the numerical analyses were repeated considering the model in presence of imperfections with reference to the data reported in section 4.2

For each block, the results are reported in Figure 73 highlighting the bounds which provides the best match with the experimental response. The effect of the uncertain parameter in the response of the blocks is reported in Figure 75. As shown, the adopted uncertainty range is always able to get a reliable prediction of the experimental response of the blocks. For each block, the upper bound of the maximum numerical response (grey line) anticipate the experimental one (grey region) in correspondence with the PGA value in which the start of motion actually occurs. The upper bound relating to the numerical model for block *C* is lower than the experimental one in correspondence with PGA values equal to 0.4 g. This occurs in correspondence with band 2 which can be assumed safe considering the values of maximum rotation peak negligible. The solid black vertical line identifies the uplift of blocks for both the experimental and numerical case and usually precedes the dashed one.

Finally, the new numerical curves almost coincide with the theoretical one and no significant changes in the rotation peaks are encountered.

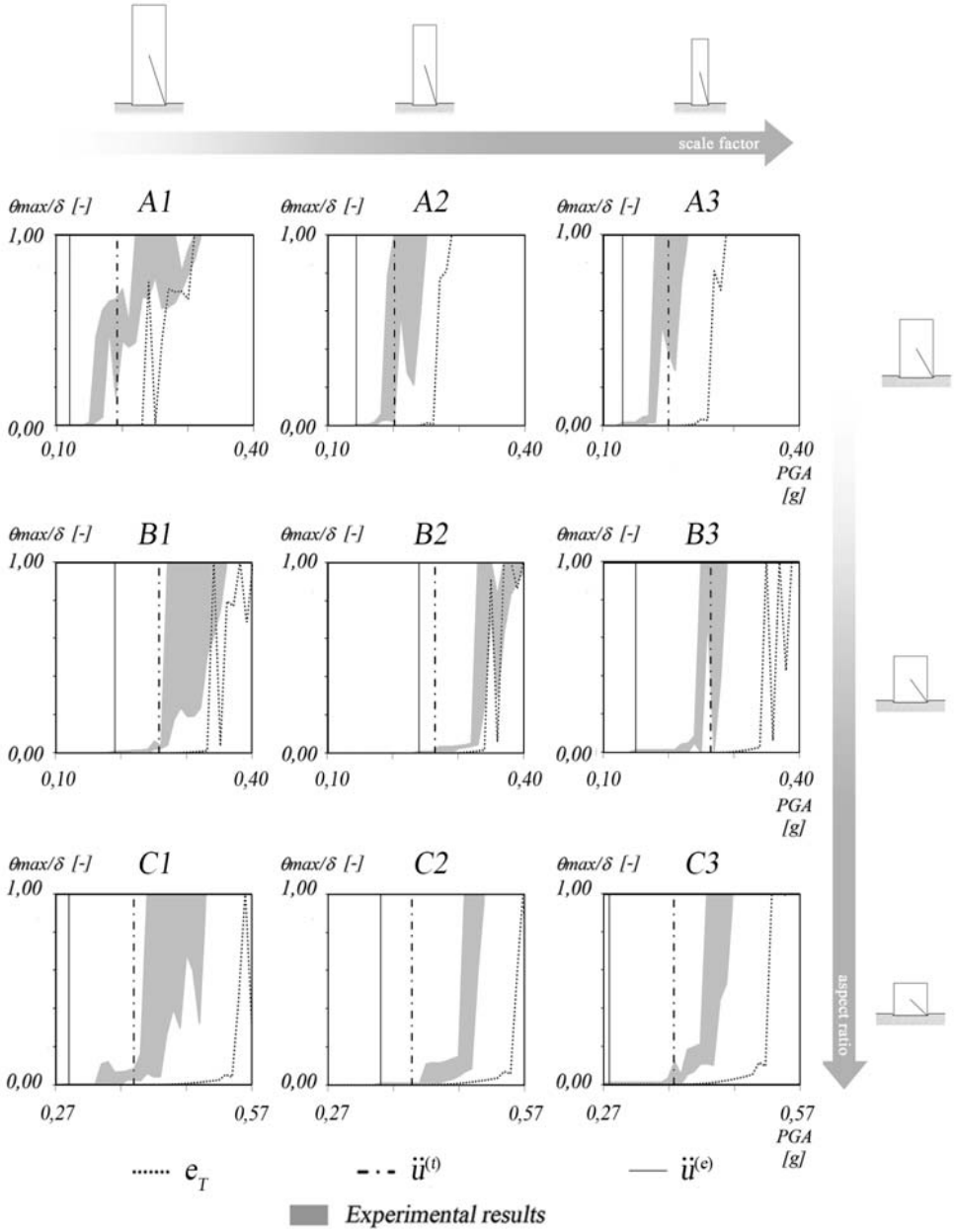

Figure 73 – Comparison between experimental and numerical *maximum rotation variability graph* using the coefficient of restitution as proposed by Housner. [Author's image].

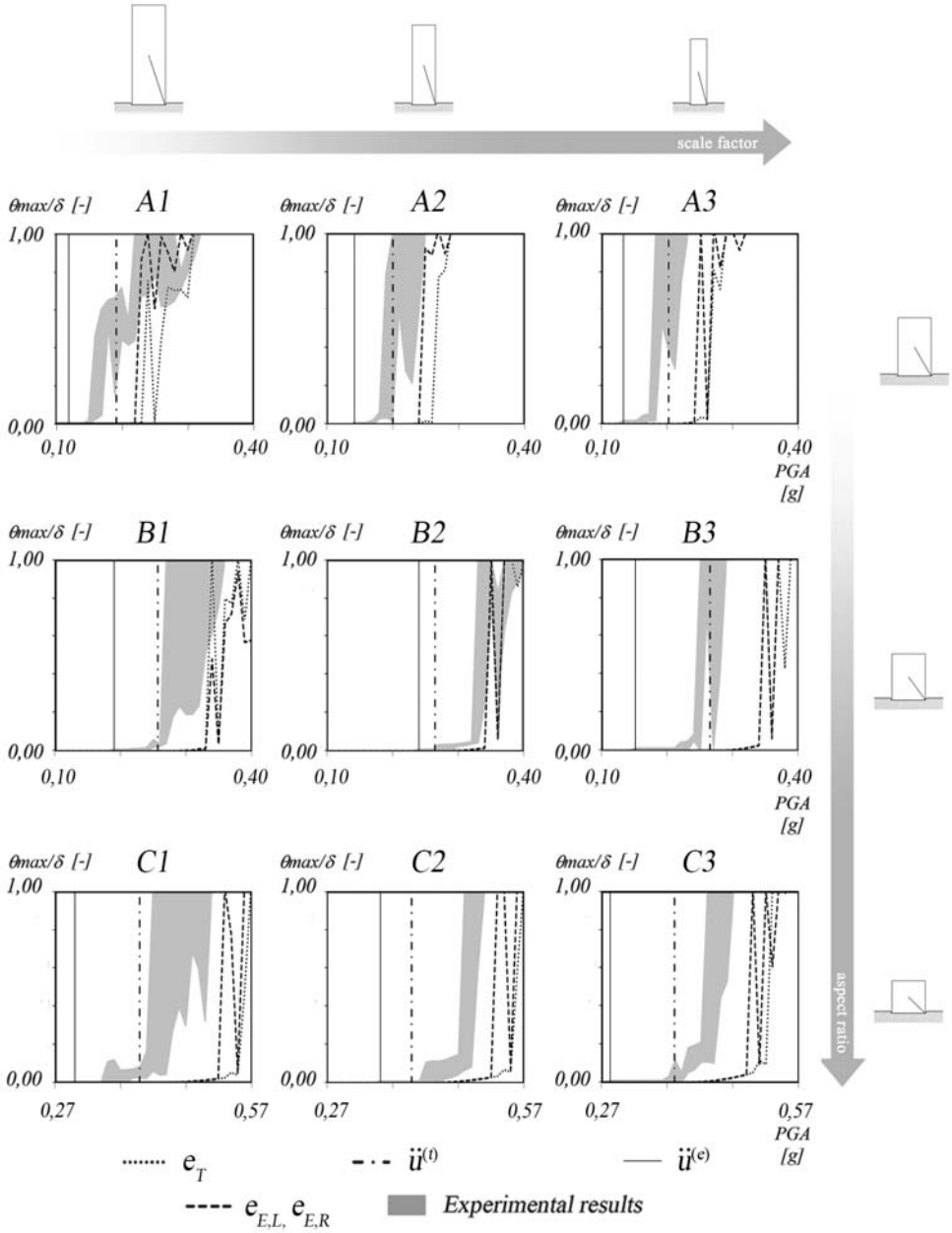

Figure 74 – Comparison between experimental vs numerical *maximum rotation variability graph* using the experimentally measured coefficient of restitution. [Author's image].

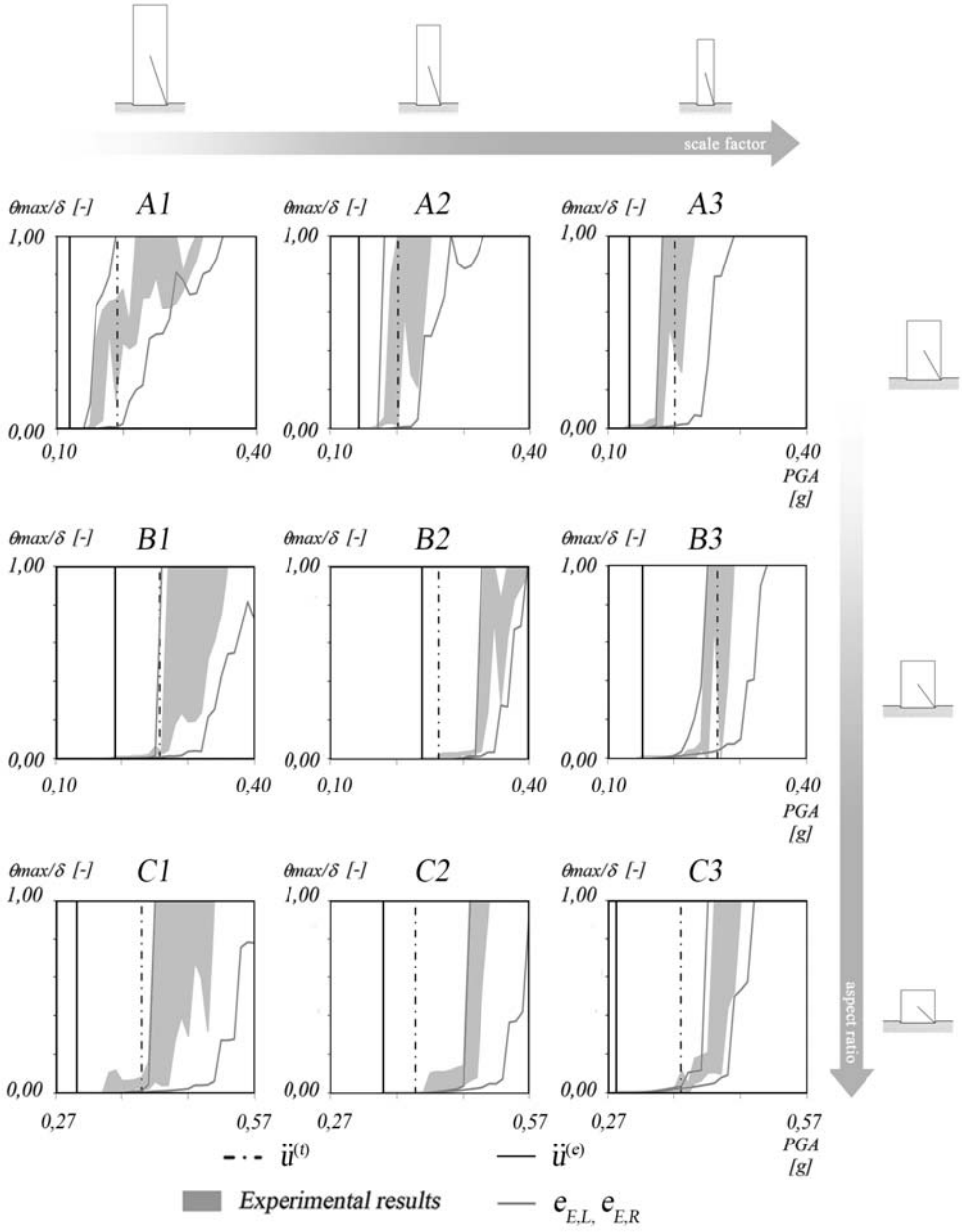

Figure 75 - Comparison between experimental vs numerical *maximum rotation variability graph* using the experimentally measured coefficient of restitution and model with imperfections. [Author's image].

4.2.3 Remarks

All parametric analyses summarized in Figure 65, Figure 66 and Figure 67, allow extrapolating general observations about rocking, stability, and overturning behavior in case of blocks subjected to one-cosine pulse. The obtained results confirm findings of previous studies, such as: "*for a given value of critical angle a block with larger scale factor will be more stable…the danger of overturning generally increases with the aspect ratio of the block*".

The stability spectra reported in Figure 67 are not so different from those shown in Figure 66. Comparing the graph obtained employing the Housner coefficient of restitution with that experimentally measured it can be observed that the safe and unsafe regions remained almost unaltered. When the experimental restitution coefficient is more accurate, the distance between the two numerical curves drastically decreases. In fact, larger differences in the coefficient of restitution evaluation lead to larger response discrepancies.

The responses in free vibration of type *B* and *C* blocks make difficult to measure the experimental coefficient of restitution because the peaks quickly decay and the response in the first cycle might be polluted by the initial conditions (likely non-zero angular velocity). The two graphs are identical with regard to the transition between *mode 1* and *mode 2* because of the absence of impacts. A limited discrepancy is encountered in the transition band between *mode 2* and *rocking region* being the transition phase affected by a single impact. No change in the *no motion zone* is observed.

Interesting remarks arise the analysis of the 9.326 experimental tests which were compared with the numerical simulations. A first difference is that the experimental *stability spectrum* exhibits an additional region with respect to the numerical one, corresponding to the observed tremors for acceleration amplitude lower than the

theoretical uplift acceleration. The imperfections causing the tremors are difficult to identify and alter the original configuration of the block by moving its centre of mass horizontally, Figure 76. Other possible imperfection causes are the inhomogeneous density of the material and the imperfect verticality of the block. Consequently, the blocks uplift at lower accelerations than geometrically ideal counterparts.

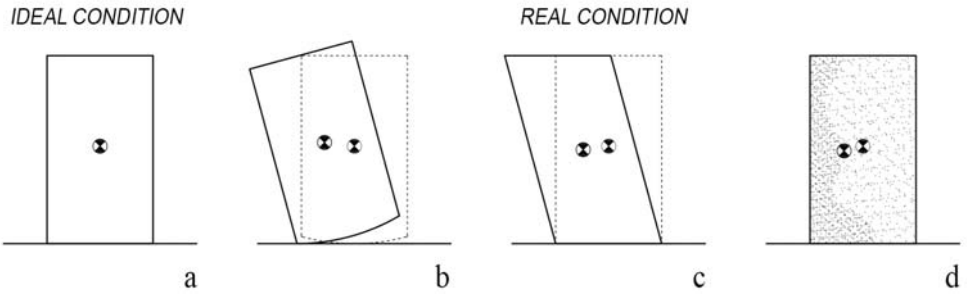

Figure 76 – Possible causes of reduced uplift acceleration: (a) ideal block; (b) concavity of base; (c) asymmetries and absence of verticality; (d) inhomogeneous density of the material. [Author's image].

The average line separating the *no motion* and *rolling zones* is shifted downwards highlighting a premature start of motion and consequently all the others zones are shifted towards lower accelerations. All nine blocks leave the full contact phase for acceleration lower than the theoretical one provided by the West's formula and prematurely overturn with respect to the numerical spectra.

From the analysis of the time history of all the blocks subjected to the one-cosine pulse, a greater propensity to overturn in the case of real blocks is encountered. The numerical model based on the ideal block is unable to predict the response and fails to determine the rotation peaks, the instant of overturning and the collapse mode. Appropriate modifications, able to account for the block imperfections, are needed to obtain a stability spectrum closer to the experimental results. Parametric analyses summarized in Figure 73-Figure 74 allow extrapolating more general considerations about rocking, stability, and overturning behavior in the case of blocks subjected to Friuli earthquake.

By repeating the experiments (claiming to consider the same conditions in terms of ground motion, specimen, and initial conditions), it can be observed that the reproducibility of the tests is almost impossible if the block uplifts. The chaotic character of the dynamic response of rigid blocks and the consequent deterministic unpredictability is experimentally observed. The unpredictability of the response is drastically reduced when the collapse is preceded by a limited number of impacts and the numerical responses, although employing different coefficients of restitution, Figure 75, almost coincide.

The incorrect identification of the incipient uplift time instant shifts the numerical curves towards the left side of the response spectra. The premature start of motion finds a physical justification in the presence of imperfections at the base of the block that modify the ideal geometry and generate very small unwanted rotations. This experimental evidence led to the introduction of and improved model described in section 4.1. The numerical results usually underestimate the actual response of the blocks. The experimental results show a significant response variability of the outcome in specific conditions and highlight the limits of several numerical assumptions commonly accepted.

In addition, the results obtained in the experimental campaign led to some more general remarks on the seismic vulnerability and on the possible seismic protection strategies of structures. In particular, the correct identification of the uplift acceleration conditions is crucial for an effective design of a seismic isolation device.

Chapter 5 Dynamics of a rolling ball isolator

This chapter illustrates the development and characterization of a low-cost rolling ball system pendulum isolating device. The proposed system is described, and two wooden prototypes (with three and four grooves) are manufactured and experimentally tested. After introducing the prototype and design requirements, the methodology carried out to characterize the system behaviour using free-vibration tests is presented. Then, the tests carried out under sinusoidal ground acceleration inputs on a shaking table are illustrated, followed by the developed numerical model of the system, validated against experimental tests.

The effect of the application of a rubber layer on the grooves surface is also tested and the corresponding dynamic behavior is characterized.

In order to avoid indentation of the groove and to guarantee a rigid behavior under impact forces, the device was endowed with an additional release mechanism that was further tested.

5.1 Prototype realization end design

The prototype consists of two beech wood plates carved with spherical grooves, where the spheres can roll. The overall dimensions of the device are not governed, as for the isolation of buildings, by the trace of a single groove on the plate but they are rather they must be able to allocate three or more grooves.

The first prototype was created by minimizing its size so to obtain the minimum footprint by reducing the number of spheres and grooves. The trace of the three wooden grooves that accommodate the three vertical supports (so to guarantee the equilibrium in static condition) have been suitably positioned within a square shape.

The first prototype consisted of two wooden plates with a square footprint of 0,30 m per edge and 0,03 m thick. The radius of curvature of the spherical grooves must be chosen to obtain the desired isolation period and is limited by the amount of removable material without compromising the efficiency of the device (in terms of

maximum excavation depth) and by the radius of the circumference intersection between the groove and the wooden plate, see Figure 77. The main criticalities of the specimen are related to possible uplift of the top plate. The equilibrium is assured in static conditions, but the horizontal forces acting in dynamic conditions could be capable of tilting the top plate around point A, Figure 77. In the latter case the vertical resultant falls outside the distance L_{cr}. Therefore, the allowable displacement of the device can be inferred enforcing the rotational equilibrium considering the vertical loads and the expected maximum horizontal forces in seismic conditions. A simple strategy to prevent the top plate to overturn consists in appropriately spacing the spherical grooves, as shown in section 5.3.

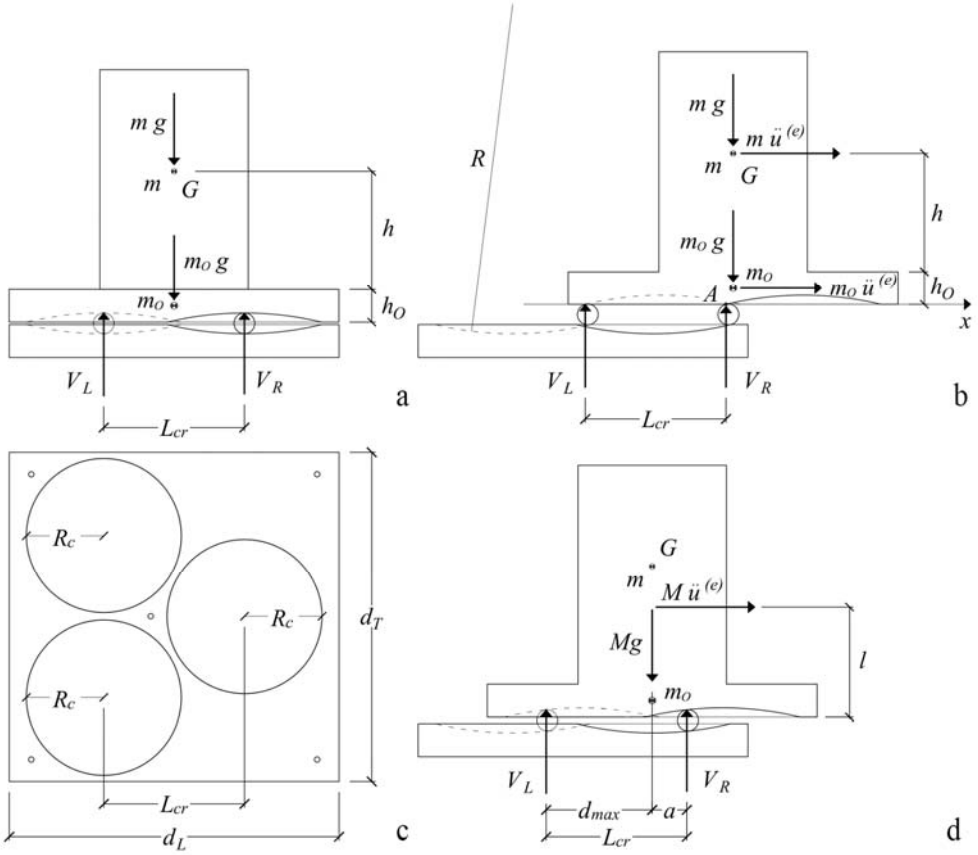

Figure 77 - Stability condition under static and dynamic action. [Author's image].

According to Figure 77, the geometric restriction due to the plates size influences the seismic acceleration capable of overturning the device. The design fundamental period (closely related to the acceleration of the top plate in seismic conditions) is conveniently chosen to guarantee the full contact of the rigid body placed on the isolator. Therefore, it is important to define the actual uplift acceleration of the isolated object, for example using the procedure described in section 4.1.2. Considering the symbols introduced in Figure 77a and the reference system *x* in Figure 77b, the approximated point of application of the total horizontal and vertical forces are calculated according to the following equation, obtained by considering

the hypothesis that the balls pass through the entire stroke defined by the geometry of the grooves

$$l = \frac{m\left(h + h_o\right) + m_o\left(h_o/2\right)}{m + m_o} \tag{47}$$

In the design phase of the device, a minimum safety distance a between the vertical reaction and the resultant of the vertical loads capable of preventing overturning must be guaranteed. For the latter reason the safety length a can be determined enforcing the limit moment equilibrium with respect to point *A*, as follows

$$a = \frac{\ddot{u}^{(e)}}{g} l \tag{48}$$

Consequently, the allowable displacement Figure 77d, that is the maximum value reached when the overturning occurs, can be obtained as

$$d_{\max} = L_{cr} - a \tag{49}$$

The meaning of the symbols is shown in Figure 77. The arrangement of the circumferences on plate surface R_c, shown in Figure 77 and Figure 78, is compatible with a radius of curvature of the grooves equal to R = 0,30 m. The geometric properties of the device were defined by preparing a three-dimensional digital model which, exported in *.cad* format, is useful for the numerical control milling machine to accurately carve the wooden plates, Figure 78. The period of vibration is calculated also in relation to the geometry of the spheres. In the case of steel balls with radius r = 0,0095 m, according to the formulation reported in section 2.4.1,

one obtains $T = 1,53$ s; instead in case of resin balls with radius equal to $r = 0,0183$ m, $T = 1,51$ s.

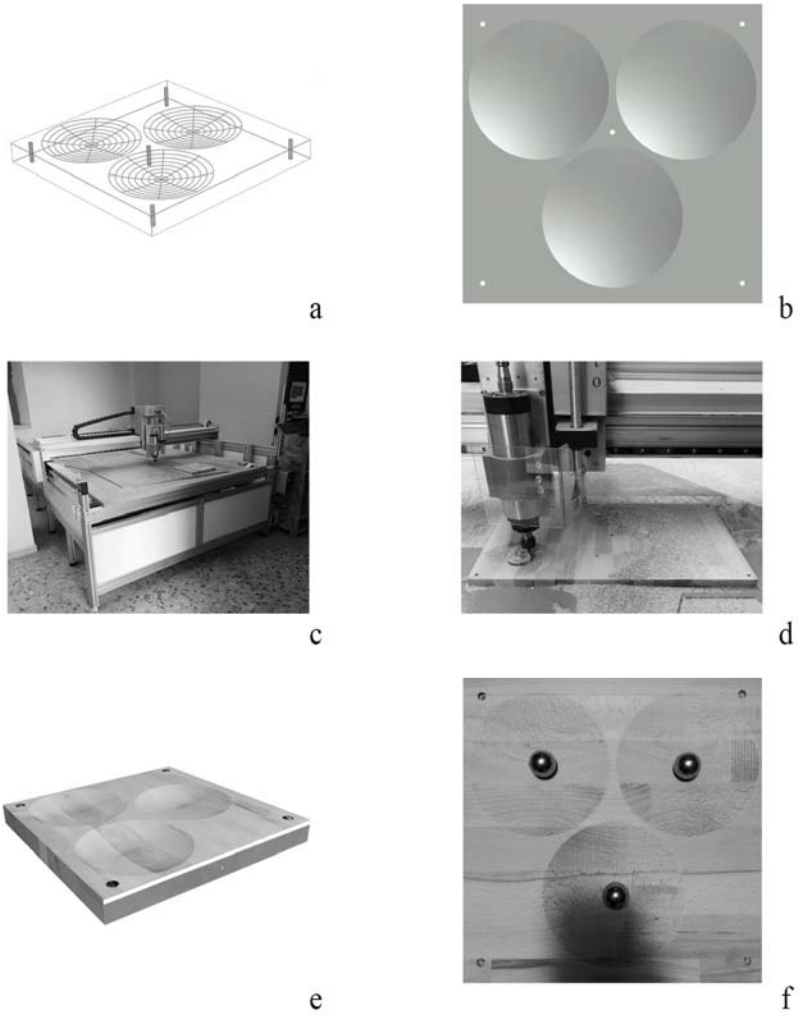

Figure 78 - Manufacturing process: (a-b) design; (c-d) realization; (e-f) final result. [Author's image].

5.2 Experimental investigation

By employing uniaxial shaking table and making use of the contactless acquisition data strategy described in section 3.1.1 and 3.2, some aspects of the dynamic behavior of the first prototype, for different vertical loads, have been investigated as

discussed hereinafter. The specimen has been subjected to different vertical loads (see Figure 81) considering steel balls (with radius r = 0,0095 m) and resin balls (with radius r = 0,0183 m) with and without natural rubber layer - series Linatex® Premium rubber and thickness equal to 3,2 mm - glued on spherical grooves surfaces, see Figure 80. The insertion of the rubber layers is motivated by the need to improve the dissipation of energy thanks to the increase in the rolling friction.

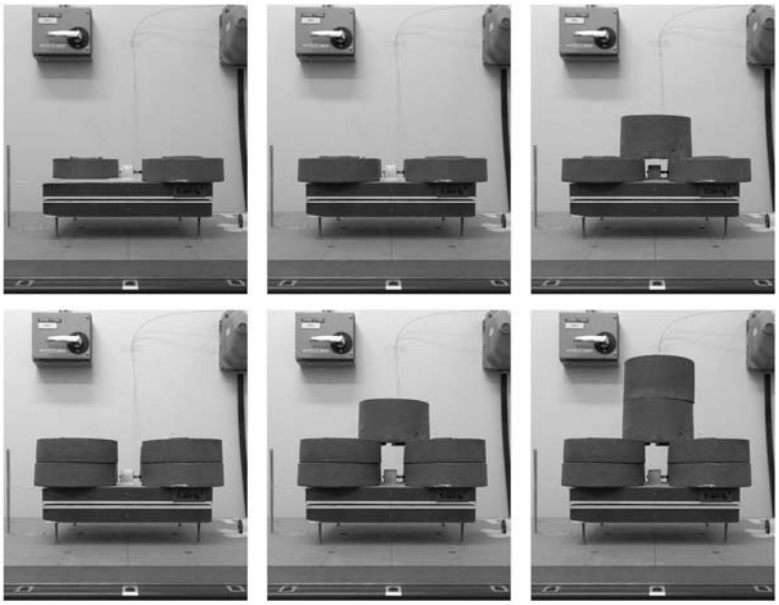

Figure 79 - Photographic survey before the tests. [Author's image].

Figure 80 - Tested configurations. [Author's image].

The centre of gravity of the additional mass is aligned with the barycentre of the square base of the device. The *i*-th configuration can be identified by the stiffness k_i given by the ratio between the vertical load $W_i = (m_o + m_i)g = M_i g$ and the equivalent radius of curvature $\hat{R} = 2(R - r)$. The horizontality of the specimens was assured with four screws at the edges. The performance of the device is compared also evaluating the improvements in terms of energy dissipation when the grooves are coated with a rubber layer. Table 17 and Table 18 show the main features of each load scheme.

i-th load scheme	M_i [kg]	W_i [N]	$\hat{R}$ [m]	k_i [N/m]
1	11,664	114,394	0,581	196,892
2	21,664	212,494	0,581	365,739
3	31,664	310,594	0,581	534,586
4	41,664	408,694	0,581	703,433
5	51,664	506,794	0,581	872,280
6	61,664	604,894	0,581	1041,126

Table 17 - Main parameters of the tested configurations (balls with radius r = 0.0095 m).

i-th load scheme	M_i [kg]	W_i [N]	$\hat{R}$ [m]	k_i [N/m]
1	11,664	114,394	0,581	203,043
2	21,664	212,494	0,581	377,164
3	31,664	310,594	0,581	551,286
4	41,664	408,694	0,581	725,407
5	51,664	506,794	0,581	899,529
6	61,664	604,894	0,581	1073,650

Table 18 - Main parameters of the tested configurations (balls with radius r = 0.0183 m).

The characterization of the device was performed by evaluating the displacement decay during free vibrations tests. Forced vibrations tests with sinusoidal input with frequency equal to 1 Hz were also performed. Three PGA values equal to 0,070 g, 0,035 g and 0,020 g were considered. The results are reported in terms of force-

displacement curves, which also help identifying the indentation of the grooves due to the passage of the balls.

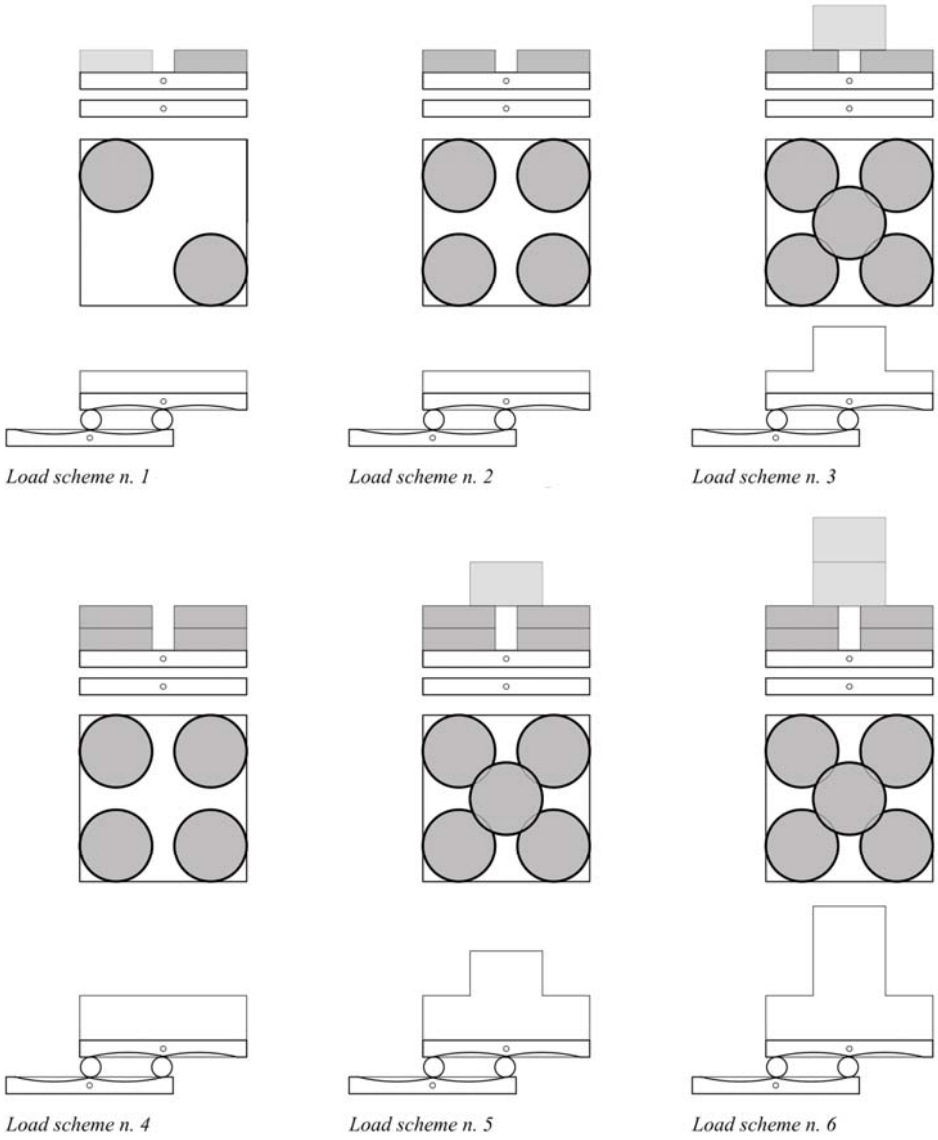

Figure 81 - Arrangement of the load on the device during the experiments. [Author's image].

5.2.1 Free vibration tests and measurement of rolling friction

The beneficial dissipation of energy is due to the rolling friction that develops on the contact surface between spheres and spherical grooves. By analysing the peaks at each cycle of free vibrations tests, as reported in Figure 83-Figure 85, it is clear how the decay of the response follows a linear trend typical of Coulomb damped systems. It is known from the literature that systems with Coulomb friction are characterized by a decrease in the peak of response at each cycle equal to $\left(4\mu_i M_i g\right)/k_i = 4\mu_i \hat{R}$ [66]. According to the scheme in Figure 82 the following condition can be exploited to evaluate the friction coefficient.

$$u_j - u_{j+2} = \frac{4\mu_i M_i g}{k_i} = \frac{4\mu_i g}{\omega_i^2} \tag{50}$$

where $M_i = \left(m_b + m_l\right)$ is the total mass, the subscript *j* identifies the cycle and the subscript *i* refers to the load scheme. Manipulating eq. (50) the coefficient of rolling friction for a single cycle is:

$$\mu_i = \frac{\omega_i^2 \left(u_j - u_{j+2}\right)}{4g} \tag{51}$$

Contrarily to viscously damped systems which exhibit a higher natural period than the undamped counterpart, in the case of Coulomb damping system, the fundamental period does not change [66]. The results of an experimental parametric analysis, aiming at evaluating the equivalent coefficient of rolling friction, changing the load conditions, radius, and material of the spheres, is presented. The tests characterized by a low vertical load, facilitate the identification of the alignment on a straight line of the peaks envelope, as shown in Figure 83a-b, Figure 84a-b-c, Figure 85a.

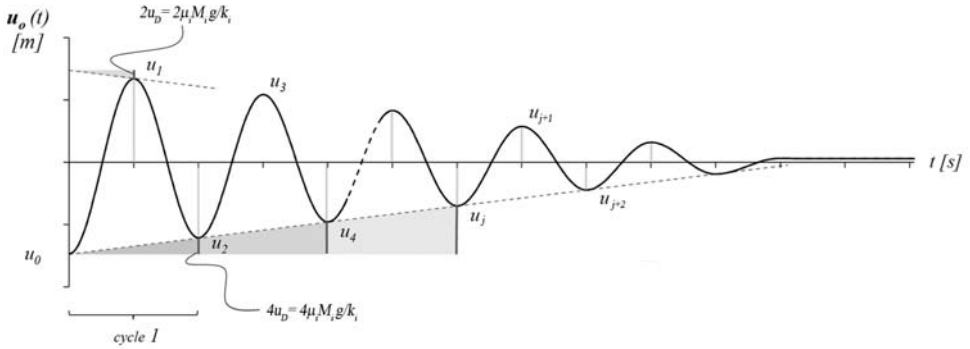

Figure 82 – Scheme for measurement of rolling friction. [Author's image].

Free vibrations with steel balls in the absence of rubber layers, show that the device is unable to complete a cycle, making difficult the measure of the rolling friction, Figure 83c-d-f. Moreover Figure 83e shows the presence of the pit for small displacements and low velocities. The number of cycles increased after the surface treatment of the grooves with sandpaper and using balls with r = 0.0183 m (see Figure 84).

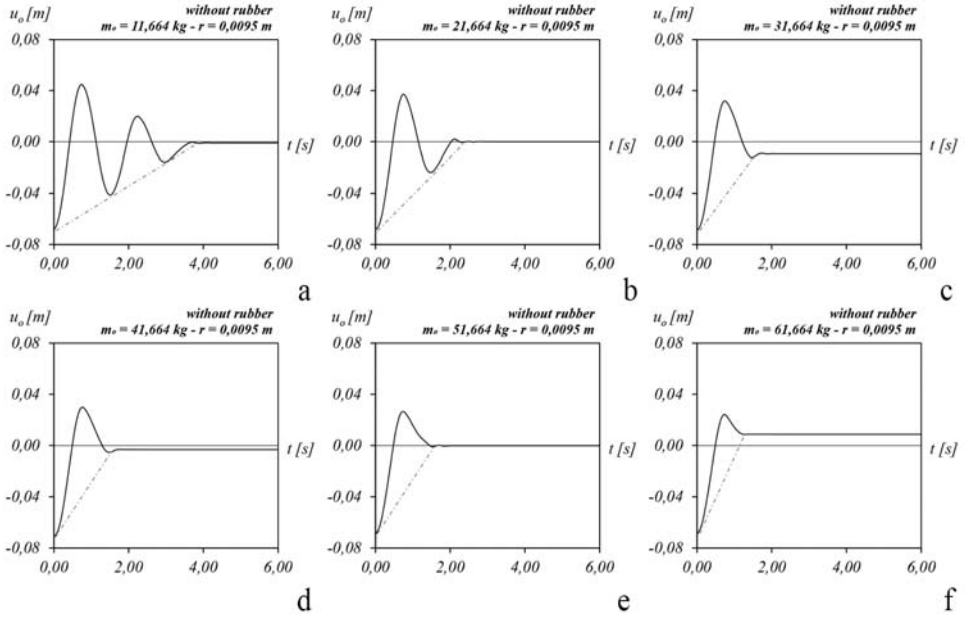

Figure 83 – Free vibration tests without rubber layer and steel balls (r = 0,0095 m). [Author's image].

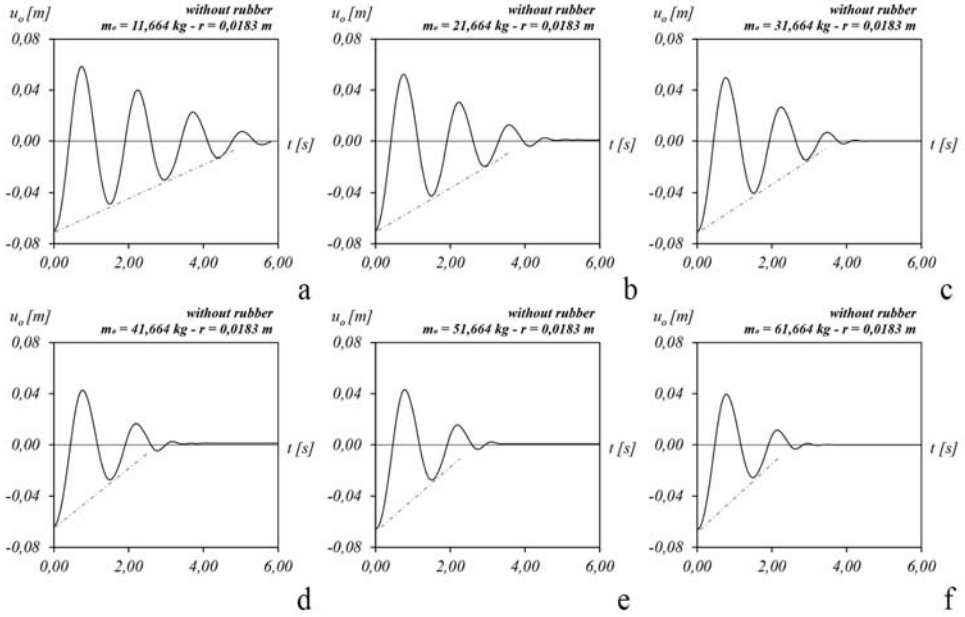

Figure 84 – Free vibration tests without rubber layer and resin balls (r = 0,0183 m). [Author's image].

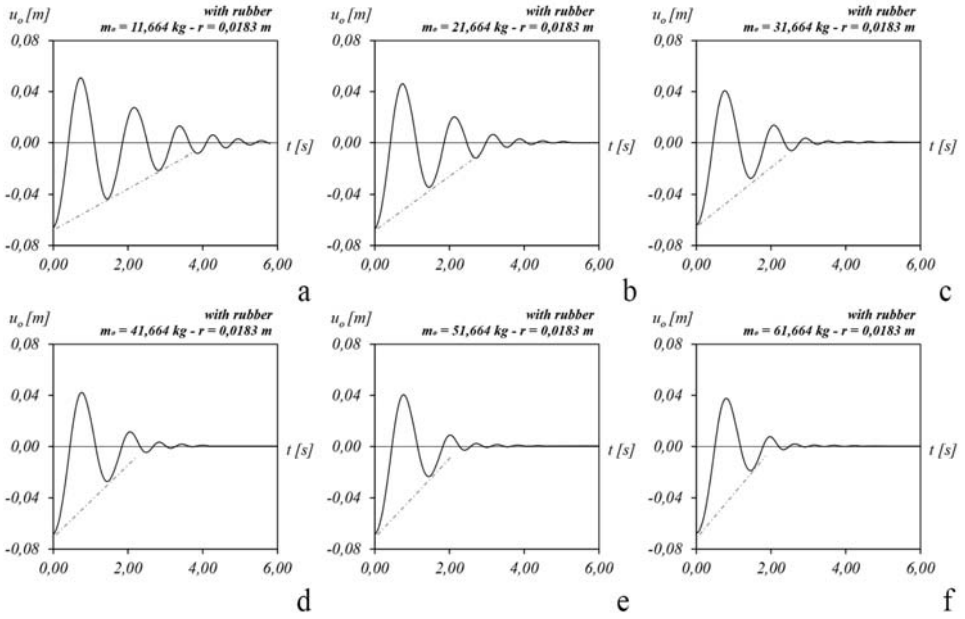

Figure 85 - Free vibration tests with rubber layer and resin balls (r = 0,0183 m). [Author's image].

Figure 84 shows that in the case of low vertical mass (below 30 kg) the number of cycles increases, facilitating the measurement of the friction coefficient. When the device is loaded with masses larger than 30 kg, the displacement amplitude and period variations with respect to the reference model are justified by the presence of pits on the surface of the grooves. Even in presence of rubber layer, the displacement peaks are aligned along a straight line, Figure 85a. In the remaining cases, see Figure 85b-c-d-e-f, the influence of the pit is decisive. It is interesting to note that the vibration period changes for small oscillation amplitudes. An analogous behavior was found in [41]: "…*the experimental response oscillates at a smaller frequency than the simulated response at the end of the record, which can be explained as the effect of an undesired excessive flatness of the rolling groove around its bottom…*". The results of the experiments reported in Figure 85 confirm the variation of the radius of curvature of the groove caused by the passage of balls through the pit due

to the vertical loads in static conditions. However, as proposed in [41] a possible solution could be the: "*Reduction of the vertical load on the single ball through multiplying the number of bearings or restricting the application of the device to light structural or non-structural systems; interposition of softer materials between the ball and the guide, such as rubber*". The results of the experimental parametric analysis in which the rolling friction coefficient was evaluated by applying eq. (51) are summarized in Table 19.

i-th load scheme	M_i [kg]	Without rubber layer r=0,0095 [m] μ_i [-]	Without rubber layer r=0,0183 [m] μ_i [-]	With rubber layer r=0,0183 [m] μ_i [-]
1	11,664	0,0131	0,0094	0,0133
2	21,664	0,0194	0,0114	0,0150
3	31,664	0,0254	0,0130	0,0170
4	41,664	0,0312	0,0154	0,0193
5	51,664	0,0370	0,0170	0,0209

Table 19 - Measured rolling friction for the three grooves device.

In Figure 86 the estimated rolling friction coefficient μ_i versus the vertical load is reported, showing an approximately linear trend. The effect produced by the presence of the pit can be easily identified by analysing the force-displacements relationship in all the considered configurations. The graphs are obtained by plotting the displacement of the device versus the forces generated by the absolute accelerations applying eq. (31). The performance shown in Figure 87 is due to deterioration caused by the balls on the spherical wooden groove under static load and after the recurring passage of the balls. This peculiarity is very evident when the balls pass at low velocity. The reduction of energy entering the system is accompanied by a significant increase in the displacement of the device. This problem can be overcome by increasing the ability of the device to dissipate energy, for example coating the spherical grooves with rubber layers. For this reason, the

behavior of the device equipped with rubber layers was experimentally analysed to evaluate the influence on the rolling friction coefficient and on the overall behavior.

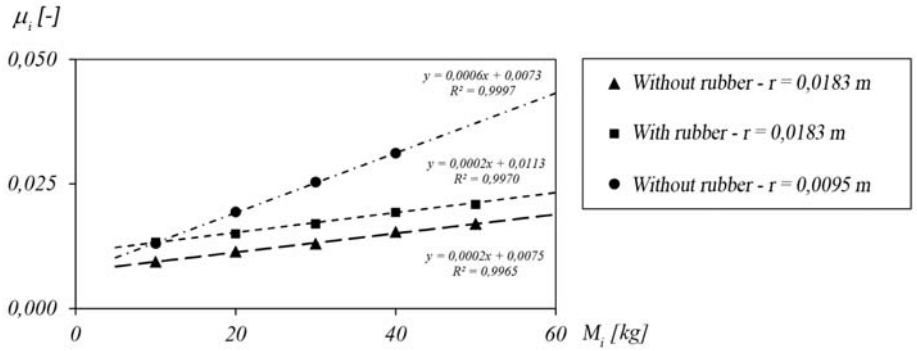

Figure 86 – Trend of the rolling friction coefficient vs the vertical load. [Author's image].

From the comparison of the force-displacement relationship, Figure 87-Figure 89, the response of the device seems to be influenced by the elasticity of the balls or surface. In particular, in the presence of steel balls, when the device achieves the maximum displacement (i.e. when the sign of velocity reverse), there is a sudden jump in force equal to $2\mu_i W_i$ in accordance with the theoretical models for frictional systems. In the presence of resin spheres this effect decreases (i.e. there is a more smooth behaviour), Figure 88, and disappears completely in the case of device equipped with rubber layers, Figure 89.

The forces shown in the following graphs are calculated according to the procedure shown in section 3.1.1 in particular with reference to eqs. (27)-(31).

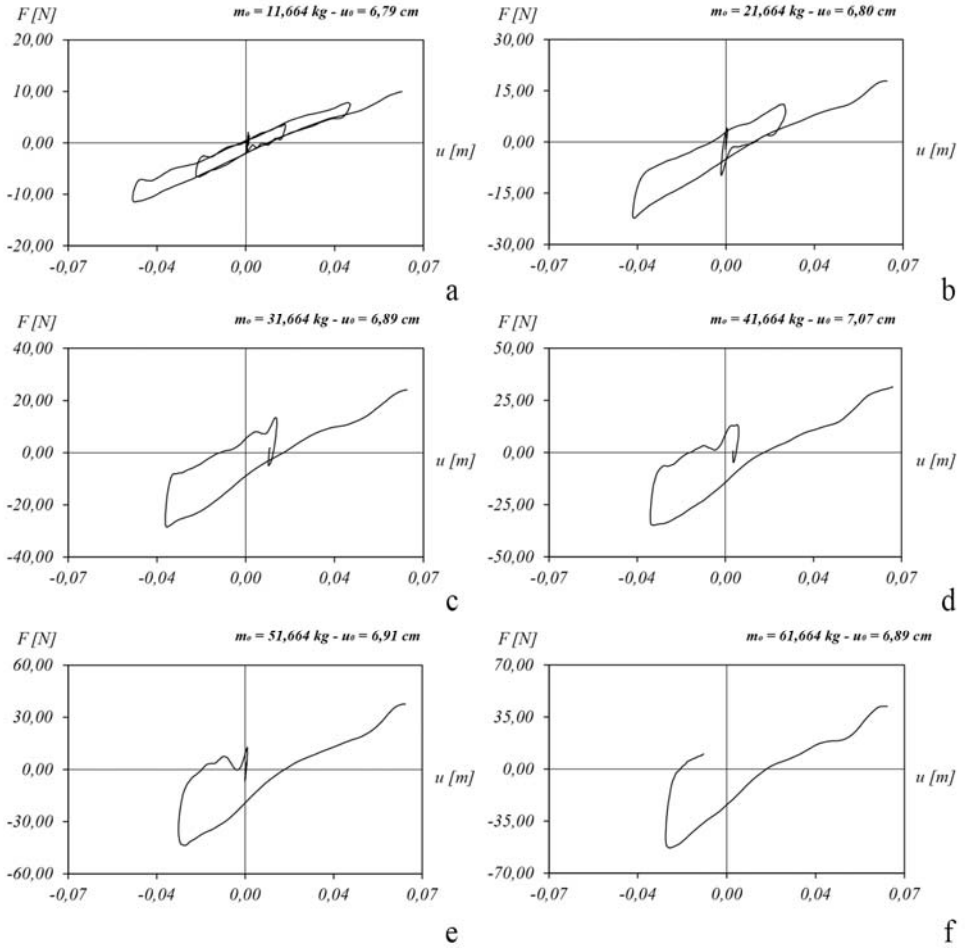

Figure 87 - Experimental free vibration without rubber layer and employing steel balls (r=0,0095m). [Author's image].

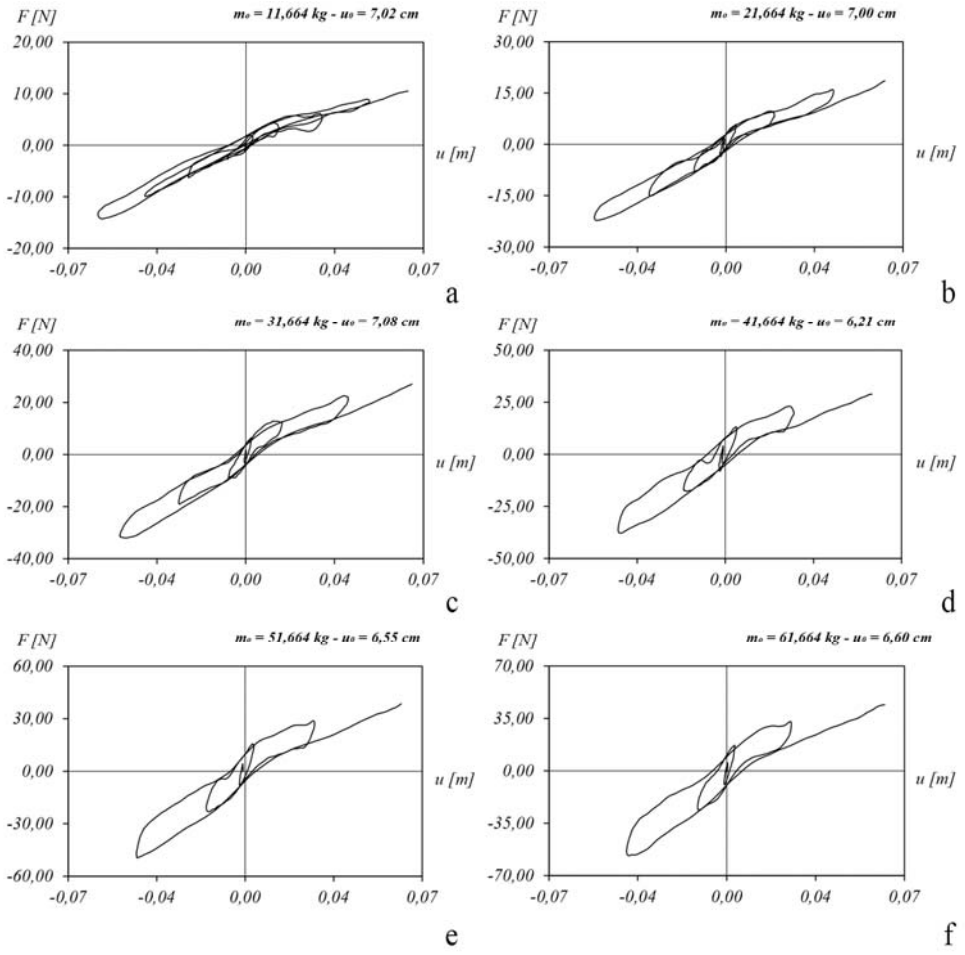

Figure 88 - Experimental free vibration without rubber layer and employing resin balls (r=0,0183m). [Author's image].

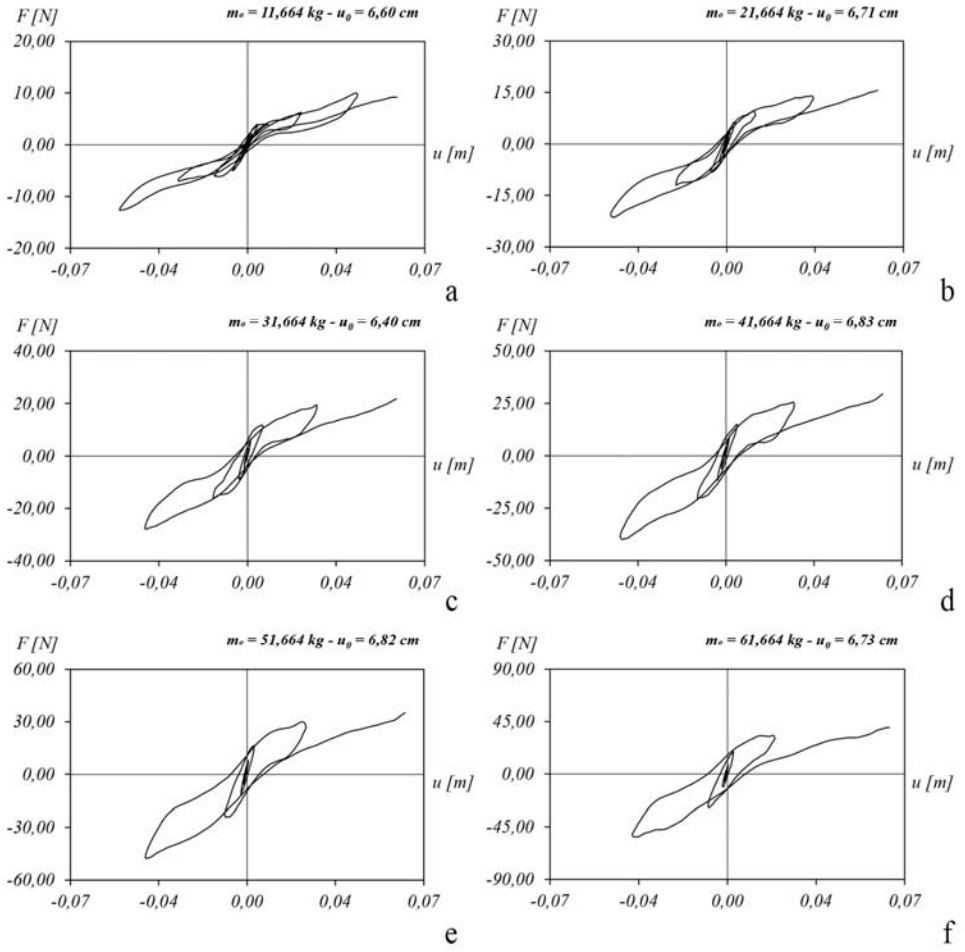

Figure 89 – Experimental free vibration with rubber layer and employing resin balls (r=0,0183m). [Author's image].

5.2.2 Sine ground motion input

The results of the experimental campaign on the dynamic behavior of the considered wooden ball pendulum system, excited by sine ground motion with frequency equal to 1 Hz and associated to three PGA values (0,070g - 0,035g - 0,020g), is presented. Six load configurations are analysed. The results are reported in terms of force-displacement relationships.

Experimental constitutive laws for increasing PGA values are derived, highlighting the influence of the geometrical imperfections on the surface of spherical grooves caused by excessive vertical load. Three increasing levels of PGA intensity are considered. This way it is possible evaluating the behavior for three levels of displacement: *large*, corresponding to displacement values greater than 6 cm; *medium*, corresponding to displacement values between 1 and 6 cm and *small*, corresponding to displacement values lower than 1 cm. Moreover, for each PGA value, six tests are performed for different vertical loads and device setups. In the case of device equipped with resin balls without rubber layer, the additional masses, lower than 20 kg, did not produce significant changes in the radius of curvature of the grooves. As the number of tests increases, the device shows signs of wear caused by the passage of the balls. Analysing the shape of the bond in Figure 90, when the load exceeds 30 kg, a variation in stiffness is noted with displacements close to 2 cm. This proves how the excessive load associated with the repeated passage of the spheres has changed the original curvature of the spherical grooves. In this new configuration, the system shows slightly different stiffnesses. The initial stiffness tends to change due to the formation of pits caused by the application of the vertical load when the device is in static conditions, whereas the stiffness does not change outside the pit.

The first cycles in Figure 90d-e-f show how the peaks force is capable of taking the ball out of the pit (which represents the roll out force threshold). When the roll out force is exceeded, the restoring force is characterized by a constant stiffness with an almost instantaneous change of its verse when the velocity inverts its sign. The smooth shape at the maximum displacement value, as already highlighted above, seems to depend on the elasticity of the sphere. Although the behavior of the device is displacement dependent, the pit modifies the behavior of the device in relation to the velocity response.

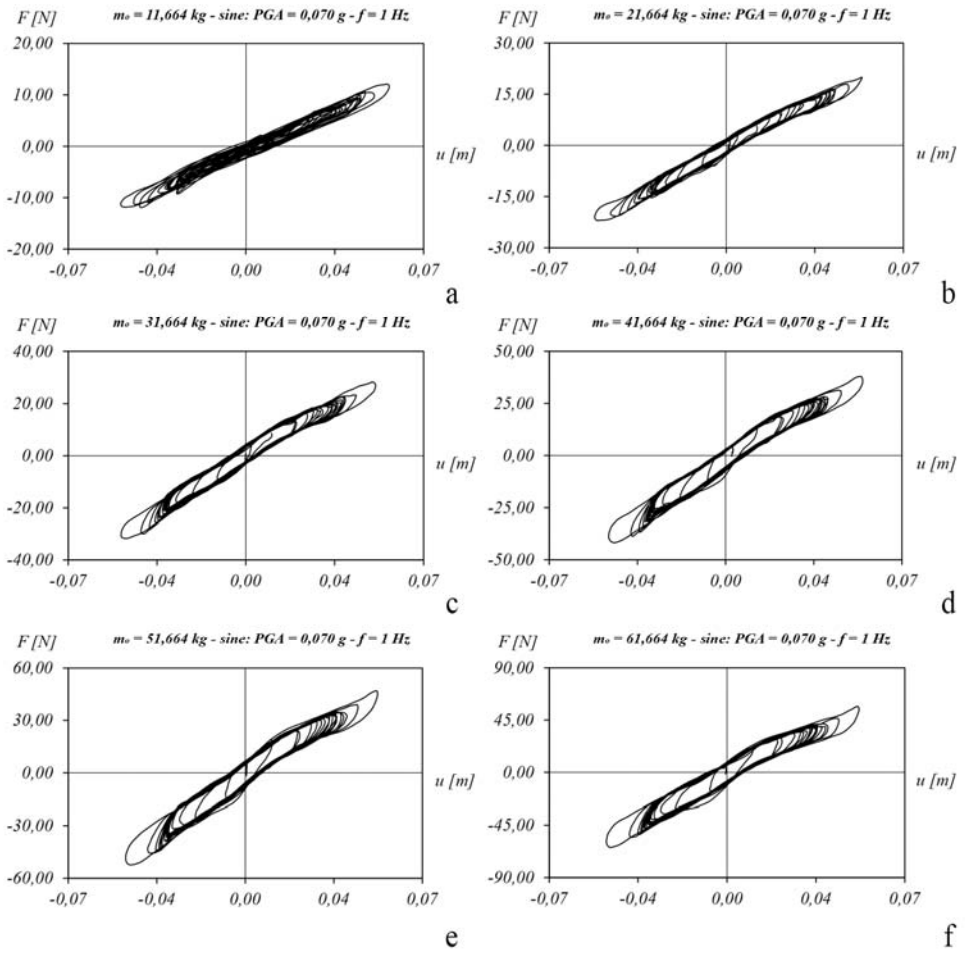

Figure 90 - Experimental sine ground motion (PGA=0,070g, f = 1Hz) without rubber layer and employing resin balls (r=0,0183m). [Author's image].

Although it is difficult to set up tests with a shaking table in which the response of the specimen is controlled in terms of displacement, tests with sinusoidal forces with PGA values equal to 0,035 g and 0,020 g have been prepared to shed light on the behavior at small displacements (below 2 cm). In Figure 91 the effect of the pit is highlighted by two peaks of force for both positive and negative displacements in agreement with the double exponential function used by Donà [52] to model its effects. In this case the shape of the constitutive law changes even for limited vertical

loads and tends to stabilize in the typical trapezoidal shape when the vertical load increases once the roll out force is exceeded. In the case of tests with a lower PGA (0.02 g), Figure 92, the behavior dominated by the continuous localization of the balls inside a viscoelastic depression is added. This type of behavior becomes evident in relation to the supported mass.

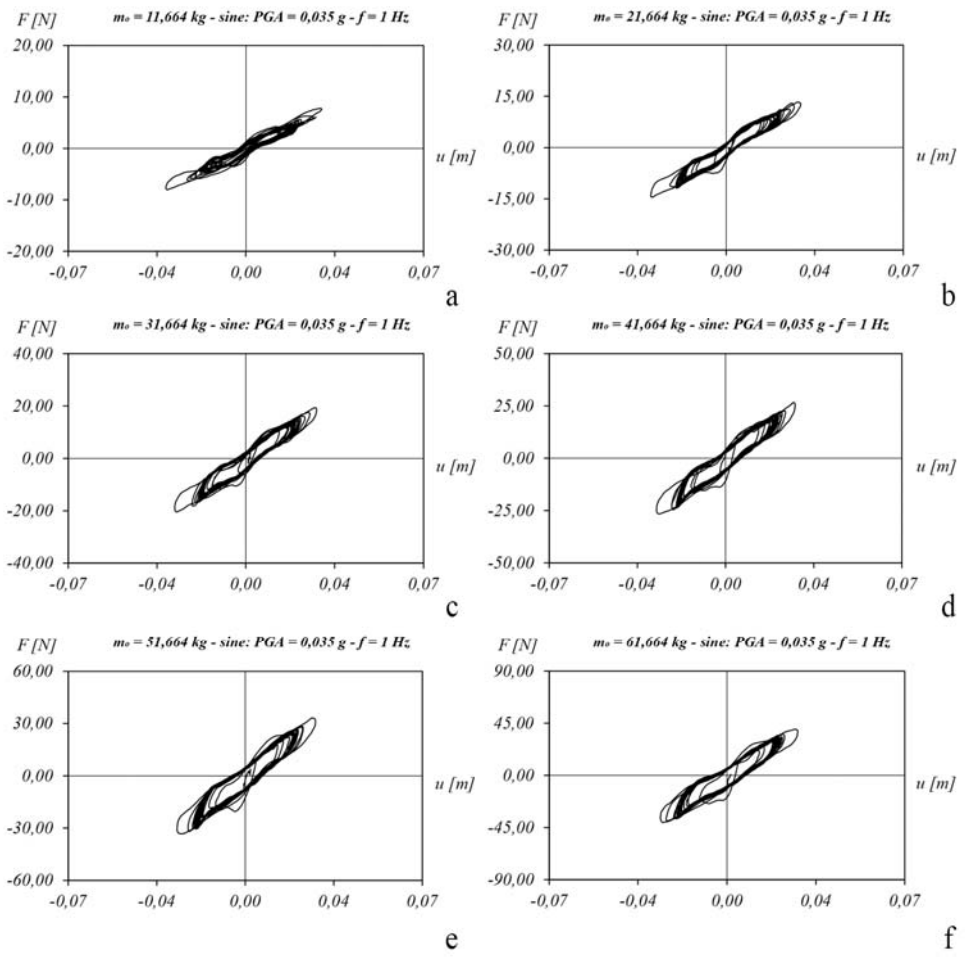

Figure 91 - Experimental sine ground motion (PGA=0,035g, f = 1Hz) without rubber layer and employing resin balls (r=0,0183m). [Author's image].

In particular, up to 30 kg the system exhibits a rolling behavior, whereas for a larger mass it oscillates around the initial position, the ball tends to fall into the pit without getting out of it, Figure 92. From a comparative analysis of the diagrams obtained for different PGA values, it is evident that even in the absence of a rubber layer, albeit with resin balls, the system shows the three behavior regimes as highlighted in [67].

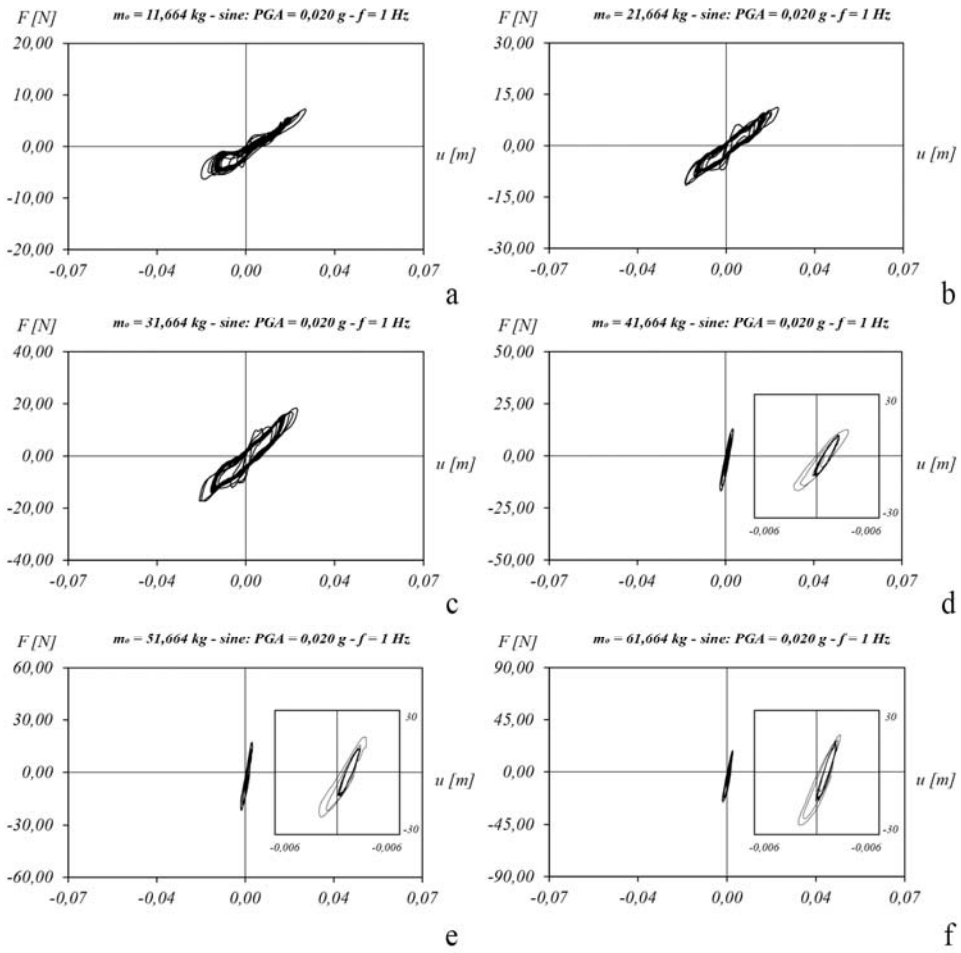

Figure 92 - Experimental sine ground motion (PGA=0,020g, f = 1Hz) without rubber layer and employing resin balls (r=0,0183m). [Author's image].

Figure 92d-e-f, shows the behavior for small displacements inside the pit which is dominated by the continued location of the balls within a viscoelastic depression; Figure 92a-b-c shows in the first cycles the phase at which the balls try to get out of pit; when the roll out force is exceeded, and the system assumes the characteristics of a typical rolling system. Figure 90-Figure 91 represent the typical rolling once the roll out forces are exceeded.

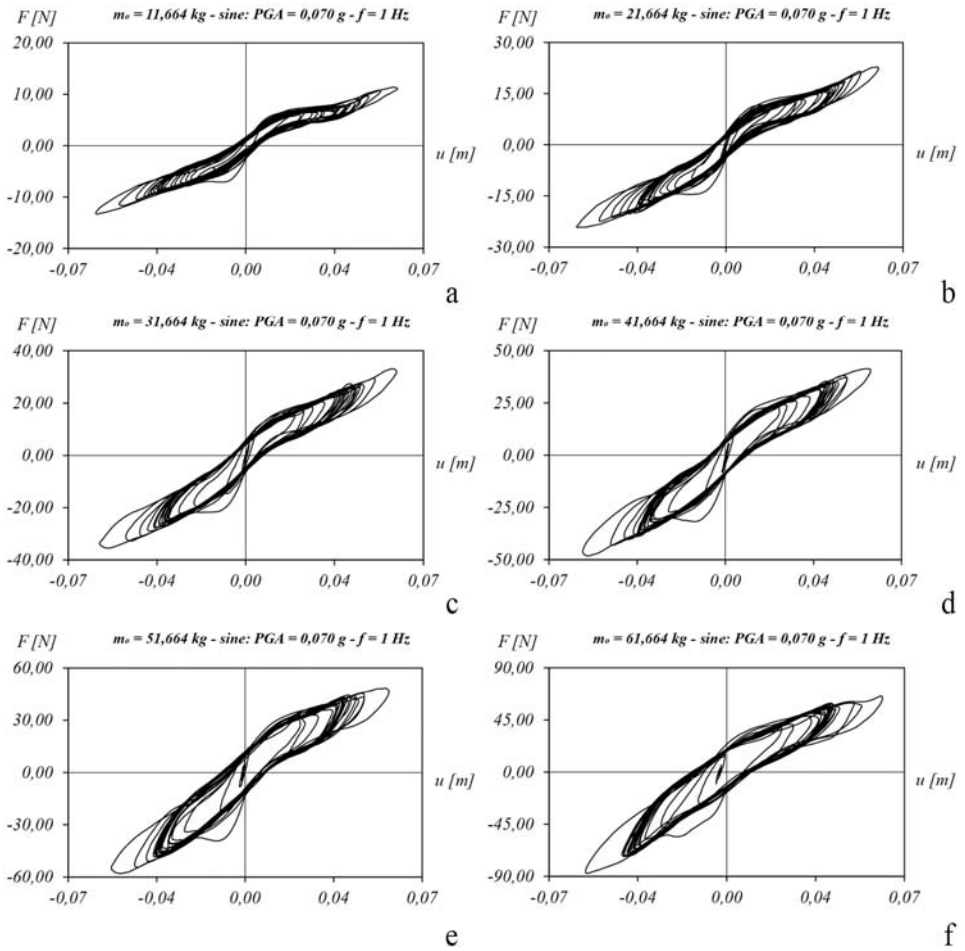

Figure 93 - Experimental sine ground motion (PGA=0,070g, f = 1Hz) with rubber layer and employing resin balls (r=0,0183m). [Author's image].

The analysis of the force-displacement relationships in the case of a device equipped with rubber layers has the same characteristics valid in the absence of a rubber layer. The presence of two different stiffnesses is confirmed as in the previous cases. The increase in stiffness for small displacements is evidently given by the sum of the effects of the pit and the presence of the deformable material. Moreover, it is evident how the influence of the pit varies not only with the balls velocity but also according to the applied vertical load. Comparing Figure 93a and b, the latter one shows a more regular cycle also in first cycles, on the contrary the effect of the indentation is more evident in Figure 93a also when the isolator start its motion.

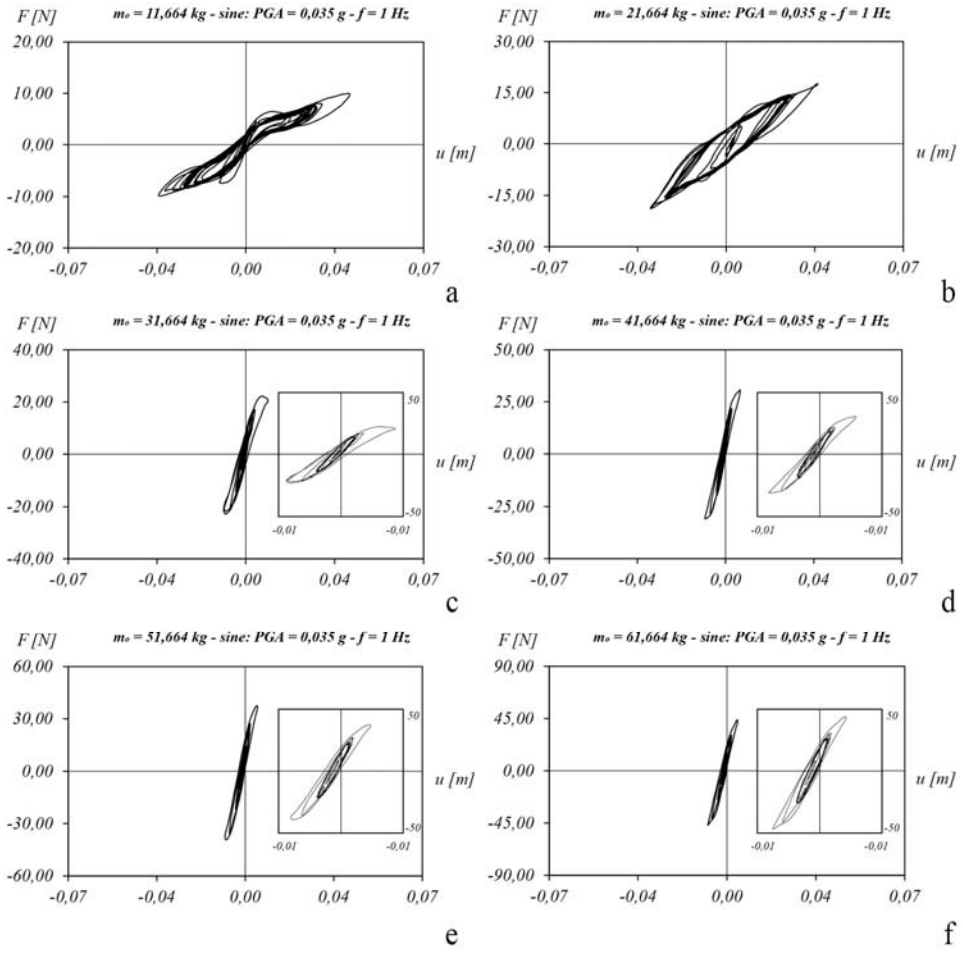

Figure 94 - Experimental sine ground motion (PGA=0,035g, f = 1Hz) with rubber layer and employing resin balls (r=0,0183m). [Author's image].

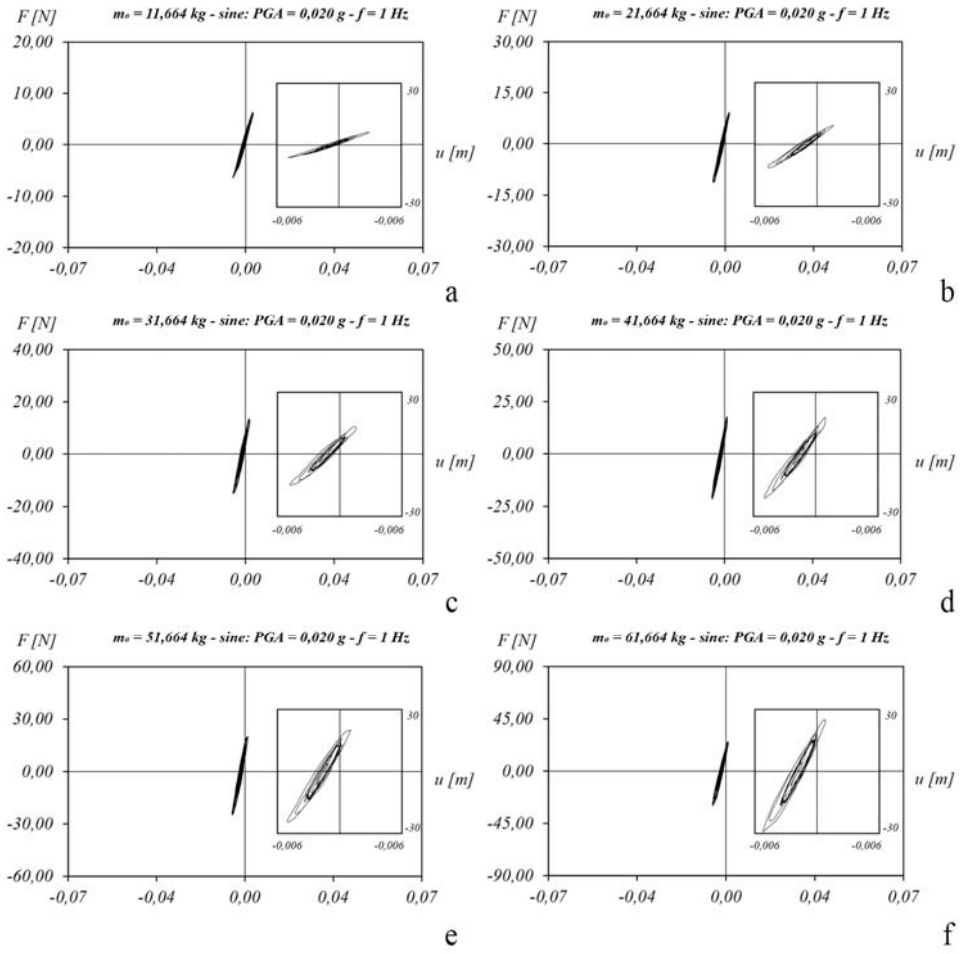

Figure 95 - Experimental sine ground motion (PGA=0,020g, f = 1Hz) with rubber layer and employing resin balls (r=0,0183m). [Author's image].

Furthermore, the experiments confirmed (especially in the full load setting) that the spheres tends to alter the geometry of the groove causing an indentation on the spherical surface and the formation of tracks on the surface of grooves. The indentation could cause stick phenomena with an acceleration increase that could compromise the safeguard of the asset; in addition, the track also changes the original radius of curvature modifying the dynamic properties of the device.

Figure 96 - Surface of the spherical grooves: devices (a) without and (b) with rubber layer.
[Author's image].

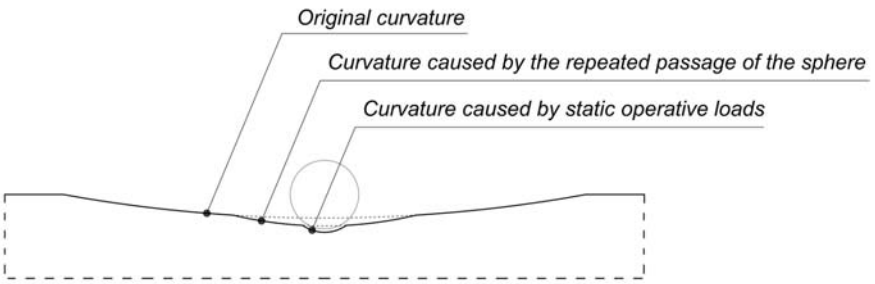

Figure 97 – Indented groove.
[Author's image].

5.2.3 Numerical interpretation of the experimental tests

The numerical model proposed in section 2.4.1 is here applied to simulate the experimental campaign described in the previous section with reference to the case of added mass equal to 10, 20, 30, 40 and 50 kg. The reference properties adopted for the scheme are summarized in Table 20. All the properties of the isolator are considered deterministic and obtained as follows:

- geometric parameters (R, r) are directly inferred from the digital 3D model, Figure 78b, and in Table 20 are identified with the apex (^{1});
- other geometric parameters ($\hat{R}$) are indirectly evaluated considering the formulation in section 2.4.1 and are identified with the apex (^{2});
- the rolling friction coefficient (μ), identified with the apex (^{3}) in Table 20, is evaluated as described in section 5.2.1.
- the mass $M = m_o + m_i$ was obtained weighting the specimen. Consequently, the weight (W), the stiffness (k), identified with the subscript (^{4}) in Table 20, have been evaluated as described in section 2.4.1.

According to the approach reported in section 2.4.1, the initial stiffness is considered as a multiple of the stiffness given by the grooves. The values here considered are $q = 30$ (high initial stiffness) to model cases without rubber layer and $q = 5$ (experimentally estimated) for cases with rubber layer.

i-th load scheme	m_o (^{3}) [kg]	m_i (^{3}) [kg]	M_i (^{4}) [kg]	W_i (^{4}) [N]	R (^{1}) [m]	r (^{1}) [m]	$\hat{R}$ (^{2}) [m]	k_i (^{4}) [N/m]
1	1,664	10,000	11,664	114,394	0,300	0,0095	0,581	196,892
1 (*)	1,664	10,000	11,664	114,394	0,300	0,0183	0,563	203,043
2	1,664	20,000	21,664	212,494	0,300	0,0095	0,581	365,739
2 (*)	1,664	20,000	21,664	212,494	0,300	0,0183	0,563	377,164
3	1,664	30,000	31,664	310,594	0,300	0,0095	0,581	534,585

i-th load scheme	m_o ([3]) [kg]	m_i ([3]) [kg]	M_i ([4]) [kg]	W_i ([4]) [N]	R ([1]) [m]	r ([1]) [m]	$\hat{R}$ ([2]) [m]	k_i ([4]) [N/m]
3 (*)	1,664	30,000	31,664	310,594	0,300	0,0183	0,563	551,677
4	1,664	40,000	41,664	408,694	0,300	0,0095	0,581	703,433
4 (*)	1,664	40,000	41,664	408,694	0,300	0,0183	0,563	725,407
5	1,664	50,000	51,664	506,794	0,300	0,0095	0,581	872,280
5 (*)	1,664	50,000	51,664	506,794	0,300	0,0183	0,563	899,529

Table 20 - Reference properties adopted for the numerical model. Values ([1]) directly and ([2]) indirectly obtained from the 3D digital model, values ([3]) experimentally obtained and ([4]) obtained from theoretical formulations. The symbol ([*]) indicates tests with rubber layer.

The analyses are carried out by solving the direct dynamic problem. The solution was obtained integrating eq. (24) using a 4th-5th order Runge-Kutta method. The solution was implemented in Matlab using the state-space formulation in terms of time history displacements. The structural response of isolator devices in terms of kinematic and dynamic quantities was numerically predicted. The response of the device is modelled assuming the following hypotheses:

- large radius of curvature of the grooves, leading to the assumption $\tan\varphi \simeq u_o / \hat{R}$;
- the top plate is sufficiently rigid to transmit the same vertical load to the balls;
- the rolling friction coefficient remains constant during the test;
- the restoring force is modelled according to the Bouc-Wen model[23];

[23] The Bouc-Wen model allows considering an initial stiffness as a multiple of the isolator stiffness.

- the effects of the pit on the small-displacement range are neglected.

The numerical model is validated by comparing the displacement time histories with those experimentally obtained. In particular, comparisons with the results of the free and forced (sine input with PGA 0.07g and frequency 1 Hz) vibrations tests are presented.

Figure 100a-b-c shows the results of the simulation of the free rolling test of the device in three different setups, assuming the reference properties of Table 20. The numerical model (black line) is able to accurately reproduce the experimental response in terms of period and amplitude of oscillation. The experimental response exhibits a low number of oscillations, characterized by a regular trend for larger oscillation amplitudes and by a response affected by the imperfections in the last cycles. The rolling friction coefficient seems to be correctly modelled in the simulations.

The numerical response seems to be more conservative although it does not account for the pit effects. In Figure 98-Figure 102b-c, the peaks of the experimental response in free vibration are not aligned along a line due to the modification of the geometric properties of the grooves due to the repeated passage of the spheres. At the end of the test, when the system oscillates around zero displacement values, the amplitude and period of oscillation are modified indicating that the rolling occurs inside the pit.

The simulation of the forced test, assuming the reference properties of Table 20 in case of device with and without rubber layer, is reported in Figure 98-Figure 102 d-e. In both cases the effect of the pit is more evident at the beginning of the test. After the transient phase, when the stationary phase prevails, the differences between the theoretical and experimental curves become negligible.

On the basis of the results showed in Figure 98-Figure 102, it can be stated that the analytical model is able to predict the response with a good level of approximation and is therefore an adequate tool to simulate the response of the isolation system.

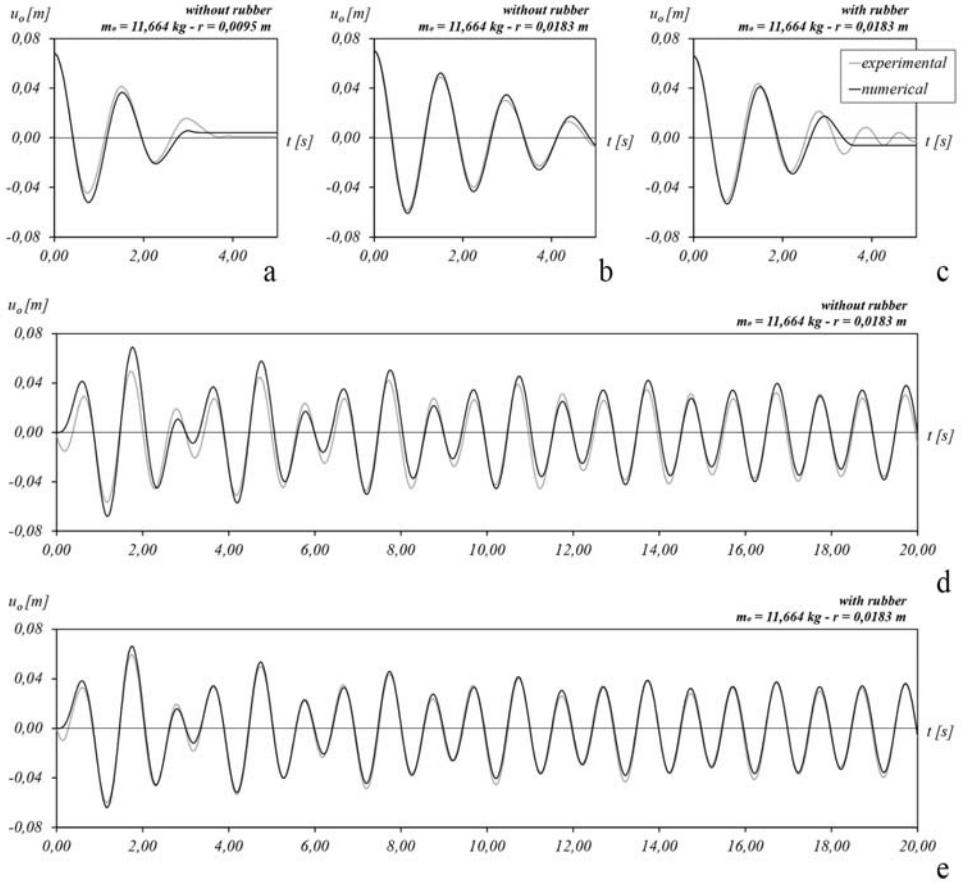

Figure 98 - Comparison between numerical vs experimental time histories (carried mass equal to 10 kg). [Author's image].

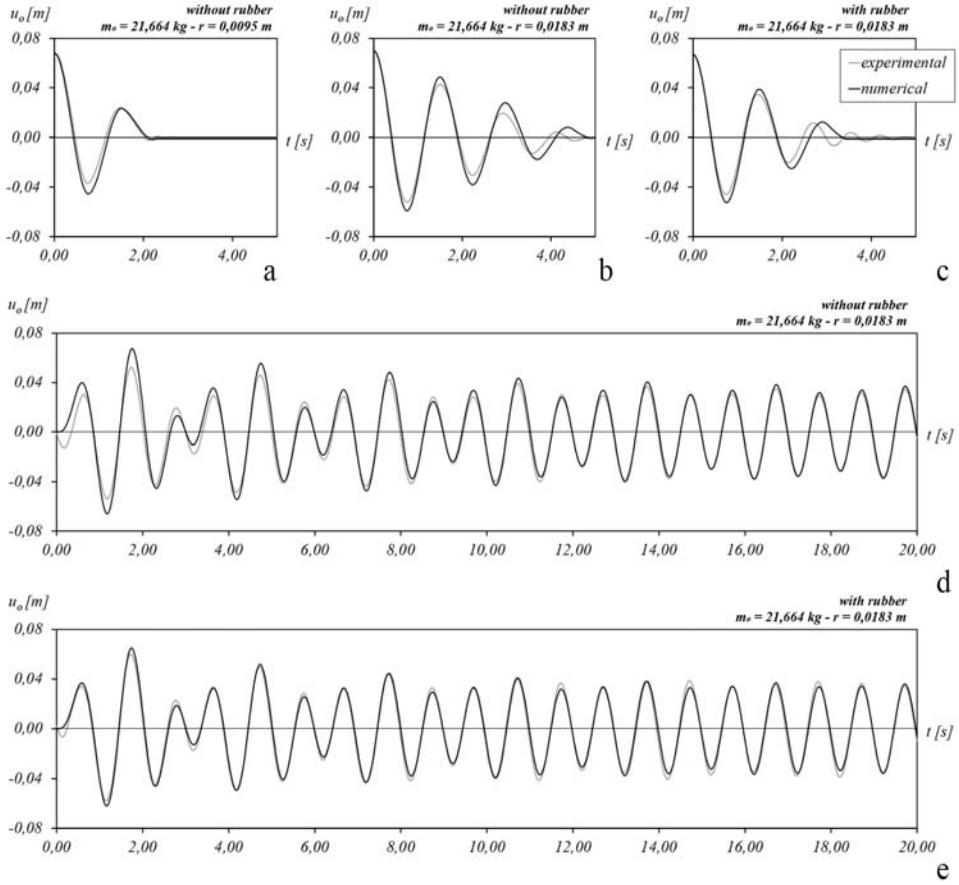

Figure 99 - Comparison between numerical vs experimental time histories (carried mass equal to 20 kg). [Author's image].

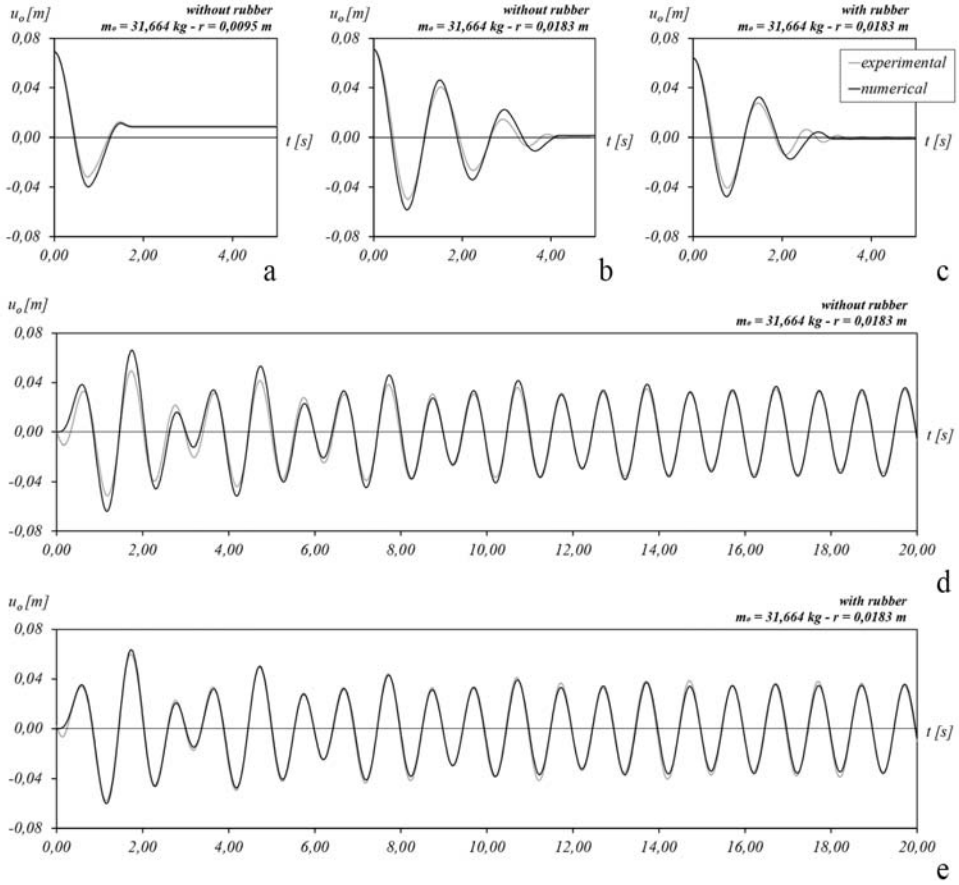

Figure 100 – Comparison between numerical vs experimental time histories (carried mass equal to 30 kg). [Author's image].

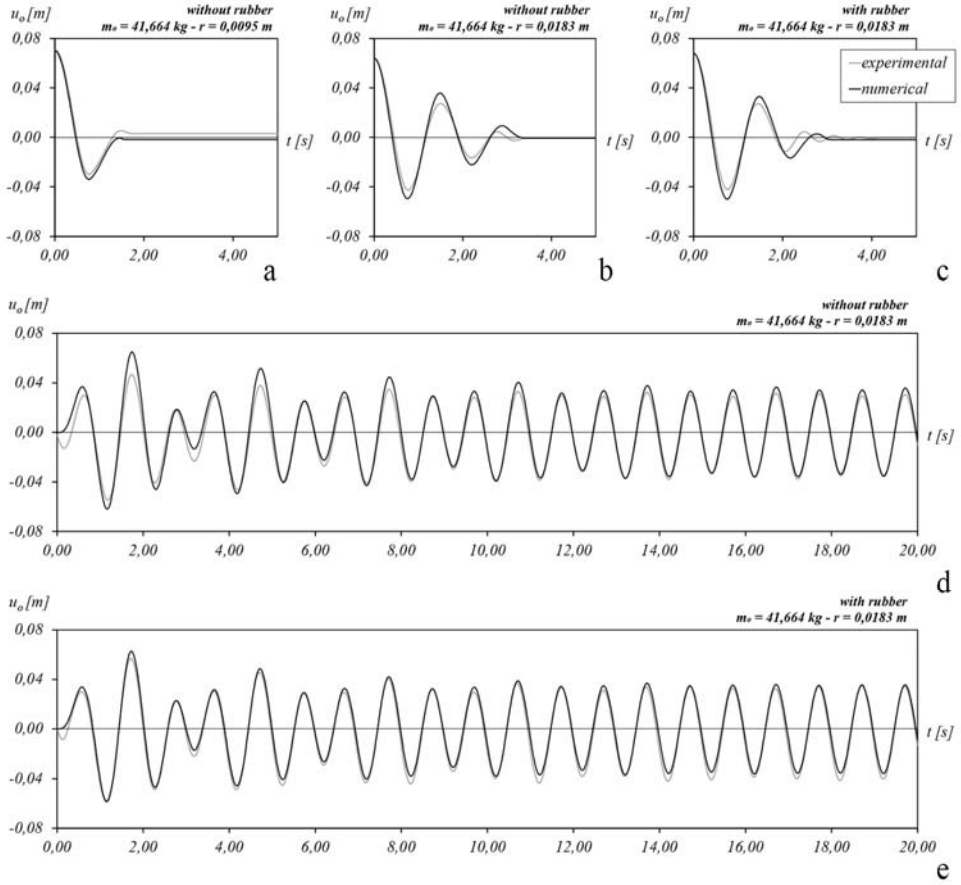

Figure 101 - Comparison between numerical vs experimental time histories (carried mass equal to 40 kg). [Author's image].

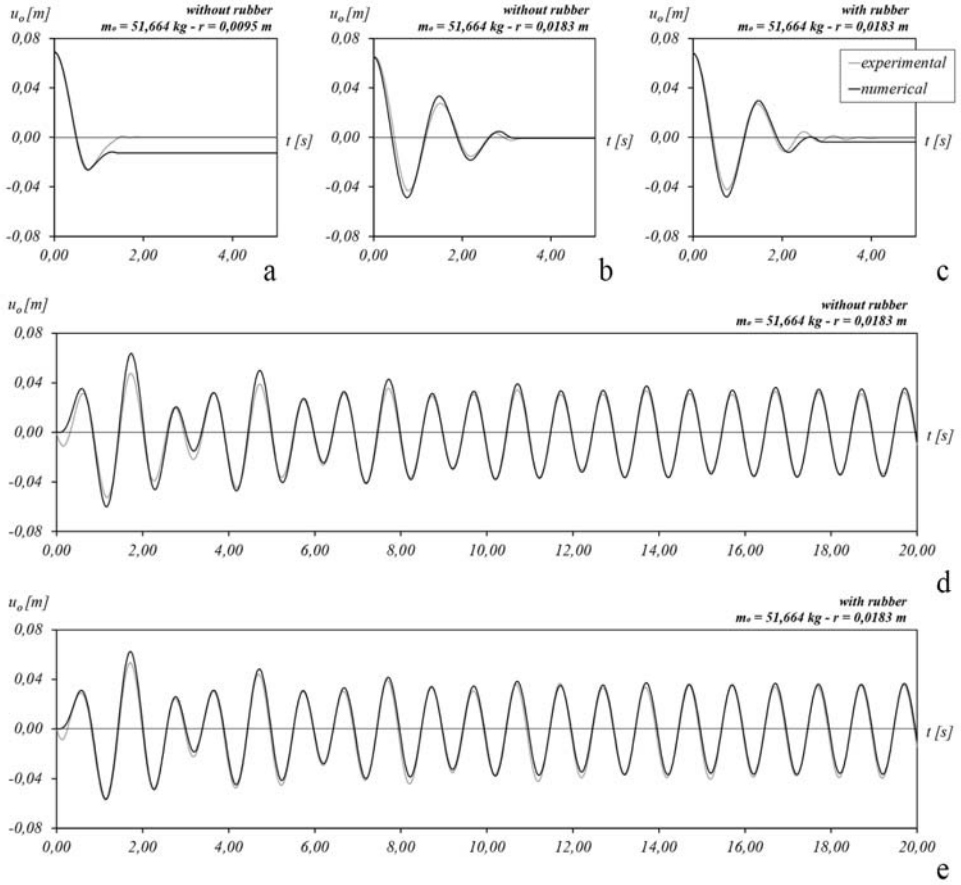

Figure 102 - Comparison between numerical vs experimental time histories (carried mass equal to 50 kg). [Author's image].

5.3 A release mechanism for the stability of the device in static conditions

The system tested in section 5.2 presents two main drawbacks, that is the wear (i.e., indentation) of the spherical grooves due to the passage of the balls and the low horizonal stiffness which might lead to excessive displacements due to accidental impacts. Generally, in museum context, this problem is solved by installing barriers

around the artifact, but this expedient might not be applicable in some cases (e.g. glass cases). In this context, a new Static Dynamic Interchangeable - Ball Pendulum System is proposed. A new prototype was made (with four grooves) and equipped with supplementary balls that absorb vertical loads under operating conditions. Contrary to the system proposed in [40], the solution is designed avoiding during dynamic motion any contact between the additional balls and the top plate. Indeed, when supplementary balls are released ceasing their support function against the vertical load, they fall into a hole on the internal faces of the plates, Figure 103.

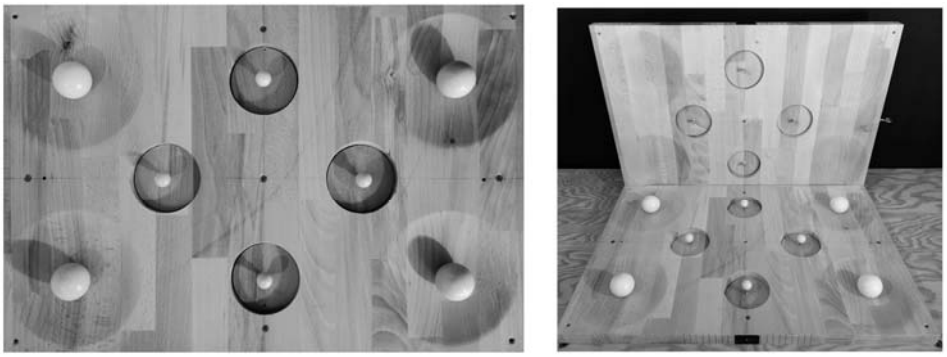

Figure 103 - Arrangement of the two orders of spheres: (a) plan view; (b) internal faces of both plates. [Author's image].

Figure 104 shows the operating scheme. In the static condition, (step 1, Figure 104c), the system is supported only by the supplementary balls unloading the main balls inside the grooves. In this configuration, the contact between the main balls and the grooves must be ensured by adjusting the height of the cylindrical head screws where the additional balls are placed, see Figure 104a, b. This way, when the supplementary balls are no longer effective, the top plate immediately finds contact with the main balls, positioning itself in a configuration similar to that which occurs in the absence of supplementary balls (step 2, Figure 104c). By increasing the horizontal forces, the top plate moves horizontally resting simultaneously on all the spheres, until the supplementary ones fall into a groove (step 3, Figure 104c). Finally, the top plate is

free to oscillate without impacting at each passage from the rest position once its contact with the supplementary balls is lost, (step 4, Figure 104c).

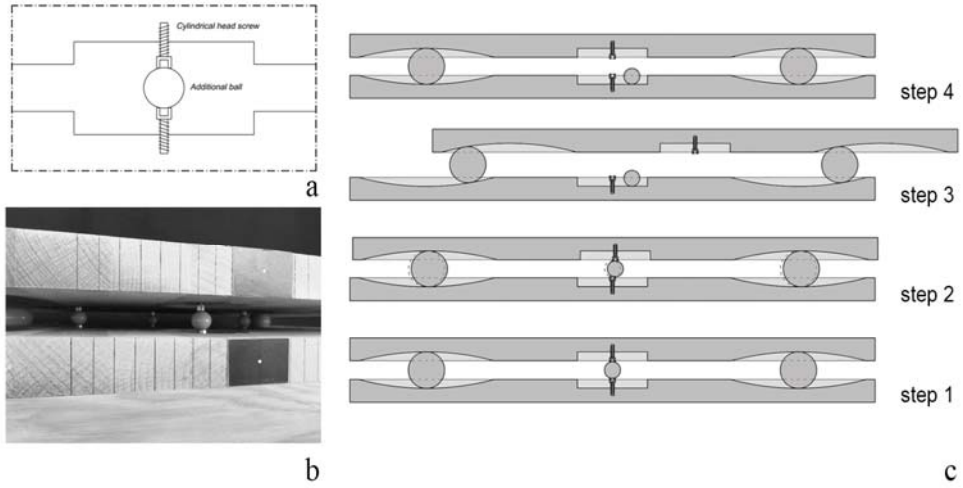

Figure 104 – (a-b) Particular of the vertical load retaining system; (c) operating scheme. [Author's image].

The auxiliary system of supplementary balls works as a release mechanism to be carefully designed to avoid any stick phase and rocking of the carried object and the overturning of the upper plate of device. The characteristics of a rolling ball system isolator are usually designed with regard to the rolling phase, evaluating the maximum displacement of the device and the size to avoid its overturning. The methodology used for designing the new prototype is modified as described below.
The dynamic parameters of the new device, endowed with four grooves, are the same proposed for the first prototype (with three grooves), see section 5.1. Specifically, the same radius of curvature equal to 0,30 m is adopted, a larger allowable displacement than in the previous case simply was considered by adjusting the plates size. The design aims at avoiding the top plate to overturn. In the absence of horizontal forces, no spacing is needed between the grooves to guarantee the equilibrium, Figure 105a. In the presence of horizontal forces, the grooves must be

suitably spaced so that the moment around the right contact point due to the vertical forces must be able to balance that associated to the horizontal forces, Figure 105b.

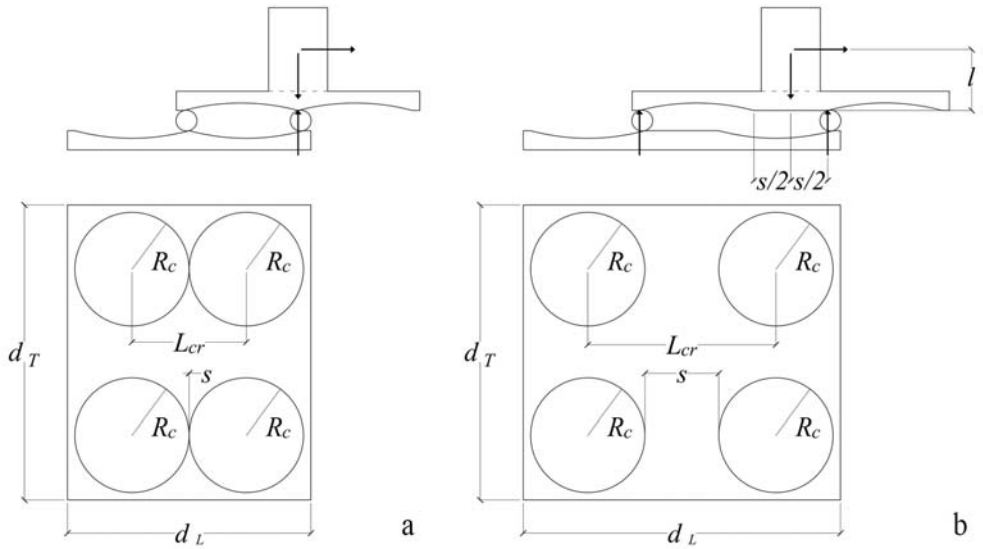

Figure 105 – Design criterion to guarantee the design displacement and avoiding overturning. [Author's image].

The experimental results in Figure 110b-d-f-h show that it is necessary to evaluate the force capable of deactivating the fuse. Even when the fuse is active, if the horizontal forces acting on the device exceed the forces associated to the maximum design displacement, overturning of the top plate can occur if the distance s is underestimated. For this reason, a procedure to estimate the activation force of the fuse was arranged, aiming to appropriately choose the diameter of the additional balls, or the safety distance s, or the geometry of the fuse.

With reference to the scheme in Figure 106, the fuse remains effective for accelerations lower than that in eq. (52) determined considering the rotational equilibrium of the forces with respect to point C.

$$\ddot{u}_o^{(*)} = \frac{g\sqrt{2rz - z^2}}{2(r - z)} \tag{52}$$

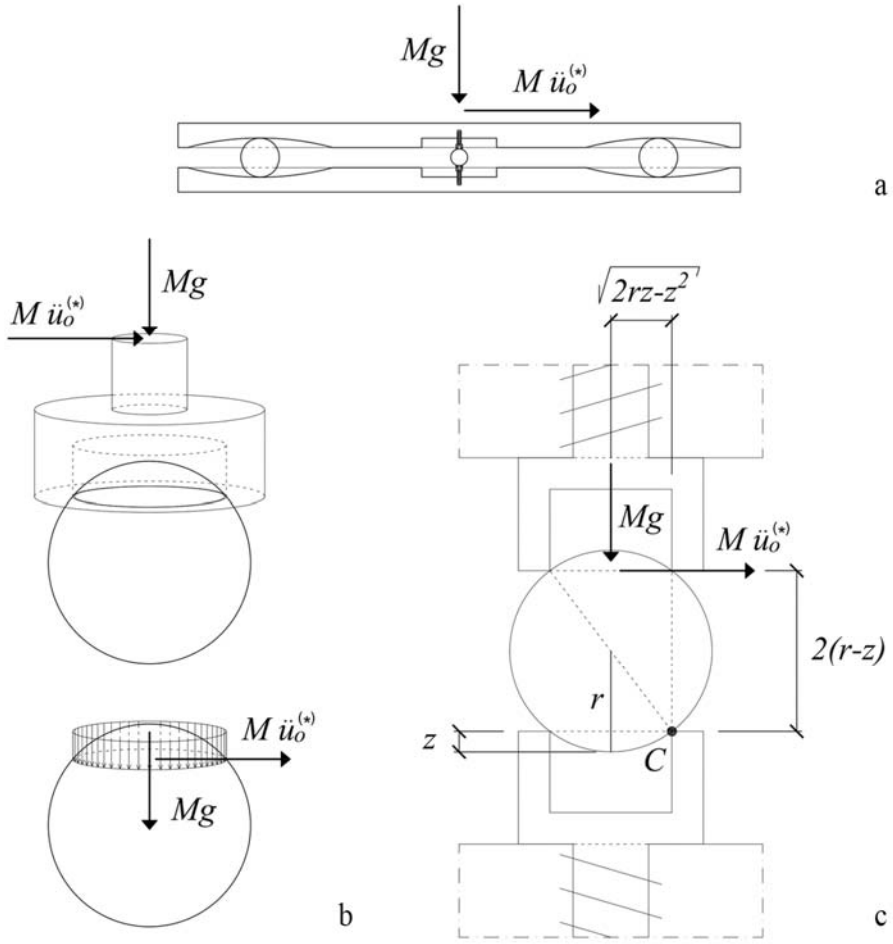

Figure 106 - Scheme for evaluation of the deactivation acceleration of the fuse: (a) global scheme; (b) 3D distribution load in static condition; (c) simplified 2D scheme. [Author's image].

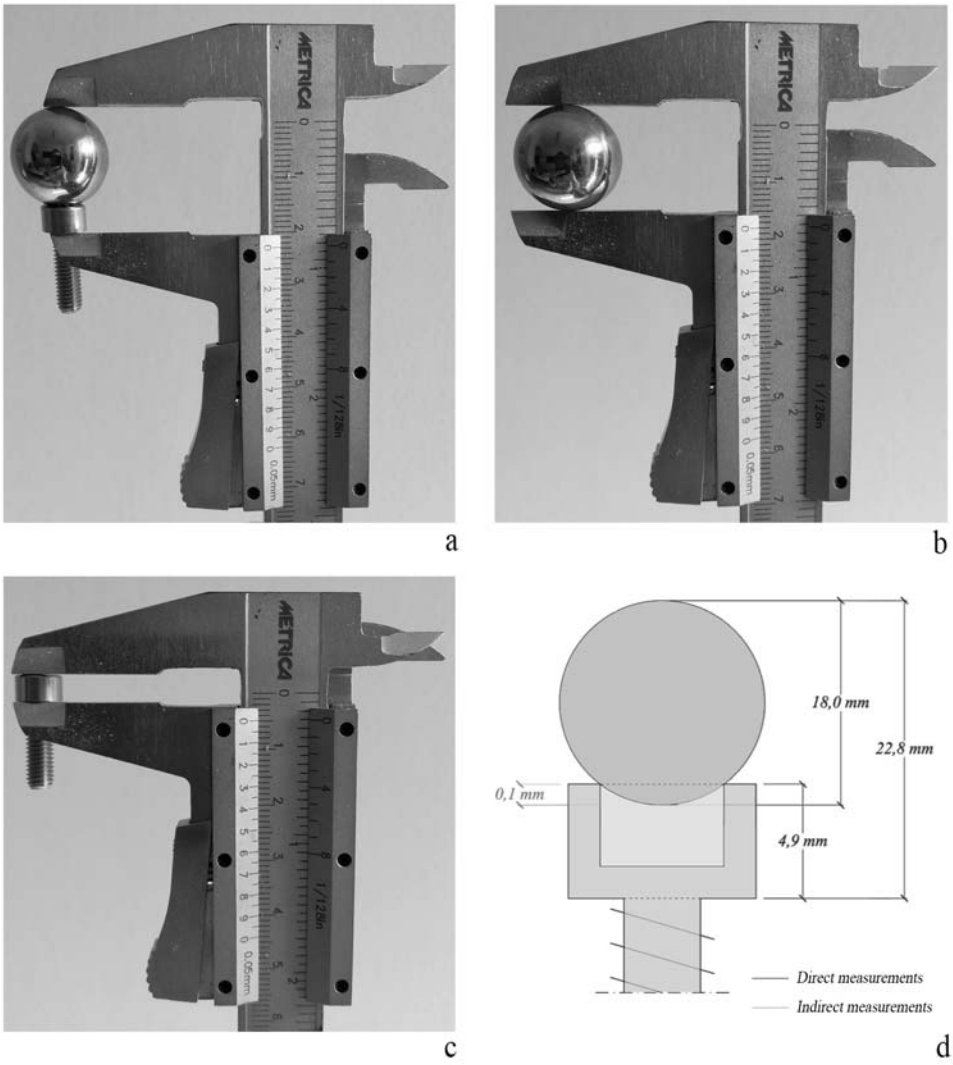

Figure 107 – Survey of fuse geometry.
[Author's image].

Applying eq. (52) the additional spheres become ineffective for accelerations greater than or equal to 0,075 g. The efficiency of the fuse was experimentally evaluated in the case of forced vibrations. The experiments are performed using a sinusoidal input with frequency equal to 1 Hz and increasing PGA values, from 0,040 g to 0,080 g, with steps of 0,005 g, and aim at identifying the acceleration able to trigger the

rolling. The results are reported in terms of force-displacement relationship useful for identifying the effects of the release mechanism. The specimen was tested under different load configurations as better specified in Table 21. The additional mass is aligned with the centre of gravity of the base of device, Figure 108. The tests were performed considering principal ivory balls with radius r = 0,0200 m and supplementary steel balls with radius r = 0,0090 m, Figure 103c-d.

i-th load scheme	M_i [kg]	W_i [N]	$\hat{R}$ [m]	k_i [N/m]
1	9,359	91,812	0,560	163,950
2	14,359	140,862	0,560	251,539
3	19,359	189,912	0,560	339,128
4	24,359	238,962	0,560	426,717

Table 21 - Reference parameters in case of principal ivory balls with radius r = 0.0200 m and additional balls with radius r = 0.0090 m.

For all load configurations, the spheres come out of their seat for an acceleration intensity equal to 0.075 g. A comparison for the time history associated to the load scheme 1 (M = 9,359 kg and PGA equal to 0.075 g), between the device configurations with and without fuse, shows discrepancies in the first phases of the motion, Figure 109a-b. When the activation acceleration of the fuse is not achieved, no appreciable displacement of the device is observed, as shown Figure 109a for t<0,3 s. Figure 110 shows the comparison between the force-displacement relationship with and without fuse for PGA equal to 0.075 g. Two behaviors for two different levels of PGA can be observed: the first one, corresponding to the phase in which the top and bottom plates move almost together; the second one, when the fuse effect is lost and the device behavior depends on the main mechanism only. The fuse can be considered as an artificial pit that does not change its characteristics over time and whose geometry can be identified and measured. It should be mentioned

that the adopted contactless acquisition technique (2D) is efficient only in the case of measurements made on in-plane behavior. Measurement errors may occur when the device exhibits behavior outside the plane, as for the case reported in Figure 110h, where a pronounced out-of-plane response was observed.

Figure 108 - Arrangement of the load on the device with fuse. [Author's image].

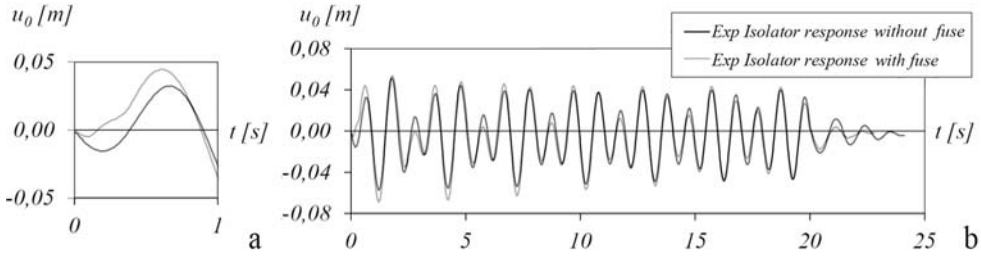

Figure 109 – Experimental response of device with four grooves: (a-b) without and (c-d) with release mechanism. [Author's image].

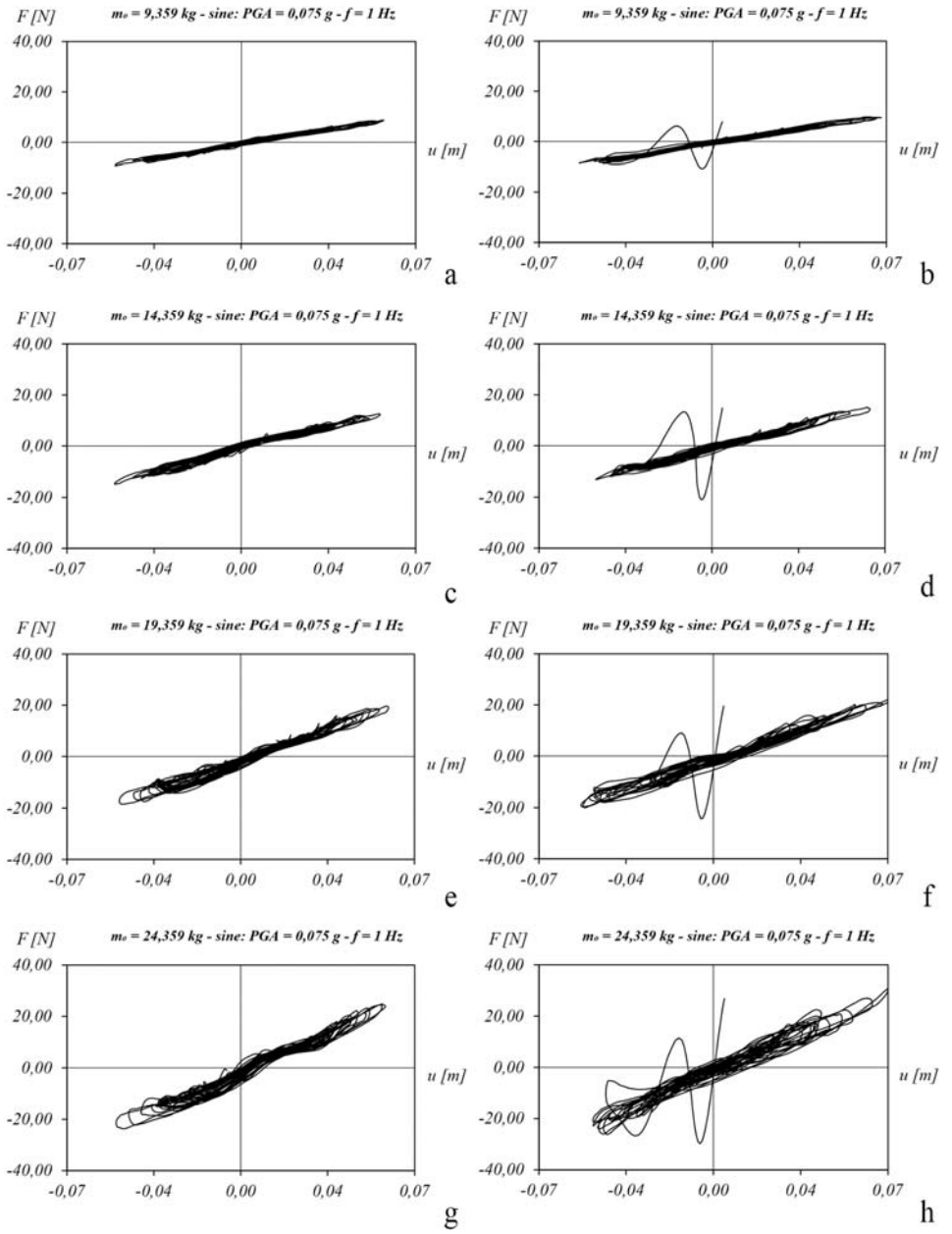

Figure 110 – Force-displacement relationship of a BPS device with four grooves, without rubber layer with ball r=0,020m and supplemental balls with r=0,0090m: (a-c-e-g) without and (b-d-f-h) with release mechanism. [Author's image].

Chapter 6 Case study: Venere Landolina statue.

This chapter is focused on the seismic behavior of statues, which generally present a quite complex geometry and are mostly characterized by a pronounced unsymmetrical response under seismic excitations. The proposed study involves both numerical analyses and experimental tests and is applied to the masterpiece of Paolo Orsi museum in Syracuse (Italy), that is the Venere Landolina [68]. Specifically, analytical simulations are conducted according to the novel rigid block model which accounts for asymmetric behavior and contact impairments. The experimental campaign is conducted on a scaled physical prototype, built according to a highly detailed and complete digital model obtained by 3D survey. The numerical and experimental campaign is conducted with reference to compatible seismic ground motions, conveniently scaled to cope with scale effects. The results are finally correlated and discussed, showing the potentiality of the proposed approach for modelling artworks in seismic conditions and the reliability of a combined experimental and numerical strategy to assess the seismic safety of real statues.

6.1 General methodology and presentation of the case study

Due to the impossibility to perform experimental tests directly on the statues, numerical analyses are usually preferred to assess the seismic safety of artefacts. In this study a combined methodology is exploited by performing: *i*) experimental tests with a shaking table on a low-cost scaled prototype reproducing the original geometry of the statue, *ii*) numerical analyses according to the model described in the previous section 0. To this purpose, Figure 111 depicts the main phases of the proposed methodology.

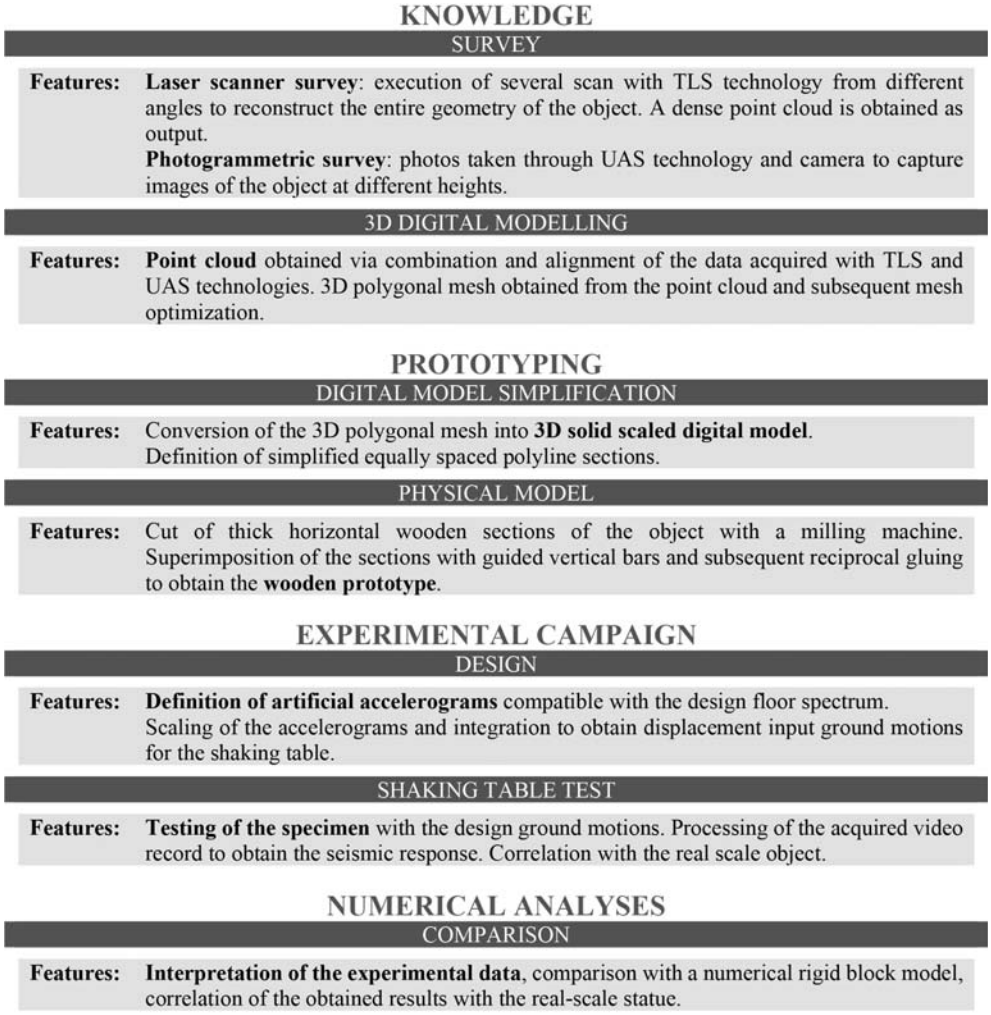

Figure 111 - The proposed methodology.

[Author's image].

The first phase (knowledge) consists of the geometry inspection of the statue, to be obtained by means of a non-invasive three-dimensional survey, which allows reconstructing a faithful digital model. Based on the 3D reconstruction of the artefact, a conveniently scaled prototype is produced.

According to the perfect homogeneous rigid body model, the geometry of the object and its scale ratio should be faithfully replicated to determine its dynamic response. Nevertheless, whenever possible, materials with properties similar to the original object should be adopted. In the present study a different material is used with the aim of pursuing a low-cost strategy.

Once the physical scaled prototype is ready, it can be tested on the shaking table (experimental campaign). This phase, as better shown in section 6.3, first aims at obtaining reliable values for some of the properties to be adopted in the numerical model (uplift accelerations and coefficients of restitution); to this purpose, very simple tests can be performed, such as pulse ground motions or free rocking motion. Then, the prototype is subjected to ground motions compatible with the design spectrum. The results of the experimental campaign are finally validated and crosschecked with those obtained by numerical analyses, which can also retrieve some of the parameters that cannot be experimentally measured. Thus, a reasoned and trustworthy safety judgement can be finally formulated.

The proposed methodology is applied to the Venere Landolina, a marble statue masterpiece of "Paolo Orsi" archaeological museum in Siracusa (Italy), Figure 112. The marble structure goes back to the II century A.D. and probably is a copy of a former Greek statue; its name is related to Saverio Landolina, the archaeologist who discovered the Venere in 1804. The statue was chosen for its artistic relevance, but also as a representative case of an asymmetric slender object, which may favour the uplift.

The statue, placed on a high pedestal, is 174 cm tall and its base can be inscribed in a 56x56 cm square. The mass of the statue, approximatively equal to 467 kg, is estimated considering a volume of 0.176 m^3 and a density ρ = 2650 kg/m^3.

Figure 112 - Venere Landolina: (a) right side; (b) front side; (c) left side. [Author's image].

6.2 From real model to physical scaled specimen

In this section the knowledge and prototyping phases are described. The two steps are intimately connected since the digital model must be arranged according to required criteria to create the scaled physical model. Specifically, in the first subsection the survey actions are elucidated. This are aimed at the production of a detailed three-dimensional digital model.

In the second subsection, the steps to simplify the digital model and to create a low-cost scaled physical model are described.

6.2.1 Survey

The experimental procedure follows the operational protocol for the virtual rendering of artistic and museum objects proposed in [69] in order to acquire a 3D model. To cope with the complex shape of Venere Landolina, an integrated survey analysis obtained through the combination of range-based and image-based

techniques had been implemented [70]. Starting from data acquired by a *Terrestrial Laser Scanner* (*TLS*) according to the *Structure from Motion* (*SfM*) imaging technique, the 3D model is derived. It includes complex information, formal material and colour data, Figure 113b. From an operational point of view, two survey campaigns have been conducted: the first one with a *Leica Scan Station C10*; the second one with a digital camera and *Unmanned Aerial System* (*UAS*) technology. In the first campaign, four targeted scans were obtained in order to accurately align the various digital images in the post processing phase through Cyclone Software. In the second campaign various shots were taken at different heights around the sculpture. *SfM* technique gave back a texturized 3D model starting from a set of digital shots. The detected features were then gathered in a 3D sparse point cloud and all the coordinates of the key-points of the surrounding items were optimized to generate a dense point cloud. To acquire a greater amount of data, *UAS* technology has been introduced so to produce high-resolution imagery which is almost impossible to obtain with traditional systems. A quadcopter *DJI Spark weighing 3 Ngrams* captured aerial imagery of the upper surface of the Venere and generated the data to produce an accurate model also exploiting vertical and oblique imagery. The point cloud acquired with instrumental survey was aligned to that obtained from digital automatic photogrammetry, Figure 113c. The data conducted to the generation to a photorealistic 3D model by means of a texture mesh, Figure 113d.
Finally, *Geomagic Wrap* performed a retopology procedure in order to optimise the polygonal model generated through the integration of the different applied techniques, Figure 113e.

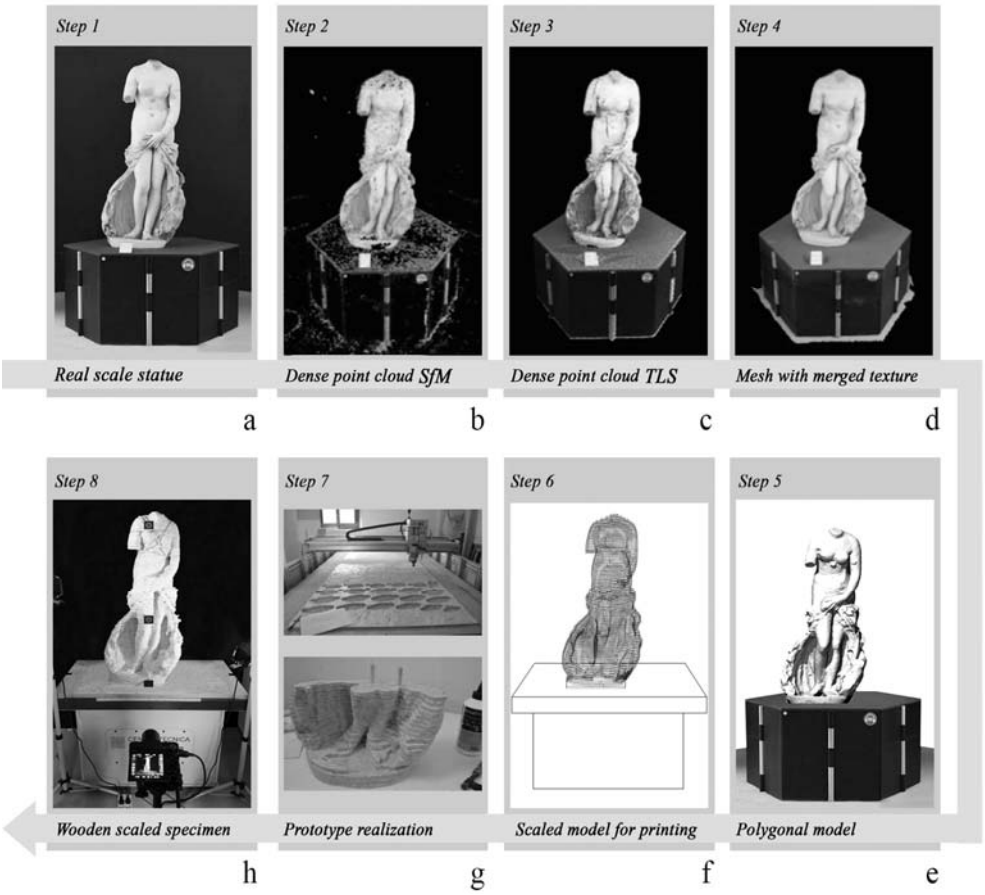

Figure 113 - From the real statue to the wooden specimen: (a-e) elaboration of the 3D textured model; (f) simplified digital model, (g) CNC machine on top and superimposition of the sections on bottom; (h) final physical specimen. [Author's image].

6.2.2 Prototyping

Aiming at creating a scaled specimen with size and weight compatible with unidirectional shaking table at disposal for the experimental campaign, a scale factor 1:2 was assumed. To limit the realization cost of the prototype, a technique based on the superimposition of flat wooden disks glued to each other is here adopted. Each

disk is a 9 mm thick *OSB* (*Oriented Strand Board*, a product made of glued wood shavings layers) panel. A simplification of the digital model is therefore necessary to reproduce the scaled physical model of the statue by 91 wooden sections, Figure 113f, accounting for the additional thickness of the glue interposed between subsequent layers. Each section represents the perimeter of an *OSB* layer, which is then cut off from larger panels with a *Computer Numerical Control* (*CNC*) milling machine, Figure 113g (top). Since the real statue is made of marble, it will exhibit different properties from those associated to the wooden specimen. Preferably, the scaled specimen should be realized with the same material of the real object to avoid significant differences in the restitution coefficient. The analyses performed on the wooden statue have to be intended not fully representative of the real statue, since based on a different material, but are useful for describing the methodology that can be adopted in a real vulnerability assessment on a statue by investigating the experimental response of a prototype at a different scale. Additional tests could be performed to investigate the influence of different restitution coefficients on a reduced scaled marble specimen. On the wooden specimen the cuts were performed adopting a cutter with a diameter of 3 mm. To guide the superimpositions of the layers, each disk hosts two holes for the insertion of vertical bars, Figure 113g (bottom). The disks are then refined sanding their border. It is worth noting that the proposed procedure represents a low-cost strategy to create a three-dimensional physical model of the statue. The final physical specimen, Figure 113h, has a height of 87 cm, a volume of about 0,022 m^3 and a footprint of about 28x28 cm. The location of the centre of gravity is indicated in Figure 114a. The simplified scaled digital model of the statue, Figure 113, was also exploited to infer the geometric properties of the numerical model.

6.3 Experimental campaign

The experimental campaign conducted on the scaled wooden specimen is described herein. Although a significant amount of experimental studies has been conducted

on the dynamics of rigid blocks, asymmetric blocks have been rarely treated [71]. The equipment and the contactless displacement measurement strategy are described in section 3.1.1 and 3.2. Then, the experimental identification of some parameters to be employed in the numerical analysis is shown; specifically, the uplift accelerations and the coefficients of restitution have been obtained by means of simple tests. Finally, the specimen will be subjected to ground motions conveniently chosen, that will be adopted as reference data for the numerical analyses. The ground motions act along the *x* axis (see the reference system in Figure 57).

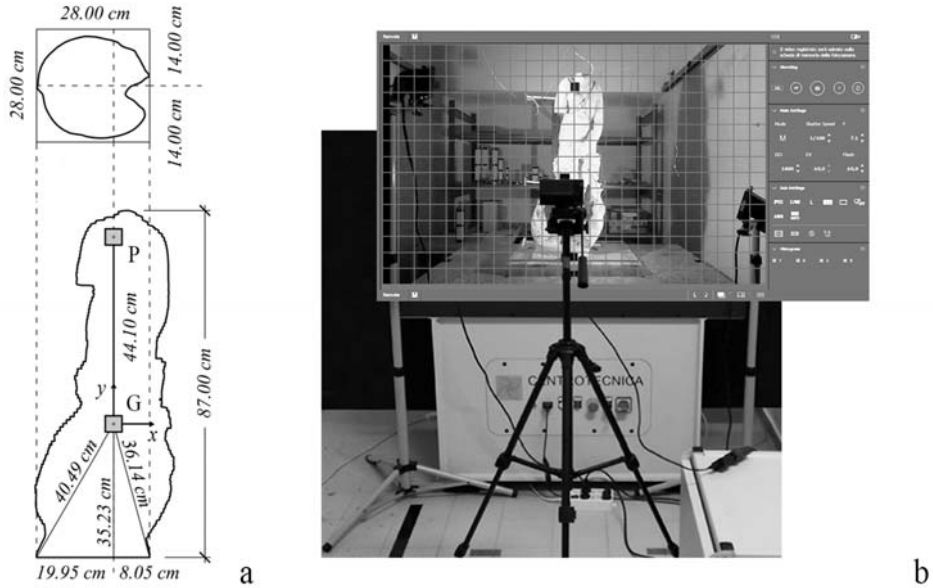

Figure 114 - (a) Experimental setup and (b) main geometric features of the wooden specimen. [Author's image].

6.3.1 Identification of the main parameters

The ratio between real and theoretical left and right uplift accelerations is expressed by means of the coefficients α_L and α_R, respectively. Their evaluation is pursued by

analysing the response when the body is subjected to a base cosine pulse with increasing amplitude, see Table 22, where the superscripts (*t*) and (*e*) indicate theoretical and experimental conditions, respectively.

$\ddot{u}_L^{(t)}$	$\ddot{u}_L^{(e)}$	α_L	$\ddot{u}_R^{(t)}$	$\ddot{u}_R^{(e)}$	α_R
[g]	[g]	[-]	[g]	[g]	[-]
0,566	0,090	0,159	0,229	0,040	0,175

Table 22 - Comparison between theoretical (*t*) end experimental (*e*) uplift accelerations.

Figure 115 plots the measured experimental potential, E_u, kinetic, E_k, total, E_t, energies of the block during a free rocking motion at the *i*-th step, according to eqs. (40)-(42).

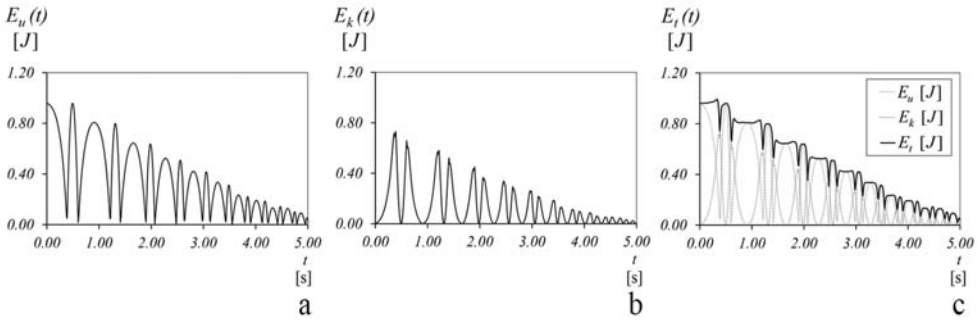

Figure 115 - Energy decay scheme during free vibration: (a) potential (b) kinetic and (c) total energy contents. [Author's image].

Application of eqs. (40)-(42) leads to an experimental evaluation of the coefficient of restitution according to the observed energy decay at each impact.

With reference to the free rocking motion test of Figure 116a, the trend of the coefficients of restitution and the relevant correspondence with the angular velocity of the impact are depicted in Figure 116b-c. Due to the asymmetry of the block, the results, summarized in Table 23, are differentiated according to the edge around which the block is rotating at the impact. As the total energy of the block decreases,

the angular velocity of impact reduces, and a trend of the coefficient of restitution versus the impact velocity is reconstructed.

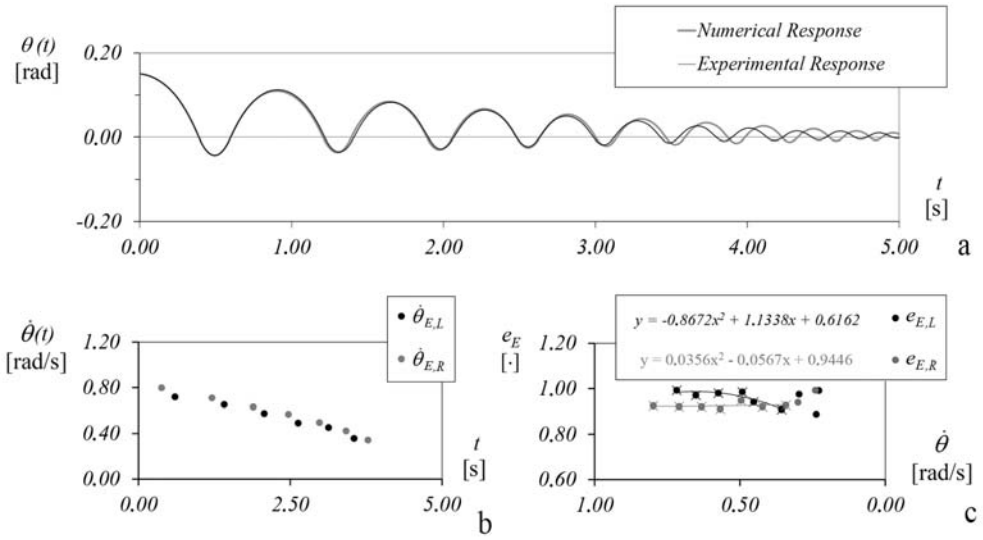

Figure 116 – Response for the characterization of Venere statue: (a) free rocking motion; (b) estimated impact velocity vs impact instants; (c) coefficient of restitutions vs angular velocities. [Author's image].

i [-]	t [s]	$\lvert\dot{\theta}\rvert$ [rad/s]	$e_{E,R}$ [·]	i [-]	t [s]	$\lvert\dot{\theta}\rvert$ [rad/s]	$e_{E,L}$ [·]
0	0,38	0,7980	0,9249	1	0,60	0,7176	0,9924
2	1,21	0,7094	0,9208	3	1,41	0,6517	0,9706
4	1,89	0,6320	0,9202	5	2,07	0,5745	0,9800
6	2,47	0,5680	0,9111	7	2,63	0,4920	0,9848
8	2,98	0,4958	0,9472	9	3,13	0,4527	0,9410
10	3,42	0,4226	0,9211	11	3,55	0,3570	0,9089
12	3,78	0,3423	0,9273	-	-	-	-

Table 23 - Measured restitution coefficients for right, $e_{E,R}$ and left, $e_{E,L}$ impacts.

6.3.2 Ground motion tests

After preliminary calibration of some parameters of the numerical model, specifically, the uplift accelerations and the coefficients of restitution, the experimental campaign was conducted considering seven compatible ground motions [72]. They have been generated following Italian guidelines for artistic heritage [73], according to *Artistic Limit State* (*SLA*) limit state design spectrum of the site where the Venere is located (Syracuse, Italy and soil type C). A floor spectrum is duly considered (the statue is located at the second of three levels where the interstorey of first two floor is $H = 4,0$ m and the total height is $H_{tot} = 11,5$ m). The approximate fundamental period T_S of the structure, equal to 0,32 s, was estimated according to the Italian code using the formula $T_S = CH_{tot}^{3/4}$ (the coefficient $C = 0,05$ takes into account the type of construction). Figure 117a-b depicts the adopted design spectrum along with the relevant parameters needed for its definition (with V_N life cycle, c_u class of use, n number of control cycles carried out on artistic asset in the time interval normally adopted by the Administration responsible for the protection, T_R return period of the earthquake, C type of soil, $T1$ topographic category, a_g maximum horizontal acceleration at the site, F_0 amplification factor of the design spectrum in horizontal acceleration, F_c^* reference value for determining the start period with constant velocity segment on the acceleration horizontal design spectrum).

The spectrum-compatible accelerograms were generated through the software *SeismoArtif* [74] and then the time values were scaled by a factor $\sqrt{\lambda} = \sqrt{2}$ according to the Froude analogy [75], to account for the scale factor of the specimen with respect to the original statue. Time rescaling allows to obtain, for the reduced model, the same nonlinear differential equations that holds for the real statue. The specimen and the real scale statue, according to the Buckingham theorem [76],

should provide the same response in terms of time-history if characterised by the same restitution coefficient. However, since the reduced scale model is characterised by a different material the actual response of the real statue and of the scaled object will be comparable but not identical.

One of the generated accelerograms is reported in Figure 117c (light grey) together with the corresponding scaled one (black). In the same figure the theoretical $\ddot{u}_L^{(t)}$ and $\ddot{u}_R^{(t)}$ (dashed lines) and experimental $\ddot{u}_L^{(e)}$ and $\ddot{u}_R^{(e)}$ (dash-dot lines) uplift accelerations are also reported. The spectrum compatibility of the generated accelerograms is duly verified, Figure 117b. Then, the scaled accelerograms are integrated twice thus defining the input ground motions to be applied to the specimen, Figure 117d.

The results, after being processed considering the markers layout, are collected and reported in Figure 119 (black lines). As the experimental uplift accelerations is much smaller than the theoretical one, the specimen uplifts for all the considered ground motions, however, no overturning is observed.

The obtained responses in terms of rotation angle θ, normalized by the critical angle, show that the specimen tends to a more pronounced rocking around the right edge (the one closer to the centre of mass).

The average maximum rotation angle over the seven ground motions is $\bar{\theta}_{max} = 4{,}72°$; the maximum achieved angle is $\bar{\theta}_{max} = 6{,}28°$ (observed for the 6th accelerogram).

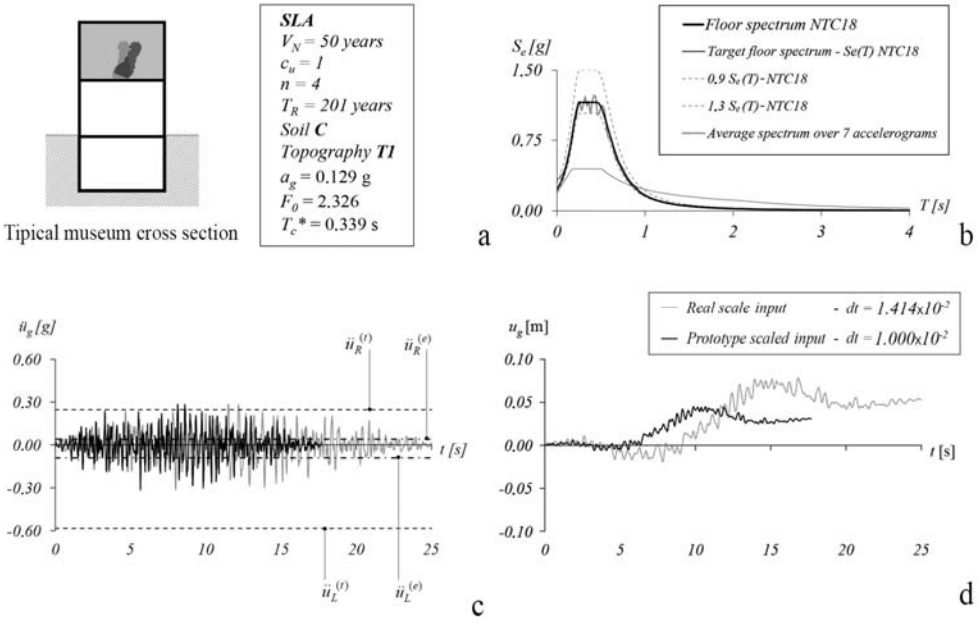

Figure 117 - Design of the experimental campaign: (a) main data for definition of adopted design spectrum; (b) adopted design spectrum to generate the ground motions and spectrum compatibility; (c) artificial accelerogram and corresponding scaled one, (d) input ground motion for the shaking table. [Author's image].

6.4 Numerical analyses

The numerical model proposed in section 0 is here validated against the experimental campaign described in the previous section. The reference properties adopted for the block are summarized in Table 24. Most of the properties of the block are considered deterministic and obtained as follows:

- some of the geometric (h , b_L , b_R) and inertial (I_G) parameters are directly inferred from the simplified digital 3D model and in Table 24 are identified with the subscript ([1]);
- other geometric (d_L , d_R , δ_L , δ_R) and inertial (I_L , I_R) parameters of the block are indirectly evaluated considering the formulation in section 4.1.1 and are identified with the subscript ([2]);

- the coefficients for the reduction of the uplift accelerations (α_L and α_R), identified with the subscript ([3]) in Table 24, and the coefficients of restitution ($e_{E,L}$ and $e_{E,R}$) are evaluated as described in section 0; in addition, the mass m is obtained weighting the specimen.

The remaining independent parameters are the transition rotations θ_L and θ_R, which are considered as uncertain parameters. A rough estimation of the two angles θ_L and θ_R is provided considering that the full uplift of the statue, for both sides, is approximately associated to rotation angles $\theta_L = \theta_R = 4{,}55 \times 10^{-3}$ rad, corresponding to the normalized values of $\theta_L/\delta_L = 0{,}88 \times 10^{-2}$ and $\theta_R/\delta_R = 2{,}02 \times 10^{-2}$ for the left and right sides, respectively. This value is related to horizontal displacements of the upper marker (point P, Figure 114) equal to $3{,}961 \times 10^{-3}$ m and $3{,}959 \times 10^{-3}$ m for the left and right sides, respectively. The simulation of the free rocking tests of the statue, assuming the reference properties of Table 24, is reported in Figure 116a, showing that the model (grey line) is able to accurately reproduce the experimental response for the first impacts; when the amplitude of the rotations reduces, the numerical equivalent period of the block tends to become larger than the observed experimental one. From a preliminary sensitivity analysis, the response of the block did not show appreciable sensitivity to the transition angle θ_L (strong side); on the contrary, the response appeared to be significantly sensitive to the transition rotation θ_R relative to the weak side. For this reason, the influence of the uncertainty in the parameter θ_R is considered in the numerical analyses. Specifically, the interval of the normalized transition angle $\theta_R/\delta_R = [1{,}78; 2{,}26] \times 10^{-2}$ is adopted (with reference value $2{,}02 \times 10^{-2}$ and radius $0{,}24 \times 10^{-2}$), assuming equally spaced steps of 10^{-4} for a total amount of 49 outcomes.

a

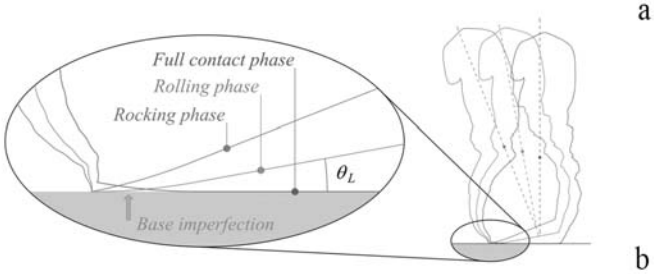

b

Figure 118 – Geometric imperfections at base: (a) details of the base of the specimen and (b) interpretation of the behavior due to the base imperfections. [Author's image].

Geometric parameters

h (1) [m]	b_L (1) [m]	b_R (1) [m]	d_L (2) [m]	d_R (2) [m]	δ_L (2) [rad]	δ_R (2) [rad]
0,3523	0,1995	0,0805	0,4049	0,3614	0,5152	0,2247

a

Inertial parameters

m (3) [kg]	I_G (1) [kg m^2]	I_L (2) [kg m^2]	I_R (2) [kg m^2]
12,0740	0,7994	2,7344	2,3490

b

Uplift coefficients

α_L (3) [·]	α_R (3) [·]
0,1590	0,1750

c

Table 24 - Reference properties adopted for the numerical model: (a) geometric parameters; (b) inertial parameters; (c) uplift coefficients. Values (1) directly and (2) indirectly obtained from the 3D digital model, and (3) values obtained by experimental measures.

For each of the seven ground motions the results are reported in Figure 119a-g highlighting the value of θ_R/δ_R which provides the best match with the experimental response.

As shown, smaller or greater values than the reference one may provide closer results to the experimental response; indeed, the adopted uncertainty range is always able to get a reliable prediction of the experimental response of the statue. It is worth to note that the considered accelerograms rarely exceeds the theoretical uplift accelerations, which if adopted would have led to unrealistic simulations.

For a better understanding of the influence of the uncertain parameter in the response of the statue, in Figure 119h the maximum achieved rotations are summarized for all the seven ground motions and considering all the 49 simulations. For each of the seven ground motions, the maximum experimental response (black dots) is compared with the frequency distributions of the numerical simulations (grey bars). For ground motions 1, 4 and 6, the experimental response is centred on the frequency distribution and for 5 and 7 the experimental response is close to the interval with the highest occurrence of the numerical simulations, showing that a sensitivity analysis embedding an uncertain parameter in the numerical simulations provides comforting results.

On the contrary, for ground motions 2 and 3, the maximum experimental response is located peripherally with respect to the numerical frequency distribution, showing the unavoidable chaotic character of the rigid body motion.

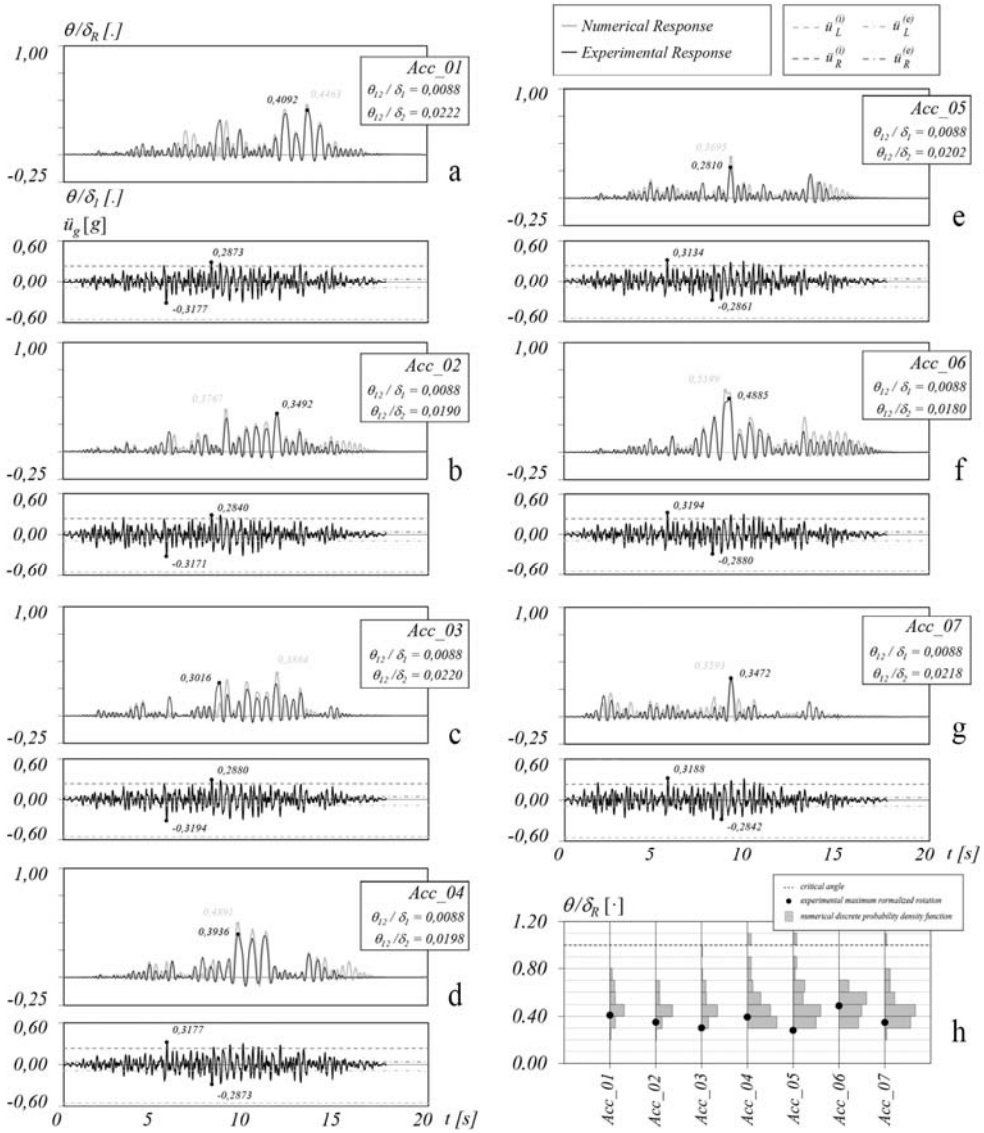

Figure 119 - (a-g) Comparison between experimental tests and numerical simulations for seven spectrum-compatible ground motions; (h) frequency distributions for the seven ground motions of the maximum response considering θ_R as uncertain parameter. [Author's image].

The efficiency of the seismic isolation system presented in section 5.3 (device with four grooves) is assessed for the configuration without rubber layer and fuses.

Considering the approximate radius of curvature (excluding the contribution of the spheres) of the device equal to 0,60 m, the natural period is equal to 1,55 s.

According to the reference design spectrum, Figure 117b and the period of device, the design acceleration for the isolated system is set to 0,3917 m/s^2 , a value smaller than the minimum uplift acceleration of the statue equal to 0,3924 m/s^2. The maximum displacement achievable by the device, geometrically obtained by drawings, is equal to 0,15 m. This is compatible with the design value evaluated on the response spectrum in terms of displacements.

The characterization of the device was performed by evaluating the decay of the response in terms of displacement from free vibration tests, in accordance with the methodology set out in section 5.2.1. The results of the analyses, Figure 120f, show the trend of the rolling friction coefficient varying the vertical load conditions.

M_i [kg]	μ_i [-]
4,359	0,0039
9,359	0,0055
14,359	0,0070
19,359	0,0081
24,359	0,0108

Table 25 - Measured rolling friction for the device with four grooves without fuse or rubber layer.

The friction coefficient for the adopted load configuration can be obtained by linearly interpolating the data shown in Table 25, considering a total mass equal to 16,433 kg given by the sum of the mass of the top plate of the device (4,359 kg) and the statue (12,074 kg).

The estimated friction coefficient in the configuration in which the scaled model of the Venere Landolina is placed on the device is μ = 0,0073.

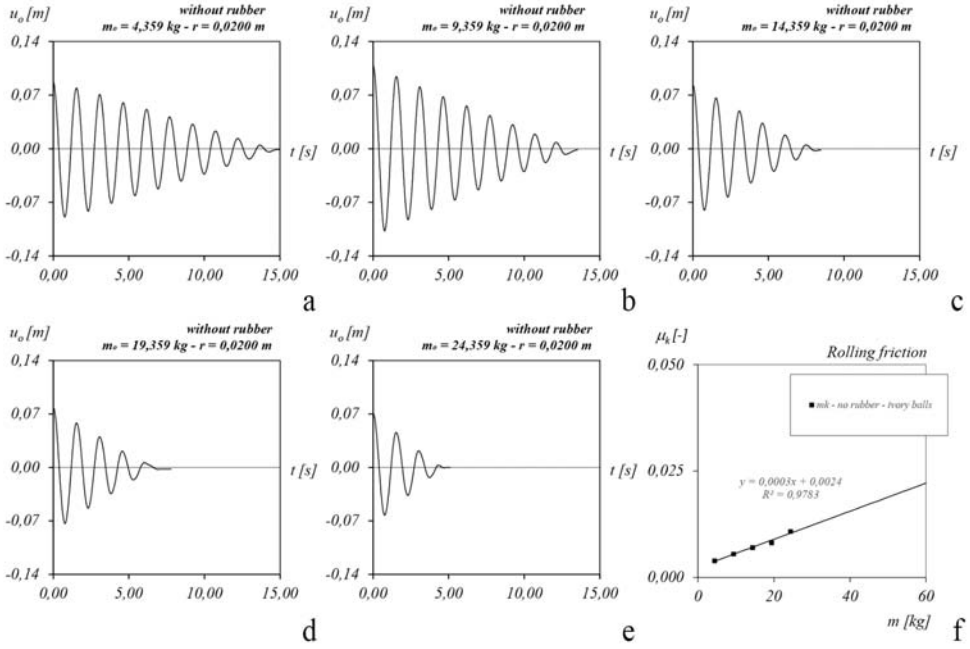

Figure 120 – Characterization of the device with four grooves. [Author's image].

From the visual analysis of Figure 120 emerges that the device does not show signs of damage on the surface of the grooves being all the peaks of response, even for small oscillation amplitudes, aligned on a straight line. The presence of a small mass, less than 30 kg, excluded damages on the grooves.

A simple measure of the effectiveness of the system is the ratio between the peak acceleration values related to the isolated and non-isolated settings, see Table 26.

	$\ddot{u}_{o,\max}^{(not\ iso)}$ [m/s^2]	$\ddot{u}_{o,\max}^{(iso)}$ [m/s^2]	$\ddot{u}_{o,\max}^{(iso)} / \ddot{u}_{o,\max}^{(not\ iso)}$ [-]
Acc_01	3,117	0,642	0,206
Acc_02	3,111	0,638	0,205
Acc_03	3,133	0,766	0,244
Acc_04	3,117	0,592	0,190

	$\ddot{u}_{o,max}^{(not\ iso)}$ [m/s^2]	$\ddot{u}_{o,max}^{(iso)}$ [m/s^2]	$\ddot{u}_{o,max}^{(iso)} / \ddot{u}_{o,max}^{(not\ iso)}$ [-]
Acc_05	3,075	0,676	0,220
Acc_06	3,133	0,535	0,171
Acc_07	3,127	0,529	0,169

Table 26 – Efficiency of the isolating system.

Figure 121 shows the design accelerogram (gray line), the absolute accelerations measured on the top plate during the experiment (black line) and the real uplift acceleration of the statue (dashed line). In all the time histories, the measured acceleration is lower than that required for uplift, therefore the statue is in full contact.

Figure 122 shows a comparison between the accelerations at the base of the statue before the intervention with those after the intervention according to the experimental test and the numerical model. This latter is developed following section 5.2.2. The numerical model is less accurate, failing to capture the maximum acceleration values. Although the grooves show no damage, the effect of indentation due to static loads remains. Differently from the case of harmonic excitation, for which a very good match was observed for the displacements, in this case the numerical model underestimates quite significantly the absolute accelerations. This is explained by the fact that the proposed numerical model does not account for the effect of the pit induced in the grooves by the static loads, which results in a reduction of radius of curvature and thus in higher stiffness and accelerations compared to those obtained disregarding this effect.

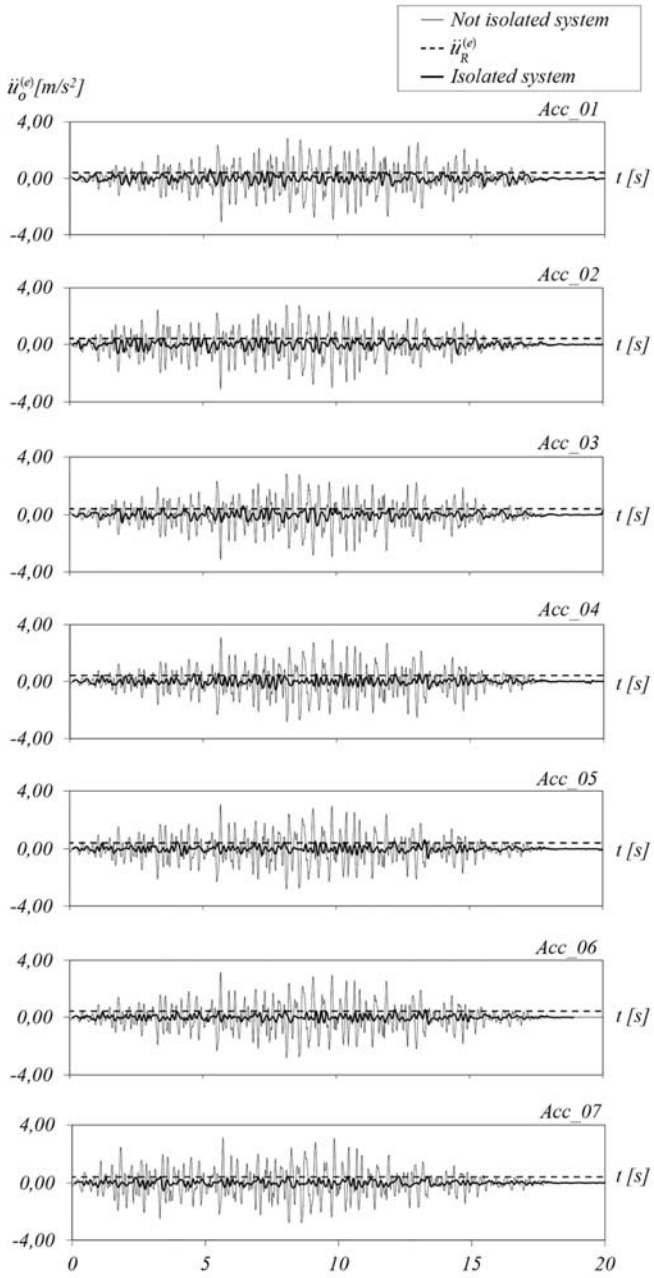

Figure 121 - Acceleration at the base of the statue before and after the intervention. [Author's image].

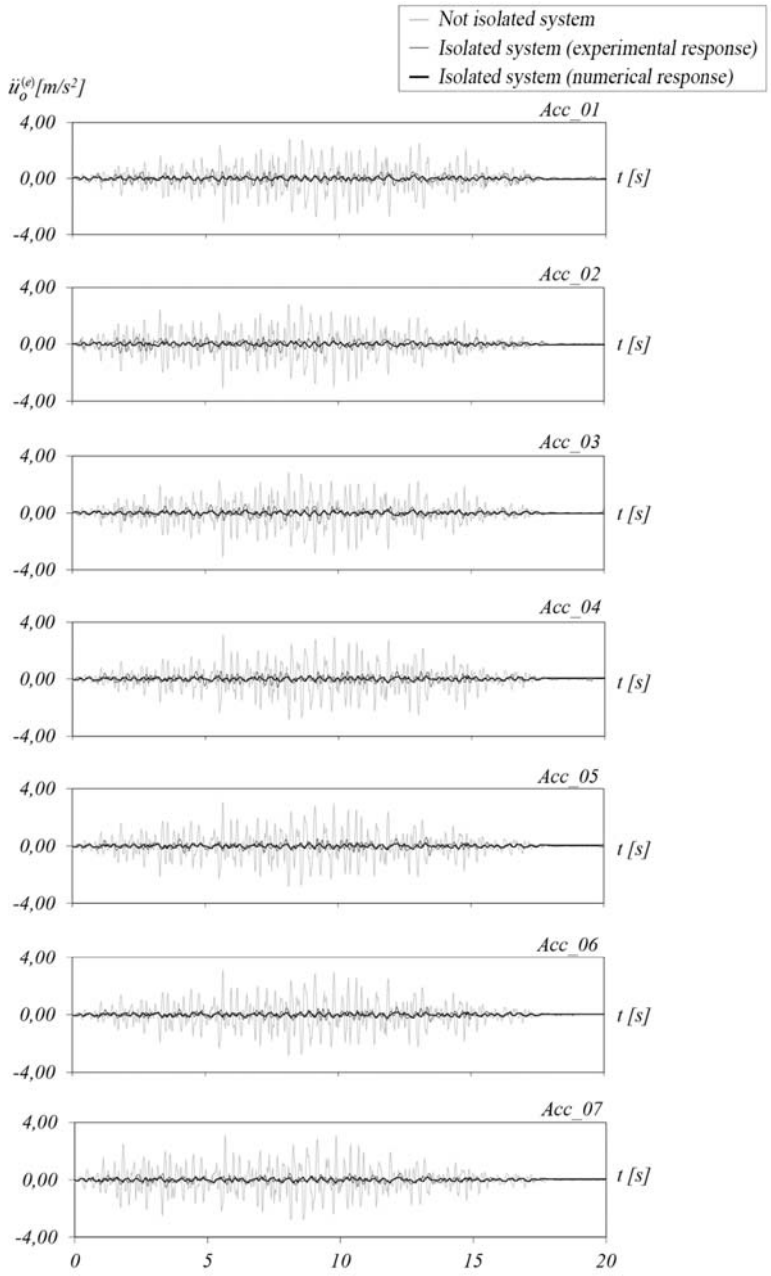

Figure 122 - Comparison between the accelerations at the base of the statue before the intervention with those after the intervention numerically and experimentally obtained. [Author's image].

Chapter 7 Conclusions

The study, taking advantage of an extensive experimental campaign, clarified some aspects concerning the behavior of rigid bodies with small dimensions, such as artworks, and their seismic protection using a novel low-cost rolling ball isolator system.

A contactless measurement strategy was adopted to assess the response of all the specimens (prismatic wooden blocks, scaled prototype of the Venere Landolina, ball system isolator and static-dynamic interchangeable ball system isolator prototypes), monitoring target points using a high resolution and high acquisition frequency camera. A test protocol, based on 2D point tracking technique, was arranged and its effectiveness confirmed by the analysis of the oscillatory motion of the rigid blocks and isolating devices. The principal innovative results achieved in the present Ph.D. research are pointed hereafter.

- *Experimental database and observation of phenomena from tests involving prismatic rigid blocks.*

  A detailed and overall characterization of the real dynamic behavior of small symmetrical rigid blocks with different aspect ratios and size factors was presented, arranging experimental *stability spectra* (in case of one-cosine pulse input) and *maximum rotation variability graphs* (considering the Friuli earthquake ground motion). The use of videogrammetry allowed identifying the reduced uplift acceleration registered during laboratory experiments and its comparison with the theoretical value pertaining ideal conditions. Consequently, it was demonstrated the reduced capacity in terms precocious overturning. Geometric imperfections are identified as the main factors that influence the premature start of rocking and give rise to a marked uncertainty of the response. It was confirmed that the seismic capacity of the real block is lower than that evaluated with reference to the classical formulation based

on Housner's theory. The restitution coefficient is the main parameter governing the block response and must be carefully evaluated especially to numerically predict the character of the response in presence of many impacts.

- *Rocking behavior of unsymmetrical rigid bodies with imperfections*

  A novel numerical model for the analysis of lightweight asymmetric imperfect bodies is presented. The model can account for a reduced uplift acceleration with respect to the theoretical one related to the ideal conditions (i.e. perfect contact and sharp basement edges) and a procedure for its determination is proposed. Moreover, the model comprises imperfect conditions typical of existing objects, for instance statues, vases, and artworks in general, considering the possibility that the body can oscillate without rocking. The experimental results proved that classical numerical models could fail in the prediction of the actual dynamic response of rigid blocks leading to wrong safety considerations.

- *Combined experimental and numerical strategy to assess the seismic safety of real statues*

  To validate the proposed model, a methodology based on experimental results, performed on scaled objects, and numerical simulations was proposed. The procedures allows the identification of the coefficient of restitution accounting for impact velocity in case of asymmetric specimens subjected to free rocking motion. Moreover, it is possible to evaluate the unbiased initial condition of motion by detecting actual uplift acceleration, thanks to the coefficients α_L and α_R, experimentally determined using

one-cosine input ground motion. A great advantage of the proposed strategy is the possibility to assess the seismic safety of real statues by experimentally investigating the nonlinear dynamic response of 'scaled' objects on the basis of a detailed 3D digital model of the real object. The numerical simulations were compared with experimental results demonstrating the model's capability to predict the response with a sufficient approximation.

- *The behavior of wooden rolling ball isolating devices, with rubber layer and fuse*

  The parameters of an effective protection device must be chosen only after a correct assessment of the uplift acceleration of the asset to be preserved avoiding the uplift of the top plate of the device. A design procedure for the BPS and SDI-BPS isolation system, is proposed to this aim. A procedure for estimating the rolling friction coefficient was arranged; its increase due to the presence of rubber layers was evaluated. The different behavior with respect to the theoretical model is justified by the presence of imperfections in the geometry of the device as evidenced by the experimental force-displacement relationship. It was experimentally demonstrated that the application of excessive vertical loads alters the shape of grooves if a rubber layer is missing and consequently modifies the dynamic behavior. The behavior of a novel prototype equipped with a restraint system for vertical loads (fuse) was experimentally evaluated. Two types of behavior for different levels of PGA are recognized in the presence of fuse. In the first case the upper and lower plates move almost together with the ground, whereas in the second case the behavior is governed by the geometry of the grooves.

- *Development of a numerical model for describing the seismic response of rigid blocks endowed with a rolling ball system isolator.*

  The efficiency of the device for the protection of the scaled model representing the Venere Landolina was evaluated experimentally. It was demonstrated that the procedure for designing the device works well when the rocking of the statue does not trigger.

  It was also demonstrated that, although the caps show no damage, the numerical model works well for simple inputs (e.g. sinusoidal) able to produce a pronounced response. On the other hand, a reduced accuracy is observed in the motion phases corresponding to small displacements close to the static equilibrium position; the latter aspect is probably associated to the effects of indentation caused by the application of static loads, which are neglected by the model.

References

[1] M.S. Agbabian, S.F. Masri, R.L. Nigbor, W.S.Ginell, *Seismic damage mitigation concepts for art objects in museum*, Proceeding of Ninth World Conference on Earthquake Engineering, August 2-9, 1988, Tokyo-Kyoto, Japan (Vol. III).

[2] M.S. Agbabian, W.S.Ginell, S.F. Masri, R.L. Nigbor, *Evaluation of earthquake damage mitigation methods for museum objects*, Studies in Conservation 36 (1991), 111-120.

[3] J. Milne, *Experiments in observational seismology*, Trans, seism. Soc. Japan 3, 12-64, 1881.

[4] G. W. Housner, *The behavior of inverted pendulum structures during earthquakes*, Bulletin of the Seismological Society of America, Vol. 53, No. 2, pp. 403-417, 1963.

[5] C. S. Yim, A. K. Chopra, J. Penzien, *Rocking Response of rigid block to earthquakes*, Earthquake engineering research centre, Report no. UCB/EERC-80/02, January 1980.

[6] M. Aslam, W.G. Godden, D. T. Scalise, *Earthquake Rocking Response of Rigid Bodies*, Prepared for the Department of Energy under Contract W-7405-ENG-48.

[7] P. D. Spanos, A. S. Koh, *Rocking of rigid blocks due to harmonic shaking*, J. Eng. Mech., 1984, 110(11): 1627-1642.

[8] P. R. Lipscombe, S. Pellegrino, *Free rocking of prismatic blocks*, J. Eng. Mech., 1993, 119(7): 1387-1410.

[9] E. Ferretti, A. Rosati, I. Caliò, *Modellazione del comportamento dinamico di oggetti d'arte*, Nota Tecnica n. 146, Anno 2004, DISTART, Università degli Studi di Bologna.

[10] N. Makris, Y. Roussos, *Rocking response of rigid blocks under near-source ground motions*, Géotechnique 50, No. 3, 243-262, 2000.

[11] F. Peña, F. Prieto, P. B. Lourenco, A. Campos Costa, J. V. Lemos, *On the*

dynamics of rocking motion of single rigid-block structures, Earthquake Engineering and Structural Dynamics, Earthquake Engng struct. Dyn. 2007; 36:2383–2399.

[12] N. Makris, *A half-century of rocking isolation*, Earthquakes and Structures, Vol. 7, No. 6 (2014) 1187-1221.

[13] C. Tocci, *Dinamica delle strutture a blocchi sovrapposti. Le colonne isolate*, Tesi presentata per il conseguimento del titolo di Dottore di Ricerca in Storia delle Scienze e delle tecniche costruttive, Facoltà di architettura Università di Roma "La Sapienza", 1996, Roma.

[14] C. Casapulla, L. Giresini, P. B. Lourenço, *Rocking and kinematic approaches for rigid block analysis of masonry walls: state of the art and recent developments*, Buildings 2017, 7, 69; doi:10.3390/buildings 7030069.

[15] H. Al Abadi, V. Paton-Cole, E. Gad, N. Lam, V. Patel, *Rocking Behavior of Irregular Free-Standing Objects Subjected to Earthquake Motion*, Bulletin of Earthquake Engineering, 2017-Journal of Earthquake Engineering.

[16] Christine Erin Wittich, *Seismic Response of Freestanding Structural Systems: Shake Table Tests and Model Validation*, dissertation submitted in partial satisfaction of the requirements for the degree Doctor of Philosophy in Structural Engineering, University of California, San Diego.

[17] G. Augusti, A. Sinopoli, *Modelling the dynamics of large block structures*, Meccanica 27: 195-211, 1992.

[18] I. N. Psycharis, P. Jennings, *Upthrow of objects due to horizontal impulse excitation*, Bulletin of the Seismological Society of America, Vol. 75, No. 2, pp. 543-561, April 1985.

[19] Q. T. Ma, J. W. Butterworth, *Simplified Expressions for Modelling Rigid Rocking Structures on Two-spring Foundations*, 2010 NZSEE Conference.

[20] A. Chopra, M. Asce, S. C. S. Yim, A. M. Asce, *Simplified earthquake analysis of structures with foundation uplift*, J. Struct. Eng., 1985, 111(4): 906-930.

[21] O. Al Shawa, G. De Felice, A. Mauro, L. Sorrentino, *Out-of-plane seismic behavior of rocking masonry walls*, Earthquake Engng Struct. Dyn. 2012; 41:949–968.

[22] D. Capecchi, R. Giannini, R. Masiani, *Motion of a rigid body with a rounded base due to harmonic motion*, Int. J. Non-Linear Mechanics, Vol. 3, No. 2, pp. 175-191, 1996.

[23] J. A. Bachmann, M. F. Vassiliou, B. Stojadinovic, *Rolling and rocking of rigid uplifting structures*, Earthquake Engng Struct Dyn. 2019;48:1556-1574.

[24] J. A. Bachmann, P. Blöchlinger, M. Wellauer, M. F. Vassiliou, B. Stojadinović, *Experimental investigation of the seismic response of a column rocking and rolling on a concave base*, ECCOMAS Congress 2016 VII European Congress on Computational Methods in Applied Sciences and Engineering M. Papadrakakis, V. Papadopoulos, G. Stefanou, V. Plevris (eds.) Crete Island, Greece, 5–10 June 2016.

[25] H. Lin, C.S. Yim, *Nonlinear rocking motion. I: Chaos under noisy periodic excitations*, Journal of engineering mechanics, 719, August 1996.

[26] M.A. ElGawady, Q. Ma, J. Butterworth, J.M. Ingham, *Probabilistic Analysis of Rocking Blocks*, 2006 NZSEE Conference, Paper Number XXX.

[27] N. Torunbalci, *Seismic isolation and energy dissipating systems in earthquake resistant design*, 13th World Conference on Earthquake Engineering, Vancouver, B.C., Canada, August 1-6, 2004, Paper No. 3273.

[28] L. Di Sarno, A. S. Elnashai, *Innovative strategies for seismic retrofitting of steel and composite structures*, Wiley InterScience, DOI: 10.1002/pse.195.

[29] N. K. Rai, G.R. Reddy, S. Ramanujam, V. Venkatraj and P. Agrawal, *Seismic Response Control Systems for Structures,* Defence Science Journal, Vol. 59, No. 3, May 2009, pp. 239-251.

[30] J. Podany, *Protecting Collections in the J. Paul Getty Museum from Earthquake Damage*, WAAC Newsletter, Volume 29, Number 3 September 2007.

[31] J. Podany, *An Overview of Seismic Damage Mitigation for Museums*, International Symposium on Advances of Protection Devices for Museum Exhibits, April 13-17, 2015 Beijing and Shanghai China.

[32] J. Podany, *Earthquake damage mitigation for museum collections*, 10th Anniversary 1999 Chi Chi Earthquake International Conference on Historical Building Restoration, September 21-23, 2009 Puli Taiwan.

[33] Nevra Ertürk, *Seismic protection of museum collections: lessons learned after the 1999 earthquakes in Turkey*, Metu Jfa, 2012.

[34] T. Favaretto, Assessment and Reduction of Seismic Vulnerability of Art Objects, Dissertation for degree Doctor of Philosophy, University of Florence, 2012.

[35] D. M. Fenz, M. C. Constantinou, *Behavior of the double concave Friction Pendulum bearing*, Earthquake Engng Struct. Dyn. 2006; 35:1403–1424.

[36] P. M. Calvi, M. Moratti, G. M. Calvi, *Isolatori sismici a scorrimento con materiali a diverso coefficiente di attrito*, Progettazione Sismica – Vol. 6, N. 1, Anno 2015.

[37] V. Zayas, *Earthquake protective column support*, United States patent US4644714A. 1987.

[38] S. Baggio, L. Berto, I. Rocca, A. Saetta, *Vulnerability assessment and seismic mitigation intervention for artistic assets: from theory to practice*, Engineering Structures 167 (2018) 272–286.

[39] C.S. Tsai, Y. C. Lin, H. C. Su, *Characterization and modelling of multiple friction pendulum isolation system with numerous sliding interfaces*, Earthquake Engng Struct. Dyn. 2010; 39:1463–1491.

[40] C. S. Tsai, W.S. Chen, Y. C. Lin, C. P. Tsou, C. C. Chen, C. L. Lin, *Shaking Table Tests of Motion Sensitive Equipment Isolated with Static Dynamics Interchangeable-Ball Pendulum System*, The 14th World Conference on Earthquake Engineering October 12-17, 2008, Beijing, China.

[41] E. Matta, A. De Stefano, B. F. Spencer, *A new passive rolling-pendulum vibration absorber using a non-axial-symmetrical guide to achieve bidirectional tuning*, Earthquake Engng Struct. Dyn. 2009; 38:1729–1750 K.

[42] M.G. Kesti, W. Mowrtage, M. Erdik, *Earthquake Risk Reduction of Structures by A Low-Cost Base Isolation Device : Experimental Study on BNC Bearings*, 14th European Conference on Earthquake Engineering 2010 Ohrid, Republic of Macedonia 30 August - 3 September 2010.

[43] A. Tayaran, M. Hosseini, *Pillow-Shape Base Isolation System and Its Seismic Behavior*, Journal of Structural Engineering and Geotechnics 5 (2), 25-34, Spring 2015.

[44] C. Y. Yang, C. H. Hsieh, L. L. Chung, H. M. Chen, L. Y. Wu, *Effectiveness of an eccentric rolling isolation system with friction damping*, Journal of Vibration and Control, 18(14) 2149–2163.

[45] M. Froli, L. Giresini, F. Laccone, *A new seismic isolation device based on tribological smooth rocking*, 7th ECCOMAS Thematic Conference on Computational Methods in Structural Dynamics and Earthquake Engineering M. Papadrakakis, M. Fragiadakis (eds.) Crete, Greece, 24–26 June 2019.

[46] M. Ismail,J. Rodellar, *Experimental investigations of a rolling-based seismic isolation system*, Journal of Vibration and Control 1–20.

[47] A. Jamalzadeh, M. Barghian, *Dynamic Response of a Pendulum Isolator System under Vertical and Horizontal Earthquake Excitation*, Periodica Polytechnica Civil Engineering, 59(3), pp. 433–440, 2015.

[48] M. Donà, A. Muhr, G. Tecchio, G. Granello, *Rolling ball rubber layer isolation system. Small deflection and vibrational behavior*, SECED 2015 Conference: Earthquake Risk and Engineering towards a Resilient World, 9-10 July 2015, Cambridge UK.

[49] A. E. Charalampakis, *Parameters of Bouc-Wen hysteretic model revisited*, 9th HSTAM International Congress on Mechanics Limassol, Cyprus, 12 – 14 July, 2010.

[50] A. H. Muhr, G. Bergamo, *Shaking Table Tests On Rolling-Ball Rubber-Layer Isolation System*, 14th ECEE European Conference on Earthquake Engineering 2010, Ohrid, Republic of Macedonia, 30 August - 3 September 2010.

[51] L. Guerreiro , J. Azevedo, A. H. Muhr, *Seismic tests and numerical modelling of a rolling ball isolation system*, Journal of Earthquake Engineering, 11:49–66, 2007.

[52] M. Donà, A. H. Muhr, *Biaxial model for the Rolling-Ball Rubber-Layer Isolation System*, In Constitutive Models for Rubber IX – Marvalova & Petrikova (Eds), Publ. Taylor & Francis Group, London, 2015 pp585-590.

[53] P.D. Spanos, A. Di Matteo, A. Pirrotta, M. Di Paola, *Nonlinear rocking of rigid blocks on flexible foundation: analysis and experiments*, Procedia Engineering 199 (2017) 284–289.

[54] M. A. ElGawady, Q. Ma, J. Butterworth, J. M. Ingham, *The effect of interface material on the dynamic behavior of free rocking blocks*, Proceedings of the 8th U.S. National Conference on Earthquake Engineering, April 18-22, 2006, San Francisco, California, USA, Paper No. 589.

[55] D. Kalliontzis, and S. Sritharan, *Characterizing Dynamic Decay of Motion of Free-standing Rocking Members*, Earthquake Spectra(2018),34(2):843

[56] J. A. Bachmann, M. Strand, M. F. Vassiliou, M. Broccardo, B. Stojadinovic, *Is rocking motion predictable?*, Earthquake Engng Struct Dyn. 2018;47: 535–552.

[57] I. Caliò, M. Marletta, *Passive control of the seismic rocking response of art objects*, Engineering Structures 25 (2003) 1009–1018.

[58] A. Di Egidio, A. *Contento, Base isolation of slide-rocking non-symmetric rigid blocks under impulsive and seismic excitations*, Engineering Structures 31 (2009) 2723-2734.

[59] Y. Kishi, K. Izuno, K. Toki, *Protection of art objects in earthquakes with seismic devices*, The 14th World Conference on Earthquake Engineering

October 12-17, 2008, Beijing, China.

[60] J. Baqersad, P. Poozesh, C. Niezrecki, P. Avitabile, *Photogrammetry and optical methods in structural dynamics – A review*, Mechanical Systems and Signal Processing, 86(2017)17–34.

[61] G. De Canio, M. Mongelli, I. Roselli, A. Tatì, *Elaborazione di dati di spostamento da sistema di motion capture 3D per prove su tavola vibrante*, Conference: XV Convegno ANIDIS, June 2013.

[62] Centrotecnica s.r.l., Lo.F.Hi.S. user manual.

[63] A. N. Kounadis, *On the Overturning Instability of a Rectangular Rigid Block Under Ground Excitation*, The Open Mechanics Journal (2010) 4:43-57.

[64] G. Cocuzza Avellino, I. Caliò, F. Cannizzaro, S. Caddemi, N. Impollonia, Response spectra of rigid blocks with uncertain behavior, COMPDYN 2019 7th ECCOMAS Thematic Conference on Computational Methods in Structural Dynamics and Earthquake Engineering M. Papadrakakis, M. Fragiadakis (eds.) Crete, Greece, 24–26 June 2019.

[65] N. Makris, *A half-century of rocking isolation*, Earthquakes and Structures, Vol. 7, No. 6 (2014) 1187-1221.

[66] A. K. Chopra, *Dynamics of structures. Theory and applications to earthquake engineering. Third edition*, Pearson Prentice Hall, Upper Saddle River, New Jersey.

[67] M. Donà, G. Tecchio, C. Modena, A. H. Muhr, *Rolling-ball rubber-layer isolation system: state of the art, performance and design procedure*, 5th ECCOMAS Thematic Conference on Computational Methods in Structural Dynamics and Earthquake Engineering, M. Papadrakakis, V. Papadopoulos, V. Plevris (eds.), Crete Island, Greece, 25–27 May 2015.

[68] G. Cocuzza Avellino, F. Cannizzaro, A. Di Martino, R. Valenti, E. Paternò, I. Caliò, N. Impollonia, *Numerical and experimental behaviour of art objects subjected to ground motion*, submitted to International Journal of Architectural Heritage;

[69] R. Valenti, E. Paternò, *The Itineraries of Drawing: from museum works to art places*, Territories and frontiers of representation, Roma: Gangemi Editore, 2017, p. 1307-1314.

[70] R. Valenti, E. Paternò, *Imagined spaces in church architectural furnishings: Solomon's temple in small scale architectural language*, Advances in Utopian Studies and Sacred Architecture, Cham: Springer, in press, 2020.

[71] A. Di Egidio, A. Contento, , *Seismic response of a non-symmetric rigid block on a constrained oscillating base*, Engineering Structures (2010) 32:3028–3039.

[72] Ministero delle infrastrutture e dei trasporti, Decreto 17 gennaio 2018, Aggiornamento delle "Norme tecniche per le costruzioni" – NTC18.

[73] Linee guida per la valutazione e la riduzione del rischio sismico del patrimonio culturale con riferimento alle Norme tecniche per le costruzioni di cui al decreto del Ministero delle Infrastrutture e dei trasporti del 14 gennaio 2008

[74] Seismosoft 2020 "SeismoArtif - A computer program for generation of artificial accelerograms". Available from URL: www.seismosoft.com.

[75] S. Longo, *Analisi dimensionale e modellistica fisica. Principi e applicazioni alle scienze ingegneristiche*, Springer-Verlag, Italia 2011.

[76] E. Buckingham, *On physically similar systems. Illustrations of the use of dimensional equations Physical Review* (1914) 4(4):345-376.